Higher order QCD corrections to diboson production at hadron colliders

Raoul Horst Röntsch

Corpus Christi College

University of Oxford

A thesis submitted for the degree of

Doctor of Philosophy

Trinity 2012

To my parents

My sincerest thanks to my supervisor, Giulia Zanderighi, who has been a constant source of guidance, inspiration, and knowledge over the past four years. I am also deeply indebted to my collaborators Kirill Melnikov, Paolo Nason and Markus Schulze, from whom I have learned a lot. In particular, I thank Tom Melia, who has worked with me for four years and who has helped me grapple with the concepts required to do these projects. His help and energy have been invaluable. Thanks also to my examiners, Joe Conlon and Jeppe Andersen, whose suggestions have helped improve the final version of this thesis.

For my first three years, I was supported by a Rhodes Scholarship, and I am grateful to the Rhodes Trust who made it possible for me to study at Oxford, and to the Warden and his team at Rhodes House for being so welcoming to me. In my fourth year, I have been supported by the Rudolf Peierls Centre for Theoretical Physics as well as Corpus Christi College, and I thank them for their generosity. Thanks also to the administrative teams of both institutions for help along the way.

I have been priviledged to be part of an enthusiastic and vibrant department, and I thank all faculty, post-docs and students for helping to create this exciting environment in which to work. Some of the work in this thesis was done while I was a guest at Johns Hopkins University in Baltimore, USA, and at CERN in Geneva, Switzerland, and I thank both institutions for their kind hospitality. Thanks also to Warrick Ball who provided helpful comments on my thesis.

Finally, I am grateful too to my friends and family (too numerous to name) who have been supportive and entertaining. Thank you also to my amazing girlfriend Lauren Schwartzman, whose love and understanding have seen me through this task. Finally, a big thank you to my parents and my brother Marc, for love and support over the years.

Abstract

Hadronic collider experiments have played a major role in particle physics phenomenology over the last few decades. Data recorded at the Tevatron at Fermilab is still of interest, and its successor, the Large Hadron Collider (LHC) at CERN, has recently announced the discovery of a particle consistent with the Standard Model Higgs boson. Hadronic colliders look set to guide the field for the next fifteen years or more, with the discovery of more particles anticipated.

The discovery and detailed study of new particles relies crucially on the availability of high-precision theoretical predictions for both the signal and background processes. This requires observables to be calculated to next-to-leading order (NLO) in perturbative quantum chromodynamics (QCD). Many hadroproduction processes of interest contain multiple particles in the final state. Until recently, this caused a bottleneck in NLO QCD calculations, due to the difficulty in calculating one-loop corrections to processes involving three or more final state particles. Spectacular developments in on-shell methods over the last six years have made these calculations feasible, allowing highly accurate predictions for final state observables at the Tevatron and LHC.

A particular realisation of on-shell methods, generalised unitarity, is used to compute the NLO QCD cross-sections and distributions for two processes: the hadroproduction of W^+W^+jj, and the hadroproduction of W^+W^-jj. The NLO corrections to both processes serve to reduce the scale dependence of the results significantly, while having a moderate effect on the central scale choice cross-sections, and leaving the shapes of the kinematic distributions mostly unchanged. Additionally, the gluon fusion contribution to the next-to-next-to-leading order (NNLO) QCD corrections to W^+W^-j productions are studied. These contributions are found to be highly dependent on the kinematic cuts used. For cuts used in Higgs searches, the gluon fusion effect can be as large as the NLO scale uncertainty, and should not be neglected. All of the higher-order QCD corrections increase the accuracy and reliability of the theoretical predictions at hadronic colliders.

Contents

Chapter 1

Introduction

1.1 Motivation and background

Our current understanding of elementary particle physics is described by the Standard Model (SM). This posits two types of fermions: quarks and leptons, each existing in three generations with two particles per generation. Quarks are charged under an $SU(N_c)$ colour symmetry, with $N_c = 3$, and their interactions with the gauge bosons of this symmetry – gluons – are governed by quantum chromodynamics (QCD), the theory of the strong force. All fermions are charged under an $SU(2) \times U(1)$ symmetry, which is spontaneously broken by the Higgs mechanism, leading to a massless photon and massive W- and Z-bosons. The former transmits the electromagnetic interaction, experienced by quarks and charged leptons, while the latter transmits the weak interaction, which all fermions experience. The Higgs mechanism also gives masses to the fermions, as well as giving rise to a scalar Higgs boson. These theories are discussed in (slightly) more detail in sections 1.2 and 1.3. The fourth force, gravity, is not understood at the quantum level and is therefore not included in the SM; at collider energies, this force is negligible.

The SM has been confirmed by numerous experimental tests over the years. The final piece of the puzzle was the Higgs boson. Experiments at both the Tevatron proton-antiproton collider at Fermilab and the LEP electron-positron collider at CERN were inconclusive: no evidence of a Higgs was observed, but fairly stringent exclusion limits were placed on its mass [1,2]. The recent discovery by the Large Hadron Collider (LHC) of a boson "consistent with the Standard Model Higgs boson" in the mass range m_H = 124-127 GeV [3,4] completes the experimental observation of all SM particles. Notwithstanding this groundbreaking discovery, until the couplings of the new particle to the SM fermions and electroweak gauge bosons are measured, it is not possible to say whether it is the simplest (SM) Higgs mechanism that breaks electroweak symmetry, or whether some New Physics is at play[1]. The remainder of the current LHC run, and more importantly, the higher-energy run beginning in 2014, will give further insight into its properties. The era of Higgs phenomenology is just beginning.

The discovery of the scalar Higgs boson also intensifies the so-called hierarchy problem, essentially a statement that electroweak symmetry should naturally be bro-

---

[1] Hereafter, unless otherwise indicated, "Higgs boson" refers to the SM Higgs boson.

ken at the GUT scale, rather than at a scale some 12 orders of magnitude lower. This, together with several other unanswered questions – including the presence of dark matter, the strong CP-problem, and the non-zero masses of neutrinos – suggests that the Standard Model is a low-energy effective theory of some more fundamental higher-energy theory. Foremost among these Beyond the Standard Model (BSM) theories is supersymmetry (SUSY), which is based on the idea of an additional space-time symmetry present at high energies, which is broken at SM energies $\mathcal{O}(0.1 - 1 \text{ TeV})$. Finding evidence of this or other BSM theories is another goal of the LHC. To date, no evidence of BSM physics has been observed, although there are some tensions between experimental results and Standard Model predictions (e.g. the anomalous magnetic moment of the muon [5] and the top asymmetry [6]).

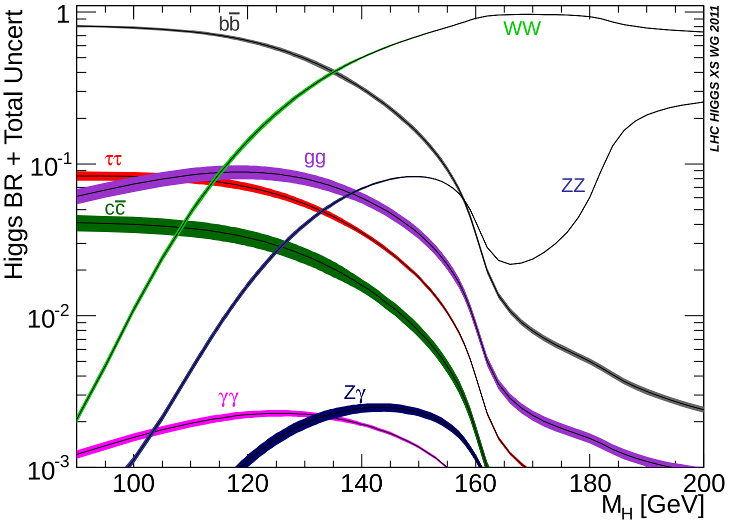

Figure 1.1: Branching ratios of various Higgs decay modes as a function of Higgs mass. The figure is taken from ref. [7].

Figure 1.1 shows the branching ratios of the various decay modes of the Higgs boson. A full mass reconstruction is possible in the $H \to \gamma\gamma$ and $H \to ZZ \to l_1^+ l_1^- l_2^+ l_2^-$ channels. This allowed these channels to drive the discovery of the Higgs [3,4], despite their small branching ratios for a Higgs mass $m_H \simeq 125$ GeV. In the $H \to WW$ mode, the subsequent leptonic decay of the W-bosons, $W \to l\nu$, gives the cleanest experimental signal. The final state neutrinos cannot be detected, although their presence can be inferred from the missing energy they carry. This means that a mass reconstruction is not possible in this channel. However, it is still an important channel, for two main reasons. First, its branching ratio is large. The only channel with a larger branching ratio is $H \to b\bar{b}$, which suffers from a large QCD background. There are also experimental difficulties related to the identification of b-quarks[2]. Second, the decay to a W-pair gives insight into the relationship between the Higgs boson and the electroweak bosons, which is important in order to establish whether the Higgs is SM-like or not.

---

[2] These obstacles may be circumvented by the use of jet decomposition in boosted Higgs production in association with an electroweak boson [8].

In order to investigate the properties of the Higgs boson, or to find any evidence of New Physics, it is important to have an accurate theoretical description of both the signal and background processes. At hadron colliders, the effects of the strong force are important. At collider energies, for processes involving the production of hard jets and/or massive electroweak bosons or other heavy particles, the strong coupling is small and the factorisation theorem allows observables to be calculated order-by-order in perturbative QCD (pQCD). This will be discussed in more detail in section 2.1. As can be seen in figure 1.2, comparison of these perturbative expansions with the data from Tevatron reveals that a leading-order (LO) description is often not sufficient: next-to-leading order (NLO) calculations[3] are needed [9]. Furthermore, two scales are present in QCD calculations: a renormalisation scale μ_R and a factorisation scale μ_F (see section 1.2). An observable calculated to all orders in pQCD is independent of these scales, but truncating the pQCD expansion leads to an unphysical dependence on these scales. This dependence is far smaller at NLO in pQCD than at LO, enabling a more reliable result to be obtained.

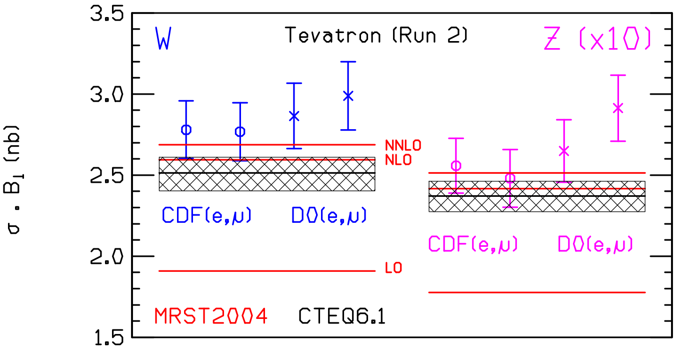

Figure 1.2: Comparison of cross-sections of W- and Z-boson production observed at the Tevatron (data points) to leading-order and next-to-leading order pQCD predictions (shaded regions). The figure is taken from ref. [9]

Higgs signals are binned according to the number of jets produced in association with the signal. The background processes in the n-jet channel can then be identified. The results[4] for the 0-jet bin have been calculated to NLO in QCD [11–13] and to next-to-next-to-leading order (NNLO) in the limit of an infinitely heavy top quark [14–16]. The NLO corrections to $H + j$ production are known [17–19]. Higgs production in association with two jets can occur through either gluon fusion (GF) or weak boson fusion (WBF). The cross-sections to NLO for both production mechanisms have been calculated [20–22]. These calculations have been implemented in several Monte Carlo parton-level programs, such as `MCFM` [23–25], `HAWK` [26, 27] and `VBFNLO` [28]. Interface to parton showering programs such as `PYTHIA` [29] or `HERWIG++` [30] are also provided through the `POWHEG` [31–33] and `MC@NLO` programs [34].

The hadroproduction of W^+W^- with $0, 1$ or 2 jets is an irreducible background to Higgs processes in the $H \to W^+W^-$ decay channel. This background without

---

[3] Unless otherwise stated, LO, NLO and NNLO refer to the expansion in pQCD throughout this work.

[4] For a review, see the LHC Higgs Cross Section Working Group reports [7, 10] and references therein.

associated jets is known to NLO [35–38], and has been implemented in `MCFM` [39], `POWHEG` [40], and `MC@NLO` [41]. The important gluon fusion contribution to the NNLO cross-section is also known [42, 43]. The production of $W^+W^- + j$ is known to NLO [44–46]. Prior to the work reported in this thesis, the production with two associated jets was not known, nor had the gluon fusion process been studied for W-pair production in association with jets.

Computations of the signal, and more notably, the background processes to NLO in QCD are hampered by the difficulty of computing one-loop corrections to processes with three or more final state particles. Indeed, until 2006, no 2 → 4 particle process was known to NLO. The situation has improved dramatically during the intervening six years. Improvements [47–49] to the Feynman diagram-based Passarino-Veltman reduction [50] allowed several 2 → 4 processes to be computed to NLO using these methods [51–54]. More importantly, a revolution in the application of unitarity to one-loop amplitudes [55–63] opened the floodgates, and to date all the 2 → 4 NLO processes published in the "Experimentalists' Wishlists" [64–66] have been calculated [67–74, 74–82] (for a detailed breakdown, see ref. [83]). These methods rely heavily on the colour-ordering of external particles. The work reported in this thesis represents their first application to processes involving more than one colour-neutral external particle.

This thesis will report on NLO calculations of the hadroproduction of both same-sign W^+W^+ [77] and opposite sign W^+W^- [82] production in association with two jets, as well as the calculation of the gluon fusion contribution to the NNLO description of $W^+W^- + j$ [84]. Virtual amplitudes are calculated using the Ossola-Papadoupoulos-Pittau (OPP) subtraction procedure [57] with generalised D-dimensional unitarity [61–63] (for a review, see ref. [85]). These methods allow one-loop amplitudes to be evaluated through tree-level helicity amplitudes.

The remainder of the thesis is organised as follows. The next two sections of the Introduction provide a brief summary of QCD and electroweak theory (including electroweak symmetry breaking through the Higgs mechanism). The basics of computing observables to NLO is discussed in chapter 2. A detailed discussion of the methods used to calculate one-loop amplitudes follows in chapter 3. The evaluation of the tree-level amplitudes that are used in these methods is discussed in chapter 4. The computation of the hadroproduction of W^+W^+jj and W^+W^-jj to NLO is reported in chapters 5 and 6. In chapter 7, the computation of the gluon-induced NNLO contribution to W^+W^-j is discussed. I conclude in chapter 8.

As a final note, the work discussed in this thesis was done in collaboration with T. Melia, K. Melnikov, M. Schulze and G. Zanderighi, and reported in refs. [77,82,84]. It is not straightforward to disentangle who was responsible for what part of the work. The generalised unitarity framework had been implemented previously. In the case of refs. [77, 82] this was embedded in `MCFM` and used for the study of $W + 3j$ [70, 86, 87]. The implementation in the private code `TOPAZ`, used in top-quark phenomenology [88–92], was used for ref. [84]. My contribution to the collaboration was focused on computing the leading-order and real radiation matrix elements, as well as the primitive amplitudes, especially for the W^+W^+jj process and the four-quark W^+W^-jj sub-processes. To do so, I constructed most of the Berends-Giele currents involving two electroweak bosons. I also computed the fermion loop primitive amplitudes used in chapter 7, modifying `TOPAZ` extensively in the process. I had little to do with the computation of the subtraction dipoles or integrated dipoles. I have tried to reflect this in the emphasis placed on the various sections throughout.

1.2 Quantum Chromodynamics

Quantum chromodynamics (QCD) is the quantum field theory describing the strong force. It is based on a local $SU(N_c)$ symmetry, with $N_c = 3$ colours. The fundamental (antifundamental) representations of this group are quarks (antiquarks); the adjoint representation are gluons. It has both infrared and ultraviolet divergences, but is fully renormalisable through a redefinition of the wave functions, strong coupling constant g_s, and the quark mass m. The renormalised coupling is a decreasing function of energy – this leads to the famed asymptotic freedom, allowing perturbative QCD (pQCD) to be applied at sufficiently high energies.

1.2.1 QCD Lagrangian

The QCD Lagrangian is [93]

$$\mathcal{L}_{\text{QCD}} = \mathcal{L}_{\text{gl}} + \mathcal{L}_{\text{quark}} + \mathcal{L}_{\text{FP}} + \mathcal{L}_{\text{gh}}. \tag{1.2.1}$$

The first term describes the purely gluonic part of the Lagrangian

$$\mathcal{L}_{\text{gl}} = -\frac{1}{4} G^{a\mu\nu}(x) G^a_{\mu\nu}(x), \tag{1.2.2}$$

with

$$G^a_{\mu\nu}(x) = \partial_\mu B^a_\nu(x) - \partial_\nu B^a_\mu(x) + g_s f^{abc} B^b_\mu(x) B^c_\nu(x), \tag{1.2.3}$$

where Roman superscripts a, b, c are indices for the adjoint representation of the $SU(3)$ colour group, f^{abc} are the structure constants of this group, B are the gluonic fields, and g_s is the strong coupling constant. Writing $\mathcal{L}_{\text{gl}}$ in full

$$\mathcal{L}_{\text{gl}} = -\frac{1}{4}\Big((\partial_\mu B^a_\nu - \partial_\nu B^a_\mu)^2 + 4 g_s f^{abc} (\partial_\mu B^a_\nu) B^{b\mu} B^{c\nu} + g_s^2 f^{abc} f^{ade} B^{b\mu} B^{c\nu} B^d_\mu B^e_\nu \Big). \tag{1.2.4}$$

The second and third terms imply three- and four-point self-interactions between gluons, and are a result of the non-Abelian nature of the $SU(3)$ group.

The second term of $\mathcal{L}_{\text{QCD}}$ describes the coupling between quarks and gluons

$$\mathcal{L}_{\text{quark}} = \sum_{\text{flav}} \bar{q}_\alpha (i \not{D}_{\alpha\beta} - m\delta_{\alpha\beta}) q_\beta \tag{1.2.5}$$

where the sum runs over the six flavours of quarks, flav $= \{u, d, c, s, t, b\}$, and the covariant derivative is

$$D^\mu_{\alpha\beta} = \partial^\mu \delta_{\alpha\beta} - i g_s B^{a\mu} t^a_{\alpha\beta}. \tag{1.2.6}$$

Greek subscripts α, β are indices for the fundamental representation $\mathbf{3}$ of $SU(3)$, and t^a is a generator of this representation. The antifundamental representation $\bar{\mathbf{3}}$ has generators $-t^a$. The non-Abelian nature of $SU(3)$ may be expressed through the relationship between the generators of the fundamental and adjoint representations

$$[t^a, t^b] = i f^{abc} t^c \Leftrightarrow f^{abc} = -i \text{Tr}\Big([t^a, t^b] t^c \Big), \tag{1.2.7}$$

with the normalisation $\text{Tr}\big(t^a t^b\big) = \delta^{ab}$ used throughout this work.

The Fadeev-Popov and ghost Lagrangians are a result of quantising the $SU(3)$ Lagrangian. The Fadeev-Popov quantisation procedure circumvents singularities that appear during quantisation, originating from the gauge invariance of the gluons. This leaves a term

$$\mathcal{L}_{\mathrm{FP}} = -\frac{1}{2\xi}(\partial^\mu B^a_\mu)^2, \tag{1.2.8}$$

with ξ a parameter which reflects the gauge choice. This procedure generates additional terms in the Lagrangian, which can be expressed by ghost fields c in the adjoint of $SU(3)$. These fields are Lorentz scalars yet obey anticommutation relations; they therefore have the "wrong" spin statistics and are unphysical. The Lagrangian is

$$\mathcal{L}_{\mathrm{gh}} = \bar{c}^a\Big(-\partial^\mu(\partial_\mu\delta^{ac} - g_s f^{abc}B^b_\mu)\Big)c^c. \tag{1.2.9}$$

The cubic and quartic gluonic terms in (1.2.4) allow non-trivial gluonic scattering. In the absence of ghost fields, these scattering amplitudes do not satisfy unitarity.

1.2.2 Renormalisation and running coupling

At next-to-leading order in an expansion in the strong coupling constant, quantum chromodynamics contains ultraviolet divergences in loop diagrams. These can be renormalised by writing the QCD Lagrangian as a sum of a renormalised Lagrangian and a counter-term Lagrangian, which absorbs renormalisations of the fermion, gauge, and ghost fields, and the quark mass m and strong coupling g_s. One result of this procedure is that the mass and couplings become functions of an arbitrary energy scale μ introduced by the renormalisation procedure, $m = m(\mu)$ and $g_s = g_s(\mu)$. Neglecting masses, an observable R at an energy scale Q^2 can only depend on $\frac{Q^2}{\mu^2}$, and the coupling $\alpha_s \equiv \frac{g_s^2}{4\pi}$, $R = R(\frac{Q^2}{\mu^2}, \alpha_s(\mu^2))$ [94]. The observable R cannot be dependent on μ^2:

$$\mu^2\frac{d}{d\mu^2}R\Big(\frac{Q^2}{\mu^2}, \alpha_s(\mu^2)\Big) = \Big(\mu^2\frac{\partial}{\partial\mu^2} + \mu^2\frac{\partial\alpha_s(\mu^2)}{\partial\mu^2}\frac{\partial}{\partial\alpha_s}\Big)R = 0. \tag{1.2.10}$$

The beta-function is defined as $\beta(\alpha_s) = \mu^2\frac{\partial\alpha_s}{\partial\mu^2}$, and I define $t = \log\frac{Q^2}{\mu^2}$. Then equation (1.2.10) can be rewritten as

$$-\frac{\partial R(e^t, \alpha_s)}{\partial t} + \beta(\alpha_s)\frac{\partial R(e^t, \alpha_s)}{\partial\alpha_s} = 0, \tag{1.2.11}$$

and the beta function as

$$\beta = \frac{\partial\alpha_s}{\partial t}. \tag{1.2.12}$$

Then

$$t = \int_{\alpha_s(\mu^2)}^{\alpha_s(Q^2)}\frac{du}{\beta(u)}, \tag{1.2.13}$$

through which the running coupling $\alpha_s(Q^2)$ is defined. A solution to equation (1.2.11) is given by $R(1, \alpha_s(Q^2))$, and this can be calculated at any other value of t and α_s

using equation (1.2.13). The price for the independence of R on the arbitrary scale μ^2 is that the coupling α_s is now dependent on the physical scale Q^2.

This dependence of the coupling on the physical scale Q^2 can be expressed through the beta function $\beta(\alpha_s) = \mu^2 \frac{\partial \alpha_s}{\partial \mu^2}$, which can be calculated perturbatively. In QCD, including amplitudes to one loop in pQCD, the beta function is

$$\beta(\alpha_s) = -\frac{11N_c - 2n_f}{12\pi}\alpha_s^2, \tag{1.2.14}$$

where $N_c = 3$ is the number of colours, and n_f is the number of massless flavours. Since $n_f \leq 6$, $\beta < 0$, meaning that the strength of the strong coupling decreases as the energy scale of the dynamics increases. This means that pQCD can be meaningfully applied at sufficiently large energies. It is found that the strong coupling becomes large at hadronic energy scales, so that the lowest energy at which pQCD can be applied is $\Lambda_{\text{QCD}} \sim 1$ GeV. Energy scales in collider physics are typically $100 - 1000$ GeV, so pQCD is fully applicable. This is borne out by the value of $\alpha_s(Q^2 = M_Z^2) \simeq 0.1$. The scale Q is often called the *renormalisation scale* μ_R.

1.2.3 Parton distributions

While it is true that pQCD is applicable to partonic scattering in hadron collisions, there are also low-energy (soft) effects coming from the confinement of the partons within the hadrons (typically protons and antiprotons). The behaviour of the partons within the hadrons – specifically, their momentum distribution – is parametrised by parton distributions.

The partons are considered to be moving in the same direction as the hadrons, with negligible momentum transverse to this direction. Suppose the hadrons have known four-momenta P_1 and P_2, and the partons have unknown four-momenta p_1 and p_2. The parton distribution functions (PDFs) $f_{a/A}(x_i, \mu_F^2)$ represent the number density of partons of type a in a hadron of type A which contain momentum fraction $x_i = p_i/P_i$ at the *factorisation scale* μ_F. The factorisation theorem allows these soft effects to be treated separately from the hard partonic scattering, and the hadronic cross-section is written as

$$\sigma(P_1, P_2) = \sum_{a,b} \int dx_1 dx_2 f_{a/A}(x_1, \mu_F^2) f_{b/B}(x_2, \mu_F^2) \hat{\sigma}_{ab}(p_1, p_2, \alpha_s(\mu_R^2), Q^2/\mu_R^2, Q^2/\mu_F^2), \tag{1.2.15}$$

where $\hat{\sigma}_{a,b}$ is the partonic cross-section, evaluated using pQCD at a scale Q. The factorisation scale forms the boundary between hard and soft processes, with $\mu_F \sim Q$. The cross-sections to all orders is independent of both the factorisation and renormalisation scales, but truncating the perturbative expansion introduces a scale dependence. Calculating the cross-section to higher orders in pQCD reduces this dependence. Often, the factorisation and renormalisation scales are set equal to each other and to the scale of the process, $\mu_F = \mu_R = Q$.

The PDFs are derived primarily from deep inelastic scattering (DIS) data, and are then evolved to the factorisation scale of the hadronic collision through the Dokshitzer-Gribov-Lipatov-Altarelli-Parisi (DGLAP) equations [95–97]. Several different PDF fits are available: amongst the most frequently used are the MSTW [98], NNPDF [99] and CT (formerly CTEQ) [100] distributions.

1.3 Electroweak symmetry breaking

The quantum field theory describing the electromagnetic and weak forces postulates an $SU(2) \times U(1)$ symmetry, mediated by massless gauge bosons A^a_μ ($a = 1, 2, 3$) and B_μ, and with couplings g and g' [101–103]. This brief discussion follows ref. [93]. The symmetry is broken by a complex scalar Higgs field ϕ [104–107], which is charged under the $SU(2) \times U(1)$ group, and has a potential

$$V(\phi) = -\mu^2|\phi|^2 + \frac{\lambda}{2}|\phi|^4. \tag{1.3.1}$$

The minimum of this potential is not at $\phi = 0$, and as a result the Higgs field acquires a vacuum expectation value (vev) of

$$<\phi>= \frac{1}{\sqrt{2}} \begin{pmatrix} 0 \\ v \end{pmatrix}. \tag{1.3.2}$$

This breaks the $SU(2) \times U(1)$ and realigns the gauge boson fields, giving rise to three massive gauge bosons

$$\begin{aligned} W^\pm_\mu =& \frac{1}{\sqrt{2}}\Big(A^1_\mu \mp iA^2_\mu\Big), \\ Z_\mu =& \frac{1}{\sqrt{g^2 + g'^2}}\Big(gA^3_\mu - g'B_\mu\Big), \end{aligned} \tag{1.3.3}$$

with masses $m_W = \frac{gv}{2}$ and $m_Z = \frac{v}{2}\sqrt{g^2 + g'^2}$. The final gauge boson is massless

$$A_\mu = \frac{1}{\sqrt{g^2 + g'^2}}\Big(g'A^3_\mu + gB_\mu\Big). \tag{1.3.4}$$

In this manner, three massive weak bosons, the $W^\pm-$ and Z-bosons, and one massless photon, are described. The coupling of a fermion to the photon is expressed through its electromagnetic charge $Q = T^3 + Y$, where Y is the hypercharge under the original $U(1)$ symmetry, and T^3 is a generator of the $SU(2)$ symmetry. The mixing of the original $SU(2) \times U(1)$ fields into the weak bosons and photon is parametrised through the weak mixing angle θ_w, with

$$\cos\theta_w = \frac{g}{\sqrt{g^2 + g'^2}}. \tag{1.3.5}$$

The coupling strength of the photon is

$$e = \frac{gg'}{\sqrt{g^2 + g'^2}} \tag{1.3.6}$$

and is related to the weak coupling strength by $e = g_w \sin\theta_w$. This also implies a relation between the weak mixing angle and the masses of the W- and Z-boson

$$\cos\theta_w = \frac{m_W}{m_Z}. \tag{1.3.7}$$

The Lagrangian describing the interactions of the electroweak bosons to the fermions is

$$\mathcal{L}_{\mathrm{EW}} = g_w\Big(W^+_\mu J^\mu_{W^+} + W^-_\mu J^\mu_{W^-} + Z^0_\mu J^\mu_Z\Big) + eA_\mu J^\mu_{\mathrm{EM}}, \tag{1.3.8}$$

with currents

$$\begin{aligned}
J^\mu_{W^+} =& \frac{1}{\sqrt{2}}\Big(\bar{\nu}_L\gamma^\mu e_L + \bar{u}_L\gamma^\mu d_L\Big)\\
J^\mu_{W^-} =& \frac{1}{\sqrt{2}}\Big(\bar{e}_L\gamma^\mu \nu_L + \bar{d}_L\gamma^\mu u_L\Big)\\
J^\mu_Z =& \frac{1}{\cos\theta_w}\Big(\bar{\nu}_L\gamma^\mu T^3_\nu \nu_L + \bar{e}_L\gamma^\mu\big(-Q_e\sin^2\theta_w + T^3_e\big)e_L\\
&+ \bar{e}_R\gamma^\mu\big(-Q_e\sin^2\theta_w\big)e_R + \bar{u}_L\gamma^\mu\big(-Q_u\sin^2\theta_w + T^3_u\big)u_L\\
&+ \bar{u}_R\gamma^\mu\big(-Q_u\sin^2\theta_w\big)u_R + \bar{d}_L\gamma^\mu\big(-Q_d\sin^2\theta_w + T^3_d\big)d_L\\
&+ \bar{d}_R\gamma^\mu\big(-Q_d\sin^2\theta_w\big)d_R\Big)\\
J^\mu_{\mathrm{EM}} =& \bar{e}\gamma^\mu(Q_e)e + \bar{u}\gamma^\mu(Q_u)u + \bar{d}\gamma^\mu(Q_d)d.
\end{aligned} \tag{1.3.9}$$

The electromagnetic charges in the above are

$$Q_e = -1; \qquad Q_u = \frac{2}{3}; \qquad Q_d = -\frac{1}{3} \tag{1.3.10}$$

and the T^3 are

$$T^3_e = T^3_d = -\frac{1}{2}; \qquad T^3_\nu = T^3_u = \frac{1}{2}. \tag{1.3.11}$$

The interactions of the W- and Z-bosons violate parity maximally, with the W-bosons coupling only to left-handed fermions.

The non-Abelian nature of the $SU(2)$ symmetry allows couplings between the gauge bosons. In the basis of massless bosons A^a_μ and B_μ, this can be expressed through the Yang-Mills Lagrangian [108]

$$\mathcal{L}_{\mathrm{YM}} = -\frac{1}{4}\Big(\partial_\mu A^a_\nu - \partial_\nu A^a_\mu + g\epsilon^{abc}A^b_\mu A^c_\nu\Big)^2 - \frac{1}{4}\Big(\partial_\mu B_\nu - \partial_\nu B_\mu\Big)^2, \tag{1.3.12}$$

leading to both three- and four-point interactions. For the purposes of this work, only the three-point interactions will be necessary. In the basis of the W-bosons, Z-bosons and photons, these three-point interactions can be expressed through

$$\begin{aligned}
\mathcal{L}_{\mathrm{WWV}} =& ig_w\Big\{\Big[\big(\partial_\mu W^+_\nu - \partial_\nu W^+_\mu\big)W^{-\mu} - \big(\partial_\mu W^-_\nu - \partial_\nu W^-_\mu\big)W^{+\mu}\Big]\times\\
&\Big[\cos\theta_w Z^\nu + \sin\theta_w A^\nu\Big]\\
&+\frac{1}{2}\Big[\cos\theta_w\big(\partial_\mu Z_\nu - \partial_\nu Z_\mu\big) + \sin\theta_w\big(\partial_\mu A_\nu - \partial_\nu A_\mu\big)\Big]\times\\
&\Big[W^{+\mu}W^{-\nu} - W^{-\mu}W^{+\nu}\Big]\Big\}.
\end{aligned} \tag{1.3.13}$$

Chapter 2

Next-to-leading Order Calculations

2.1 Perturbative calculation of cross-sections

At hadronic colliders, the energies are large enough for asymptotic freedom to be manifest, meaning the strong coupling α_s is small. The matrix elements can then be calculated in perturbative QCD (pQCD). Suppose that N final state particles of momenta $p_i = (E_i, \mathbf{p}_i)$, $i = 1, ..., N$, are created in the collision of two initial state partons of momenta k_1 and k_2, with n of final state particles having colour. The cross-section can be expanded as

$$\sigma = \alpha_s^n \Big(\sigma^0 + \alpha_s \big(\sigma^{\mathrm{R}} + \sigma^{\mathrm{V}} \big) + \mathcal{O}(\alpha_s^2) \Big), \tag{2.1.1}$$

where σ^0 is the leading-order (LO) cross-section, and σ^{R} and σ^{V} are the real and virtual contributions to the next-to-leading order (NLO) correction. These are obtained from the matrix elements by convoluting with the PDFs and integrating over phase space:

$$\begin{aligned}
\sigma^0 &= \int_N d\sigma^0 \\
&= \int d\Phi_N \sum_{\mathrm{hel}} |\mathcal{M}^0(k_1, k_2, p_1, ..., p_N)|^2 \mathcal{J}^{(N)}(k_1, k_2; p_1, ..., p_N) \\
\sigma^{\mathrm{V}} &= \int_N d\sigma^{\mathrm{V}} \\
&= \int d\Phi_N \sum_{\mathrm{hel}} 2 \ \mathrm{Real}\big(\mathcal{M}^0(k_1, k_2, p_1, ..., p_N) \mathcal{M}^{\mathrm{V}*}(k_1, k_2, p_1, ..., p_N)\big) \\
&\qquad\qquad \times \mathcal{J}^{(N)}(k_1, k_2; p_1, ..., p_N) \\
\sigma^{\mathrm{R}} &= \int_{N+1} d\sigma^{\mathrm{R}} \\
&= \int d\Phi_{N+1} \sum_{\mathrm{hel}} |\mathcal{M}^{\mathrm{R}}(k_1, k_2, p_1, ..., p_{N+1})|^2 \mathcal{J}^{(N+1)}(k_1, k_2; p_1, ..., p_{N+1})
\end{aligned} \tag{2.1.2}$$

where $\mathcal{M}^0$ is the Born matrix element, $\mathcal{M}^{\mathrm{R}}$ is the matrix element due to the real radiation (brehmsstrahlung) of a coloured particle, and $\mathcal{M}^{\mathrm{V}}$ is the one-loop virtual matrix element. The sum is over all allowed helicities of the external particles, and the integration over phase space and momentum fractions is [93, 94]

$$\begin{aligned}\int d\Phi_N =&\sum_{a,b}\int dx_1 dx_2 f_{a/A}(x_1,\mu_F) f_{b/B}(x_2,\mu_F)\frac{1}{4|k_2^0 k_1^z - k_1^0 k_2^z|}\times \\ &\prod_{i=1}^{N}\int \frac{d^4 p_i}{(2\pi)^4}\theta(E_i)\delta(p_i^2-m_i^2)(2\pi)^4\delta^4\Big(\sum_{i=1}^{N} p_i - k_1 - k_2\Big),\end{aligned} \tag{2.1.3}$$

where the sum is over all parton types a, b of the colliding hadrons A and B, and the product is over all final state particles. Calculations are usually performed in the centre-of-mass frame or a boost-related frame, in which the boost-invariant denominator $4|k_2^0 k_1^z - k_1^0 k_2^z| = 2E_{CM}^2$. The integrations over the parton distribution functions and over phase space are done numerically, using a Monte Carlo method. There are $4N$ integration variables from the four momenta, and another two from the parton momentum fractions, and N on-shell constraints and 4 energy-momentum conservation constraints, meaning that the integration is over $3N-2$ random variables.

The function $\mathcal{J}$ in equation (2.1.2) provides an infrared safe definition of the jet observable in terms of the N final state partons. For example, $\mathcal{J}$ may define an inclusive cross-section or a differential cross-section, with an appropriate definition of the jets. Irrespective of the exact form of $\mathcal{J}$, its infrared safety property is crucial. This property means that the jet observable should not be changed by the addition of partons in the final state which have either vanishing four-momentum or are collinear to another parton. Infrared safety is guaranteed if the jet function satisfies the following criteria:

$$\begin{aligned}\lim_{p_i\to 0}\mathcal{J}^{(N+1)}(k_1,k_2;p_1,...,p_i,...,p_{N+1}) &= \mathcal{J}^{(N)}(k_1,k_2;p_1,...,p_{N+1})\\ \lim_{p_i||p_j}\mathcal{J}^{(N+1)}(k_1,k_2;p_1,...,p_j,...,p_i,...,p_{N+1}) &= \mathcal{J}^{(N)}(k_1,k_2;p_1,...,p_j+p_i,...,p_{N+1})\\ \lim_{p_i\to(1-x)k_1}\mathcal{J}^{(N+1)}(k_1,k_2;p_1,...,p_i,...,p_{N+1}) &= \mathcal{J}^{(N)}(xk_1,k_2;p_1,...,p_{N+1})\\ \lim_{p_i\to(1-x)k_2}\mathcal{J}^{(N+1)}(k_1,k_2;p_1,...,p_i,...,p_{N+1}) &= \mathcal{J}^{(N)}(k_1,xk_2;p_1,...,p_{N+1})\\ \lim_{p_i\cdot p_j\to 0}\mathcal{J}^{(N)}(k_1,k_2;p_1,...,p_j,...,p_i,...,p_N) &= 0\\ \lim_{k_m\cdot p_j\to 0}\mathcal{J}^{(N)}(k_1,k_2;p_1,...,p_j,...,p_i,...,p_N) &= 0; \qquad m=1,2.\end{aligned} \tag{2.1.4}$$

Jets are usually defined using either the k_t [109,110] or anti-k_t [111] algorithms, which are both infrared safe. It is also worthwhile noting that additional kinematic cuts, for example on the transverse momentum of the jets, may be imposed on equation (2.1.2).

The cross-section of equation (2.1.1) is finite order-by-order. This means that the leading-order cross-section is always finite. However, divergences are present in the real and virtual matrix elements. In the real matrix element, these are infrared (IR) divergences due to the emission of a soft or collinear particle. In the virtual matrix element, IR divergences appear from the transfer of a soft or collinear virtual particle, and ultraviolet (UV) divergences are also present. Both of these can be regulated by dimensional regularisation [112, 113], in which the momenta of the internal particles is continued to $D = 4 - 2\epsilon$ dimensions. The limit $\epsilon \to 0$ is then taken, and the UV divergences emerge as single $1/\epsilon$ poles, while the IR divergences appear as double $1/\epsilon^2$ and single $1/\epsilon$ poles. In a renormalisable theory like QCD, the UV divergences can be absorbed into the bare (unobservable) masses, couplings and wave functions. This renormalisation procedure results in a counterterm, which in the $\overline{MS}$ scheme is proportional to the Born matrix element. For massless amplitudes, the counterterm is [114]:

$$\mathcal{M}^{\text{UV}} = -\frac{N(4\pi)^\epsilon}{2\epsilon\Gamma(1-\epsilon)}\big(g_s/(4\pi)\big)^2\beta_0\mathcal{M}^0, \tag{2.1.5}$$

where Γ is the Euler gamma function, and β_0 is the first term of the β-function (see section 1.2.2), $\beta_0 = (11N_c - 2N_f)/3$. The regularised IR poles in the real and virtual contributions will cancel after integration over phase space, leaving a finite next-to-leading order cross-section. However, since the integration is performed numerically, this cancellation is not straightforward, and will be discussed in the next section.

2.2 Subtraction method

In the previous section, I mentioned that the regularised infrared (IR) poles originating from the real cross-section should cancel those coming from the virtual cross-section. However, it is not possible to numerically integrate an expression which diverges in some subspace. Therefore, it is preferable to cancel these divergences *prior* to integration. The difficulty in doing so is that the virtual cross-section involves an integration over an N-particle phase space, while the real cross-section has an integration over an $(N+1)$-particle phase space. To solve this problem, a subtraction scheme [115] is employed, defining a counterterm $d\sigma^{\mathrm{A}}$ with the following two properties: it has the same singular structure as $d\sigma^{\mathrm{R}}$, and it can be integrated analytically over the one-particle phase space associated with the singularities. Then

$$\sigma^{\mathrm{R}} + \sigma^{\mathrm{V}} = \int_{N+1} \Big(d\sigma^{\mathrm{R}} - d\sigma^{\mathrm{A}} \Big) + \int_{N} \Big(d\sigma^{\mathrm{V}} + \int_{\mathrm{sing}} d\sigma^{\mathrm{A}} \Big), \tag{2.2.1}$$

where the integral $\int_{\mathrm{sing}}$ is over the phase subspace that leads to soft and collinear divergences. The first property of the counterterm ensures that the divergences cancel in the integrand of the first integral, so that the numerical integration over $(N+1)$-particle phase space can be performed with no trouble. The second property of the counterterm ensures that the poles of $\int_{\mathrm{sing}} d\sigma^{\mathrm{A}}$ can be obtained and then cancelled with the poles of $d\sigma^{\mathrm{V}}$ in the integrand of the second term, allowing the numerical integration over the N-particle phase space to be performed.

The problem of finding the counterterm $d\sigma^{\mathrm{A}}$ for a general process was solved by Catani and Seymour [116, 117], and later extended to massive partons [118][1]. Here I shall only consider singularities originating from final state partons which become soft, or which are emitted collinear to another final state parton. This is sufficient for a brief outline of the idea. Including initial state singularities is a nontrivial extension discussed in ref. [117]. In the soft and collinear regions, the $(N+1)$-particle amplitude $\mathcal{M}^{\mathrm{R}}$ can be written in terms of an N-particle amplitude $\mathcal{M}_N$, and the singular part of $|\mathcal{M}^{\mathrm{R}}|^2$ can be expressed as a dipole $\mathcal{D}_{ij,k}$:

$$\begin{aligned}\mathcal{D}_{ij,k}(p_1, ..., p_{N+1}) = & \frac{-1}{2p_i \cdot p_j} < c^{\mathrm{R}}_{n+1} ... c^{\mathrm{R}}_{\tilde{k}} ... c^{\mathrm{R}}_{\tilde{ij}} ... c^{\mathrm{R}}_{1} | \frac{\mathbf{T}_{\tilde{k}} \cdot \mathbf{T}_{\tilde{ij}}}{\mathbf{T}^2_{\tilde{ij}}} | c^{\mathrm{R}}_{1} ... c^{\mathrm{R}}_{\tilde{ij}} ... c^{\mathrm{R}}_{\tilde{k}} ... c^{\mathrm{R}}_{n+1} > \\ & \mathcal{M}^*_N(p_1, ..., p_{\tilde{ij}}, ..., p_{\tilde{k}}, ..., p_{N+1}) \mathbf{V}_{ij,k} \mathcal{M}_N(p_1, ..., p_{\tilde{ij}}, ..., p_{\tilde{k}}, ..., p_{N+1}).\end{aligned} \tag{2.2.2}$$

In order to construct $\mathcal{M}_N$, the partons i and j are replaced by a single parton $\tilde{ij}$ (called the emitter), and the parton k with $\tilde{k}$ (called the spectator). The spectator $\tilde{k}$ has the same quantum numbers as k, while the quantum numbers of parton $\tilde{ij}$ are defined according to the splitting $\tilde{ij} \to i + j$. Thus, as an example, if i is a quark and j a gluon, then $\tilde{ij}$ must be a quark of the same flavour as i. The operators $\mathbf{T}_i$ are colour matrices: the generator of the fundamental representation $t^a_{\alpha\beta}$ for an emitting quark and the generator of the adjoint representation if^a_{bc} for an emitting

---

[1] Subtraction methods using different formalisms are also widely used, such as FKS subtraction [119, 120] and antenna methods [121, 122].

gluon. These act on the colour state of the amplitude, written as $|c_1^{\mathrm{R}}...c_{\tilde{ij}}^{\mathrm{R}}...c_{\tilde{k}}^{\mathrm{R}}...c_{n+1}^{\mathrm{R}}>$, with each coloured particle contributing a colour matrix c_i^{R}. These are also generators of either the fundamental, antifundamental or adjoint representations. There is no colour dependence in $\mathcal{M}_N$. The operator $\mathbf{V}$ acts on the spin and momentum of the emitter. The momenta of the emitter and spectator are

$$\begin{aligned} p_{\tilde{ij}} =& p_i + p_j - \frac{y_{ij,k}}{1-y_{ij,k}} p_k \\ p_{\tilde{k}} =& \frac{1}{1-y_{ij,k}} p_k \end{aligned} \tag{2.2.3}$$

with

$$y_{ij,k} = \frac{p_i p_j}{p_i p_j + p_j p_k + p_i p_k}. \tag{2.2.4}$$

The emitter and spectator remain massless, $p_{\tilde{ij}}^2 = p_{\tilde{k}}^2 = 0$, and momentum is conserved, $p_{\tilde{ij}} + p_{\tilde{k}} = p_i + p_j + p_k$. This means that double counting is avoided if one parton becomes both soft and collinear to another parton. A pointwise cancellation of singularities is therefore possible. The excess momentum caused by the splitting $\tilde{ij} \to i + j$ is absorbed by one particle, the spectator. This is in contrast to the Nagy-Soper dipole method [123, 124], where the excess momentum is absorbed by all particles not involved in the splitting.

The dipole formula equation (2.2.2) reproduces the soft-gluon and Altarelli-Parisi collinear factorisation [116], but is also defined in non-singular regions of phase space. The subtraction term $d\sigma^{\mathrm{A}}$ is defined as

$$d\sigma^{\mathrm{A}} = d\Phi_{N+1} \sum_{i,j} \sum_{k \neq i,j} \mathcal{D}_{ij,k} \mathcal{J}^{(N)}(p_1, ..., p_{\tilde{ij}}, ..., p_{\tilde{k}}, ..., p_{N+1}). \tag{2.2.5}$$

In the singular regions, the $(N+1)$-particle phase space is the same as the dipole phase space, so that

$$\mathcal{J}^{(N+1)}(p_1, ..., p_i, ..., p_j, ..., p_k, ..., p_{N+1}) = \mathcal{J}^{(N)}(p_1, ..., p_{\tilde{ij}}, ..., p_{\tilde{k}}, ..., p_{N+1}). \tag{2.2.6}$$

Furthermore, in these regions, $\mathcal{D}_{ij,k}$ has the same behaviour as $|\mathcal{M}^{\mathrm{R}}|^2$ by definition. It is clear then that $d\sigma^{\mathrm{R}} - d\sigma^{\mathrm{A}}$ is finite. In fact, equation (2.2.6) ensures that this cancellation occurs for any infrared safe observable.

Turning now to the second term of equation (2.2.1), the $(N+1)$-particle phase space factorises as

$$d\Phi_{N+1} = d\Phi_N \frac{d^D p_i}{(2\pi)^{D-1}} \delta_+(p_i^2) \Theta(1-z_i) \Theta(1-y_{ij,k}) \frac{(1-y_{ij,k})^{D-3}}{1-z_i}, \tag{2.2.7}$$

with $d\Phi_N$ the N-particle dipole phase space and $z_i = \frac{p_i p_{\tilde{k}}}{p_{\tilde{ij}} p_{\tilde{k}}}$. With this factorisation, the integration of the dipole counterterm over the singular regions of phase space can be performed analytically in D-dimensions, with the result

$$\begin{aligned} \int d\Phi_{N+1} d\sigma^{\mathrm{A}} &= \int d\Phi_N \int_{\mathrm{sing}} d\sigma^{\mathrm{A}} \\ &= \int d\Phi_N \mathcal{M}^{0*} \mathbf{I}(\epsilon) \mathcal{M}^0 \mathcal{J}(p_1, ..., p_N). \end{aligned} \tag{2.2.8}$$

Thus the singularities of the integrated dipole can be expressed in terms of the Born matrix element squared, with an operator in colour space

$$\mathbf{I}(p_1, ..., p_m; \epsilon) = -\frac{\alpha_s}{2\pi}\frac{1}{\Gamma(1-\epsilon)}\sum_i \mathbf{T}_i^{-2} S_i(\epsilon) \sum_{k\neq i} \mathbf{T}_i.\mathbf{T}_k \Big(\frac{4\pi\mu^2}{2p_i.p_k}\Big)^{\epsilon}, \qquad (2.2.9)$$

with

$$S_i(\epsilon) = \mathbf{T}_i^2\Big(\frac{1}{\epsilon^2} - \frac{\pi^3}{3}\Big) + \frac{\gamma_i}{\epsilon} + \gamma_i + K_i + \mathcal{O}(\epsilon) \qquad (2.2.10)$$

and

$$\begin{array}{lllll lll} \gamma_q & = & \gamma_{\bar{q}} & = & \frac{3}{2}C_F & \gamma_g & = & \frac{11}{6}N_c - \frac{1}{3}T_R N_f \\ K_q & = & K_{\bar{q}} & = & C_F\Big(\frac{7}{2} - \frac{\pi^2}{6}\Big) & K_g & = & N_c\Big(\frac{67}{18} - \frac{\pi^2}{6}\Big) - \frac{5}{9}T_R N_f. \end{array} \qquad (2.2.11)$$

The colour factors are $T_R = 1$ and $C_F \equiv \frac{N_c^2-1}{2N_c}$. The singularities of the integrated dipole $\mathcal{M}^{0*}\mathbf{I}(\epsilon)\mathcal{M}^0$ cancel with those from the virtual matrix element squared [116]. The integrand of the second term of equation (2.2.1) is finite, and the integration over N-particle phase space can be performed. Thus the IR poles in both N- and $(N+1)$-particle phase space can be cancelled prior to integration, and the resulting finite terms integrated to yield the next-to-leading order cross-section.

2.3 Virtual amplitudes

The leading-order, real and virtual matrix elements include a dependence on colour factors. If more than one colour-charged particle is present in the final state, then the matrix element will contain terms with different permutations of colour factors, even at tree-level. At one-loop level, the colour structure is even more complicated. For this reason, it is useful to introduce colour-stripped *partial amplitudes* [125], which are functions of the kinematics of the scattering only. The matrix element, at either tree-level or one-loop, can be expressed as a sum over the partial amplitudes, with each multiplied by a unique permutation of the colour factors.

Equation (1.2.7) relates the generators of the adjoint representation to the generators of the fundamental representation

$$f^{abc} = -i\mathrm{Tr}\big([t^a, t^b]t^c\big). \tag{2.3.1}$$

Thus all the colour factors in an amplitude – the coefficients of the partial amplitudes – can be written in terms of fundamental generators t^a. As a simple example, the tree-level amplitude involving a quark-antiquark pair and two gluons can be written in terms of two partial amplitudes A and B:

$$\mathcal{M}^0(\bar{q}_1, q_2, g_3, g_4) = (t^{a_3}t^{a_4})_{\bar{i}_1 i_2} A + (t^{a_4}t^{a_3})_{\bar{i}_1 i_2} B. \tag{2.3.2}$$

The one-loop partial amplitudes can further be decomposed into *primitive amplitudes*, which have a set ordering of the colour-charged external particles that preserves $SU(N_c)$ gauge invariance[2]. Bern, Dixon and Kosower proved [126] that such a decomposition is possible for every one-loop partial amplitude in the scattering of a quark and antiquark with n gluons. Partial amplitudes do not have a fixed ordering of coloured particles and therefore a partial amplitude is usually decomposed into several primitive amplitudes. Similarly, a primitive amplitude may appear in the decomposition of multiple partial amplitudes.

The particles circulating in the loop may be only gluons, gluons and quarks, or only quarks[3]. The first two are grouped together, and referred to as gluonic primitive amplitudes A_1. Amplitudes with only quarks circulating in the loop are called fermionic primitive amplitudes $A_{[1/2]}$. These are accompanied by a factor of N_f, the number of flavours in the loop. Primitive amplitudes for a process involving a quark-antiquark pair may be further defined as either "left" or "right" oriented, depending on where the loop is located relative to the fermion line (and irrespective of the type of particles circulating in the loop). These are indicated by an L or R superscript. The left and right, fermionic and gluonic virtual amplitudes are illustrated in figure 2.1. Left and right (fermionic and gluonic) primitives can be shown to be separately $SU(N_c)$ gauge invariant by appealing to a supersymmetric Yang-Mills theory [126]. Furthermore, the sums $A_1^L + A_1^R$ and $A_{[1/2]}^L + A_{[1/2]}^R$ are also gauge invariant under this symmetry.

---

[2] Particles charged under other symmetries, such as $SU(2) \times U(1)$ electroweak symmetry, are not ordered in primitive amplitudes. Similarly, other gauge invariances which may be present in the theory are not preserved in primitive amplitudes, but will be recovered when the primitives are recombined to form the full virtual amplitude.

[3] In ref. [126], a supersymmetric extension of the gauge group is considered, and scalars are also allowed in the loop. This is not relevant for this work.

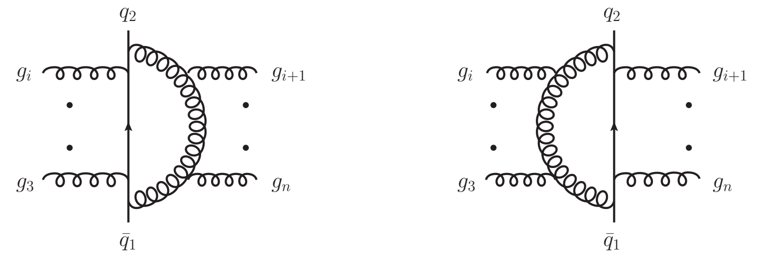

$A^L_{[1]}(\bar{q}_1, g_3, ..., g_i, q_2, g_{i+1}, ..., g_n)$ $A^R_{[1]}(\bar{q}_1, g_3, ..., g_i, q_2, g_{i+1}, ..., g_n)$

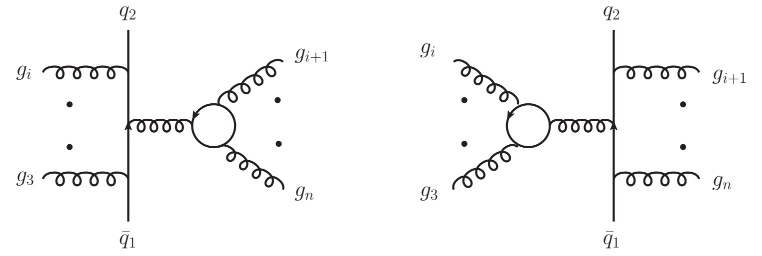

$A^L_{[1/2]}(\bar{q}_1, g_3, ..., g_i, q_2, g_{i+1}, ..., g_n)$ $A^R_{[1/2]}(\bar{q}_1, g_3, ..., g_i, q_2, g_{i+1}, ..., g_n)$

Figure 2.1: Colour-ordered primitive amplitudes. Gluonic primitive amplitudes are shown on the top row, with the left oriented amplitude on the left and the right oriented amplitude on the right. Left and right fermionic primitive amplitudes are shown on the bottom row.

In general, a partial amplitude is related to both left and right, gluonic and fermionic primitive amplitudes $A^L_1, A^R_1, A^L_{[1/2]}, A^R_{[1/2]}$, multiplied by various colour factors. It is possible to eliminate the dependence on right primitives, as these can be written as left primitives under the exchange of gluons

$$A^R_{[J]}(\bar{q}_1, g_3, g_4, ..., g_i, q_2, g_{i+1}, ..., g_{n-1}, g_n) = (-1)^n A^L_{[J]}(\bar{q}_1, g_n, g_{n-1}, ..., g_{i+1}, q_2, g_i, ..., g_4, g_3) \tag{2.3.3}$$

for $J = 1/2, 1$, so that the partial amplitude can be written in terms of left gluonic and fermionic primitive amplitudes. The exact relationship must be determined separately for each process, and will be discussed in sections 5.4, 6.4 and 7.2.

The residues of the IR single and double poles of the primitive amplitudes A^L_1 have a simple expression in terms of the tree-level amplitude A^0 with the same colour-ordering as the primitive. The ratio

$$R = \frac{1}{c_\Gamma} \frac{\mathrm{Res}\big(A^1_L(\bar{q}_1, g_3, ..., g_i, q_2, g_{i+1}, ..., g_n)\big)}{A^0(\bar{q}_1, g_3, ..., g_i, q_2, g_{i+1}, ..., g_n)} \tag{2.3.4}$$

where

$$c_\Gamma = (4\pi)^{\epsilon-2} \frac{\Gamma(1+\epsilon)\Gamma^2(1-\epsilon)}{\Gamma(1-2\epsilon)} \tag{2.3.5}$$

is

$$\begin{aligned} R &= -\frac{1}{\epsilon^2}\Big(\frac{\mu^2}{-s_{q,i+1}}\Big)^\epsilon - \frac{1}{\epsilon^2}\Big(\frac{\mu^2}{-s_{\bar{q},n}}\Big)^\epsilon - \frac{1}{\epsilon^2}\sum_{j=i+1}^{n-1}\Big(\frac{\mu^2}{-s_{j,j+1}}\Big)^\epsilon \\ &= -\frac{2}{\epsilon^2} - \frac{1}{\epsilon}\ln\Big(\frac{\mu^2}{-s_{q,i+1}}\Big) - \frac{1}{\epsilon}\ln\Big(\frac{\mu^2}{-s_{\bar{q},n}}\Big) - \sum_{j=i+1}^{n-1}\Big[-\frac{1}{\epsilon^2} - \frac{1}{\epsilon}\ln\Big(\frac{\mu^2}{-s_{j,j+1}}\Big)\Big] \end{aligned} \tag{2.3.6}$$

if $i < n$. If $i = n$, then the ratio is simply

$$R = -\frac{1}{\epsilon^2}\Big(\frac{\mu^2}{-s_{q,\bar{q}}}\Big)^{\epsilon} = -\frac{1}{\epsilon^2} - \frac{1}{\epsilon}\ln\Big(\frac{\mu^2}{-s_{q,\bar{q}}}\Big). \tag{2.3.7}$$

In the above, I have used $s_{ij} = (p_i + p_j)^2$, $s_{q,i+1} = (p_q + p_{i+1})^2$, $s_{\bar{q},n} = (p_n + p_{\bar{q}})^2$ and $s_{q,\bar{q}} = (p_q + p_{\bar{q}})^2$, and μ is the energy scale introduced by renormalisation. The logarithm has the usual continuation if the argument is negative

$$\ln\Big(\frac{\mu^2}{-s_{ij}}\Big) = \ln\Big(|\frac{\mu^2}{-s_{ij}}|\Big) + i\pi\Theta(s_{ij}), \tag{2.3.8}$$

where Θ is the Heaviside function. The above contribution to the single and double poles is universal; there is also a constant contribution to the single poles which is process-dependent. For all the processes considered in this work, these contributions are given in refs. [114, 126].

The simplicity of the singular structure is one motivation for the use of primitive amplitudes. Another is the compactness of the virtual amplitude when written in terms of primitives. One can dispense with different permutations of coloured particles when evaluating a primitive amplitude, since it is colour-ordered. At the same time, unlike individual Feynman diagrams, primitive amplitudes preserve the $SU(N_c)$ invariance. In the following chapter, I will discuss a unitarity-based method for evaluating one-loop amplitudes. While this method is applicable to any one-loop amplitude, its application to primitive amplitudes allows the use of off-shell recursive Berends-Giele currents (see section 4.3), making this a very efficient implementation of the unitarity method.

Chapter 3

One-Loop Amplitudes

3.1 Introduction

In this chapter, I shall consider the problem of evaluating the one-loop N-particle scattering amplitude (see figure 3.1) in D-dimensions

$$\begin{aligned}\mathcal{A}_N(p_1, p_2, ..., p_N) &= \int \frac{d^D l}{(2\pi)^D} \mathcal{A}_N(p_1, p_2, ..., p_N; l) \\ &= \int \frac{d^D l}{(2\pi)^D} \frac{\mathcal{N}(p_1, p_2, ..., p_N, J_1, J_2, ..., J_N; l)}{D_0 D_1 ... D_{N-1}},\end{aligned} \tag{3.1.1}$$

where p_i are external momenta, and the $J_i = J_i(p_i)$ are external polarisation vectors or spinors. The propagators are given by

$$D_i = (l + q_i)^2 - m_i^2 = \Big(l + q_0 + \sum_{j=1}^{i} p_j\Big)^2 - m_i^2, \tag{3.1.2}$$

where l is the loop momentum, q_0 is an arbitrary parametrisation momentum, and m_i is the mass of the off-shell particle. In general, the integral must be performed in D-dimensions to allow regularisation of the infrared and ultraviolet poles. The interpolation $D = 4 - 2\epsilon$ and the limit $\epsilon \to 0$ are eventually taken (see section 3.2). In a renormalisable field theory, each vertex can contribute at most one factor of l to the numerator $\mathcal{N}$, and there are at most N vertices at one loop. This means that the maximum number of times that l can appear explicity in $\mathcal{N}$ – called the *rank* r of the integral – is N. An integral having n propagators in the denominator ($n \leq N$) is known as an n-point integral, also called a pentagon, box, triangle, bubble, or tadpole integral for $n = 5, 4, 3, 2, 1$. Thus I will refer to rank-r n-point integrals, with $r \leq n \leq N$. As an example, a rank-2 three-point (triangle) integral is $C^{\mu\nu}(l) = \int \frac{d^D l}{(2\pi)^D} \frac{l^\mu l^\nu}{D_0 D_1 D_2}$.

It is possible to write the amplitude in terms of a basis of scalar (i.e. rank-0)

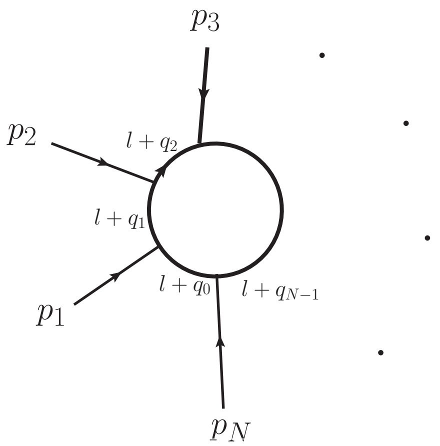

Figure 3.1: Diagrammatic representation of a one-loop N-particle scattering amplitude.

integrals

$$\begin{aligned}\mathcal{A}_N(p_1,p_2,...,p_N) = &\sum_{[i_1|i_5]}\beta_{5;i_1i_2i_3i_4i_5}(p_i)I^D_{i_1i_2i_3i_4i_5}+\sum_{[i_1|i_4]}\beta_{4;i_1i_2i_3i_4}(p_i)I^D_{i_1i_2i_3i_4}+\\ &\sum_{[i_1|i_3]}\beta_{3;i_1i_2i_3}(p_i)I^D_{i_1i_2i_3}+\sum_{[i_1|i_2]}\beta_{2;i_1i_2}(p_i)I^D_{i_1i_2}+\\ &\sum_{i_1}\beta_{1;i_1}(p_i)I^D_{i_1},\end{aligned} \tag{3.1.3}$$

where I have used the notation $[i_1|i_k] = 0 \leq i_1 \leq i_2... \leq i_k \leq N$. The coefficients β of the scalar master integrals are independent of loop momentum l. Equation (3.1.3) does not need to go beyond five-point scalars, since with the identification $D = 4-2\epsilon$, every higher-point scalar integral can be written in terms of five-point scalars up to terms $\mathcal{O}(\epsilon)$ [127–129] [1] .

The scalar integrals are

$$I^D_{i_1...i_M} = \int \frac{d^Dl}{(2\pi)^D}\frac{1}{D_{i_1}...D_{i_M}}. \tag{3.1.4}$$

These integrals will be discussed again in section 3.5. For now, it suffices to say that they are known [130–132], so that the problem of evaluating equation (3.1.1) reduces to finding the coefficients β in equation (3.1.3).

An early method of finding these coefficients was proposed by Passarino and Veltman [50]. A rank-r n-point integral is expanded in terms of external momenta p_i and the metric tensor $g_{\mu\nu}$. By multiplying both sides of these equations with external momenta, a system of linear equations is created, which are solved to yield the coefficients in the expansion of the integral. This result is recursive, and a rank-r n-point integral is re-expressed in terms of a rank-$(r-1)$ n-point integral and $(n-1)$-point integrals with rank $\leq r-1$. In this manner, any integral can be reduced to a scalar integral, and the one-loop amplitude evaluated.

---

[1] Note that such terms would be important for two-loop calculations.

This summary does not do justice to the extensive refinement that this method has undergone since its initial conception [47–49]. Indeed, many cutting-edge computations are performed using this technique. However, it does have some drawbacks. First, each tensor integral is generated using Feynman diagrams and the associated rules. Since the number of Feynman diagrams for an N-particle scattering amplitude increases faster than $N!$ [62], this becomes computationally expensive. Moreover, as has been pointed out several times, e.g. in refs. [61, 85], individual Feynman diagrams do not preserve gauge invariance. This means that there are extensive cancellations between terms originating from different Feynman diagrams, leading to much simpler final results. These problems are exacerbated by the Passarino-Veltman reduction, since the number of terms produced in the reduction of a tensor integral with high rank can be very large. Second, solving the linear equations produced in the reduction procedure involves taking inverses of Gram matrices. These matrices can become singular for combinations of external momenta that do not correspond to any physical singularity. While this problem can be circumvented, it further adds to the computational time.

An alternative approach, which may now arguably be called the standard approach, is based on the unitarity property of quantum field theory. This property allows the imaginary part of the amplitude to be calculated from tree-level amplitudes obtained by putting intermediate particles on-shell. The basic idea is known as Cutkosky rules [133], and methods based on unitarity were advanced mainly by Bern, Dixon, and Kosower [134–136]. This development accelerated in recent years due to the discovery by Britto, Cachazo, and Feng [55, 56] that the coefficients of the scalar integrals in the decomposition of one-loop integrals can be obtained from tree-level helicity amplitudes admitting complex momenta. These ideas were used by Forde [58], Badger [59], and Mastrolia [60] using a spinor-helicity formalism [137]. Additionally, Ossola, Papadoupoulos and Pittau developed an algebraic method to extract the coefficients of the scalar one-loop integrals, known as the OPP subtraction method [57].

In this chapter, I shall describe an approach advanced by Ellis, Giele, Kunszt and Melnikov [61–63] (for a recent review, see ref. [85]), based on the OPP subtraction method, and called generalised unitarity. This uses unitarity cuts of multiple propagators to understand the functional dependence of the one-loop amplitude on the virtual momentum l. While it is true that certain kinematic points lead to potential instabilities in this approach, these can be avoided without greatly increasing the computational time.

The remainder of this chapter is organised as follows. In section 3.2, I will discuss the regularisation of divergent amplitudes within a numerical setting. In section 3.3, I will introduce the Vermaseren-Van Neerven basis, which allows the loop momentum to be parametrised in a convenient way. In section 3.4, I will use the ideas of generalised unitarity to write the amplitude in terms of scalar integrals with loop momentum dependent coefficients, and then show how the functional form of the coefficients is fixed and how they can be determined. Finally, I will comment on the integration of the scalar integrals in section 3.5.

3.2 Dimensionality of the amplitude

As mentioned previously, a one-loop (or higher) scattering amplitude calculated in a quantum field theory has both infrared (IR) and ultraviolet (UV) divergences. In a renormalisable field theory, these can be regularised and the UV divergences absorbed into unobservable bare parameters, such as the mass or coupling, while the IR divergences cancel against divergences originating from soft or collinear real radiation (see section 2.2). In the 't Hooft-Veltman prescription [112], the momenta and polarisations of the virtual particles are continued to D-dimensions, so that the amplitude becomes an analytic function of D. The identification $D = 4 - 2\epsilon$ is then made, and the divergences appear as poles in ϵ as the limit $\epsilon \to 0$ is taken. Importantly, this procedure contributes not only to the poles of the one-loop amplitude, but to the finite part too. The part of the finite amplitude that can only be obtained by a continuation to D-dimensions is called the *rational part*, while the remainder of the finite part – which can be obtained from a calculation in 4-dimensions – is known as the *cut-constructible part*. One way of obtaining the full amplitude is to extend the unitarity calculation to D-dimensions (other approaches, based on evaluating Feynman diagrams [138–140] or using on-shell recursion relations [141–143], are also possible).

The obvious difficulty in implementing such a procedure numerically lies in the construction of momenta and polarisations in a non-integer number of dimensions. The solution is to find the general D-dependence of a one-loop amplitude, so that the amplitude can be evaluated numerically for an integer number of dimensions and the result in a non-integer number of dimensions obtained. To do this, I will distinguish between the dimensionality of internal momenta, D, and internal polarisations, D_s, with the restriction that $D \leq D_s$ [144]. Equation (3.1.1) can then be rewritten as

$$\mathcal{A}_N^{(D,D_s)}(p_1, p_2, ..., p_N) = \int \frac{d^D l}{(2\pi)^D} \frac{\mathcal{N}^{(D_s)}(p_1, p_2, ..., p_N, J_1, J_2, ..., J_N; l)}{D_0 D_1 ... D_{N-1}}, \tag{3.2.1}$$

where the propagators D_i are in D dimensions. The numerator function $\mathcal{N}$ has explicit D_s dependence due to the number of spin eigenstates of the internal polarisations. For bosonic internal particles, there are $D_s - 2$ spin eigenstates e^i_μ, which satisfy

$$\sum_i^{D_s-2} e^i_\mu(l) e^i_\nu(l) = -g^{(D_s)}_{\mu\nu} + \frac{l_\mu b_\nu + l_\nu b_\mu}{l.b}, \tag{3.2.2}$$

where b is a light-cone vector which fixes the gauge. For fermionic internal particles, there are $2^{(D_s/2-1)}$ polarisations $u^{(s)}_i(l, m)$ satisfying the Dirac equation

$$\sum_{j=1}^{2^{D_s/2}} \left(l_\mu \Gamma^\mu_{ij} - m\delta_{ij}\right) u^{(s)}_j(l, m) = 0, \tag{3.2.3}$$

and the completeness relation

$$\sum_{s=1}^{2^{(D_s/2-1)}} u^{(s)}_i \bar{u}^{(s)}_j = l_\mu \Gamma^\mu_{ij} + m\delta_{ij}, \tag{3.2.4}$$

where Γ is the Dirac matrix in D_s-dimensions. Since l is in D-dimensions with $D \leq D_s$, the implicit sum over the space-time index μ runs from 0 to $D-1$.

Additionally, $\mathcal{N}$ has an implicit D-dependence through the D-dimensional loop momentum l. However, since all external momenta remain 4-dimensional, a contraction of the kind $\not{l}\not{p}_i$ will only involve the 4-dimensional components of l. The D-dependence of $\mathcal{N}$ appears only through

$$l^2 = l_0^2 - l_1^2 - l_2^2 - l_3^2 - \sum_{i=4}^{D-1} l_i^2 = \bar{l}^2 - \tilde{l}^2, \tag{3.2.5}$$

where $\bar{l}$ is the 4-dimensional component of l, and $\tilde{l}$ is the remaining $(D-4)$-dimensional part.

A one-loop amplitude involves closing all internal particles, or equivalently, contracting all Lorentz indices from propagators and vertices. For a one-loop amplitude with no closed fermion loops, there is a single trace over the metric tensor $g^{\mu\nu(D_s)}$. Thus the amplitude must be linear in D_s, and the numerator can be expressed as

$$\mathcal{N}^{(D_s)}(l) = \mathcal{N}_0(l) + (D_s - 4)\mathcal{N}_1(l), \tag{3.2.6}$$

where the dependence on the external momenta and polarisations has been suppressed. Neither $\mathcal{N}_0$ or $\mathcal{N}_1$ have explicit dependence on D_s, and only implicit dependence on D through l^2. By evaluating $\mathcal{N}$ at two integer values of D_s, $\mathcal{N}_0$ and $\mathcal{N}_1$ are found to be

$$\begin{aligned} \mathcal{N}_0(l) =& \frac{(D_{s_2} - 4)\mathcal{N}^{(D_{s_1})}(l) - (D_{s_1} - 4)\mathcal{N}^{(D_{s_2})}(l)}{D_{s_2} - D_{s_1}} \\ \mathcal{N}_1(l) =& \frac{\mathcal{N}^{(D_{s_2})}(l) - \mathcal{N}^{(D_{s_1})}(l)}{D_{s_2} - D_{s_1}}. \end{aligned} \tag{3.2.7}$$

If a closed fermion loop is present, the trace is taken over the internal dimensions of the Dirac matrices. This introduces a factor $T_{D_s} = 2^{D_s/2-2}$. There is no linear dependence on D_s, and the numerator is written as

$$\mathcal{N}_f^{D_s}(l) = T_{D_s}\mathcal{N}_{0,f}(l). \tag{3.2.8}$$

The interpolation of D_s can be performed either in the four-dimensional helicity (FDH) scheme [144] or in the 't Hooft-Veltman (HV) scheme [112]. The former takes the limit $D_s \to 4$, while the latter takes $D_s \to 4 - 2\epsilon$. For bosonic (or bosonic and fermionic) internal particles, the two schemes are related by

$$\mathcal{N}^{\mathrm{HV}}(l) = \mathcal{N}^{\mathrm{FDH}}(l) - 2\epsilon\mathcal{N}_1(l) \tag{3.2.9}$$

with $\mathcal{N}^{\mathrm{FDH}}(l) = \mathcal{N}_0(l)$. If the internal particles are only fermions, then the relationship is

$$\mathcal{N}_f^{\mathrm{HV}}(l) = 2^{-\epsilon}(\mathcal{N}_f^{\mathrm{FDH}}(l)) \tag{3.2.10}$$

with $\mathcal{N}_f^{\mathrm{FDH}}(l) = \mathcal{N}_0(l)$. Combining equations (3.2.7), (3.2.9) and (3.2.10), the amplitudes can then be written as

$$\begin{aligned} \mathcal{A}^{\mathrm{FDH}} =& \frac{D_{s_2} - 4}{D_{s_2} - D_{s_1}}\mathcal{A}^{(D,D_{s_1})} - \frac{D_{s_1} - 4}{D_{s_2} - D_{s_1}}\mathcal{A}^{(D,D_{s_2})} \\ \mathcal{A}^{\mathrm{HV}} =& \mathcal{A}^{\mathrm{FDH}} - \frac{2\epsilon}{D_{s_2} - D_{s_1}}\Big(\mathcal{A}^{(D,D_{s_2})} - \mathcal{A}^{(D,D_{s_1})}\Big), \end{aligned} \tag{3.2.11}$$

for bosonic internal particles, and

$$\begin{aligned}\mathcal{A}_f^{\mathrm{FDH}} =& \frac{\mathcal{A}_f^{(D,D_{s_1})}}{T_{D_{s_1}}} \\ \mathcal{A}_f^{\mathrm{HV}} =& 2^{-\epsilon}\Big(\mathcal{A}_f^{\mathrm{FDH}}\Big)\end{aligned} \tag{3.2.12}$$

for purely fermionic internal particles.

Requiring that D_s is even to allow the construction of internal spinors, and that $4 < D \leq D_s$, the simplest choice for the dimensionality of the internal momentum and polarisations is $D = 5$, $D_{s_1} = 6$ and $D_{s_2} = 8$. Thus, the programme is to perform all calculations with $D = D_s = 4$ to obtain the cut-constructible part of the amplitude, and then repeat all calculations with $D = 5$ and $D_s = 6, 8$ to obtain the rational part of the amplitude in the desired scheme through equation (3.2.11) or (3.2.12).

3.3 Vermaseren-Van Neerven Basis

I shall now make a small detour to describe the Vermaseren-Van Neerven basis [128]. This is necessary because the ability to write the loop momentum in this basis is one of the key ingredients of the generalised unitarity method discussed in section 3.4. Consider R incoming momenta (usually external momenta or sums thereof), labeled $k_1, ..., k_R$, in an integer number D of dimensions. Momentum conservation gives $\sum_{i=1}^{R} k_i = 0$, so that at most $R-1$ of the momenta are linearly independent. The dimensions of the physical space spanned by the momenta k_i is thus $D_P = \min(R-1, D)$. To see how a set of basis vectors for the physical space may be constructed, consider the Schouten identity with $R = D = 4$

$$l^\lambda \epsilon^{\mu_1\mu_2\mu_3\mu_4} = l^{\mu_1}\epsilon^{\lambda\mu_2\mu_3\mu_4} + l^{\mu_2}\epsilon^{\mu_1\lambda\mu_3\mu_4} + l^{\mu_3}\epsilon^{\mu_1\mu_2\lambda\mu_4} + l^{\mu_4}\epsilon^{\mu_1\mu_2\mu_3\lambda}, \tag{3.3.1}$$

where l is an arbitrary loop momentum vector and $\epsilon^{\mu_1\cdots\mu_D}$ is the fully antisymmetric tensor in D-dimensions. This identity implies that at most $D = 4$ incoming momenta can be linearly independent. Contracting each side with $k_{1\mu_1}k_{2\mu_2}k_{3\mu_3}k_{4\mu_4}$ gives

$$l^\lambda \epsilon^{k_1k_2k_3k_4} = (l.k_1)\epsilon^{\lambda k_2k_3k_4} + (l.k_2)\epsilon^{k_1\lambda k_3k_4} + (l.k_3)\epsilon^{k_1k_2\lambda k_4} + (l.k_4)\epsilon^{k_1k_2k_3\lambda} \tag{3.3.2}$$

where I have adopted the notation $\epsilon^{\mu_1\cdots\mu_t\cdots\mu_D}k_{\mu_t} = \epsilon^{\mu_1\cdots k_t\cdots\mu_D}$. Then define the basis vectors

$$v_i^\lambda = \frac{\epsilon_{k_1k_2k_3k_4}\epsilon^{k_1\ldots k_{i-1}\lambda k_{i+1}\ldots k_4}}{\epsilon_{k_1k_2k_3k_4}\epsilon^{k_1k_2k_3k_4}}. \tag{3.3.3}$$

to write l as

$$l^\lambda = (l.k_1)v_1^\lambda + (l.k_2)v_2^\lambda + (l.k_3)v_3^\lambda + (l.k_4)v_4^\lambda. \tag{3.3.4}$$

The component of l in the v_i direction is simply the projection of l onto the momentum k_i. The generalised Krönecker delta in R-dimensions is

$$\delta^{\mu_1\mu_2\ldots\mu_R}_{\nu_1\nu_2\ldots\nu_R} = \det\begin{pmatrix} \delta^{\mu_1}_{\nu_1} & \delta^{\mu_1}_{\nu_2} & \ldots & \delta^{\mu_1}_{\nu_R} \\ \delta^{\mu_2}_{\nu_1} & \delta^{\mu_2}_{\nu_2} & \ldots & \delta^{\mu_2}_{\nu_R} \\ \vdots & \vdots & \vdots & \vdots \\ \delta^{\mu_R}_{\nu_1} & \delta^{\mu_R}_{\nu_2} & \ldots & \delta^{\mu_R}_{\nu_R} \end{pmatrix}. \tag{3.3.5}$$

Then, using the general identity $\epsilon_{\nu_1\ldots\nu_D}\epsilon^{\mu_1\cdots\mu_D} = \delta^{\mu_1\cdots\mu_D}_{\nu_1\ldots\nu_D}$, equation (3.3.3) becomes

$$v_i^\lambda = \frac{\delta^{k_1\ldots k_{i-1}\lambda k_{i+1}\ldots k_4}_{k_1\ldots k_{i-1}k_ik_{i+1}\ldots k_4}}{\Delta(k_1, k_2, k_3, k_4)} \tag{3.3.6}$$

where the Gram determinant is

$$\Delta(k_1, k_2, ..., k_R) = \delta^{k_1k_2\ldots.k_R}_{k_1k_2\ldots k_R}. \tag{3.3.7}$$

The basis vectors v_i do not form an othornormal set, however they are orthonormal to the incoming momenta k_j, $v_i.k_j = \delta_{ij}$. While I have derived the basis vectors in the special case where $D = R = 4$, the definition is easily extendable to D_P dimensions:

$$v_i^\lambda = \frac{\delta^{k_1\ldots k_{i-1}\lambda k_{i+1}\ldots k_{D_P}}_{k_1\ldots k_{i-1}k_ik_{i+1}\ldots k_{D_P}}}{\Delta(k_1, ..., k_{D_P})}. \tag{3.3.8}$$

The remainder of the D-dimensional space is the transverse space, with dimension $D_T = \max(0, D-R+1)$. If $R \leq D$, then the metric tensor on the transverse space is

$$w^{\nu}_{\mu}(k_1, ..., k_{R-1}) = \frac{\delta^{k_1 \ldots k_{R-1} \nu}_{k_1 \ldots k_{R-1} \mu}}{\Delta(k_1, ..., k_{R-1})}, \tag{3.3.9}$$

which satisfies $w^{\mu}_{\mu} = D - R + 1$, and raising and lowering the indices of w can be accomplished through $w^{\mu}_{\alpha} w^{\alpha\nu} = w^{\mu\nu}$. Furthermore, $w^{\nu}_{\mu} k^{\mu}_i = 0$ for $i = 1, ..., R-1$, so w is also the projection operator onto the transverse space. The basis vectors for this space are defined as

$$w^{\mu\nu} = \sum_{i=1}^{D-R+1} n^{\mu}_i n^{\nu}_i. \tag{3.3.10}$$

The orthonormality property $n_i.n_j = \delta_{ij}$ follows from the trace over w, while $w^{\nu}_{\mu} k^{\mu}_i = 0$ implies that $n_r.k_i = 0$ and hence $n_r.v_i = 0$.

The metric tensor in the full D-dimensions can then be written as

$$g^{\mu\nu} = \sum_{i=1}^{D_P} k^{\mu}_i v^{\nu}_i + \sum_{i=1}^{D_T} n^{\mu}_i n^{\nu}_i. \tag{3.3.11}$$

Contracting this with l generalises equation (3.3.4) to arbitrary values of R:

$$l^{\lambda} = \sum_{i=1}^{D_P} (l.k_i) v^{\lambda}_i + \sum_{i=1}^{D_T} (l.n_i) n^{\lambda}_i. \tag{3.3.12}$$

Referring to equation (3.1.2), the i-th propagator has denominator $D_i = (l+q_i)^2 - m_i^2$ with $q_i = q_{i-1} + k_i$. Then

$$D_i - D_{i-1} = 2l.(q_i - q_{i-1}) + q_i^2 - q_{i-1}^2 - m_i^2 + m_{i-1}^2 \tag{3.3.13}$$

so

$$l.k_i = \frac{1}{2}\big(D_i - D_{i-1} - q_i^2 + q_{i-1}^2 + m_i^2 - m_{i-1}^2\big). \tag{3.3.14}$$

Substituting the above into equation (3.3.12) gives

$$l^{\lambda} = \frac{1}{2} \sum_{i=1}^{D_P} (D_i - D_{i-1}) v^{\lambda}_i + \sum_{i=1}^{D_T} (l.n_i) n^{\lambda}_i + V^{\lambda}_R \tag{3.3.15}$$

with

$$V^{\lambda}_R = \frac{1}{2} \sum_{i=1}^{D_P} (-q_i^2 + q_{i-1}^2 + m_i^2 - m_{i-1}^2) v^{\lambda}_i. \tag{3.3.16}$$

The loop momentum l is expressed in terms of propagators. The usefulness of this will become apparent when looking at the OPP subtraction procedure in the following section.

3.4 Generalised Unitarity

I now return to the evaluation of the one-loop amplitude equation (3.2.1), where the dependence of $\mathcal{A}$ and $\mathcal{N}$ on D and D_s is understood from the previous discussion and will not be indicated. The dependence on external momenta and polarisations p_i and J_i is also understood. The suggestion of Ossola, Papadoupoulos and Pittau [57] was to write the *integrand* of equation (3.2.1) as

$$\begin{aligned}\mathcal{A}_N(l) &= \frac{\mathcal{N}(l)}{D_0 D_1 ... D_{N-1}} \\ &= \frac{1}{D_0 D_1 ... D_{N-1}} \times \\ &\Bigg\{ \sum_{[i_1|i_5]} \tilde{e}_{i_1 i_2 i_3 i_4 i_5}(l) \prod_{j \neq [i_1|i_5]} D_j(l) + \sum_{[i_1|i_4]} \tilde{d}_{i_1 i_2 i_3 i_4}(l) \prod_{j \neq [i_1|i_4]} D_j(l) + \\ &\sum_{[i_1|i_3]} \tilde{c}_{i_1 i_2 i_3}(l) \prod_{j \neq [i_1|i_3]} D_j(l) + \sum_{[i_1|i_2]} \tilde{b}_{i_1 i_2}(l) \prod_{j \neq [i_1|i_2]} D_j(l) + \\ &\sum_{i_1} \tilde{a}_{i_1}(l) \prod_{j \neq i_1} D_j(l) \Bigg\}.\end{aligned} \tag{3.4.1}$$

In contrast to the coefficients in the expansion of the amplitude in terms of master integrals, equation (3.1.3), the unitarity coefficients in equation (3.4.1) are functions of loop momentum l. However, their dependence on l is quite simple. Furthermore, most of the terms are odd in l, and thus trivially integrate to zero.

In order to solve for the coefficients in equation (3.4.1), I will set groups of propagators D_j to zero, and express the coefficients as residues of the integrand. Beginning with the highest-point coefficient $\tilde{e}_{i_1 i_2 i_3 i_4 i_5}(l)$, set $l = l_{i_1 i_2 i_3 i_4 i_5}$ such that

$$\begin{aligned}D_{i_1}(l_{i_1 i_2 i_3 i_4 i_5}) &= D_{i_2}(l_{i_1 i_2 i_3 i_4 i_5}) = D_{i_3}(l_{i_1 i_2 i_3 i_4 i_5}) \\ &= D_{i_4}(l_{i_1 i_2 i_3 i_4 i_5}) = D_{i_5}(l_{i_1 i_2 i_3 i_4 i_5}) = 0,\end{aligned}$$

and write

$$\begin{aligned}\tilde{e}_{i_1 i_2 i_3 i_4 i_5}(l) &= \mathrm{Res}_{i_1 i_2 i_3 i_4 i_5}\Big(\mathcal{A}_N(l)\Big) \\ &\equiv \Big[D_{i_1}(l) D_{i_2}(l) D_{i_3}(l) D_{i_4}(l) D_{i_5}(l) \mathcal{A}_N(l)\Big]_{l = l_{i_1 i_2 i_3 i_4 i_5}}.\end{aligned} \tag{3.4.2}$$

The remaining coefficients are found after subtracting the contributions from the known higher-point coefficients. Thus $\tilde{d}_{i_1 i_2 i_3 i_4}(l)$ is found by choosing $l = l_{i_1 i_2 i_3 i_4}$ such that

$$D_{i_1}(l_{i_1 i_2 i_3 i_4}) = D_{i_2}(l_{i_1 i_2 i_3 i_4}) = D_{i_3}(l_{i_1 i_2 i_3 i_4}) = D_{i_4}(l_{i_1 i_2 i_3 i_4}) = 0$$

and then taking

$$\tilde{d}_{i_1 i_2 i_3 i_4}(l) = \mathrm{Res}_{i_1 i_2 i_3 i_4}\Big(\mathcal{A}_N(l) - \sum_{i_5 \neq i_1, i_2, i_3, i_4} \frac{\tilde{e}_{i_1 i_2 i_3 i_4 i_5}(l)}{D_{i_1}(l) D_{i_2}(l) D_{i_3}(l) D_{i_4}(l) D_{i_5}(l)}\Big). \tag{3.4.3}$$

Similarly, $\tilde{c}_{i_1i_2i_3}(l)$ is found by choosing $l = l_{i_1i_2i_3}$ such that $D_{i_1}(l_{i_1i_2i_3}) = D_{i_2}(l_{i_1i_2i_3}) = D_{i_3}(l_{i_1i_2i_3}) = 0$; $\tilde{b}_{i_1i_2}(l)$ is found by choosing $l = l_{i_1i_2}$ such that $D_{i_1}(l_{i_1i_2}) = D_{i_2}(l_{i_1i_2}) = 0$; and $\tilde{a}_{i_1}(l)$ is found by choosing $l = l_{i_1}$ such that $D_{i_1}(l_{i_1}) = 0$. These are given by

$$\begin{aligned}
\tilde{c}_{i_1i_2i_3}(l) &= \text{Res}_{i_1i_2i_3}\Big(\mathcal{A}_N(l) - \frac{1}{2!}\sum_{i_4,i_5\neq i_1,i_2,i_3}\frac{\tilde{e}_{i_1i_2i_3i_4i_5}(l)}{D_{i_1}(l)D_{i_2}(l)D_{i_3}(l)D_{i_4}(l)D_{i_5}(l)} \\
&\quad - \sum_{i_4\neq i_1,i_2,i_3}\frac{\tilde{d}_{i_1i_2i_3i_4}(l)}{D_{i_1}(l)D_{i_2}(l)D_{i_3}(l)D_{i_4}(l)}\Big), \\
\tilde{b}_{i_1i_2}(l) &= \text{Res}_{i_1i_2}\Big(\mathcal{A}_N(l) - \frac{1}{3!}\sum_{i_3,i_4,i_5\neq i_1,i_2}\frac{\tilde{e}_{i_1i_2i_3i_4i_5}(l)}{D_{i_1}(l)D_{i_2}(l)D_{i_3}(l)D_{i_4}(l)D_{i_5}(l)} \\
&\quad - \frac{1}{2!}\sum_{i_3,i_4\neq i_1,i_2}\frac{\tilde{d}_{i_1i_2i_3i_4}(l)}{D_{i_1}(l)D_{i_2}(l)D_{i_3}(l)D_{i_4}(l)} \\
&\quad - \sum_{i_3\neq i_1,i_2}\frac{\tilde{c}_{i_1i_2i_3}(l)}{D_{i_1}(l)D_{i_2}(l)D_{i_3}(l)}\Big), \\
\tilde{a}_{i_1}(l) &= \text{Res}_{i_1}\Big(\mathcal{A}_N(l) - \frac{1}{4!}\sum_{i_2,i_3,i_4,i_5\neq i_1}\frac{\tilde{e}_{i_1i_2i_3i_4i_5}(l)}{D_{i_1}(l)D_{i_2}(l)D_{i_3}(l)D_{i_4}(l)D_{i_5}(l)} \\
&\quad - \frac{1}{3!}\sum_{i_2,i_3,i_4\neq i_1}\frac{\tilde{d}_{i_1i_2i_3i_4}(l)}{D_{i_1}(l)D_{i_2}(l)D_{i_3}(l)D_{i_4}(l)} \\
&\quad - \frac{1}{2!}\sum_{i_2,i_3\neq i_1}\frac{\tilde{c}_{i_1i_2i_3}(l)}{D_{i_1}(l)D_{i_2}(l)D_{i_3}(l)} - \sum_{i_2\neq i_1}\frac{\tilde{b}_{i_1i_2}(l)}{D_{i_1}(l)D_{i_2}(l)}\Big).
\end{aligned} \tag{3.4.4}$$

Choosing loop momentum l such that J propagators are set to zero is equivalent to putting the J internal particles on-shell. As a result, the residues are calculated using J *tree-level* amplitudes (the details of how these amplitudes are calculated is the subject of chapter 4). This procedure is known as "cutting" a loop integral, and the setting of 5,4,3,2, and 1 propagators on-shell are referred to as pentuple, quadruple, triple, double and single cuts, respectively. The indices of the unitarity coefficients $\tilde{e}, \tilde{d}, \tilde{c}, \tilde{b}, \tilde{a}$, indicate which internal propagators need to be cut in order to extract that coefficient; I shall refer to these indices as "unitarity indices". There is a sum over unitarity indices for each unitarity cut – propagators should be set to zero in every permutation[2].

As an example, the coefficient of a quadruple cut (1234) of a six-point amplitude

---

[2] In fact, it is not necessary to implement massless single cuts, since the master integral multiplying these cuts vanishes in dimensional regularisation. Similarly, the master integrals multiplying massless double cuts separated by a single massless external particle also vanish, so these cuts are also discarded [85].

is

$$\begin{aligned}\tilde{d}_{1234} =&\mathrm{Res}_{1234}\Big(\mathcal{A}_N(l) - \sum_{i_5\neq 1,2,3,4} \frac{\tilde{e}_{1234i_5}}{D_1D_2D_3D_4D_{i_5}}\Big)\\ =&\sum \mathcal{A}^0(l_1;p_1,...,p_j;-l_2) \times \mathcal{A}^0(l_2;p_{j+1},...,p_k;-l_3)\\ &\times \mathcal{A}^0(l_3;p_{k+1},...,p_m;-l_4) \times \mathcal{A}^0(l_4;p_{m+1},...,p_N;-l_1)\\ &- \frac{\tilde{e}_{12345}}{D_5(l_{1234})} - \frac{\tilde{e}_{12346}}{D_6(l_{1234})}.\end{aligned} \tag{3.4.5}$$

The sum in the second line is over all quantum numbers of the cut internal particles, including the polarisations. This introduces the D_s dependence discussed in section 3.2.

In four dimensions, at most four restrictions on the loop momentum l leading to $D_i(l) = 0$ can be imposed, meaning that at most four propagators can be set to zero at a time. Since, as was discussed in the previous section, the rational part of the amplitude needs to be computed in $D = 5$, five propagators can be set to zero. This explains why the maximum number of unitarity cuts allowed is five, i.e. why equation (3.4.1) has five terms.

Determining the loop momentum

I will now address the issue of how to find loop momenta l such that a given number J propagators vanish:

$$D_{i_n} = (q_{i_n} + l)^2 - m_{i_n}^2 = 0, \tag{3.4.6}$$

for $n = 1, ..., J$. This defines J inflow momenta q_{i_n} for the J tree-level amplitudes. These can be used to construct a Vermaseren-Van Neerven basis with $D_P = \min(D, J-1)$ physical dimensions and $D_T = \max(0, D-J+1)$ transverse dimensions. Since $D \geq J$, this means that $D_T \geq 1$. One of the transverse basis vectors is identified with a basis vector in $D-4$ dimensions, and is labeled n_ϵ, as a reminder that any quantity involving this vector contributes to the rational part. The remaining transverse directions remain in four dimensions. The physical space is spanned by vectors $v_1, ..., v_{D_P}$ defined as equation (3.3.6) using the external momenta of the tree-level amplitudes, or equivalently the momentum difference between cut propagators: $q_{i_j} = \sum_{l=1}^{j} k_l$. Referring to equation (3.3.15), the loop momentum can be written as

$$l^\mu = \frac{1}{2}\sum_{n=1}^{D_P}(D_{i_n} - D_{i_{n-1}})v_{i_n}^\mu + V_R^\mu + \sum_{i=1}^{D_T-1} \alpha_i n_i^\mu + \alpha_\epsilon n_\epsilon^\mu, \tag{3.4.7}$$

with $D_{i_0} = D_{i_J}$, and $\alpha_i \equiv l.n_i$ and $\alpha_\epsilon \equiv l.n_\epsilon$. Setting the denominators D_{i_n} to zero this becomes

$$l^\mu = V_R^\mu + \sum_{i=1}^{D_T-1} \alpha_i n_i^\mu + \alpha_\epsilon n_\epsilon^\mu. \tag{3.4.8}$$

Also, using equation (3.3.16),

$$
\begin{aligned}
V_R.q_{i_j} &= -\frac{1}{2}\sum_{m=1}^{D_P}(q_{i_m}^2 - m_{i_m}^2 - q_{i_{m-1}}^2 + m_{i_{m-1}}^2)v_{i_m}^\mu . \sum_{l=1}^{j} k_l \\
&= -\frac{1}{2}(q_{i_j}^2 - m_{i_j}^2 + m_{i_0})^2,
\end{aligned}
\tag{3.4.9}
$$

where the loop momentum is parametrised by setting $q_0 = 0$. Then, returning to the expression of the propagator,

$$
\begin{aligned}
0 &= (q_{i_n} + l)^2 - m_{i_n}^2 \\
&= V_R^2 + \sum_{i=1}^{D_T-1} \alpha_i^2 + \alpha_\epsilon^2 + q_{i_n}^2 - (q_{i_n}^2 - m_{i_n}^2 + m_{i_0}^2) - m_{i_n}^2 \\
&= V_R^2 + \sum_{i=1}^{D_T-1} \alpha_i^2 + \alpha_\epsilon^2 - m_{i_0}^2.
\end{aligned}
\tag{3.4.10}
$$

The terms V_R^2 and $m_{i_0}^2$ are set by the kinematics of the unitarity cut and the masses of the cut internal propagators. There is then freedom in choosing the values of α_i used in constructing l, provided that equation (3.4.10) is satisfied.

As an aside, note that equation (3.4.10) implies that the maximum number of unitarity cuts is five for *any* $D > 4$, not just $D = 5$ as discussed above. This is because the $(D-4)$-dimensional components of l enter the denominators as α_ϵ^2, so that extending the loop momentum from 4-dimensions to D-dimensions provides only one additional variable to the denominators, irrespective of the value of D.

Functional form of unitarity coefficients

I will now consider the functional dependence of the unitarity coefficients $\tilde{e}, \tilde{d}, \tilde{c}, \tilde{b}$ and $\tilde{a}$ on the loop momentum l, beginning with the $\tilde{e}$ [3]. The first term of equation (3.4.1) is

$$
\sum_{[i_1|i_5]} \frac{\tilde{e}(l)}{D_{i_1}D_{i_2}D_{i_3}D_{i_4}D_{i_5}}. \tag{3.4.11}
$$

In a renormalisable field theory, the rank of the integral cannot be larger than the number of denominators. Thus the maximum rank of the above five-point function is five. The maximum rank numerator can be written as

$$
N^{(5)}(l) = \prod_{i=1}^{5} w_i.l, \tag{3.4.12}
$$

where the w_i are combinations of external momenta and polarisations. Using equation (3.4.7), with $D = 5, R = 5$, the loop momentum is

$$
l^\mu = \frac{1}{2}\sum_{i=1}^{4}\big(D_i - D_{i-1} - q_i^2 + q_{i-1}^2 + m_i^2 - m_{i-1}^2\big)v_i^\mu + (l.n_\epsilon)n_\epsilon^\mu. \tag{3.4.13}
$$

---

[3] For convenience, I will drop the unitarity indices, since this discussion holds for any unitarity cut.

Since w_i are four-dimensional, the product $w_i.n_\epsilon$ always vanishes. Applying this to one factor of l at a time results in

$$\begin{aligned} N^{(5)}(l) =& \prod_{i=1}^{4}(w_i.l)(w_5.l) \\ =& \frac{1}{2}\prod_{i=1}^{4}(w_i.l)w_{5\mu}.\Big(\sum_{i=1}^{4}\big(D_i - D_{i-1} - q_i^2 + q_{i-1}^2 + m_i^2 - m_{i-1}^2\big)v_i^\mu. \end{aligned} \tag{3.4.14}$$

The terms involving the propagators will cancel with the propagators in the denominator, leading to rank-four, four-point integrals. The remaining terms will lead to rank-four, five-point integrals. Repeating this procedure on all the rank-four five-point integrals (those originating from the above reduction as well as those present in the amplitude from the outset) leads to rank-three five- and four-point integrals. Exhausting this, we are left with a scalar five-point function and four-point functions of rank one through four. The coefficients of the latter can be absorbed into the coefficients of four-point functions $\tilde{d}$ in equation (3.4.1), leaving only a scalar five-point function. Thus, the coefficient $\tilde{e}$ is independent of l:

$$\tilde{e}(l) = \tilde{e}. \tag{3.4.15}$$

In fact, referring to equation (3.4.10) with $\alpha_\epsilon = l.n_\epsilon$, the projection of the loop momentum onto the transverse space is

$$(l.n_\epsilon)^2 = m_0^2 - \frac{1}{4}\sum_{i,j=1}^{4}(v_i.v_j)(-q_i^2+q_{i-1}^2+m_i^2-m_{i-1}^2)(-q_j^2+q_{j-1}^2+m_j^2-m_{j-1}^2), \tag{3.4.16}$$

meaning that either the scalar five-point integral or the integral $\int \frac{d^Dl}{(2\pi)^D}\frac{(l.n_\epsilon)^2}{D_0D_1D_2D_3D_4}$ can serve as the basis integral. The latter is preferable, since it vanishes as $D \to 4$. This avoids cancellations between five- and four-point integrals, which could lead to numerical instabilities if the integrals are large. The five-point coefficients therefore do not contribute directly to the one-loop amplitude. However, it is still important to compute $\tilde{e}$ to determine the coefficients of lower-point integrals, as in equations (3.4.3) and (3.4.4).

Focusing on the coefficients of four-point integrals, using equation (3.4.7) with $R = 4, D = 5$

$$l^\mu = \frac{1}{2}\sum_{i=1}^{3}\big(D_i - D_{i-1} - q_i^2 + q_{i-1}^2 + m_i^2 - m_{i-1}^2\big)v_i^\mu + (l.n_4)n_4^\mu + (l.n_\epsilon)n_\epsilon^\mu. \tag{3.4.17}$$

Substituting this into the four-point numerator with the highest rank of four

$$N^{(4)}(l) = \prod_{i=1}^{4} w_i.l, \tag{3.4.18}$$

will result in a rank-three three-point function, a rank-three four-point function, and an additional rank-four four-point integral

$$N^{(4)}(l) = \prod_{i=1}^{3}(w_i.l)(w_4.n_4)(l.n_4). \tag{3.4.19}$$

Repeating this procedure, a rank-four four-point integral is again kept

$$N^{(4)}(l) = \prod_{i=1}^{2}(w_i.l)(w_4.n_4)(w_3.n_4)(l.n_4)^2, \tag{3.4.20}$$

and repeating a further two times leads to terms $\sim (l.n_4)^3$ and $\sim (l.n_4)^4$. A similar procedure may be performed on the four-point functions of lower rank. Thus, the coefficients $\tilde{d}$ of the four-point integrals must be a polynomial in $(l.n_4)$ of degree 4. Squaring equation (3.4.17) and using $l^2 = D_0 + m_0^2$ implies

$$(l.n_4)^2 = -(l.n_\epsilon)^2 + \text{constant} + \mathcal{F}(D_i) \tag{3.4.21}$$

where constant terms contribute to the rank-two four-point integrals and the terms containing propagators $\mathcal{F}(D_i)$ contribute to three-point integrals. Then $\tilde{d}$ can be written as

$$\tilde{d} = \tilde{d}_0 + \tilde{d}_1(l.n_4) + \tilde{d}_2(l.n_\epsilon)^2 + \tilde{d}_3(l.n_4)(l.n_\epsilon)^2 + \tilde{d}_4(l.n_\epsilon)^4. \tag{3.4.22}$$

Importantly, the coefficients in equation (3.4.22) are independent of l: the dependence of the unitarity coefficient $\tilde{d}$ on the loop momentum is the polynomial dependence explicity shown in this equation.

Considering the coefficients of three-point integrals, the loop momentum is

$$l^\mu = \frac{1}{2}\sum_{i=1}^{2}\big(D_i - D_{i-1} - q_i^2 + q_{i-1}^2 + m_i^2 - m_{i-1}^2\big)v_i^\mu + (l.n_3)n_3^\mu + (l.n_4)n_4^\mu + (l.n_\epsilon)n_\epsilon^\mu. \tag{3.4.23}$$

Then the highest-rank numerator will be

$$\begin{aligned} N^{(3)} =& \prod_{i=1}^{3}(w_i.l) \\ =& \big(\text{const} + \mathcal{F}(D_j) + (w_1.n_3)(l.n_3) + (w_1.n_4)(l.n_4)\big)\times \\ & \big(\text{const} + \mathcal{F}(D_j) + (w_2.n_3)(l.n_3) + (w_2.n_4)(l.n_4)\big)\times \\ & \big(\text{const} + \mathcal{F}(D_j) + (w_3.n_3)(l.n_3) + (w_3.n_4)(l.n_4)\big), \end{aligned} \tag{3.4.24}$$

where the terms in $\mathcal{F}(D_j)$ contribute to the two-point integrals, and the constant terms contribute to three-point integrals of rank < 3. The three-point integrals that remain have coefficients

$$\begin{aligned} \tilde{c} =& \tilde{c}_0 + \tilde{c}_1(l.n_3) + \tilde{c}_2(l.n_4) + \tilde{c}_3(l.n_3)(l.n_4) + \tilde{c}_4(l.n_3)^2 + \tilde{c}_5(l.n_4)^2 + \\ & \tilde{c}_6(l.n_3)^3 + \tilde{c}_7(l.n_4)^3 + \tilde{c}_8(l.n_3)^2(l.n_4) + \tilde{c}_9(l.n_3)(l.n_4)^2. \end{aligned} \tag{3.4.25}$$

Squaring the loop momentum indicates that $(l.n_3)^2$, $(l.n_4)^2$ and $(l.n_\epsilon)^2$ are related to each other, with the relationship involving other terms which again contribute to either linear terms in equation (3.4.25) or two-point integrals. This is used to remove the two terms cubic in l in equation (3.4.25), to write[4]

---

[4] Equally well, the terms involving $(l.n_3)^2(l.n_4)$ and $(l.n_3)(l.n_4)^2$ could be removed to obtain

$$\begin{aligned} \tilde{c} =& \tilde{c}_0 + \tilde{c}_1(l.n_3) + \tilde{c}_2(l.n_4) + \tilde{c}_3\big((l.n_3)^2 - (l.n_4)^2\big) + \tilde{c}_4(l.n_3)(l.n_4) + \\ & \tilde{c}_5(l.n_3)^3 + \tilde{c}_6(l.n_4)^3 + \tilde{c}_7(l.n_\epsilon)^2 + \tilde{c}_8(l.n_\epsilon)^2(l.n_3) + \tilde{c}_9(l.n_\epsilon)^2(l.n_4). \end{aligned}$$

$$\begin{aligned}\tilde{c} =&\tilde{c}_0 + \tilde{c}_1(l.n_3) + \tilde{c}_2(l.n_4) + \tilde{c}_3(l.n_3)(l.n_4) + \tilde{c}_4\big((l.n_3)^2 - (l.n_4)^2\big)+\\ &\tilde{c}_5(l.n_3)^2(l.n_4) + \tilde{c}_6(l.n_3)(l.n_4)^2 + \tilde{c}_7(l.n_\epsilon)^2 + \tilde{c}_8(l.n_\epsilon)^2(l.n_3)+\\ &\tilde{c}_9(l.n_\epsilon)^2(l.n_4).\end{aligned} \tag{3.4.26}$$

This form of the expression makes solving for the coefficients $\tilde{c}_i$ easier.

Looking at the coefficients of the two-point integrals, the loop momentum is

$$\begin{aligned}l^\mu =&\frac{1}{2}\big(D_1 - D_0 - q_1^2 + m_1^2 - m_0^2\big)v_1^\mu + (l.n_2)n_2^\mu + (l.n_3)n_3^\mu + (l.n_4)n_4^\mu\\ &+ (l.n_\epsilon)n_\epsilon^\mu,\end{aligned} \tag{3.4.27}$$

and the highest-rank numerator is

$$\begin{aligned}N^{(2)} =&\prod_{i=1}^{2}(w_i.l)\\ =&\big(\text{const} + \mathcal{F}(D_j) + (w_1.n_2)(l.n_2) + (w_1.n_3)(l.n_3) + (w_1.n_4)(l.n_4)\big)\times\\ &\big(\text{const} + \mathcal{F}(D_j) + (w_2.n_2)(l.n_2) + (w_2.n_3)(l.n_3) + (w_2.n_4)(l.n_4)\big).\end{aligned} \tag{3.4.28}$$

The coefficients are then

$$\begin{aligned}\tilde{b} =&\tilde{b}_0 + \tilde{b}_1(l.n_2) + \tilde{b}_2(l.n_3) + \tilde{b}_3(l.n_4) + \tilde{b}_4(l.n_2)^2 + \tilde{b}_5(l.n_3)^2\\ &+ \tilde{b}_6(l.n_4)^2 + \tilde{b}_7(l.n_2)(l.n_3) + \tilde{b}_8(l.n_2)(l.n_4) + \tilde{b}_9(l.n_3)(l.n_4).\end{aligned} \tag{3.4.29}$$

Again, there is a relation between $(l.n_2)^2, (l.n_3)^2, (l.n_4)^2$ and $(l.n_\epsilon)^2$, and equation (3.4.29) can be rewritten as

$$\begin{aligned}\tilde{b} =&\tilde{b}_0 + \tilde{b}_1(l.n_2) + \tilde{b}_2(l.n_3) + \tilde{b}_3(l.n_4) + \tilde{b}_4\big((l.n_2)^2 - (l.n_3)^2\big)\\ &+ \tilde{b}_5\big((l.n_2)^2 + (l.n_3)^2 - 2(l.n_4)^2\big) + \tilde{b}_6(l.n_2)(l.n_3) + \tilde{b}_7(l.n_2)(l.n_4)\\ &+ \tilde{b}_8(l.n_3)(l.n_4) + \tilde{b}_9(l.n_\epsilon)^2.\end{aligned} \tag{3.4.30}$$

Finally, the coefficients of the one-point integrals can be simply written as

$$\tilde{a} = \tilde{a}_0 + \tilde{a}_1(l.n_1) + \tilde{a}_2(l.n_2) + \tilde{a}_3(l.n_3) + \tilde{a}_4(l.n_4). \tag{3.4.31}$$

Solving the OPP equations

It is worthwhile mentioning how one can go about solving the linear equations (3.4.22), (3.4.26), (3.4.30), and (3.4.31). Recall that the left-hand sides of these equations are determined by computing tree-level amplitudes. While it suffices to use any general technique to solve simulataneous equations, such as Gauss-Jordan elimination, it is also possible to do so by making astute parametrisations of the loop momentum. Of course, when solving the equations numerically, one can change parametrisations at will.

Since the coefficients of the five-point integral in equation (3.4.1) are independent of l, all one needs to do is evaluate the left-hand side of this equation for any parametrisation of l which sets five propagators to zero, and this gives the constant coefficient $\tilde{e}$.

In order to solve for the coefficient of the four-point integral, I will begin by working in four dimensions. Then only the first two terms of equation (3.4.22) are non-zero. The loop momentum can be written as $l_{\pm}^{\mu} = V_4^{\mu} \pm l_{\perp} n_4^{\mu}$, with $l_{\perp}$ the projection of l onto the transverse space, and the first two coefficients in equation (3.4.22) can be recovered:

$$\begin{aligned} \tilde{d}_0 &= \frac{\tilde{d}(l_+) + \tilde{d}(l_-)}{2}, \\ \tilde{d}_1 &= \frac{\tilde{d}(l_+) - \tilde{d}(l_-)}{2l_{\perp}}. \end{aligned} \tag{3.4.32}$$

Extending the dimensionality of l to five, and writing $\bar{l}_{\pm}^{\mu} = V_4^{\mu} \pm \frac{1}{\sqrt{2}} l_{\perp} \big(n_4^{\mu} + n_{\epsilon}^{\mu}\big)$, and $l_{\epsilon}^{\mu} = V_4^{\mu} + l_{\perp} n_{\epsilon}^{\mu}$, the remaining coefficients are

$$\begin{aligned} \tilde{d}_2 =& \frac{1}{l_{\perp}^2}\big(2\tilde{d}(\bar{l}_+) + 2\tilde{d}(\bar{l}_-) - \tilde{d}(l_{\epsilon}) - 3\tilde{d}_0\big), \\ \tilde{d}_3 =& \frac{\sqrt{2}}{l_{\perp}^3}\big(\tilde{d}(\bar{l}_+) - \tilde{d}(\bar{l}_-) - \sqrt{2}\tilde{d}_1 l_{\perp}\big), \\ \tilde{d}_4 =& \frac{2}{l_{\perp}^4}\big(-\tilde{d}(\bar{l}_+) - \tilde{d}(\bar{l}_-) + \tilde{d}(l_{\epsilon}) + \tilde{d}_0\big). \end{aligned} \tag{3.4.33}$$

When dealing with the coefficients of the three-point integrals, I again begin by working in four dimensions, so that the last three terms of equation (3.4.26) are zero, and parametrise the loop momentum as $l^{\mu} = V_4^{\mu} + l_{\perp}(\cos\theta n_3^{\mu} + \sin\theta n_4^{\mu})$. The unitarity coefficients can be rewritten as a polynomial in $t = \exp(i\theta)$

$$\tilde{c}(t) = \sum_{p=-3}^{3} \tilde{C}_p t^p. \tag{3.4.34}$$

Applying a Fourier transform, the $\tilde{C}_p$ are given by

$$\tilde{C}_p = \frac{1}{7}\sum_{m=0}^{6} \tilde{c}(t_m) t_m^{-p}, \tag{3.4.35}$$

where $t_m = \exp(2\pi m i/7)$. Using this parametrisation of the loop momentum in equation (3.4.26), expanding equation (3.4.34), and equating coefficients of $\cos\theta$ and $\sin\theta$, the coefficients can be related:

$$\begin{array}{lllllll} \tilde{c}_0 &=& \tilde{C}_0; & & & & \\ \tilde{c}_3 &=& \frac{2i}{l_{\perp}^2}\big(\tilde{C}_2 - \tilde{C}_{-2}\big); & \quad & \tilde{c}_4 &=& \frac{1}{l_{\perp}^2}\big(\tilde{C}_2 + \tilde{C}_{-2}\big); \\ \tilde{c}_5 &=& \frac{4i}{l_{\perp}^3}\big(\tilde{C}_3 - \tilde{C}_{-3}\big); & & \tilde{c}_6 &=& -\frac{4}{l_{\perp}^3}\big(\tilde{C}_3 + \tilde{C}_{-3}\big); \\ \tilde{c}_1 &=& \frac{1}{l_{\perp}}\big(\tilde{C}_1 + \tilde{C}_{-1}\big) - \frac{\tilde{c}_6}{4} l_{\perp}^2; & & \tilde{c}_2 &=& \frac{i}{l_{\perp}}\big(\tilde{C}_1 - \tilde{C}_{-1}\big) - \frac{\tilde{c}_5}{4} l_{\perp}^2. \end{array} \tag{3.4.36}$$

Moving into five dimensions to solve for the remaining three coefficients $\tilde{c}_7$, $\tilde{c}_8$, and $\tilde{c}_9$, the loop momentum is parametrised as $l_\pm^\mu = V_3^\mu + \frac{l_\perp}{\sqrt{2}}\big(\pm n_3^\mu + n_\epsilon^\mu\big)$. Subtracting from both sides of equation (3.4.26) all the terms whose coefficients are known from equation (3.4.36), and writing the resulting left-hand side expression as $\tilde{c}^{\text{subtr}}$ leads to

$$\tilde{c}^{\text{subtr}}(l_\pm) = \tilde{c}_7 \frac{l_\perp^2}{2} \pm \tilde{c}_8 \frac{l_\perp^3}{2\sqrt{2}}, \tag{3.4.37}$$

which allows $\tilde{c}_7$ and $\tilde{c}_8$ to be found. Finally, $\tilde{c}_9$ can be found for any parametrisation of l since the remaining coefficients are all known.

This procedure may run into problems if the magnitude of the transverse loop momentum $l_\perp$ is small, since this may lead to numerical errors. If this is the case, then the loop momentum is parametrised as $l_\pm^\mu = V_3^\mu + x_3 n_3^\mu \pm x_4 n_4^\mu$ with $x_3 = \exp(i\theta)$ and $x_4 = \sqrt{l_\perp^2 - x_3^2}$. The function $C_+(x_3) = \frac{\tilde{c}(l_+)+\tilde{c}(l_-)}{2}$ is written as a third degree polynomial in x_3,

$$C_+(x_3) = \sum_{n=0}^{3} \tilde{C}_n x_3^n. \tag{3.4.38}$$

The coefficients of this expansion can be found using a Fourier transform, and can then be related by equating coefficients of powers of x_3:

$$\begin{array}{rclcrcl} \tilde{c}_6 & = & -\tilde{C}_3; & \qquad & \tilde{c}_4 & = & \frac{\tilde{C}_2}{2}; \\ \tilde{c}_1 & = & \tilde{C}_1 - \tilde{c}_6 l_\perp^2; & \qquad & \tilde{c}_0 & = & \tilde{C}_0 + \tilde{c}_4 l_\perp^2. \end{array} \tag{3.4.39}$$

The remaining four-dimensional coefficients can be found by choosing specific values of x_3 in the function $C_-(x_3) = \frac{\tilde{c}(l_+)-\tilde{c}(l_-)}{2x_4}$:

$$\begin{aligned} \tilde{c}_3 &= \frac{C_-(x_3=1) - C_-(x_3=-1)}{2}, \\ \tilde{c}_2 &= \frac{C_-(x_3=1) + C_-(x_3=i) - (1+i)\tilde{c}_3}{2}, \\ \tilde{c}_5 &= \frac{C_-(x_3=1) - C_-(x_3=i) - (1-i)\tilde{c}_3}{2}. \end{aligned} \tag{3.4.40}$$

The extension to five dimensions is similar to before. Writing the loop momentum $l_\pm^\mu = V_3^\mu \pm n_3^\mu + \sqrt{l_\perp^2 - 1}n_\epsilon^\mu$, and defining $\tilde{c}^{\text{subtr}}$ by subtracting all the four-dimensional terms from $\tilde{c}$ modifies equation (3.4.37):

$$\tilde{c}^{\text{subtr}}(l_\pm) = -\tilde{c}_7(l_\perp^2 - 1) \mp \tilde{c}_8(l_\perp^2 - 1), \tag{3.4.41}$$

allowing $\tilde{c}_7$ and $\tilde{c}_8$, and hence $\tilde{c}_9$, to be found.

Turning now to equation (3.4.30) for the coefficients $\tilde{b}_1, ..., \tilde{b}_9$, the loop momentum in four dimensions is parametrised by $l_{\pm\pm}^\mu = V_2^\mu + l_\perp(\pm x_2 n_2^\mu \pm x_3 n_3^\mu)$ with $x_2 = \cos\phi$ and $x_3 = \sin\phi$. The left-hand side of equation (3.4.30) can be written as a polynomial

$$\tilde{b}_{++} = \tilde{b}(l_{++}) = \sum_{n=-2}^{2} \tilde{B}_n \exp(in\phi). \tag{3.4.42}$$

The values of $\tilde{B}_n$ are then found using a Fourier transform, as was done for the triple-cut coefficients $\tilde{c}_i$. Equating coefficients of powers of x_2 and x_3 gives

$$\begin{aligned} \tilde{b}_1 &= \tfrac{1}{l_\perp}\big(\tilde{B}_1 + \tilde{B}_{-1}\big); & \tilde{b}_2 &= \tfrac{i}{l_\perp}\big(\tilde{B}_1 - \tilde{B}_{-1}\big); \\ \tilde{b}_4 &= \tfrac{1}{l_\perp^2}\big(\tilde{B}_2 + \tilde{B}_{-2}\big); & \tilde{b}_6 &= \tfrac{2i}{l_\perp^2}\big(\tilde{B}_2 - \tilde{B}_{-2}\big). \end{aligned} \tag{3.4.43}$$

Since the calculation is performed numerically, it is possible to change the parametrisation of l. Having found these four coefficients, the loop momentum is reparametrised as $l^\mu_{\pm\pm} = V_2^\mu + l_\perp(\pm x_2 n_2^\mu \pm x_4 n_4^\mu)$, and $b_{\pm\pm} = b(l_{\pm\pm})$ are evaluated. The four known coefficients are then subtracted to obtain $b^{\text{subtr}}_{\pm\pm}$. Choosing $x_2 = x_4 = \frac{1}{\sqrt{2}}$ gives

$$\begin{aligned} \tilde{b}_7 &= \frac{b^{\text{subtr}}_{++} - b^{\text{subtr}}_{-+}}{l_\perp^2}, \\ \tilde{b}_3 &= \frac{b^{\text{subtr}}_{-+} - b^{\text{subtr}}_{+-}}{\sqrt{2} l_\perp}, \\ \tilde{b}_5 &= \frac{2}{3l_\perp^2}\left(\tilde{B}_0 - \frac{1}{2}\big(b^{\text{subtr}}_{-+} + b^{\text{subtr}}_{+-} + \tilde{b}_7 l_\perp^2\big)\right), \\ \tilde{b}_0 &= \tilde{B}_0 - \tilde{b}_5 l_\perp^2. \end{aligned} \tag{3.4.44}$$

Obtaining $\tilde{b}_8$ is simple, as all other coefficients that survive in four dimensions are known, and similarly extending to five dimensions allows $\tilde{b}_9$ to be found.

Again, numerical instabilities may arise if $l_\perp^2$ is small. If this is the case, the parametrisation $l^\mu_\pm = V_2^\mu + x_2 n_2^\mu \pm \sqrt{l_\perp^2 - x_2^2}\, n_3^\mu$, where $x_2 = \exp(i\theta)$, is used. Define

$$B_+(x_2) = \frac{b(l_+) + b(l_-)}{2}; \qquad B_-(x_2) = \frac{b(l_+) - b(l_-)}{2x_3} \tag{3.4.45}$$

and write the former as a quadratic in x_2,

$$B_+(x_2) = B_0 + B_1 x_2 + B_2 x_2^2. \tag{3.4.46}$$

The values of B_i can again be found using the Fourier method, and are related to the coefficients by

$$\tilde{b}_1 = B_1; \qquad \tilde{b}_4 = \tfrac{B_2}{2}. \tag{3.4.47}$$

Furthermore,

$$\tilde{b}_6 = \tfrac{B_-(x_2=1) - B_-(x_2=e^{2\pi i/3})}{1-e^{2\pi i/3}}; \qquad \tilde{b}_2 = B_-(x_2=1) - \tilde{b}_6. \tag{3.4.48}$$

Again, the loop momentum may be reparametrised as $l^\mu_{\pm\pm} = V_2^\mu \pm \sqrt{l_\perp^2 - 1}\, n_2^\mu \pm n_4^\mu$. Subtracting the known coefficients from b obtains $b^{\text{subtr}}_{\pm\pm} = b^{\text{subtr}}(l_{\pm\pm})$. Then

$$\begin{aligned} \tilde{b}_7 &= \tfrac{b^{\text{subtr}}_{++} - b^{\text{subtr}}_{-+}}{2\sqrt{l_\perp^2 - 1}}; & \tilde{b}_3 &= \tfrac{b^{\text{subtr}}_{++} - b^{\text{subtr}}_{--}}{2}; \\ \tilde{b}_5 &= -\tfrac{1}{3}\big(b^{\text{subtr}}_{++} - \tilde{B}_0 - \tilde{b}_3 - \tilde{b}_7\sqrt{l_\perp^2 - 1}\big); & \tilde{b}_0 &= \tilde{B}_0 - \tilde{b}_5 l_\perp^2. \end{aligned} \tag{3.4.49}$$

Finally, the last coefficient in four dimensions, $\tilde{b}_8$, as well as the five-dimensional coefficient $\tilde{b}_9$, can be obtained for any parametrisation of l.

When dealing with double cuts, the dimensionality of the physical space is one, and the physical space is spanned by $v_1^\mu = \frac{k^\mu}{k^2}$, where k is the sum of the external momenta of the tree-level amplitude that results from the unitarity cut. If the tree-level amplitude has only one external particle, which is massless, then $k^2 = 0$, and the basis vectors cannot be constructed in this manner. The parametrisation of l breaks down, as does the functional form of the unitarity coefficients of the two-point integral $\tilde{b}$, and the method outlined above to find the coefficients $\tilde{b}_i$ is not applicable. This only occurs in the double cuts – higher cuts have combinations of more than one external momentum in the denominators of the basis vectors of the physical space, and these denominators will not be zero. Furthermore, it is only a concern if the cut internal particles are massive, since massless double cuts are discarded.

In order to parametrise l, I use a frame in which the external lightlike momentum is $p = (E, 0, 0, E)$, and define the complementary momentum $\bar{p} = (E, 0, 0, -E)$. These then serve as part of the basis, with the loop momentum

$$l = x_1 p_1^\mu + x_2 \bar{p}^\mu + l_\perp^\mu, \tag{3.4.50}$$

where $l_\perp^\mu = y_3 n_3^\mu + y_4 n_4^\mu + y_\epsilon n_\epsilon^\mu$. The basis vectors of the transverse space are chosen such that they are orthogonal to both p and $\bar{p}$. Note that this transverse space is spanned by three vectors, and is therefore not the same transverse space as in the Vermaseren-Van Neerven decomposition, which has four basis vectors for a double cut. The two cut propagators on either side of the external momentum p have momenta l and $l + p$ (this can be achieved by an appropriate choice of q_0) and masses m_i and m_{i+1}. The on-shell conditions for these propagators are $l^2 = m_i^2$ and $(l + p)^2 = m_{i+1}$, whence

$$\begin{aligned} x_2 &= \frac{m_{i+1}^2 - m_i^2}{s}, \\ x_1 &= \frac{l_\perp^2 - m_i^2}{m_i^2 - m_{i+1}^2}, \end{aligned} \tag{3.4.51}$$

where $s = 2p.\bar{p}$. This fixes x_2 but allows some freedom in the choice of x_1 and $l_\perp$. The double-cut coefficient is parametrised as

$$\begin{aligned} \tilde{b} =& \tilde{b}_0 + \tilde{b}_1(l.\bar{p}) + \tilde{b}_2(l.n_3) + \tilde{b}_3(l.n_4) + \tilde{b}_4(l.\bar{p})^2 + \tilde{b}_5(l.\bar{p})(l.n_3) \\ &+ \tilde{b}_6(l.\bar{p})(l.n_4) + \tilde{b}_7\big((l.n_3)^2 - (l.n_4)^2\big) + \tilde{b}_8(l.n_3)(l.n_4) \\ &+ \tilde{b}_9(l.n_\epsilon)^2. \end{aligned} \tag{3.4.52}$$

I write $l_{\pm\pm} = x_1 p + x_2 \bar{p} \pm y_3 n_3^\mu \pm y_4 n_4^\mu$ and $b_{\pm\pm} = b(l_{\pm\pm})$, and define combinations

$$\begin{aligned} b_{36}(x_1) &= \frac{1}{4y_4}(b_{++} - b_{+-} + b_{-+} - b_{--}) = \tilde{b}_3 + \tilde{b}_6\frac{x_1 s}{2} \\ b_{25}(x_1) &= \frac{1}{2}(b_{++} - b_{-+} - 2y_3y_4\tilde{b}_8) = \tilde{b}_2 y_3 + \tilde{b}_5 y_3 \frac{s}{2} \end{aligned} \tag{3.4.53}$$

where

$$\tilde{b}_8 = \frac{1}{4y_3y_4}(b_{++} - b_{+-} - b_{-+} + b_{--}). \tag{3.4.54}$$

Exercising freedom of choice for x_1 allows four further coefficients to be found

$$\begin{aligned}
\tilde{b}_3 &= \frac{1}{2}\Big(b_{36}(x_1 = 1/2) + b_{36}(x_1 = -1/2)\Big) \\
\tilde{b}_6 &= \frac{2}{s}\Big(b_{36}(x_1 = 1/2) - b_{36}(x_1 = -1/2)\Big) \\
\tilde{b}_2 &= \frac{1}{2y_3}\Big(b_{25}(x_1 = 1/2) + b_{25}(x_1 = -1/2)\Big) \\
\tilde{b}_5 &= \frac{2}{sy_3}\Big(b_{25}(x_1 = 1/2) - b_{25}(x_1 = -1/2)\Big).
\end{aligned} \tag{3.4.55}$$

Next, subtract the terms involving the above known coefficients from b_{++} to obtain b_{++}^{subtr}. There is still the freedom to choose one of y_3, with y_4 then being restricted to $\sqrt{l_\perp^2 - y_3^2}$. This fixes another coefficient

$$\tilde{b}_7 = -\frac{2}{3}\Big[b_{++}^{\text{subtr}}(y_3 = 1/2, x_1 = 1/2) - b_{++}^{\text{subtr}}(y_3 = 1, x_1 = 1/2)\Big]. \tag{3.4.56}$$

Next, consider the combination $b_{014}(x_1) = \frac{1}{4}\big(b_{++} + b_{+-} + b_{-+} + b_{--}\big)$, where the terms with known coefficients are subtracted. This gives

$$\tilde{b}_1 = \frac{2}{s}\Big(b_{014}(x_1 = 1/2) - b_{014}(x_1 = -1/2)\Big). \tag{3.4.57}$$

Finally, the terms with known coefficients are subtracted from b_{014} and b_{++} to give b_{04} and b_{04}^{++}, and

$$\tilde{b}_0 = -\frac{1}{3}\Big(b_{04}(x_1 = 1/2) - 4b_{04}^{++}(x_1 = 1/4, y_3 = 1)\Big). \tag{3.4.58}$$

The remaining four-dimensional coefficient $\tilde{b}_4$, as well as the five-dimensional coefficient $\tilde{b}_9$, can be found from the known coefficients.

Last, the coefficients of equation (3.4.31) need to be found. However, as will be discussed in section 3.5, only the constant term contributes to the one-loop amplitude. Furthermore, there are no lower-cut unitarity coefficients from which the $\tilde{a}$ is subtracted (as was the case with $\tilde{e}$). It therefore suffices to find the constant term of equation (3.4.31). This can be done by choosing any parametrisation of l which puts the single propagator on-shell, and then computing the left-hand side of equation (3.4.31) for l and $-l$

$$\tilde{a}_0 = \frac{1}{2}\big(\tilde{a}(l) + \tilde{a}(-l)\big). \tag{3.4.59}$$

3.5 Performing the integration

Looking at equations (3.4.22), (3.4.26), (3.4.30), and (3.4.31), it is clear that the only dependence of the unitarity coefficients in equation (3.4.1) on l is through its projection onto the transverse space. Excluding the constant terms, the integral over l can be replaced by one over $l_\perp$, the projection of l onto the transverse space

$$l_\perp^\mu = \sum_{i=1}^{D_T-1} (l.n_i)n_i^\mu + (l.n_\epsilon)n_\epsilon^\mu. \tag{3.5.1}$$

This means that $(l.q_i) = 0$, so the denominators are functions of l^2, rather than l. Clearly, the angular integral $\int dl_\perp l_\perp^\mu = 0$. Furthermore, $\int dl_\perp l_\perp^\mu l_\perp^\nu = \int dl_\perp \frac{l_\perp^2}{D_T} g_{D_T}^{\mu\nu}$. Using the orthogonality of the transverse space basis vectors, it is clear then that, in equations (3.4.22), (3.4.26), (3.4.30) and (3.4.31), the only terms which survive integration over l are the constant ones, and the terms $\tilde{d}_2(l.n_\epsilon)^2$, $\tilde{d}_4(l.n_\epsilon)^4, \tilde{c}_7(l.n_\epsilon)^2$ and $\tilde{b}_9(l.n_\epsilon)^2$. Equation (3.4.1) becomes

$$\begin{aligned}
\mathcal{A}_N(l) = &\sum_{[i_1|i_5]} \tilde{e}_{0;i_1i_2i_3i_4i_5}(l.n_\epsilon)^2 \frac{1}{D_{i_1}D_{i_2}D_{i_3}D_{i_4}D_{i_5}} \\
&+ \sum_{[i_1|i_4]} \left(\tilde{d}_{0;i_1i_2i_3i_4} + \tilde{d}_{2;i_1i_2i_3i_4}(l.n_\epsilon)^2 + \tilde{d}_{4;i_1i_2i_3i_4}(l.n_\epsilon)^4\right) \frac{1}{D_{i_1}D_{i_2}D_{i_3}D_{i_4}} \\
&+ \sum_{[i_1|i_3]} \left(\tilde{c}_{0;i_1i_2i_3} + \tilde{c}_{7;i_1i_2i_3}(l.n_\epsilon)^2\right) \frac{1}{D_{i_1}D_{i_2}D_{i_3}} \\
&+ \sum_{[i_1|i_2]} \left(\tilde{b}_{0;i_1i_2} + \tilde{b}_{9;i_1i_2}(l.n_\epsilon)^2\right) \frac{1}{D_{i_1}D_{i_2}} + \sum_{i_1} \tilde{a}_{0;i_1} \frac{1}{D_{i_1}}.
\end{aligned} \tag{3.5.2}$$

Upon integrating over l, the cut-constructible part of the amplitude is given by the constant unitarity coefficients multiplied by the scalar master integrals. The remaining integrals can be written in terms of the master integrals defined as in equation (3.1.4)

$$\begin{aligned}
\int \frac{d^D l}{(2\pi)^D} \frac{s_\epsilon^2}{D_{i_1}...D_{i_n}} &= -2\pi(D-4) I_{i_1...i_n}^{D+2}; \qquad n = 1,2,3,4,5 \\
\int \frac{d^D l}{(2\pi)^D} \frac{s_\epsilon^4}{D_{i_1}D_{i_2}D_{i_3}D_{i_4}} &= 4\pi^2(D-2)(D-4) I_{i_1i_2i_3i_4}^{D+4},
\end{aligned} \tag{3.5.3}$$

where $s_\epsilon^2 = -\sum_{i=5}^{D}(l.n_i)^2$.

Then the one-loop amplitude can be expressed as

$$\begin{aligned}\mathcal{A}_N = &\sum_{[i_1|i_5]} \tilde{e}_{0;i_1i_2i_3i_4i_5}(-2\pi(D-4)I^{D+2}_{i_1i_2i_3i_4i_5}) \\ &+ \sum_{[i_1|i_4]} \tilde{d}_{0;i_1i_2i_3i_4} I^{D}_{i_1i_2i_3i_4} + \tilde{d}_{2;i_1i_2i_3i_4}(-2\pi(D-4)I^{D+2}_{i_1i_2i_3i_4}) \\ &+ \tilde{d}_{4;i_1i_2i_3i_4}(4\pi^2(D-2)(D-4)I^{D+4}_{i_1i_2i_3i_4}) \\ &+ \sum_{[i_1|i_3]} \tilde{c}_{0;i_1i_2i_3} I^{D}_{i_1i_2i_3} + \tilde{c}_{7;i_1i_2i_3}(-2\pi(D-4)I^{D+2}_{i_1i_2i_3}) \\ &+ \sum_{[i_1|i_2]} \tilde{b}_{0;i_1i_2} I^{D}_{i_1i_2} + \tilde{b}_{9;i_1i_2}(-2\pi(D-4)I^{D+2}_{i_1i_2}) + \sum_{i_1} \tilde{a}_{0;i_1} I^{D}_{i_1}.\end{aligned} \tag{3.5.4}$$

In the limit $D \to 4-2\epsilon$ [5], the scalar integrals may contain poles $\frac{1}{\epsilon^2}$ and $\frac{1}{\epsilon}$ as well as finite terms. The $(D+2)$- and $(D+4)$-dimensional scalar integrals multiply factors of $D-4=-2\epsilon$, resulting in terms that are finite + $\mathcal{O}(\epsilon)$. For an NLO calculation, the $\mathcal{O}(\epsilon)$ terms can be dropped, since the limit $\epsilon \to 0$ is taken eventually. The integrals $I^{D+2}_{i_1i_2i_3i_4i_5}$ and $I^{D+2}_{i_1i_2i_3i_4}$ vanish in this limit. The remaining rational terms are

$$\begin{aligned}&\lim_{D\to4} 4\pi^2(D-2)(D-4)I^{D+4}_{i_1i_2i_3i_4} = -\frac{16\pi^2}{3} \\ &\lim_{D\to4} -2\pi(D-4)I^{D+2}_{i_1i_2i_3} = -2\pi \\ &\lim_{D\to4} -2\pi(D-4)I^{D+2}_{i_1i_2} = -4\pi\Big(-\frac{m^2_{i_1}+m^2_{i_2}}{2} + \frac{(q_{i_1}-q_{i_2})^2}{6}\Big).\end{aligned} \tag{3.5.5}$$

The one-loop amplitude can then be written as

$$\begin{aligned}\mathcal{A}_N = &\sum_{[i_1|i_4]} \tilde{d}_{0;i_1i_2i_3i_4} I^{(4-2\epsilon)}_{i_1i_2i_3i_4} + \sum_{[i_1|i_3]} \tilde{c}_{0;i_1i_2i_3} I^{(4-2\epsilon)}_{i_1i_2i_3} + \sum_{[i_1|i_2]} \tilde{b}_{0;i_1i_2} I^{(4-2\epsilon)}_{i_1i_2} \\ &+ \sum_{i_1} \tilde{a}_{0;i_1} I^{(4-2\epsilon)}_{i_1} - \sum_{[i_1|i_4]} \frac{16\pi^2}{3}\tilde{d}_{4;i_1i_2i_3i_4} - \sum_{[i_1|i_3]} 2\pi\tilde{c}_{7;i_1i_2i_3} \\ &- 4\pi \sum_{[i_1|i_2]} \Big(-\frac{m^2_{i_1}+m^2_{i_2}}{2} + \frac{(q_{i_1}-q_{i_2})^2}{6}\Big)\tilde{b}_{9;i_1i_2}.\end{aligned} \tag{3.5.6}$$

All the scalar master integrals are computed using `QCDloop` [132]. This solves the problem presented at the beginning of the chapter. To summarise the method: for each unitarity coefficient in equation (3.4.1), put an appropriate number of propagators on-shell by constructing loop momentum as in equation (3.4.8) with the constraints of equation (3.4.10). Doing this for two different values of D_s obtains the analytic continuation of the unitarity coefficients, and allows the rational part of the amplitude to be calculated. The OPP equations (3.4.22), (3.4.26), (3.4.30) and (3.4.31) are solved for the unitarity coefficients, and equation (3.4.1) is written in terms of these coefficients and known scalar integrals, equation (3.5.6). The left-hand sides of the OPP equations are found by computing products of tree-level amplitudes. In the following chapter, I will discuss some of the details pertaining to these computations.

---

[5] The limit of D_s, according to the FDH or HV scheme, has already been taken, see section 3.4.

Chapter 4

Tree-Level Amplitudes

4.1 Introduction

In chapter 3, I discussed how to factorise a one-loop amplitude into a number of tree-level amplitudes. In this chapter, I will discuss how to compute these tree-level amplitudes. In section 4.2, I will discuss how to compute polarisation vectors for fermions and bosons in $D_s > 4$ dimensions. In section 4.3, I will discuss the Berends-Giele recursion relations [145], a technique for computing on-shell currents, which is important for this implementation of the unitarity method. These relations are connected to the concept of primitive amplitudes (see section 2.3), and the use of these two concepts greatly increases the speed of the computation of one-loop amplitudes.

4.2 Higher-dimensional polarisations

It is necessary to compute the one-loop amplitude, and hence the tree-level amplitude into which it factorises via the unitarity method, in more than four dimensions (see section 3.2). A tree-level amplitude obtained from a unitarity cut of a one-loop amplitude will have two particles that were put on-shell by the cut, which have momenta in D dimensions and polarisations in D_s dimensions, with $\{D, D_s\} = \{4, 4\}, \{5, 6\}, \{5, 8\}$. I shall call these "internal" particles, to distinguish them from the external particles of the amplitude, whose momenta and polarisations remain in four dimensions. For one-loop QCD amplitudes, internal particles may be either gluons or quarks. Having determined their momenta as described in section 3.4, I now discuss how to find their polarisations.

4.2.1 Gluonic polarisations

The momentum of an external gluon in four dimensions can be parametrised as (see e.g. [85])

$$p^\mu = E(1, s_\theta c_\phi, s_\theta s_\phi, c_\theta) \tag{4.2.1}$$

where $s_\theta = \sin\theta$, $c_\theta = \cos\theta$ *etc.*. The four-dimensional polarisation vector is

$$\epsilon_\mu^{(\lambda)} = (0, c_\theta c_\phi - \operatorname{sgn}(p_0) i\lambda s_\phi, c_\theta s_\phi + \operatorname{sgn}(p_0) i\lambda c_\phi, -s_\theta), \tag{4.2.2}$$

where $\lambda = \pm 1$ labels the two polarisation states of the gluon, and the gauge condition $p.\epsilon = 0$ is satisfied[1].

For the internal particles, the task of computing two vectors which are orthogonal to a light-like momentum and which satify $\sum_i^{D_s-2} e_\mu^i(l) e_\nu^i(l) = -g_{\mu\nu}^{(D_s)}$ has already been done, as these are precisely the vectors spanning the transverse space in the Vermaseren-Van Neerven basis (see section 3.3). In $D = D_s = 4$ dimensions, the same problem with a lightlike momentum encountered in section 3.4 is also present, but this can be solved in an identical manner, by defining an auxiliary momentum and then constructing two polarisations orthogonal to the momentum and its auxiliary. In $D = 5$ dimensions, $p_0^2 - p_1^2 - p_2^2 - p_3^2 = p_4^2$, so a lightlike five-dimensional momentum is equivalent to a spacelike four-dimensional one. Using this massive four-dimensional momentum allows three four-dimensional transverse basis vectors $n_{1,2,3}^{(4)}$ to be constructed according to equations (3.3.9) and (3.3.10). For $D_s = 6$, the six-dimensional polarisation vectors are

$$\begin{aligned} \epsilon_{1,2,3}^{(6)} =& (n_{1,2,3}^{(4)}, 0, 0) \\ \epsilon_4^{(6)} =& (0^{(4)}, 0, i). \end{aligned} \tag{4.2.3}$$

For $D_s = 8$, it suffices to define two polarisation states

$$\epsilon_+^{(8)} = (0^{(6)}, i, 0); \qquad \epsilon_-^{(8)} = (0^{(6)}, 0, i). \tag{4.2.4}$$

---

[1] Since the gluons are always on-shell, only transverse polarisations are used, and hence ghost fields do not enter into the calculation.

4.2.2 Fermionic polarisations

In order to discuss the treatment of internal quarks, I must first define the Dirac matrices in D_s dimensions [63, 85, 146]. They are defined through their algebra

$$\left\{\Gamma^{\mu}_{D_s}, \Gamma^{\nu}_{D_s}\right\} = 2g^{\mu\nu}\mathbf{1}_{2^{D_s/2}}, \tag{4.2.5}$$

where $\mu, \nu = 0, ..., D_s - 1$ and $\mathbf{1}_{2^{D_s/2}}$ is the identity matrix in the number of internal dimensions, $2^{D_s/2}$. Increasing D_s to $D_s + 2$ doubles the internal dimensionality. The Dirac matrices are defined recursively

$$\begin{aligned}
\Gamma^{0}_{D_s+2} &= \begin{pmatrix} \Gamma^{0}_{D_s} & 0 \\ 0 & \Gamma^{0}_{D_s} \end{pmatrix}; \quad \Gamma^{i}_{D_s+2} = \begin{pmatrix} \Gamma^{i}_{D_s} & 0 \\ 0 & \Gamma^{i}_{D_s} \end{pmatrix}; \\
\Gamma^{D_s}_{D_s+2} &= \begin{pmatrix} 0 & \hat{\Gamma}_{D_s} \\ -\hat{\Gamma}_{D_s} & 0 \end{pmatrix}; \quad \Gamma^{D_s+1}_{D_s+2} = \begin{pmatrix} 0 & i\hat{\Gamma}_{D_s} \\ i\hat{\Gamma}_{D_s} & 0 \end{pmatrix},
\end{aligned} \tag{4.2.6}$$

where $i = 1, ..., D_s - 1$ and the matrices are defined by $\hat{\Gamma}_{D_s} = i^{D_s/2-1}\Gamma^{0}_{D_s}\Gamma^{1}_{D_s}...\Gamma^{D_s-1}_{D_s}$, so that $\left\{\hat{\Gamma}_{D_s}, \Gamma^{\mu}_{D_s}\right\} = 0$ for even D_s, with $\mu = 0, ..., D_s - 1$.

The anticommutation relation of equation (4.2.5) in D_s+2 dimensions is inherited from the D_s-dimensional matrices for $\mu, \nu = 0, ..., D_s-1$. The definition of $\hat{\Gamma}_{D_s}$ implies $\left\{\Gamma^{\mu}_{D_s+2}, \Gamma^{j}_{D_s+2}\right\} = 0$ for $\mu = 0, ..., D_s - 1$ and $j = D_s, D_s + 1$. Finally, it is clear that $\left\{\Gamma^{j}_{D_s+2}, \Gamma^{k}_{D_s+2}\right\} = -2\delta^{jk}\mathbf{1}_{2^{D_s/2+1}}$ for $j, k = D_s, D_s + 1$. Thus, $\Gamma^{\mu}_{D_s+2}$ satisfies the anticommutation relation of equation (4.2.5).

The six- and eight-dimensional Dirac matrices can therefore be built recursively from the four-dimensional ones, $\Gamma^{\mu}_{4} \equiv \gamma^{\mu}$. These can be expressed in either the Weyl or Dirac basis

$$\begin{aligned}
\gamma^{0}_{\text{Weyl}} &= \begin{pmatrix} \mathbf{0_2} & \mathbf{1_2} \\ \mathbf{1_2} & \mathbf{0_2} \end{pmatrix}; \quad \gamma^{i}_{\text{Weyl}} = \begin{pmatrix} \mathbf{0_2} & -\sigma^{\mathbf{i}} \\ \sigma^{\mathbf{i}} & \mathbf{0_2} \end{pmatrix}; \\
\gamma^{0}_{\text{Dirac}} &= \begin{pmatrix} \mathbf{1_2} & \mathbf{0_2} \\ \mathbf{0_2} & -\mathbf{1_2} \end{pmatrix}; \quad \gamma^{i}_{\text{Dirac}} = \begin{pmatrix} \mathbf{0_2} & \sigma^{\mathbf{i}} \\ -\sigma^{\mathbf{i}} & \mathbf{0_2} \end{pmatrix},
\end{aligned} \tag{4.2.7}$$

with $\mathbf{0_2}$ and $\mathbf{1_2}$ the 2×2 zero and identity matrices, and $\sigma^{\mathbf{i}}$ the Pauli matrices ($i = 1, 2, 3$). The Weyl and Dirac bases can be related by a unitary transform $\gamma^{\mu}_{\text{Weyl}} = U^{\dagger}\gamma^{\mu}_{\text{Dirac}}U$ where $U = \frac{1}{\sqrt{2}}\begin{pmatrix} \mathbf{1_2} & \mathbf{1_2} \\ \mathbf{1_2} & -\mathbf{1_2} \end{pmatrix}$.

The matrix $\gamma^5 = i\gamma^0\gamma^1\gamma^2\gamma^3$ in four dimensions can be extended to higher dimensions through its anticommutation properties [112]:

$$\begin{aligned}
\left\{\Gamma^{\gamma_5}_{D_s}, \Gamma^{\mu}_{D_s}\right\} &= 0; \qquad \mu = 0, ..., 3 \\
\left[\Gamma^{\gamma_5}_{D_s}, \Gamma^{\mu}_{D_s}\right] &= 0; \qquad \mu > 3.
\end{aligned} \tag{4.2.8}$$

This can be achieved recursively

$$\Gamma^{\gamma_5}_{D_s+2} = \begin{pmatrix} \Gamma^{\gamma_5}_{D_s} & 0 \\ 0 & \Gamma^{\gamma_5}_{D_s} \end{pmatrix}, \tag{4.2.9}$$

with $\Gamma_4^{\gamma_5} \equiv \gamma_5$ and

$$\gamma^5_{\mathrm{Weyl}} = \begin{pmatrix} \mathbf{1_2} & \mathbf{0_2} \\ \mathbf{0_2} & -\mathbf{1_2} \end{pmatrix}; \quad \gamma^5_{\mathrm{Dirac}} = \begin{pmatrix} \mathbf{0_2} & \mathbf{1_2} \\ \mathbf{1_2} & \mathbf{0_2} \end{pmatrix} \tag{4.2.10}$$

in four dimensions.

Quarks and antiquarks are represented by spinors u and v respectively. These should satisfy the Dirac equation

$$(\not{p} - m)u(p,m) = (\not{p} + m)v(p,m) = 0, \tag{4.2.11}$$

as well as the completeness relations

$$\begin{aligned} \sum_s^{2^{D_s/2-1}} u^s(p,m)\bar{u}^s(p,m) &= \not{p} + m, \\ \sum_s^{2^{D_s/2-1}} v^s(p,m)\bar{v}^s(p,m) &= \not{p} - m, \end{aligned} \tag{4.2.12}$$

where s label the polarisations, and $\not{p} = p_\mu \Gamma^\mu$ in D_s dimensions. The two spinors of external quarks of mass m can be written in the Weyl representation as

$$u^{(1)}(p,m) = \tfrac{1}{\sqrt{p^+}} \begin{pmatrix} p^+ \\ p_x + ip_y \\ m \\ 0 \end{pmatrix}; \quad u^{(2)}(p,m) = \tfrac{1}{\sqrt{p^+}} \begin{pmatrix} 0 \\ -m \\ p_x - ip_y \\ -p^+ \end{pmatrix}, \tag{4.2.13}$$

where $p^+ = p_0 + p_z$. The spinors of the antiquarks can be written as $v^{(1,2)}(p,m) = u^{(2,1)}(p,-m)$. This set of spinors obeys both the Dirac equation (4.2.11) and the completeness relation (4.2.12). If the quarks are massless, then the above spinors reduce to helicity eigenstates, giving left- and right-handed quarks:

$$u^{(-)}(p) = \tfrac{1}{\sqrt{p^+}} \begin{pmatrix} 0 \\ 0 \\ p_x - ip_y \\ -p^+ \end{pmatrix}, u^{(+)}(p) = \tfrac{1}{\sqrt{p^+}} \begin{pmatrix} p^+ \\ p_x + ip_y \\ 0 \\ 0 \end{pmatrix}. \tag{4.2.14}$$

Now the spinors of the antiquark are given by $v^{(\pm)}(p) = u^{(\mp)}(p)$. If the fermions move in the z-direction, so that $p_0 = -p_z$, then the spinors are defined instead by

$$u^-(p) = \sqrt{2p_0} \begin{pmatrix} 0 \\ 0 \\ 1 \\ 0 \end{pmatrix}; \quad u^+(p) = \sqrt{2p_0} \begin{pmatrix} 0 \\ 1 \\ 0 \\ 0 \end{pmatrix}. \tag{4.2.15}$$

The internal massless quarks are constructed using an auxiliary vector n

$$\begin{aligned} u^{(s)}_{D_s}(p) =& \frac{\not{p}}{\sqrt{2p.n}} \chi^{(s)}_{D_s} \\ \bar{u}^{(s)}_{D_s}(p) =& \bar{\chi}^{(s)}_{D_s} \frac{\not{p}}{\sqrt{2p.n}}, \end{aligned} \tag{4.2.16}$$

where

$$\sum_{s=1}^{2^{D_s/2-1}} \chi^{(s)}_{D_s} \times \bar{\chi}^{(s)}_{D_s} = \not{n}. \tag{4.2.17}$$

Note that $\bar{u}$ is defined here, rather than through $\bar{u} = u^\dagger \gamma^0$. These spinors clearly satisfy the massless Dirac equation, and

$$\sum_{s}^{2^{D_s/2-1}} u^{(s)}(p)\bar{u}^{(s)}(p) = \frac{\not{p}\not{n}\not{p}}{2p.n} = \not{p}, \tag{4.2.18}$$

where the second identity is obtained through the manipulation of gamma matrices. Thus the completeness relation is satisfied. There is a large degree of flexibility in this definition, stemming from the choice of $\chi^{(s)}$. Defining

$$\chi^{(1)}_{4,x} = \tfrac{1}{\sqrt{2}}\begin{pmatrix}1\\1\\0\\0\end{pmatrix};\ \ \chi^{(2)}_{4,x} = \tfrac{1}{\sqrt{2}}\begin{pmatrix}0\\0\\1\\-1\end{pmatrix};$$

$$\chi^{(1)}_{4,y} = \tfrac{1}{\sqrt{2}}\begin{pmatrix}1\\i\\0\\0\end{pmatrix};\ \ \chi^{(2)}_{4,y} = \tfrac{1}{\sqrt{2}}\begin{pmatrix}0\\0\\1\\-i\end{pmatrix}; \tag{4.2.19}$$

$$\chi^{(1)}_{4,z} = \begin{pmatrix}1\\0\\0\\0\end{pmatrix};\qquad \chi^{(2)}_{4,z} = \begin{pmatrix}0\\0\\0\\-1\end{pmatrix},$$

the auxiliary vectors have $\not{n}_{x,y,z} = \frac{1}{2}\big(\Gamma^0 - \Gamma_{x,y,z}\big)$. Then whichever value of $\chi_{x,y,z}$ gives the largest value for $p.n$ is used, thereby avoiding the singularity if $p.n = 0$. This is easily extended to higher dimensions by embedding

$$\chi^{(i)}_{D_s+2} = \begin{pmatrix}\chi^{(i)}_{D_s}\\0\end{pmatrix};\ \ \chi^{(2^{D_s/2-1}+i)}_{D_s+2} = \begin{pmatrix}0\\\chi^{(i)}_{D_s}\end{pmatrix} \tag{4.2.20}$$

for $i = 1, ..., 2^{D_s/2-1}$.

For massive internal quarks, the Dirac representation is used, with the spinors

$$\begin{aligned} u^{(s)}_{D_s}(p,m) =& \frac{\not{p}+m}{\sqrt{p_0+m}}\eta^{(s)}_{D_s} \\ \bar{u}^{(s)}_{D_s}(p,m) =& \bar{\eta}^{(s)}_{D_s}\frac{\not{p}+m}{\sqrt{p_0+m}}. \end{aligned} \tag{4.2.21}$$

In four dimensions, the auxiliary vectors are

$$\eta^{(1)}_4 = \begin{pmatrix}1\\0\\0\\0\end{pmatrix};\ \ \eta^{(2)}_4 = \begin{pmatrix}0\\1\\0\\0\end{pmatrix}, \tag{4.2.22}$$

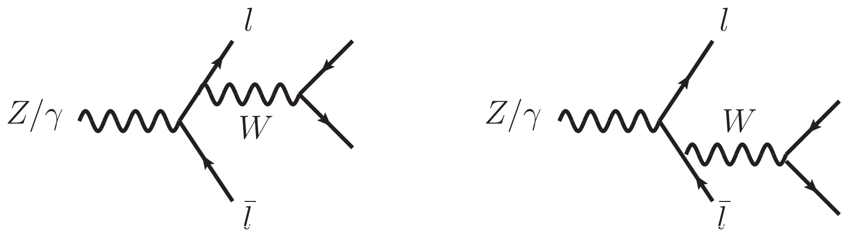

Figure 4.1: Diagrams of single resonant W-boson currents with an intermediate Z-boson or photon. Current A is shown on the left; current B on the right.

and higher dimensional spinors are created as in equation (4.2.20).

4.2.3 Electroweak bosons

Since I will be calculating amplitudes with external W-bosons, Z-bosons and photons, I need to define polarisation vectors for these as well. However, for one-loop QCD amplitudes, the electroweak bosons only appear as four-dimensional external particles, never internal ones.

The polarisation vector for a photon is the same as for an external gluon, equation (4.2.2). In fact, this can be used for the transverse directions of the polarisation vector of a massive particle too, and the longitudinal mode is

$$\epsilon^0(p,m) = \frac{1}{|\mathbf{p}|m}\big(|\mathbf{p}|^2, Ep_x, Ep_y, Ep_z\big). \tag{4.2.23}$$

However, it is better to use a polarisation vector which takes into account the leptonic decay of the electroweak bosons. The decay of a final state W into massless leptons $W \to l\bar{l}$ in the fixed-width approximation can be represented by a polarisation vector

$$\epsilon^\mu_W(p_l, p_{\bar{l}}) = \frac{-i\bar{u}(p_l)\gamma^\mu\gamma_- v(p_{\bar{l}})}{s_{l\bar{l}} - m_W^2 + i\Gamma_W m_W}, \tag{4.2.24}$$

where m_W and Γ_W are the mass and width of the W-boson, and $s_{l\bar{l}} = (p_l + p_{\bar{l}})^2$. The inclusion of $\gamma_- = \frac{1-\gamma_5}{2}$ is due to left-handed coupling of the W-bosons to fermions.

The W-bosons may also be produced through an intermediate Z-boson or photon. The intermediate boson can be regarded as an external particle with a polarisation given by the following current:

$$\begin{aligned}\epsilon^\mu_V(p_{W^+}, p_{W^-}) =& \frac{-i}{(p_{W^+} + p_{W^-})^2}\bigg((p^\mu_{W^-} - p^\mu_{W^+})\epsilon_{W^+}.\epsilon_{W^-} \\ &+ (2p_{W^+}.\epsilon_{W^-})\epsilon^\mu_{W^+} - (2p_{W^-}.\epsilon_{W^+})\epsilon^\mu_{W^-}\bigg),\end{aligned} \tag{4.2.25}$$

where $p^\mu_{W^\pm}$ and $\epsilon^\mu_{W^\pm}$ are the momenta and polarisations of the positive and negative W-bosons as defined in equation (4.2.24). The propagator of the intermediate boson, including its mass and width, will be explicitly included in the electroweak couplings, see e.g. section 6.2. Finally, a current is required to account for the single resonant production of the W-bosons. This current corresponds to two Feynman diagrams, shown in figure 4.1. These are

$$\begin{aligned}\epsilon^{\mu}_{\mathrm{SR},A}(\epsilon_W, p_W, p_l, p_{\bar{l}}) =&\bar{u}(p_l)\not{\epsilon}_W \frac{i(\not{p}_W + \not{p}_l)}{(p_W + p_l)^2}\gamma^{\mu} v(p_{\bar{l}}) \\ \epsilon^{\mu}_{\mathrm{SR},B}(\epsilon_W, p_W, p_l, p_{\bar{l}}) =&\bar{u}(p_l)\gamma^{\mu} \frac{-i(\not{p}_W + \not{p}_{\bar{l}})}{(p_W + p_{\bar{l}})^2}\not{\epsilon}_W \; v(p_{\bar{l}}),\end{aligned} \tag{4.2.26}$$

with ϵ_W as in equation (4.2.24). The intermediate boson may be either a photon or a Z-boson, and the lepton-antilepton pair $l\bar{l}$ to which it couples may either be charged leptons l^+l^-, or neutrinos $\nu\bar{\nu}$. Thus there are four coupling factors

$$C^{Z}_{l^+l^-} = \Big(-\frac{1}{2} + \sin^2\theta_w\Big)P_Z(s_Z); \qquad C^{Z}_{\nu\bar{\nu}} = \frac{1}{2}P_Z(s_Z); \tag{4.2.27}$$

$$C^{\gamma}_{l^+l^-} = -\sin^2\theta_w P_{\gamma}(s_{\gamma}); \qquad C^{\gamma}_{\nu\bar{\nu}} = 0, \tag{4.2.28}$$

where e is the electromagnetic coupling, θ_w is the weak mixing angle, and the weak coupling g_w has been factored out, as this will be added explicitly (see for example section 5.2). The propagators for the Z-boson and photon are

$$P_Z(s_Z) = \frac{-i}{s_Z - m_Z^2 + i\Gamma_Z m_Z}; \qquad P_{\gamma}(s_{\gamma}) = \frac{-i}{s_{\gamma}} \tag{4.2.29}$$

with s the momentum-squared flowing through the Z-boson or photon,

$$s_Z = s_{\gamma} = (p_{W^+} + p_{W^-})^2 = (p_{l^+} + p_{l^-} + p_{\nu} + p_{\bar{\nu}})^2. \tag{4.2.30}$$

4.3 Berends-Giele recursion relations

Having defined the polarisations in higher dimensions, I now describe how to use these to calculate tree-level amplitudes. I consider one of the internal particles in the tree-level amplitude to be off-shell, and then calculate the current of the remaining on-shell particles. The tree-level amplitude can be found by convoluting this current with the polarisation vector of the off-shell particle. It turns out that the method of calculating these currents, namely Berends-Giele recursion relations [145], is both highly efficient and highly adaptable, and is ideal for the numerical computation of a large variety of currents.

For my purposes, the off-shell particle will correspond to an internal particle which has been cut according to the unitarity procedure. For NLO QCD calculations, this means that the off-shell particle is either a quark, an antiquark, or a gluon. In addition to this particle, there may be on-shell quarks, antiquarks and electroweak bosons making up the "skeleton" of the current. This may be viewed as the minimal particle content of the current. The skeleton may be "dressed" with an arbitrary number of on-shell gluons, although for the calculations described in this work, no more than three on-shell gluons will be needed in a given current. This dressing procedure may be done recursively, and more complicated skeletons may be constructed out of simpler ones. This allows the use of numerical caching in order to speed up the calculation [147].

The currents are fully colour-ordered, meaning that the colour-charged off-shell particles, as well as the colour-charged particles in the skeleton, have a fixed ordering. The on-shell gluons have a fixed ordering with respect to the colour-charged skeleton particles, as well as with respect to the other on-shell gluons. This is essential in calculating colour-ordered primitive amplitudes. Colour-ordered Feynman rules [126], shown in figure 4.2, are used to describe the interactions between quarks and gluons. The electroweak bosons are not ordered.

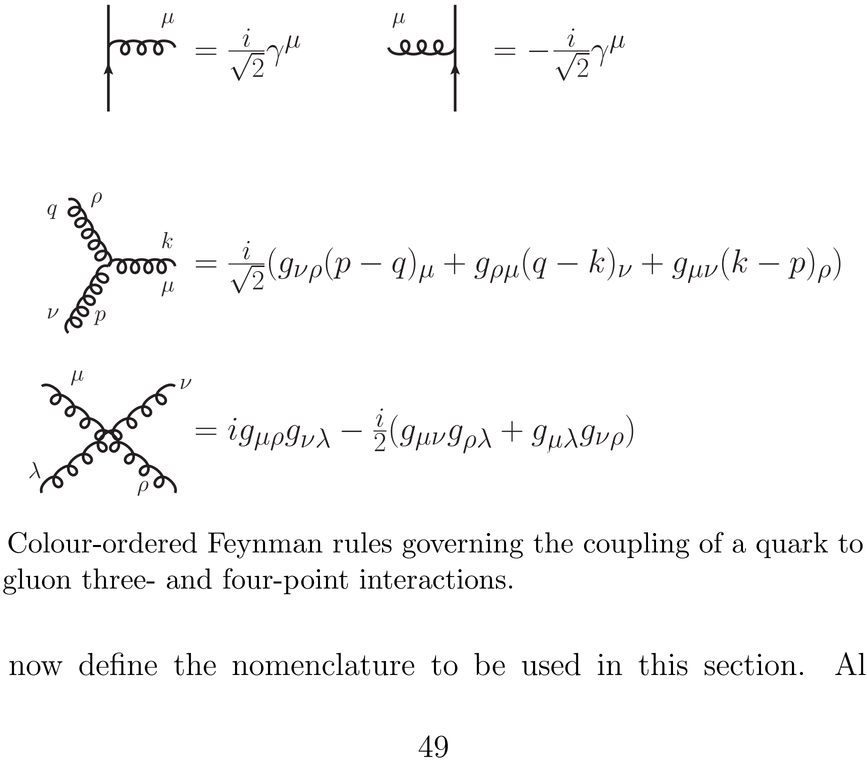

$$= \frac{i}{\sqrt{2}}\gamma^{\mu} \qquad = -\frac{i}{\sqrt{2}}\gamma^{\mu}$$

$$= \frac{i}{\sqrt{2}}(g_{\nu\rho}(p-q)_{\mu} + g_{\rho\mu}(q-k)_{\nu} + g_{\mu\nu}(k-p)_{\rho})$$

$$= i g_{\mu\rho} g_{\nu\lambda} - \tfrac{i}{2}(g_{\mu\nu} g_{\rho\lambda} + g_{\mu\lambda} g_{\nu\rho})$$

Figure 4.2: Colour-ordered Feynman rules governing the coupling of a quark to a gluon, as well as the gluon three- and four-point interactions.

I shall now define the nomenclature to be used in this section. All Berends-

Giele currents are written in this font. Quarks are indicated by f, antiquarks by $\bar{\mathsf{f}}$, gluons by g, and electroweak bosons by V. The off-shell particle is designated first, followed by an underscore, and then the remainder of the skeleton, with the electroweak bosons designated first, followed by the quarks and antiquarks as they are ordered. In diagrams, the coloured particles have clockwise ordering. The arguments of the functions are always the number of gluons between the coloured particles in the skeleton, and (for most of the currents), the skeletal quarks. Other arguments, specific to certain currents, are also used, and will be explained as they arise. When currents are combined, they are treated essentially as off-shell quarks, antiquarks, or gluons, and combined as such. I indicate the combination of currents with a $\otimes$, with the following "dictionary" assigned:

$$\begin{aligned}
&\bar{u}(p,m)\otimes\epsilon^\mu(k) = \frac{i}{\sqrt{2}}\bar{u}(p,m)P_q(p,m)P_g(k)\not{\epsilon}(k);\\
&u(p,m)\otimes\epsilon^\mu(k) = -\frac{i}{\sqrt{2}}\not{\epsilon}(k)P_g(k)P_q(p,m)u(p,m);\\
&\epsilon^\mu(k)\otimes\bar{u}(p,m) = -\frac{i}{\sqrt{2}}\bar{u}(p,m)P_q(p,m)P_g(k)\not{\epsilon}(k);\\
&\epsilon^\mu(k)\otimes u(p,m) = \frac{i}{\sqrt{2}}\not{\epsilon}(k)P_g(k)P_q(p,m)u(p,m);\\
&\bar{u}_2(p_2,m_2)\otimes u_1(p_1,m_1) = \frac{i}{\sqrt{2}}\bar{u}_2(p_2,m_2)P_q(p_2,m_2)P_q(p_1,m_1)u_1(p_1,m_1)\\
&\epsilon_1^\nu(k_1)\otimes\epsilon_2^\rho(k_2) = \frac{i}{\sqrt{2}}\Big(\epsilon_1.\epsilon_2(k_1-k_2)^\mu + 2(k_2.\epsilon_1)\epsilon_2^\mu - 2(k_1.\epsilon_2)\epsilon_1^\mu\Big)P_g(k_1)P_g(k_2);\\
&\epsilon_1^\nu(k_1)\otimes\epsilon_2^\lambda(k_2)\otimes\epsilon_3^\rho(k_3) = i\Big(\epsilon_2^\mu(\epsilon_1.\epsilon_3) - \frac{1}{2}\big(\epsilon_1^\mu(\epsilon_2.\epsilon_3)+\epsilon_3^\mu(\epsilon_1.\epsilon_2)\big)\Big)P_g(k_1)P_g(k_2)P_g(k_3);\\
&\bar{u}(p,m)\otimes V^\mu = -i\bar{u}(p,m)P_q(p,m)\not{V};\\
&V^\mu\otimes u(p,m) = -i\not{V}P_q(p,m)u(p,m),
\end{aligned} \tag{4.3.1}$$

where $\bar{u}$ refers to a current generated by an off-shell quark (f_...), u refers to a current generated by an off-shell antiquark ($\bar{\mathsf{f}}$_...), ϵ^μ refers to a current generated by an off-shell gluon (g_...), and V^μ refers to the polarisation vector of an electroweak boson. The quark and gluon propagators are

$$P_q(p,m) = \frac{i(\not{p}+m)}{p^2-m^2}; \qquad P_g(k) = \frac{-i}{k^2}. \tag{4.3.2}$$

Currents with no electroweak bosons will be described first, followed by currents with one and then two electroweak bosons.

4.3.1 Currents with no electroweak bosons

g_(n)

This current contains one off-shell gluon and no skeleton at all. It is non-zero only when there are also on-shell gluons. If there is only one on-shell gluon, the skeleton is simply the polarisation vector of this gluon. More on-shell gluons are added recursively:

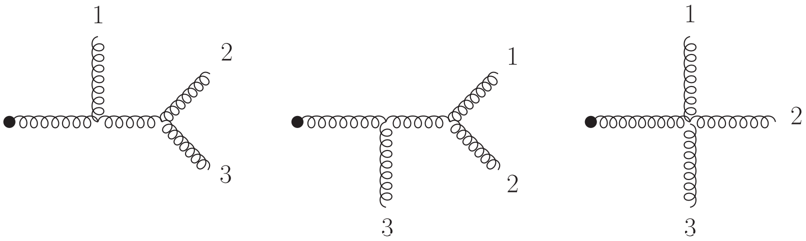

Figure 4.3: Diagrammatic representation of the current g_- with three on-shell gluons. The off-shell gluon is indicated by the solid circle.

$$\begin{aligned}\mathsf{g}_-(1:\mathsf{n}) =& \sum_{\mathsf{r}_1=1}^{\mathsf{n}-1}\Big(\mathsf{g}_-(1:\mathsf{r}_1)\otimes\mathsf{g}_-(\mathsf{r}_1+1:\mathsf{n})\\ &+\sum_{\mathsf{r}_2=\mathsf{r}_1+1}^{\mathsf{n}-1}\mathsf{g}_-(1:\mathsf{r}_1)\otimes\mathsf{g}_-(\mathsf{r}_1+1:\mathsf{r}_2)\otimes\mathsf{g}_-(\mathsf{r}_2+1:\mathsf{n})\Big).\end{aligned} \tag{4.3.3}$$

In order to simplify the notation, I will write only the *number* of on-shell gluons as the argument for the current. The labels of the gluons are understood from the colour ordering. Thus, the above recursion relation becomes

$$\mathsf{g}_-(\mathsf{n}) = \sum_{\mathsf{r}_1=1}^{\mathsf{n}-1}\Big(\mathsf{g}_-(\mathsf{r}_1)\otimes\mathsf{g}_-(\mathsf{n}-\mathsf{r}_1)+\sum_{\mathsf{r}_2=\mathsf{r}_1+1}^{\mathsf{n}-1}\mathsf{g}_-(\mathsf{r}_1)\otimes\mathsf{g}_-(\mathsf{r}_2-\mathsf{r}_1)\otimes\mathsf{g}_-(\mathsf{n}-\mathsf{r}_2)\Big). \tag{4.3.4}$$

In the first term on the right-hand side, the first current includes the first r_1 gluons, i.e. those labeled $1, ..., r_1$, while the second current includes the remaining $n - r_1$ gluons, which are understood to be labeled $r_1 + 1, ..., n$. The second term on the right-hand side has the first r_1 gluons, labeled $1, ..., r_1$, in the first current. The $r_2 - r_1$ gluons labeled $r_1 + 1, ..., r_2$ are in the second current, and the final $n - r_2$ gluons (labeled $r_2 + 1, ..., n$) are in the final current. This notation is purely for convenience, and will be used throughout.

As an example, consider the current $\mathsf{g}_-(3)$, which has three on-shell gluons in addition to the off-shell one. Written in the form of equation (4.3.3), this current is constructed as:

$$\mathsf{g}_-(1:3) = \mathsf{g}_-(1:1)\otimes\mathsf{g}_-(2:3)+\mathsf{g}_-(1:2)\otimes\mathsf{g}_-(3:3)+\mathsf{g}_-(1:1)\otimes\mathsf{g}_-(2:2)\otimes\mathsf{g}_-(3:3). \tag{4.3.5}$$

Written in the form of equation (4.3.4), the current is:

$$\mathsf{g}_-(3) = \mathsf{g}_-(1)\otimes\mathsf{g}_-(2)+\mathsf{g}_-(2)\otimes\mathsf{g}_-(1)+\mathsf{g}_-(1)\otimes\mathsf{g}_-(1)\otimes\mathsf{g}_-(1). \tag{4.3.6}$$

In the first term, the first current $\mathsf{g}_-(1)$ contains the first on-shell gluon g_1. The other current $\mathsf{g}_-(2)$ contains the next two on-shell gluons, g_2 and g_3. In the second term, $\mathsf{g}_-(2)$ contains g_1 and g_2 with $\mathsf{g}_-(1)$ containing g_3. In the final term, the three currents $\mathsf{g}_-(1)$ contain g_1, g_2 and g_3 respectively. A diagrammatic representation is shown in figure 4.3, with each term corresponding to a diagram.

$\underline{\mathsf{f\_\bar{f}}(\bar{\mathsf{q}}_2;\mathsf{n}_1,\mathsf{n}_2)}$

This current contains an off-shell quark and an on-shell antiquark forming a single quark line, with n_1 gluons to its left, labeled $1,...,n_1$, and n_2 gluons to its right, labeled $n_1+1,...,n_1+n_2$. The skeleton is simply the spinor of the on-shell antiquark. The current vanishes if the flavours of the quark and antiquark are different, since this would violate charge conservation. Gluons are added as:

$$\mathsf{f\_\bar{f}}(\mathsf{n}_1,\mathsf{n}_2) = \sum_{\mathsf{r}_1=1}^{\mathsf{n}_1} \mathsf{g\_}(\mathsf{r}_1) \otimes \mathsf{f\_\bar{f}}(\mathsf{n}_1-\mathsf{r}_1,\mathsf{n}_2) + \sum_{\mathsf{r}_2=0}^{\mathsf{n}_2-1} \mathsf{f\_\bar{f}}(\mathsf{n}_1,\mathsf{r}_2) \otimes \mathsf{g\_}(\mathsf{n}_2-\mathsf{r}_2), \qquad (4.3.7)$$

with the quark labels understood.

As an example, the current

$$\mathsf{f\_\bar{f}}(1,2) = \mathsf{g\_}(1) \otimes \mathsf{f\_\bar{f}}(0,2) + \mathsf{f\_\bar{f}}(1,0) \otimes \mathsf{g\_}(2) + \mathsf{f\_\bar{f}}(1,1) \otimes \mathsf{g\_}(1), \qquad (4.3.8)$$

is shown in figure 4.4. The first term generates the first two diagrams on the top row, and the second term generates the third diagram on this row. The two diagrams on the bottom row originate from the final term.

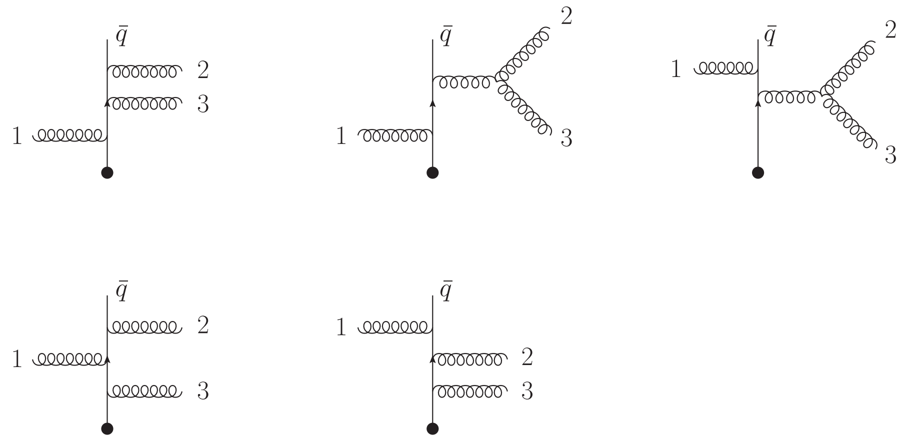

Figure 4.4: Diagrammatic representation of the current $\mathsf{f\_\bar{f}}(\bar{\mathsf{q}}_2,\mathsf{n}_1=1,\mathsf{n}_2=2)$. The off-shell quark is indicated by the solid circle.

$\underline{\mathsf{\bar{f}\_f}(\mathsf{q}_1;\mathsf{n}_1,\mathsf{n}_2)}$

This is the "conjugate current" to $\mathsf{f\_\bar{f}}$, and consists of an off-shell antiquark and an on-shell quark. The skeleton is the quark spinor. The recursion relation is the same as for the previous current:

$$\mathsf{\bar{f}\_f}(\mathsf{n}_1,\mathsf{n}_2) = \sum_{\mathsf{r}_1=1}^{\mathsf{n}_1} \mathsf{g\_}(\mathsf{r}_1) \otimes \mathsf{\bar{f}\_f}(\mathsf{n}_1-\mathsf{r}_1,\mathsf{n}_2) + \sum_{\mathsf{r}_2=0}^{\mathsf{n}_2-1} \mathsf{\bar{f}\_f}(\mathsf{n}_1,\mathsf{r}_2) \otimes \mathsf{g\_}(\mathsf{n}_2-\mathsf{r}_2), \qquad (4.3.9)$$

where again there are n_1 gluons to the left of the quark line, and n_2 gluons to the right.

$\mathsf{g\_f\bar{f}}(\mathsf{q}_1, \bar{\mathsf{q}}_2, ; \mathsf{n}_1, \mathsf{n}_2, \mathsf{n}_3)$

This current consists of an off-shell gluon and an on-shell antiquark-quark pair. The skeleton is thus constructed as

$$\mathsf{g\_f\bar{f}}(\mathsf{q}_1, \bar{\mathsf{q}}_2; 0, 0, 0) = \mathsf{\bar{f}\_f}(\mathsf{q}_1; 0, 0) \otimes \mathsf{f\_\bar{f}}(\bar{\mathsf{q}}_2; 0, 0). \tag{4.3.10}$$

There are n_1 gluons between the off-shell gluon and the quark, n_2 gluons between the quark and antiquark, and n_3 gluons between the antiquark and off-shell gluon (see figure 4.5). Additional on-shell gluons are added as

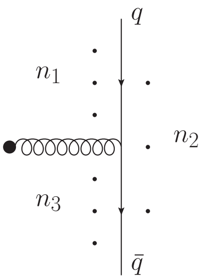

Figure 4.5: Diagrammatic representation of the current $\mathsf{g\_f\bar{f}}(\mathsf{q}_1, \bar{\mathsf{q}}_2, ; \mathsf{n}_1, \mathsf{n}_2, \mathsf{n}_3)$. The small dots indicate where n_1, n_2 and n_3 on-shell gluons may be added.

$$\begin{aligned}
&\mathsf{g\_f\bar{f}}(\mathsf{q}_1, \bar{\mathsf{q}}_2; \mathsf{n}_1, \mathsf{n}_2, \mathsf{n}_3) = \\
&\quad \sum_{\mathsf{r}_1=1}^{\mathsf{n}_1} \Big(\mathsf{g\_}(\mathsf{r}_1) \otimes \mathsf{g\_f\bar{f}}(\mathsf{n}_1 - \mathsf{r}_1, \mathsf{n}_2, \mathsf{n}_3) + \sum_{\mathsf{r}_3=0}^{\mathsf{n}_3-1} \mathsf{g\_f\bar{f}}(\mathsf{n}_1, \mathsf{n}_2, \mathsf{r}_3) \otimes \mathsf{g\_}(\mathsf{n}_3 - \mathsf{r}_3) \Big) \\
&\quad + \sum_{\mathsf{r}_1=1}^{\mathsf{n}_1-1} \sum_{\mathsf{r}_2=\mathsf{r}_1+1}^{\mathsf{n}_1} \mathsf{g\_}(\mathsf{r}_1) \otimes \mathsf{g\_}(\mathsf{r}_2 - \mathsf{r}_1) \otimes \mathsf{g\_f\bar{f}}(\mathsf{n}_1 - \mathsf{r}_2, \mathsf{n}_2, \mathsf{n}_3) \\
&\quad + \sum_{\mathsf{r}_1=1}^{\mathsf{n}_1} \sum_{\mathsf{r}_3=0}^{\mathsf{n}_3-1} \mathsf{g\_}(\mathsf{r}_1) \otimes \mathsf{g\_f\bar{f}}(\mathsf{n}_1 - \mathsf{r}_1, \mathsf{n}_2, \mathsf{r}_3) \otimes \mathsf{g\_}(\mathsf{n}_3 - \mathsf{r}_3) \\
&\quad + \sum_{\mathsf{r}_3=0}^{\mathsf{n}_3-2} \sum_{\mathsf{r}_4=\mathsf{r}_3+1}^{\mathsf{n}_3-1} \mathsf{g\_f\bar{f}}(\mathsf{n}_1, \mathsf{n}_2, \mathsf{r}_3) \otimes \mathsf{g\_}(\mathsf{r}_4 - \mathsf{r}_3) \otimes \mathsf{g\_}(\mathsf{n}_3 - \mathsf{r}_4) \Big) \\
&\quad + \sum_{\mathsf{r}_2=0}^{\mathsf{n}_2} \mathsf{\bar{f}\_f}(\mathsf{q}_1; \mathsf{n}_1, \mathsf{r}_2) \otimes \mathsf{f\_\bar{f}}(\bar{\mathsf{q}}_2; \mathsf{n}_2 - \mathsf{r}_2, \mathsf{n}_3).
\end{aligned} \tag{4.3.11}$$

$\mathsf{g\_\bar{f}f}(\bar{\mathsf{q}}_1, \mathsf{q}_2; \mathsf{n}_1, \mathsf{n}_2, \mathsf{n}_3)$

This is the conjugate current to $\mathsf{g\_f\bar{f}}$. The skeleton is constructed as

$$\mathsf{g\_\bar{f}f}(\bar{\mathsf{q}}_1, \mathsf{q}_2) = \mathsf{f\_\bar{f}}(\bar{\mathsf{q}}_1) \otimes \mathsf{\bar{f}\_f}(\mathsf{q}_2), \tag{4.3.12}$$

with the gluon labels again understood to be zero. This is the same as the skeleton of $\mathsf{g\_f\bar{f}}$ with the replacements $\mathsf{q}_1 \to \bar{\mathsf{q}}_1$, $\bar{\mathsf{q}}_2 \to \mathsf{q}_2$ and $\mathsf{\bar{f}} \leftrightarrow \mathsf{f}$. The recursive addition of on-shell gluons can likewise be obtained from equation (4.3.11) under the same replacements.

$\mathsf{f\_\bar{f}f\bar{f}}(\bar{\mathsf{q}}_1, \mathsf{q}_2, \bar{\mathsf{q}}_3; \mathsf{n}_1, \mathsf{n}_2, \mathsf{n}_3, \mathsf{n}_4)$

The skeleton of this current consists of two quark-antiquark lines. The off-shell quark may be on the same line as either antiquark $\bar{q}_1$ or $\bar{q}_3$. I shall refer to these as "s" and "t" channels, respectively. The flavours of the quarks can be used to determine whether the current is in the s-channel, t-channel or both. The skeleton is constructed by

$$\begin{aligned}\mathsf{f\_\bar{f}f\bar{f}}(\bar{\mathsf{q}}_1, \mathsf{q}_2, \bar{\mathsf{q}}_3; 0,0,0,0) =& \mathsf{f\_\bar{f}}(\bar{\mathsf{q}}_1, 0, 0) \otimes \mathsf{g\_f\bar{f}}(\mathsf{q}_2, \bar{\mathsf{q}}_3; 0,0,0) \\ &+ \mathsf{g\_\bar{f}f}(\bar{\mathsf{q}}_1, \mathsf{q}_2; 0,0,0) \otimes \mathsf{f\_\bar{f}}(\bar{\mathsf{q}}_3, 0, 0),\end{aligned} \tag{4.3.13}$$

with the first term corresponding to the s-channel current and the second corresponding to the t-channel current. Additional gluons, distributed between the skeleton as shown in figure 4.6, are given by

$$\begin{aligned}&\mathsf{f\_\bar{f}f\bar{f}}(\bar{\mathsf{q}}_1, \mathsf{q}_2, \bar{\mathsf{q}}_3; \mathsf{n}_1, \mathsf{n}_2, \mathsf{n}_3, \mathsf{n}_4) = \\ &\quad + \sum_{\mathsf{r}_1=1}^{\mathsf{n}_1} \mathsf{g\_}(\mathsf{r}_1) \otimes \mathsf{f\_\bar{f}f\bar{f}}(\mathsf{n}_1 - \mathsf{r}_1, \mathsf{n}_2, \mathsf{n}_3, \mathsf{n}_4) \\ &\quad + \sum_{\mathsf{r}_2=0}^{\mathsf{n}_2} \mathsf{f\_\bar{f}}(\bar{\mathsf{q}}_1, \mathsf{n}_1, \mathsf{r}_2) \otimes \mathsf{g\_f\bar{f}}(\mathsf{q}_2, \bar{\mathsf{q}}_3; \mathsf{n}_2 - \mathsf{r}_2, \mathsf{n}_3, \mathsf{n}_4) \\ &\quad + \sum_{\mathsf{r}_3=0}^{\mathsf{n}_3} \mathsf{g\_\bar{f}f}(\bar{\mathsf{q}}_1, \mathsf{q}_2; \mathsf{n}_1, \mathsf{n}_2, \mathsf{r}_3) \otimes \mathsf{f\_\bar{f}}(\bar{\mathsf{q}}_3; \mathsf{n}_3 - \mathsf{r}_3, \mathsf{n}_4) \\ &\quad + \sum_{\mathsf{r}_4=0}^{\mathsf{n}_4-1} \mathsf{f\_\bar{f}f\bar{f}}(\bar{\mathsf{q}}_1, \mathsf{q}_2, \bar{\mathsf{q}}_3; \mathsf{n}_1, \mathsf{n}_2, \mathsf{n}_3, \mathsf{r}_4) \otimes \mathsf{g\_}(\mathsf{n}_4 - \mathsf{r}_4).\end{aligned} \tag{4.3.14}$$

The currents $\mathsf{f\_\bar{f}f\bar{f}_s}$ and $\mathsf{f\_\bar{f}f\bar{f}_t}$ can also be defined, in which only the terms in the s- or t-channels appear. The former is constructed using only the first term of equation (4.3.13) and omitting the third term of the recursion relation, equation (4.3.14). The latter is constructed using only the second term of equation (4.3.13) and omitting the second term of equation (4.3.14). In both cases, the recursion relation uses $\mathsf{f\_\bar{f}f\bar{f}_{s,t}}$ in place of $\mathsf{f\_\bar{f}f\bar{f}}$. Additionally, the conjugate current $\mathsf{\bar{f}\_f\bar{f}f}$ can be defined by replacing $\mathsf{f} \leftrightarrow \mathsf{\bar{f}}$ in this current.

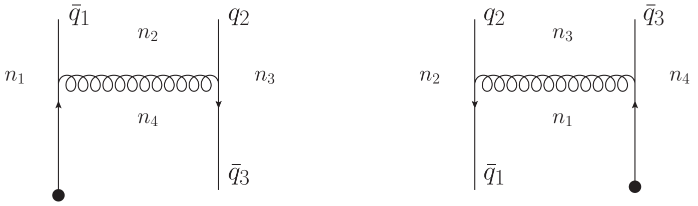

Figure 4.6: Representation of the current $\mathsf{f\_\bar{f}f\bar{f}}(\bar{\mathsf{q}}_1, \mathsf{q}_2, \bar{\mathsf{q}}_3; \mathsf{n}_1, \mathsf{n}_2, \mathsf{n}_3, \mathsf{n}_4)$. The s-channel is shown on the left; the t-channel on the right. On-shell gluons may be added as indicated by n_1, n_2, n_3 and n_4.

$\underline{\mathsf{g\_f_1\bar{f}_1f_2\bar{f}_2(q_1,\bar{q}_2,q_3,\bar{q}_4;n_1,n_2,n_3,n_4,n_5)}}$

This current consists of an off-shell gluon and two on-shell quark-antiquark lines comprising the skeleton. The quark flavours are such that q_1 and $\bar{q}_2$ must make up one of these lines, with q_3 and $\bar{q}_4$ making up the other line, as indicated by the subscripts in the name of the current. The skeleton is constructed by

$$\begin{aligned}
&\mathsf{g\_f_1\bar{f}_1f_2\bar{f}_2(q_1,\bar{q}_2,q_3,\bar{q}_4)} = \\
&\qquad \mathsf{g\_f\bar{f}(q_1,\bar{q}_2)\otimes g\_f\bar{f}(q_3,\bar{q}_4)+\bar{f}\_f(q_1)\otimes f\_\bar{f}f\bar{f}_s(\bar{q}_2,q_3,\bar{q}_4)} \\
&\qquad \mathsf{+\bar{f}\_f\bar{f}f_t(q_1,\bar{q}_2,q_3)\otimes f\_\bar{f}(\bar{q}_4).}
\end{aligned} \tag{4.3.15}$$

These three configurations are shown in figure 4.7. The additional gluons are added via

$$\begin{aligned}
&\mathsf{g\_f_1\bar{f}_1f_2\bar{f}_2(q_1,\bar{q}_2,q_3,\bar{q}_4;n_1,n_2,n_3,n_4,n_5)} = \\
&\quad \sum_{\mathsf{r_1=1}}^{\mathsf{n_1}}\sum_{\mathsf{r_3=0}}^{\mathsf{n_3}} \mathsf{g\_(r_1)\otimes g\_f\bar{f}(q_1,\bar{q}_2;n_1-r_1,n_2,r_3)\otimes g\_f\bar{f}(q_3,\bar{q}_4;n_3-r_3,n_4,n_5)} \\
&\quad +\sum_{\mathsf{r_3=0}}^{\mathsf{n_3-1}}\sum_{\mathsf{r_4=r_3+1}}^{\mathsf{n_3}} \mathsf{g\_f\bar{f}(q_1,\bar{q}_2;n_1,n_2,r_3)\otimes g\_(r_4-r_3)\otimes g\_f\bar{f}(q_3,\bar{q}_4;n_3-r_4,n_4,n_5)} \\
&\quad +\sum_{\mathsf{r_5=0}}^{\mathsf{n_5-1}}\sum_{\mathsf{r_3=0}}^{\mathsf{n_3}} \mathsf{g\_f\bar{f}(q_1,\bar{q}_2;n_1,n_2,r_3)\otimes g\_f\bar{f}(q_3,\bar{q}_4;n_3-r_3,n_4,r_5)\otimes g\_(n_5-r_5)} \\
&\quad +\sum_{\mathsf{r_1=1}}^{\mathsf{n_1-1}}\sum_{\mathsf{r_2=r_1+1}}^{\mathsf{n_1}} \mathsf{g\_(r_1)\otimes g\_(r_2-r_1)\otimes g\_f_1\bar{f}_1f_2\bar{f}_2(n_1-r_2,n_2,n_3,n_4,n_5)} \\
&\quad +\sum_{\mathsf{r_3=0}}^{\mathsf{n_3-1}}\sum_{\mathsf{r_4=r_3+1}}^{\mathsf{n_3}} \mathsf{g\_f\bar{f}(q_1,\bar{q}_2;n_1,n_2,r_3)\otimes g\_(r_4-r_3)\otimes g\_f\bar{f}(q_3,\bar{q}_4;n_3-r_4,n_4,n_5)} \\
&\quad +\sum_{\mathsf{r_5=0}}^{\mathsf{n_5-2}}\sum_{\mathsf{r_6=r_5+1}}^{\mathsf{n_5-1}} \mathsf{g\_f_1\bar{f}_1f_2\bar{f}_2(n_1,n_2,n_3,n_4,r_5)\otimes g\_(r_6-r_5)\otimes g\_(n_5-r_6)} \\
&\quad +\sum_{\mathsf{r_1=1}}^{\mathsf{n_1}} \mathsf{g\_(r_1)\otimes g\_f_1\bar{f}_1f_2\bar{f}_2(n_1-r_1,n_2,n_3,n_4,n_5)} \\
&\quad +\sum_{\mathsf{r_3=0}}^{\mathsf{n_3}} \mathsf{g\_f\bar{f}(q_1,\bar{q}_2;n_1,n_2,r_3)\otimes g\_f\bar{f}(q_3,\bar{q}_4;n_3-r_3,n_4,n_5)} \\
&\quad +\sum_{\mathsf{r_5=0}}^{\mathsf{n_5-1}} \mathsf{g\_f_1\bar{f}_1f_2\bar{f}_2(n_1,n_2,n_3,n_4,r_5)\otimes g\_(n_5-r_5)} \\
&\quad +\sum_{\mathsf{r_2=0}}^{\mathsf{n_2}} \mathsf{\bar{f}\_f(q_1;n_1,r_2)\otimes f\_\bar{f}f\bar{f}_s(\bar{q}_2,q_3,\bar{q}_4;n_2-r_2,n_3,n_4,n_5)} \\
&\quad +\sum_{\mathsf{r_4=0}}^{\mathsf{n_4}} \mathsf{\bar{f}\_f\bar{f}f_t(q_1,\bar{q}_2,q_3;n_1,n_2,n_3,r_4)\otimes f\_\bar{f}(\bar{q}_4),n_4-r_4,n_5).}
\end{aligned} \tag{4.3.16}$$

The last two terms correspond to attaching a gluon current directly to the first and second quark line, respectively. All the other terms add gluons to the off-shell gluon. This can be through a four-gluon coupling, as with the first six terms, or through a three-gluon coupling, as with the seventh, eighth and ninth terms.

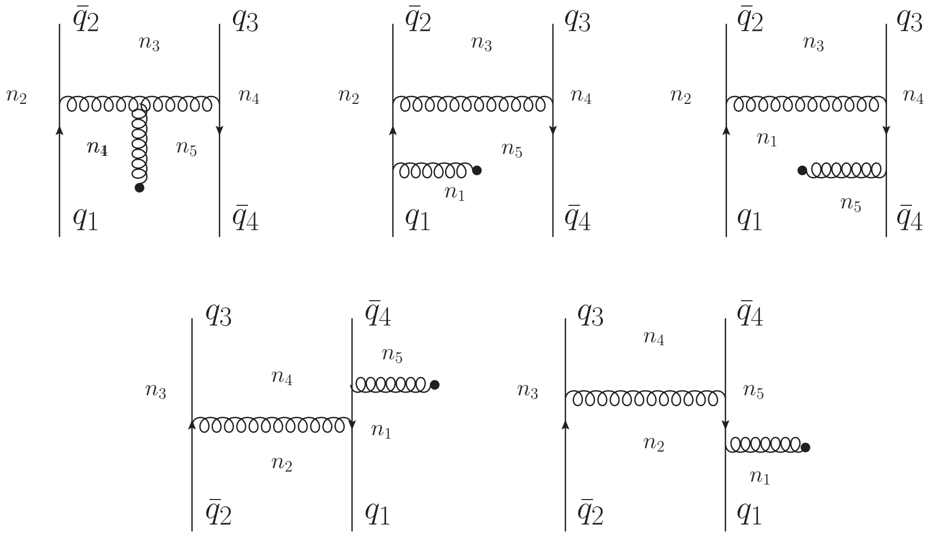

Figure 4.7: Representations of the currents $\mathsf{g\_f_1\bar{f}_1f_2\bar{f}_2(q_1,\bar{q}_2,q_3,\bar{q}_4;n_1,n_2,n_3,n_4,n_5)}$ (top) and $\mathsf{g\_f_1\bar{f}_2f_2\bar{f}_1(q_1,\bar{q}_2,q_3,\bar{q}_4;n_1,n_2,n_3,n_4,n_5)}$ (bottom).

.

$\underline{\mathsf{g\_f_1\bar{f}_2f_2\bar{f}_1(q_1,\bar{q}_2,q_3,\bar{q}_4;n_1,n_2,n_3,n_4,n_5)}}$

This current is similar to the previous one, but with the first quark-antiquark line being made up from q_1 and $\bar{q}_4$, and the second made up from q_3 and $\bar{q}_2$. This skeleton is shown in figure 4.7, and is constructed by

$$\begin{aligned}\mathsf{g\_f_1\bar{f}_2f_2\bar{f}_1(q_1,\bar{q}_2,q_3,\bar{q}_4;0,0,0,0,0)} =&\mathsf{\bar{f}\_f(q_1)}\otimes\mathsf{f\_\bar{f}f\bar{f}_t(\bar{q}_2,q_3,\bar{q}_4)}\\ &+\mathsf{\bar{f}\_f\bar{f}f_s(q_1,\bar{q}_2,q_3)}\otimes\mathsf{f\_\bar{f}(\bar{q}_4)};\end{aligned} \tag{4.3.17}$$

while additional gluons are added according to

$$\begin{aligned}
&\mathsf{g\_f_1\bar{f}_2f_2\bar{f}_1(q_1,\bar{q}_2,q_3,\bar{q}_4;n_1,n_2,n_3,n_4,n_5)} = \\
&\qquad \sum_{r_1=1}^{n_1-1}\sum_{r_2=r_1+1}^{n_1} \mathsf{g\_(r_1)} \otimes \mathsf{g\_(r_2-r_1)} \otimes \mathsf{g\_f_1\bar{f}_2f_2\bar{f}_1(n_1-r_2,n_2,n_3,n_4,n_5)} \\
&\qquad +\sum_{r_1=1}^{n_1}\sum_{r_5=0}^{n_5-1} \mathsf{g\_(r_1)} \otimes \mathsf{g\_f_1\bar{f}_2f_2\bar{f}_1(n_1-r_2,n_2,n_3,n_4,r_5)} \otimes \mathsf{g\_(n_5-r_5)} \\
&\qquad +\sum_{r_5=0}^{n_5-2}\sum_{r_6=r_5+1}^{n_5-1} \mathsf{g\_f_1\bar{f}_2f_2\bar{f}_1(n_1,n_2,n_3,n_4,r_5)} \otimes \mathsf{g\_(r_6-r_5)} \otimes \mathsf{g\_(n_5-r_6)} \\
&\qquad +\sum_{r_1=1}^{n_1} \mathsf{g\_(r_1)} \otimes \mathsf{g\_f_1\bar{f}_2f_2\bar{f}_1(n_1-r_1,n_2,n_3,n_4,n_5)} \\
&\qquad +\sum_{r_5=0}^{n_5-1} \mathsf{g\_f_1\bar{f}_2f_2\bar{f}_1(n_1,n_2,n_3,n_4,r_5)} \otimes \mathsf{g\_(n_5-r_5)} \\
&\qquad +\sum_{r_2=0}^{n_2} \mathsf{\bar{f}\_f(q_1;n_1,r_2)} \otimes \mathsf{f\_\bar{f}f\bar{f}_t(\bar{q}_2,q_3,\bar{q}_4;n_2-r_2,n_3,n_4,n_5)} \\
&\qquad +\sum_{r_4=0}^{n_4} \mathsf{\bar{f}\_f\bar{f}f_s(q_1,\bar{q}_2,q_3;n_1,n_2,n_3,r_4)} \otimes \mathsf{f\_\bar{f}(\bar{q}_4),n_4-r_4,n_5)}.
\end{aligned} \tag{4.3.18}$$

$\underline{\mathsf{f_1\_\bar{f}_1f_2\bar{f}_2f_3\bar{f}_3(\bar{q}_1,q_2,\bar{q}_3,q_4,\bar{q}_5;n_1,n_2,n_3,n_4,n_5,n_6)}}$

The skeleton of this current includes three quark-antiquark lines. The subscripts indicate that these are formed by the off-shell quark and $\bar{q}_1$, q_2 and $\bar{q}_3$, and q_4 and $\bar{q}_5$. The skeleton is given by

$$\begin{aligned}
\mathsf{f_1\_\bar{f}_1f_2\bar{f}_2f_3\bar{f}_3(\bar{q}_1,q_2,\bar{q}_3,q_4,\bar{q}_5)} = &\mathsf{f\_\bar{f}(\bar{q}_1)} \otimes \mathsf{g\_f_1\bar{f}_1f_2\bar{f}_2(q_2,\bar{q}_3,q_4,\bar{q}_5)} \\
&+\mathsf{f\_\bar{f}f\bar{f}_s(\bar{q}_1,q_2,\bar{q}_3)} \otimes \mathsf{g\_f\bar{f}(q_4,\bar{q}_5)},
\end{aligned} \tag{4.3.19}$$

as shown in figure 4.8. The recursion relations are

$$\begin{aligned}
&\mathsf{f_1\_\bar{f}_1f_2\bar{f}_2f_3\bar{f}_3(\bar{q}_1,q_2,\bar{q}_3,q_4,\bar{q}_5;n_1,n_2,n_3,n_4,n_5,n_6)} = \\
&\qquad \sum_{r_2=0}^{n_2} \mathsf{f\_\bar{f}(\bar{q}_1;n_1,r_2)} \otimes \mathsf{g\_f_1\bar{f}_1f_2\bar{f}_2(q_2,\bar{q}_3,q_4,\bar{q}_5;n_2-r_2,n_3,n_4,n_5,n_6)} \\
&\qquad +\sum_{r_1=1}^{n_1} \mathsf{g\_(r_1)} \otimes \mathsf{f_1\_\bar{f}_1f_2\bar{f}_2f_3\bar{f}_3(n_1-r_1,n_2,n_3,n_4,n_5,n_6)} \\
&\qquad +\sum_{r_4=0}^{n_4} \mathsf{f\_\bar{f}f\bar{f}_s(\bar{q}_1,q_2,\bar{q}_3;n_1,n_2,n_3,r_4)} \otimes \mathsf{g\_f\bar{f}(q_4,\bar{q}_5;n_4-r_4,n_5,n_6)} \\
&\qquad +\sum_{r_6=0}^{n_6-1} \mathsf{f_1\_\bar{f}_1f_2\bar{f}_2f_3\bar{f}_3(n_1,n_2,n_3,n_4,n_5,r_6)} \otimes \mathsf{g\_(n_6-r_6)}.
\end{aligned} \tag{4.3.20}$$

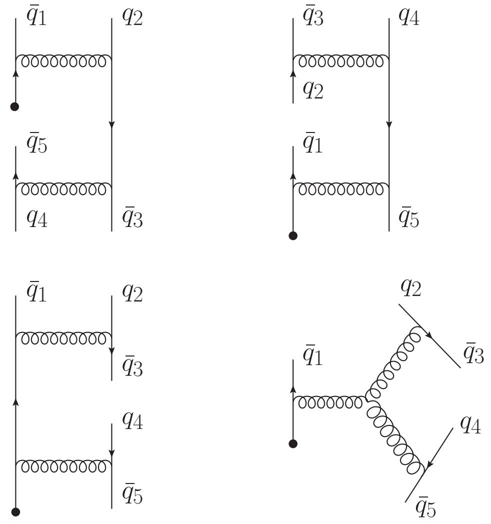

Figure 4.8: Representation of the current $\mathsf{f_1\_\bar{f}_1f_2\bar{f}_2f_3\bar{f}_3}(\bar{\mathsf{q}}_1,\mathsf{q}_2,\bar{\mathsf{q}}_3,\mathsf{q}_4,\bar{\mathsf{q}}_5;\mathsf{n}_1,\mathsf{n}_2,\mathsf{n}_3,\mathsf{n}_4,\mathsf{n}_5,\mathsf{n}_6)$.

$\underline{\mathsf{f_1\_\bar{f}_2f_2\bar{f}_1f_3\bar{f}_3}(\bar{\mathsf{q}}_1,\mathsf{q}_2,\bar{\mathsf{q}}_3,\mathsf{q}_4,\bar{\mathsf{q}}_5;\mathsf{n}_1,\mathsf{n}_2,\mathsf{n}_3,\mathsf{n}_4,\mathsf{n}_5,\mathsf{n}_6)}$

This current is similar to the previous one, but with the off-shell quark forming a quark-antiquark line with $\bar{q}_3$, and remaining two lines being formed with q_2 and $\bar{q}_1$ and q_4 and $\bar{q}_5$. The skeleton is given by

$$\begin{aligned}\mathsf{f_1\_\bar{f}_2f_2\bar{f}_1f_3\bar{f}_3}(\bar{\mathsf{q}}_1,\mathsf{q}_2,\bar{\mathsf{q}}_3,\mathsf{q}_4,\bar{\mathsf{q}}_5) =&\mathsf{g\_\bar{f}f}(\bar{\mathsf{q}}_1,\mathsf{q}_2)\otimes\mathsf{f\_\bar{f}f\bar{f}_s}(\bar{\mathsf{q}}_3,\mathsf{q}_4,\bar{\mathsf{q}}_5)\\ &+\mathsf{f\_\bar{f}f\bar{f}_t}(\bar{\mathsf{q}}_1,\mathsf{q}_2,\bar{\mathsf{q}}_3)\otimes\mathsf{g\_f\bar{f}}(\mathsf{q}_4,\bar{\mathsf{q}}_5),\end{aligned}\tag{4.3.21}$$

while the recursion relation is

$$\begin{aligned}&\mathsf{f_1\_\bar{f}_2f_2\bar{f}_1f_3\bar{f}_3}(\bar{\mathsf{q}}_1,\mathsf{q}_2,\bar{\mathsf{q}}_3,\mathsf{q}_4,\bar{\mathsf{q}}_5;\mathsf{n}_1,\mathsf{n}_2,\mathsf{n}_3,\mathsf{n}_4,\mathsf{n}_5,\mathsf{n}_6) =\\ &\qquad\sum_{\mathsf{r}_3=0}^{\mathsf{n}_3}\mathsf{g\_\bar{f}f}(\bar{\mathsf{q}}_1,\mathsf{q}_2;\mathsf{n}_1,\mathsf{n}_2,\mathsf{r}_3)\otimes\mathsf{f\_\bar{f}f\bar{f}_s}(\bar{\mathsf{q}}_3,\mathsf{q}_4,\bar{\mathsf{q}}_5;\mathsf{n}_3-\mathsf{r}_3,\mathsf{n}_4,\mathsf{n}_5,\mathsf{n}_6)\\ &\qquad+\sum_{\mathsf{r}_4=0}^{\mathsf{n}_4}\mathsf{f\_\bar{f}f\bar{f}_t}(\bar{\mathsf{q}}_1,\mathsf{q}_2,\bar{\mathsf{q}}_3;\mathsf{n}_1,\mathsf{n}_2,\mathsf{n}_3,\mathsf{r}_4)\otimes\mathsf{g\_f\bar{f}}(\mathsf{q}_4,\bar{\mathsf{q}}_5;\mathsf{n}_4-\mathsf{r}_4,\mathsf{n}_5,\mathsf{n}_6)\\ &\qquad+\sum_{\mathsf{r}_1=1}^{\mathsf{n}_1}\mathsf{g\_}(\mathsf{r}_1)\otimes\mathsf{f_1\_\bar{f}_2f_2\bar{f}_1f_3\bar{f}_3}(\mathsf{n}_1-\mathsf{r}_1,\mathsf{n}_2,\mathsf{n}_3,\mathsf{n}_4,\mathsf{n}_5,\mathsf{n}_6)\\ &\qquad+\sum_{\mathsf{r}_6=0}^{\mathsf{n}_6-1}\mathsf{f_1\_\bar{f}_2f_2\bar{f}_1f_3\bar{f}_3}(\mathsf{n}_1,\mathsf{n}_2,\mathsf{n}_3,\mathsf{n}_4,\mathsf{n}_5,\mathsf{r}_6)\otimes\mathsf{g\_}(\mathsf{n}_6-\mathsf{r}_6).\end{aligned}\tag{4.3.22}$$

$\underline{\mathsf{f_1\_\bar{f}_1f_2\bar{f}_3f_3\bar{f}_2}(\bar{\mathsf{q}}_1,\mathsf{q}_2,\bar{\mathsf{q}}_3,\mathsf{q}_4,\bar{\mathsf{q}}_5;\mathsf{n}_1,\mathsf{n}_2,\mathsf{n}_3,\mathsf{n}_4,\mathsf{n}_5,\mathsf{n}_6)}$

This current has quark-antiquark lines formed by q_2 and $\bar{q}_5$, q_4 and $\bar{q}_3$, and by $\bar{q}_1$ and the off-shell quark. The skeleton is

$$\mathsf{f_1\_\bar{f}_1f_2\bar{f}_3f_3\bar{f}_2}(\bar{\mathsf{q}}_1,\mathsf{q}_2,\bar{\mathsf{q}}_3,\mathsf{q}_4,\bar{\mathsf{q}}_5) = \mathsf{f\_\bar{f}}(\bar{\mathsf{q}}_1)\otimes\mathsf{g\_f_1\bar{f}_2f_2\bar{f}_1}(\mathsf{q}_2,\bar{\mathsf{q}}_3,\mathsf{q}_4,\bar{\mathsf{q}}_5),\tag{4.3.23}$$

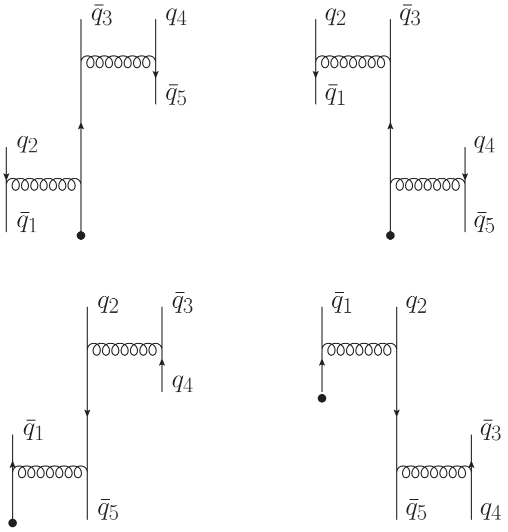

Figure 4.9: Currents $\mathsf{f_1\_\bar{f}_2f_2\bar{f}_1f_3\bar{f}_3(\bar{q}_1, q_2, \bar{q}_3, q_4, \bar{q}_5; n_1, n_2, n_3, n_4, n_5, n_6)}$ (top) and $\mathsf{f_1\_\bar{f}_1f_2\bar{f}_3f_3\bar{f}_2(\bar{q}_1, q_2, \bar{q}_3, q_4, \bar{q}_5; n_1, n_2, n_3, n_4, n_5, n_6)}$ (bottom).

while the recursion relation is

$$
\begin{aligned}
&\mathsf{f_1\_\bar{f}_1f_2\bar{f}_3f_3\bar{f}_2(\bar{q}_1, q_2, \bar{q}_3, q_4, \bar{q}_5; n_1, n_2, n_3, n_4, n_5, n_6)} = \\
&\qquad \sum_{\mathsf{r_1=1}}^{\mathsf{n_1}} \mathsf{g\_(r_1) \otimes f_1\_\bar{f}_1f_2\bar{f}_3f_3\bar{f}_2(n_1 - r_1, n_2, n_3, n_4, n_5, n_6)} + \\
&\qquad \sum_{\mathsf{r_6=0}}^{\mathsf{n_6-1}} \mathsf{f_1\_\bar{f}_1f_2\bar{f}_3f_3\bar{f}_2(n_1, n_2, n_3, n_4, n_5, r_6) \otimes g\_(n_6 - r_6)} + \\
&\qquad \sum_{\mathsf{r_2=0}}^{\mathsf{n_2}} \mathsf{f\_\bar{f}(\bar{q}_1; n_1, r_2) \otimes g\_f_1\bar{f}_2f_2\bar{f}_1(q_2, \bar{q}_3, q_4, \bar{q}_5; n_2 - r_2.n_3, n_4, n_5, n_6)}.
\end{aligned}
\tag{4.3.24}
$$

The above two six-quark currents are shown in figure 4.9.

4.3.2 Currents with one electroweak boson

$\underline{\mathsf{f\_V\bar{f}(\bar{q}_1; n_1, n_2)}}$

The skeleton consists of an on-shell antiquark and electroweak (EW) boson. The EW boson is not colour-charged and therefore is not ordered: one needs to consider all possible insertions of it relative to the on-shell gluons. Again, the number of gluons to the left and to the right of the quark-antiquark line are denoted as n_1 and n_2 respectively. The skeleton is simply the coupling of the electroweak boson to the antiquark

$$\mathsf{f\_V\bar{f}(\bar{q}_2, V) = f\_\bar{f}(\bar{q}_2) \otimes V}. \tag{4.3.25}$$

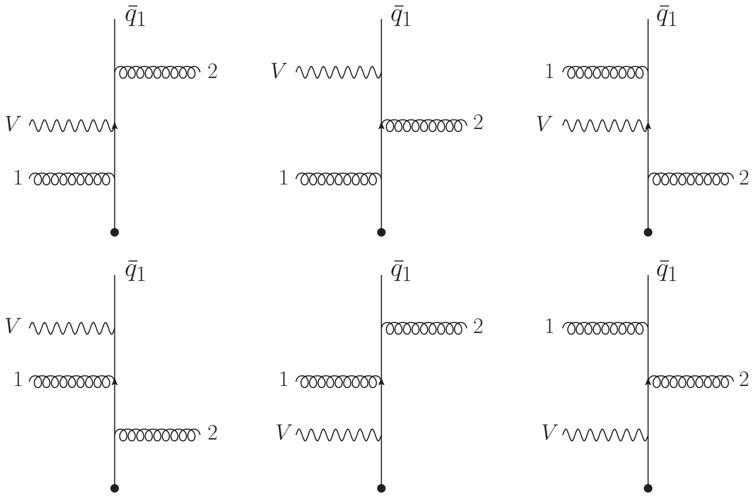

Figure 4.10: Current $\mathsf{f\_V\bar{f}}(\bar{\mathsf{q}}_1, \mathsf{n}_1 = 1, \mathsf{n}_2 = 1)$. Note that all insertions of the electroweak boson relative to the coloured particles are allowed.

The recursion relation is

$$\begin{aligned} \mathsf{f\_V\bar{f}}(\mathsf{n}_1, \mathsf{n}_2) =& \sum_{\mathsf{r}_1=1}^{\mathsf{n}_1} \mathsf{g\_}(\mathsf{r}_1) \otimes \mathsf{f\_V\bar{f}}(\mathsf{n}_1 - \mathsf{r}_1, \mathsf{n}_2) + \mathsf{f\_\bar{f}}(\bar{\mathsf{q}}_2; \mathsf{n}_1, \mathsf{n}_2) \otimes \mathsf{V} \\ &+ \sum_{\mathsf{r}_2=0}^{\mathsf{n}_2-1} \mathsf{f\_V\bar{f}}(\mathsf{n}_1, \mathsf{r}_2) \otimes \mathsf{g\_}(\mathsf{n}_2 - \mathsf{r}_2). \end{aligned} \tag{4.3.26}$$

As an example, the current

$$\mathsf{f\_V\bar{f}}(1,1) = \mathsf{g\_}(1) \otimes \mathsf{f\_V\bar{f}}(0,1) + \mathsf{f\_V\bar{f}}(1,0) \otimes \mathsf{g\_}(1) + \mathsf{f\_\bar{f}}(1,1) \otimes \mathsf{V} \tag{4.3.27}$$

is shown in figure 4.10. From this, the advantage of Berends-Giele recursion relations is plain: this one current encodes the equivalent information of six Feynman diagrams. The conjugate current $\mathsf{\bar{f}\_Vf}$ can be defined as before, with the only modification being that the EW boson should now couple to an on-shell quark.

$\underline{\mathsf{f\_V\bar{f}^*}(\bar{\mathsf{q}}_1; \mathsf{n}, \mathsf{f}_\mathsf{p}, \mathsf{f}_\mathsf{g})}$

This current is similar to the above, but the insertion of the electroweak boson is restricted to be either before or after a "reference" gluon. For this reason, this current is called a "restricted" current. The argument f_g defines which gluon is used as the reference, and the argument f_p gives its position along the quark-antiquark line, including both electroweak bosons and gluons. Thus, $f_g = f_p$ implies that the electroweak boson comes after the reference gluon, whereas $f_p = f_g + 1$ implies that the electroweak boson comes first. The gluons are always to the left of the quark-antiquark line, so there is only one argument n to fix the number of gluons. The skeleton is the same as for $\mathsf{f\_V\bar{f}}$, but the recursion relation becomes

$$\begin{aligned}\mathsf{f\_V\bar{f}^*(\bar{q}_1; n, f_p, f_g)} =&\delta_{\mathsf{f_p,f_g}}\Big(\sum_{\mathsf{r_1=1}}^{\mathsf{f_g-1}} \mathsf{g\_(r_1) \otimes f\_V\bar{f}^*(n-r_1, f_p-r_1, f_g-r_1)}\\ &+\sum_{\mathsf{r_1=f_g}}^{\mathsf{n}} \mathsf{g\_(r_1) \otimes f\_V\bar{f}(n-r_1, 0)}\Big)\\ &+\delta_{\mathsf{f_p-1,f_g}}\Big(\mathsf{f\_\bar{f}(n,0) \otimes V}\\ &+\sum_{\mathsf{r_1=1}}^{\mathsf{f_g-1}} \mathsf{g\_(r_1) \otimes f\_V\bar{f}^*(n-r_1, f_p-r_1, f_g-r_1)}\Big).\end{aligned} \tag{4.3.28}$$

This recursion relation will be used extensively in chapter 7.

$\underline{\mathsf{g\_Vf\bar{f}(q_1, \bar{q}_2; n_1, n_2, n_3)}}$
The skeleton for this current is

$$\mathsf{g\_Vf\bar{f}(q_1, \bar{q}_2) = \bar{f}\_Vf(q_1) \otimes f\_\bar{f}(\bar{q}_2) + \bar{f}\_f(q_1) \otimes f\_V\bar{f}(\bar{q}_2)}. \tag{4.3.29}$$

The recursion relation is similar to those for $\mathsf{g\_f\bar{f}}$:

$$\begin{aligned}&\mathsf{g\_Vf\bar{f}(q_1, \bar{q}_2; n_1, n_2, n_3)} =\\ &\quad+\sum_{\mathsf{r_1=1}}^{\mathsf{n_1}}\big(\mathsf{g\_(r_1) \otimes g\_Vf\bar{f}(n_1-r_1, n_2, n_3)}\\ &\quad+\sum_{\mathsf{r_3=0}}^{\mathsf{n_3-1}} \mathsf{g\_Vf\bar{f}(n_1, n_2, r_3) \otimes g\_(n_3-r_3)}\big)\\ &\quad+\sum_{\mathsf{r_1=1}}^{\mathsf{n_1-1}}\sum_{\mathsf{r_2=r_1+1}}^{\mathsf{n_1}} \mathsf{g\_(r_1) \otimes g\_(r_2-r_1) \otimes g\_Vf\bar{f}(n_1-r_2, n_2, n_3)}\\ &\quad+\sum_{\mathsf{r_1=1}}^{\mathsf{n_1}}\sum_{\mathsf{r_3=0}}^{\mathsf{n_3-1}} \mathsf{g\_(r_1) \otimes g\_Vf\bar{f}(n_1-r_1, n_2, r_3) \otimes g\_(n_3-r_3)}\\ &\quad+\sum_{\mathsf{r_3=0}}^{\mathsf{n_3-2}}\sum_{\mathsf{r_4=r_3+1}}^{\mathsf{n_3-1}} \mathsf{g\_Vf\bar{f}(n_1, n_2, r_3) \otimes g\_(r_4-r_3) \otimes g\_(n_3-r_4)}\\ &\quad+\sum_{\mathsf{r_2=0}}^{\mathsf{n_2}}\big(\mathsf{\bar{f}\_Vf(q_1; n_1, r_2) \otimes f\_\bar{f}(\bar{q}_2; n_2-r_2, n_3)}\\ &\quad+\mathsf{\bar{f}\_f(q_1; n_1, r_2) \otimes f\_V\bar{f}(\bar{q}_2; n_2-r_2, n_3)}\big),\end{aligned} \tag{4.3.30}$$

and similarly the conjugate current $\mathsf{g\_V\bar{f}f}$ can be defined.

$\underline{\mathsf{f\_V\bar{f}f\bar{f}}(\bar{\mathsf{q}}_1, \mathsf{q}_2, \bar{\mathsf{q}}_3; \mathsf{s_w}; \mathsf{n}_1, \mathsf{n}_2, \mathsf{n}_3, \mathsf{n}_4)}$

The skeleton of this current consists of two quark-antiquark lines and an EW boson. The new argument s_w controls which quark-antiquark line the EW boson will couple to. Additionally, it is possible to specify a flavour of quark to which the EW boson cannot couple (by definition). Contributions to the current involving quarks of this flavour coupling to the EW bosons are zero. The skeleton depends on the value of s_w:

$$\begin{aligned}
\mathsf{f\_V\bar{f}f\bar{f}}(\bar{\mathsf{q}}_1, \mathsf{q}_2, \bar{\mathsf{q}}_3) = &\Big(\mathsf{f\_V\bar{f}}(\bar{\mathsf{q}}_1) \otimes \mathsf{g\_f\bar{f}}(\mathsf{q}_2, \bar{\mathsf{q}}_3) + \mathsf{f\_\bar{f}f\bar{f}} \otimes \mathsf{V}\Big)\delta_{\mathsf{s_w}1} \\
&+\Big(\mathsf{g\_V\bar{f}f}(\bar{\mathsf{q}}_1, \mathsf{q}_2) \otimes \mathsf{f\_\bar{f}}(\bar{\mathsf{q}}_3) + \mathsf{f\_V\bar{f}}(\bar{\mathsf{q}}_1) \otimes \mathsf{g\_f\bar{f}}(\mathsf{q}_2, \bar{\mathsf{q}}_3)\Big)\delta_{\mathsf{s_w}2} \\
&+\Big(\mathsf{f\_\bar{f}}(\bar{\mathsf{q}}_1) \otimes \mathsf{g\_Vf\bar{f}}(\mathsf{q}_2, \bar{\mathsf{q}}_3) + \mathsf{g\_\bar{f}f}(\bar{\mathsf{q}}_1, \mathsf{q}_2) \otimes \mathsf{f\_V\bar{f}}(\bar{\mathsf{q}}_3)\Big)\delta_{\mathsf{s_w}3} \\
&+\Big(\mathsf{g\_\bar{f}f}(\bar{\mathsf{q}}_1, \mathsf{q}_2) \otimes \mathsf{f\_V\bar{f}}(\bar{\mathsf{q}}_3) + \mathsf{f\_\bar{f}f\bar{f}} \otimes \mathsf{V}\Big)\delta_{\mathsf{s_w}4}.
\end{aligned} \tag{4.3.31}$$

As can be seen in figure 4.11, the different values of s_w allow both s- and t-channel currents. However, the flavours of the quarks can be used to eliminate the contributions from one of these channels. As an example, if the off-shell quark is a top, and the on-shell quarks are bottom, top and top with $s_w = 1$, then it is clear that the t-channel contribution will vanish, since the line formed by $\bar{q}_1$ and q_2 will violate charge conservation.

Additional gluons are given by

$$\begin{aligned}
&\mathsf{f\_V\bar{f}f\bar{f}}(\bar{\mathsf{q}}_1, \mathsf{q}_2, \bar{\mathsf{q}}_3; \mathsf{n}_1, \mathsf{n}_2, \mathsf{n}_3, \mathsf{n}_4) = \\
&\quad \sum_{\mathsf{r}_1=1}^{\mathsf{n}_1} \mathsf{g\_}(\mathsf{r}_1) \otimes \mathsf{f\_V\bar{f}f\bar{f}}(\mathsf{n}_1 - \mathsf{r}_1, \mathsf{n}_2, \mathsf{n}_3, \mathsf{n}_4) \\
&\quad + \sum_{\mathsf{r}_4=0}^{\mathsf{n}_4-1} \mathsf{f\_V\bar{f}f\bar{f}}(\bar{\mathsf{q}}_1, \mathsf{q}_2, \bar{\mathsf{q}}_3; \mathsf{n}_1, \mathsf{n}_2, \mathsf{n}_3, \mathsf{r}_4) \otimes \mathsf{g\_}(\mathsf{n}_4 - \mathsf{r}_4) \\
&\quad + \big(\delta_{\mathsf{s_w}1} + \delta_{\mathsf{s_w}2}\big) \sum_{\mathsf{r}_2=0}^{\mathsf{n}_2} \mathsf{f\_V\bar{f}}(\bar{\mathsf{q}}_1, \mathsf{n}_1, \mathsf{r}_2) \otimes \mathsf{g\_f\bar{f}}(\mathsf{q}_2, \bar{\mathsf{q}}_3; \mathsf{n}_2 - \mathsf{r}_2, \mathsf{n}_3, \mathsf{n}_4) \\
&\quad + \big(\delta_{\mathsf{s_w}1} + \delta_{\mathsf{s_w}4}\big) \mathsf{f\_\bar{f}f\bar{f}}(\mathsf{n}_1, \mathsf{n}_2, \mathsf{n}_3, \mathsf{n}_4) \otimes \mathsf{V} \\
&\quad + \big(\delta_{\mathsf{s_w}3} + \delta_{\mathsf{s_w}4}\big) \sum_{\mathsf{r}_3=0}^{\mathsf{n}_3} \mathsf{g\_\bar{f}f}(\bar{\mathsf{q}}_1, \mathsf{q}_2; \mathsf{n}_1, \mathsf{n}_2, \mathsf{r}_3) \otimes \mathsf{f\_V\bar{f}}(\bar{\mathsf{q}}_3, \mathsf{n}_3 - \mathsf{r}_3, \mathsf{n}_4) \\
&\quad + \big(\delta_{\mathsf{s_w}2}\big) \sum_{\mathsf{r}_3=0}^{\mathsf{n}_3} \mathsf{g\_V\bar{f}f}(\bar{\mathsf{q}}_1, \mathsf{q}_2; \mathsf{n}_1, \mathsf{n}_2, \mathsf{r}_3) \otimes \mathsf{f\_\bar{f}}(\bar{\mathsf{q}}_3, \mathsf{n}_3 - \mathsf{r}_3, \mathsf{n}_4) \\
&\quad + \big(\delta_{\mathsf{s_w}3}\big) \sum_{\mathsf{r}_2=0}^{\mathsf{n}_2} \mathsf{f\_\bar{f}}(\bar{\mathsf{q}}_1, \mathsf{n}_1, \mathsf{r}_2) \otimes \mathsf{g\_Vf\bar{f}}(\mathsf{q}_2, \bar{\mathsf{q}}_3; \mathsf{n}_2 - \mathsf{r}_2, \mathsf{n}_3, \mathsf{n}_4).
\end{aligned} \tag{4.3.32}$$

The conjugate current $\mathsf{\bar{f}\_Vf\bar{f}f}$ can be defined analogously.

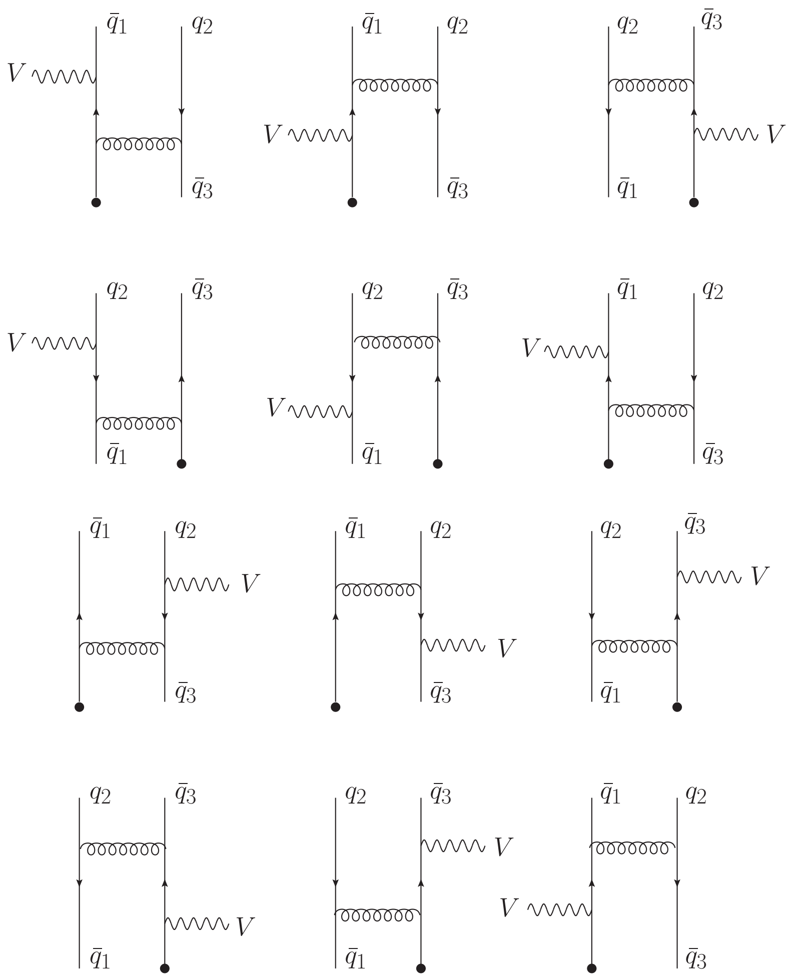

Figure 4.11: Current $\mathsf{f\_V\bar{f}f\bar{f}}(\mathsf{\bar{q}_1, q_2, \bar{q}_3; s_w; n_1, n_2, n_3, n_4})$, for $s_w = 1$ (top row), $s_w = 2$ (second row), $s_w = 3$ (third row) and $s_w = 4$ (bottom row).

$\mathsf{f\_V\bar{f}f\bar{f}_t}(\mathsf{\bar{q}_1, q_2, \bar{q}_3; s_w; n_1, n_2, n_3, n_4})$

This current is similar to the above, but in the t-channel, i.e. the two quark-antiquark lines are always made up of $\bar{q}_1$ and q_2, and the off-shell quark and $\bar{q}_3$. Note that for $s_w = 1$ and $s_w = 3$, this has the effect of keeping the electroweak boson on one side of the gluon propagator between the quark-antiquark lines. The skeleton is

$$\begin{aligned}\mathsf{f\_V\bar{f}f\bar{f}_t}(\mathsf{\bar{q}_1, q_2, \bar{q}_3}) =& \Big(\mathsf{f\_\bar{f}f\bar{f}_t} \otimes \mathsf{V}\Big)\delta_{\mathsf{s_w}1} + \Big(\mathsf{g\_V\bar{f}f}(\mathsf{\bar{q}_1, q_2}) \otimes \mathsf{f\_\bar{f}}(\mathsf{\bar{q}_3})\Big)\delta_{\mathsf{s_w}2} + \\ & \Big(\mathsf{g\_\bar{f}f}(\mathsf{\bar{q}_1, q_2}) \otimes \mathsf{f\_V\bar{f}}(\mathsf{\bar{q}_3})\Big)\delta_{\mathsf{s_w}3} + \\ & \Big(\mathsf{g\_\bar{f}f}(\mathsf{\bar{q}_1, q_2}) \otimes \mathsf{f\_V\bar{f}}(\mathsf{\bar{q}_3}) + \mathsf{f\_\bar{f}f\bar{f}_t} \otimes \mathsf{V}\Big)\delta_{\mathsf{s_w}4}.\end{aligned} \tag{4.3.33}$$

The recursion relation is

$$
\begin{aligned}
&\mathsf{f\_V\bar{f}f\bar{f}_t}(\bar{\mathsf{q}}_1, \mathsf{q}_2, \bar{\mathsf{q}}_3; \mathsf{n}_1, \mathsf{n}_2, \mathsf{n}_3, \mathsf{n}_4) = \\
&\qquad + \sum_{\mathsf{r}_1=1}^{\mathsf{n}_1} \mathsf{g\_}(\mathsf{r}_1) \otimes \mathsf{f\_V\bar{f}f\bar{f}_t}(\mathsf{n}_1 - \mathsf{r}_1, \mathsf{n}_2, \mathsf{n}_3, \mathsf{n}_4) \\
&\qquad + \sum_{\mathsf{r}_4=0}^{\mathsf{n}_4-1} \mathsf{f\_V\bar{f}f\bar{f}_t}(\bar{\mathsf{q}}_1, \mathsf{q}_2, \bar{\mathsf{q}}_3; \mathsf{n}_1, \mathsf{n}_2, \mathsf{n}_3, \mathsf{r}_4) \otimes \mathsf{g\_}(\mathsf{n}_4 - \mathsf{r}_4) \\
&\qquad + \big(\delta_{\mathsf{s_w}1} + \delta_{\mathsf{s_w}4}\big) \mathsf{f\_\bar{f}f\bar{f}_t}(\mathsf{n}_1, \mathsf{n}_2, \mathsf{n}_3, \mathsf{n}_4) \otimes \mathsf{V} \\
&\qquad + \big(\delta_{\mathsf{s_w}3} + \delta_{\mathsf{s_w}4}\big) \sum_{\mathsf{r}_3=0}^{\mathsf{n}_3} \mathsf{g\_\bar{f}f}(\bar{\mathsf{q}}_1, \mathsf{q}_2; \mathsf{n}_1, \mathsf{n}_2, \mathsf{r}_3) \otimes \mathsf{f\_V\bar{f}}(\bar{\mathsf{q}}_3, \mathsf{n}_3 - \mathsf{r}_3, \mathsf{n}_4) \\
&\qquad + \big(\delta_{\mathsf{s_w}2}\big) \sum_{\mathsf{r}_3=0}^{\mathsf{n}_3} \mathsf{g\_V\bar{f}f}(\bar{\mathsf{q}}_1, \mathsf{q}_2; \mathsf{n}_1, \mathsf{n}_2, \mathsf{r}_3) \otimes \mathsf{f\_\bar{f}}(\bar{\mathsf{q}}_3, \mathsf{n}_3 - \mathsf{r}_3, \mathsf{n}_4).
\end{aligned}
\tag{4.3.34}
$$

$\mathsf{g\_Vf_1\bar{f}_1f_2\bar{f}_2}(\mathsf{q}_1, \bar{\mathsf{q}}_2, \mathsf{q}_3, \bar{\mathsf{q}}_4; \mathsf{s_w})$

The skeleton of this current consists of an off-shell gluon and an on-shell EW boson with two quark-antiquark lines. Quark q_1 and antiquark $\bar{q}_2$ make up one of these lines, q_3 and $\bar{q}_4$ make up the other. This is achieved by using different flavours for these pairs. The argument s_w again gives the location of the EW boson: for our needs, it suffices to consider it either between q_1 and $\bar{q}_2$ (corresponding to $s_w = 2$) or between q_3 and $\bar{q}_4$ (corresponding to $s_w = 4$). Including other values of s_w would not be difficult but is not necessary for the calculations in this work. Similarly, it is not necessary to dress this current with on-shell gluons, so only the skeleton need be defined. It is

$$
\begin{aligned}
&\mathsf{g\_Vf\bar{f}f\bar{f}}(\mathsf{q}_1, \bar{\mathsf{q}}_2, \mathsf{q}_3, \bar{\mathsf{q}}_4; \mathsf{s_w}) = \\
&\Bigg(\mathsf{\bar{f}\_f}(\mathsf{q}_1) \otimes \mathsf{f\_V\bar{f}f\bar{f}}(\bar{\mathsf{q}}_2, \mathsf{q}_3, \bar{\mathsf{q}}_4; \mathsf{s_w} = 1) + \mathsf{\bar{f}\_Vf}(\mathsf{q}_1) \otimes \mathsf{f\_\bar{f}f\bar{f}}(\bar{\mathsf{q}}_2, \mathsf{q}_3, \bar{\mathsf{q}}_4) \\
&+ \mathsf{\bar{f}\_Vf\bar{f}f}(\mathsf{q}_1, \bar{\mathsf{q}}_2, \mathsf{q}_3; \mathsf{s_w} = 2) \otimes \mathsf{f\_\bar{f}}(\bar{\mathsf{q}}_4) + \mathsf{g\_Vf\bar{f}}(\mathsf{q}_1, \bar{\mathsf{q}}_2) \otimes \mathsf{g\_f\bar{f}}(\mathsf{q}_3, \bar{\mathsf{q}}_4)\Bigg) \delta_{\mathsf{s_w}2} \\
&+ \Bigg(\mathsf{\bar{f}\_f}(\mathsf{q}_1) \otimes \mathsf{f\_V\bar{f}f\bar{f}}(\bar{\mathsf{q}}_2, \mathsf{q}_3, \bar{\mathsf{q}}_4; \mathsf{s_w} = 3) + \mathsf{\bar{f}\_Vf\bar{f}f}(\mathsf{q}_1, \bar{\mathsf{q}}_2, \mathsf{q}_3; \mathsf{s_w} = 4) \otimes \mathsf{f\_\bar{f}}(\bar{\mathsf{q}}_4) \\
&+ \mathsf{\bar{f}\_f\bar{f}f}(\mathsf{q}_1, \bar{\mathsf{q}}_2, \mathsf{q}_3) \otimes \mathsf{f\_V\bar{f}}(\bar{\mathsf{q}}_4) + \mathsf{g\_f\bar{f}}(\mathsf{q}_1, \bar{\mathsf{q}}_2) \otimes \mathsf{g\_Vf\bar{f}}(\mathsf{q}_3, \bar{\mathsf{q}}_4)\Bigg) \delta_{\mathsf{s_w}4}.
\end{aligned}
\tag{4.3.35}
$$

Diagrammatically, this current would look like figure 4.7 dressed with an electroweak boson either between q_1 and $\bar{q}_2$ (if $s_w = 2$) or between q_3 and $\bar{q}_4$ (if $s_w = 4$).

$\mathsf{g\_Vf\bar{f}f\bar{f}\_1}(\mathsf{q}_1, \bar{\mathsf{q}}_2, \mathsf{q}_3, \bar{\mathsf{q}}_4)$

This current is similar to the one above, but with some unusual restrictions. If one of the quark-antiquark lines is made up of q_1 and $\bar{q}_2$, then the EW boson will attach to this line only. On the other hand, if one of the quark-antiquark lines is made up of q_1 and $\bar{q}_4$, the the EW boson attaches to this one only, with the additional restriction that it is always on one side of the gluon propagator: the gluon propagator should be between the EW boson and $\bar{q}_4$. The flavours of the quarks should always be such that only one of these options is realised. This unusual configuration is shown in figure 4.12. Again, the addition of on-shell gluons will not be described, but, as for the previous current, making these extensions would not be difficult.

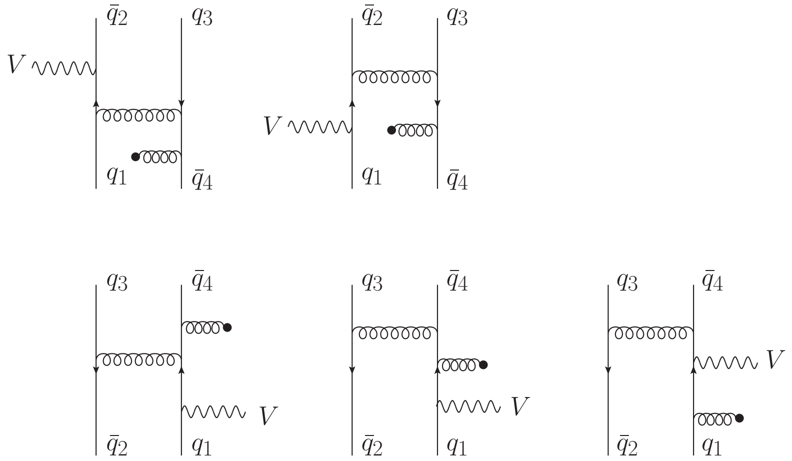

Figure 4.12: Current $\mathsf{g\_Vf\bar{f}f\bar{f}\_1}(\mathsf{q}_1, \bar{\mathsf{q}}_2, \mathsf{q}_3, \bar{\mathsf{q}}_4)$. The quark flavours are such that either the top or bottom row, not both, contribute to the current.

$$\begin{aligned}
&\mathsf{g\_Vf\bar{f}f\bar{f}\_1}(\mathsf{q}_1, \bar{\mathsf{q}}_2, \mathsf{q}_3, \bar{\mathsf{q}}_4) = \\
&\qquad \mathsf{\bar{f}\_f}(\mathsf{q}_1) \otimes \mathsf{f\_V\bar{f}f\bar{f}_t}(\bar{\mathsf{q}}_2, \mathsf{q}_3, \bar{\mathsf{q}}_4; \mathsf{s_w} = 1) + \mathsf{\bar{f}\_Vf}(\mathsf{q}_1) \otimes \mathsf{f\_\bar{f}f\bar{f}_t}(\bar{\mathsf{q}}_2, \mathsf{q}_3, \bar{\mathsf{q}}_4) \\
&\qquad + \mathsf{\bar{f}\_Vf\bar{f}f}(\mathsf{q}_1, \bar{\mathsf{q}}_2, \mathsf{q}_3; \mathsf{s_w} = 2) \otimes \mathsf{f\_\bar{f}}(\bar{\mathsf{q}}_4).
\end{aligned} \tag{4.3.36}$$

Note that in the final term, the flavours of the quarks determine the formation of the quark-antiquark lines.

$\underline{\mathsf{f_1\_V\bar{f}_1f_2\bar{f}_2f_3\bar{f}_3}(\bar{\mathsf{q}}_1, \mathsf{q}_2, \bar{\mathsf{q}}_3, \mathsf{q}_4, \bar{\mathsf{q}}_5; \mathsf{s_w})}$

The skeleton of this current includes three quark-antiquark lines and an EW boson. The position of the boson is determined by s_w, and the quark-antiquark lines are formed by the off-shell quark and $\bar{q}_1$, q_2 and $\bar{q}_3$, and q_4 and $\bar{q}_5$. The skeleton is given by

$$
\begin{aligned}
&\mathsf{f_1\_V\bar{f}_1f_2\bar{f}_2f_3\bar{f}_3(\bar{q}_1, q_2, \bar{q}_3, q_4, \bar{q}_5; s_w)} = \\
&\qquad\Big(\mathsf{f_1\_\bar{f}_1f_2\bar{f}_2f_3\bar{f}_3} \otimes \mathsf{V} + \mathsf{f\_V\bar{f}(\bar{q}_1)} \otimes \mathsf{g\_f_1\bar{f}_1f_2\bar{f}_2(q_2, \bar{q}_3, q_4, \bar{q}_5)} \\
&\qquad+\mathsf{f\_V\bar{f}f\bar{f}(\bar{q}_1, q_2, \bar{q}_3; s_w = 1)} \otimes \mathsf{g\_f\bar{f}(q_4, \bar{q}_5)}\Big)\delta_{\mathsf{s_w1}} \\
&\qquad+\Big(\mathsf{f\_\bar{f}(\bar{q}_1)} \otimes \mathsf{g\_Vf_1\bar{f}_1f_2\bar{f}_2(q_2, \bar{q}_3, q_4, \bar{q}_5; s_w = 2)} \\
&\qquad+\mathsf{f\_V\bar{f}f\bar{f}(\bar{q}_1, q_2, \bar{q}_3; s_w = 3)} \otimes \mathsf{g\_f\bar{f}(q_4, \bar{q}_5)}\Big)\delta_{\mathsf{s_w2}} \\
&\qquad+\Big(\mathsf{f\_\bar{f}(\bar{q}_1)} \otimes \mathsf{g\_Vf_1\bar{f}_1f_2\bar{f}_2(q_2, \bar{q}_3, q_4, \bar{q}_5; s_w = 4)} \\
&\qquad+\mathsf{f\_\bar{f}f\bar{f}_s(\bar{q}_1, q_2, \bar{q}_3)} \otimes \mathsf{g\_Vf\bar{f}(q_4, \bar{q}_5)}\Big)\delta_{\mathsf{s_w3}}.
\end{aligned}
\tag{4.3.37}
$$

Diagrammatically, this is the same as in figure 4.8, but with EW bosons at all insertions between $\bar{q}_1$ and q_2 (for $s_w = 1$), q_2 and $\bar{q}_3$ (for $s_w = 2$), or q_4 and $\bar{q}_5$ (for $s_w = 3$).

$\underline{\mathsf{f_1\_V\bar{f}_1f_2\bar{f}_3f_3\bar{f}_2(\bar{q}_1, q_2, \bar{q}_3, q_4, \bar{q}_5; s_w)}}$

This current is the same as the above, but with quark-antiquark lines being formed from q_2 and $\bar{q}_5$ and q_4 and $\bar{q}_3$. The skeleton is

$$
\begin{aligned}
&\mathsf{f_1\_V\bar{f}_1f_2\bar{f}_3f_3\bar{f}_2(\bar{q}_1, q_2, \bar{q}_3, q_4, \bar{q}_5; s_w)} = \\
&\qquad\Big(\mathsf{f_1\_\bar{f}_1f_2\bar{f}_3f_3\bar{f}_2} \otimes \mathsf{V} + \mathsf{f\_V\bar{f}(\bar{q}_1)} \otimes \mathsf{g\_f_1\bar{f}_2f_2\bar{f}_1(q_2, \bar{q}_3, q_4, \bar{q}_5)}\Big)\delta_{\mathsf{s_w1}} \\
&\qquad\Big(\mathsf{f\_\bar{f}(\bar{q}_1)} \otimes \mathsf{g\_Vf_1\bar{f}_2f_2\bar{f}_1(q_2, \bar{q}_3, q_4, \bar{q}_5; s_w = 2)}\Big)\delta_{\mathsf{s_w2}} \\
&\qquad\Big(\mathsf{f\_\bar{f}(\bar{q}_1)} \otimes \mathsf{g\_Vf_1\bar{f}_2f_2\bar{f}_1(q_2, \bar{q}_3, q_4, \bar{q}_5; s_w = 4)}\Big)\delta_{\mathsf{s_w3}}.
\end{aligned}
\tag{4.3.38}
$$

Diagrammatically, this current is the same as depicted on the bottom row of figure 4.9, with EW bosons at all insertions between the off-shell quark and $\bar{q}_1$ for $s_w = 1$, between q_2 and $\bar{q}_3$ for $s_w = 2$, and between q_4 and $\bar{q}_5$ (for $s_w = 3$).

$\underline{\mathsf{f_1\_V\bar{f}_2f_2\bar{f}_1f_3\bar{f}_3(\bar{q}_1, q_2, \bar{q}_3, q_4, \bar{q}_5; s_w)}}$

In this current the quark-antiquark lines are formed from q_2 and $\bar{q}_1$, q_4 and $\bar{q}_5$ and the off-shell quark and $\bar{q}_3$.

$$
\begin{aligned}
&\mathsf{f_1\_V\bar{f}_2f_2\bar{f}_1f_3\bar{f}_3(\bar{q}_1, q_2, \bar{q}_3, q_4, \bar{q}_5; s_w)} = \\
&\qquad\Big(\mathsf{f_1\_\bar{f}_2f_2\bar{f}_1f_3\bar{f}_3} \otimes \mathsf{V} + \mathsf{f\_V\bar{f}f\bar{f}_t(\bar{q}_1, q_2, \bar{q}_3; s_w = 1)} \otimes \mathsf{g\_f\bar{f}(q_4, \bar{q}_5)}\Big)\delta_{\mathsf{s_w1}} \\
&\qquad\Big(\mathsf{g\_\bar{f}f(\bar{q}_1, q_2)} \otimes \mathsf{f\_V\bar{f}f\bar{f}(\bar{q}_3, q_4, \bar{q}_5; s_w = 3)} \\
&\qquad+\mathsf{f\_\bar{f}f\bar{f}_t(\bar{q}_1, q_2, \bar{q}_3)} \otimes \mathsf{g\_Vf\bar{f}(q_4, \bar{q}_5)}\Big)\delta_{\mathsf{s_w3}}.
\end{aligned}
\tag{4.3.39}
$$

Diagrammatically, this current is the same as the top row of figure 4.9, with the same insertions of EW bosons as described in the previous current. Note that in the above relations, it is important to specify the flavours such that none of the currents used to build up the skeleton give contributions with the wrong quark and antiquark fields joined to a single line. This can be done by specifying a different flavour for each quark-antiquark line (these are merely labels and do not need to correspond to actual flavours). For example, in the first $s_w = 3$ term in equation (4.3.39), the t-channel terms in the current $\mathsf{f\_V\bar{f}f\bar{f}}$ should vanish, meaning that the flavours of $\bar{q}_3$ and q_4 should be different.

4.3.3 Currents with two electroweak bosons

$\underline{\mathsf{f\_VV\bar{f}}(\bar{\mathsf{q}}_2; \mathsf{n}_1, \mathsf{n}_2)}$

Although the ordering of the electroweak bosons with respect to the coloured particles is not fixed, they do need to be fixed with respect to one another. This is because the order of opposite-sign W-bosons in an amplitude is fixed by the flavours of the initial state quarks (see sections 6.2 and 6.3), and the amplitudes are computed using Berends-Giele currents. For this reason, the electroweak bosons are labeled V_1 and V_2. The skeleton of this current is

$$\mathsf{f\_VV\bar{f}}(\bar{\mathsf{q}}_2, \mathsf{V}_1, \mathsf{V}_2) = \mathsf{f\_V\bar{f}}(\bar{\mathsf{q}}_2, \mathsf{V}_2) \otimes \mathsf{V}_1, \tag{4.3.40}$$

with the recursion relation

$$\begin{aligned} \mathsf{f\_VV\bar{f}}(\mathsf{n}_1, \mathsf{n}_2) =& \sum_{\mathsf{r}_1=1}^{\mathsf{n}_1} \mathsf{g\_}(\mathsf{r}_1) \otimes \mathsf{f\_VV\bar{f}}(\mathsf{n}_1 - \mathsf{r}_1, \mathsf{n}_2) + \mathsf{f\_V\bar{f}}(\bar{\mathsf{q}}_2, \mathsf{V}_2; \mathsf{n}_1, \mathsf{n}_2) \otimes \mathsf{V}_1 \\ &+ \sum_{\mathsf{r}_2=0}^{\mathsf{n}_2-1} \mathsf{f\_VV\bar{f}}(\mathsf{n}_1, \mathsf{r}_2) \otimes \mathsf{g\_}(\mathsf{n}_2 - \mathsf{r}_2). \end{aligned} \tag{4.3.41}$$

The conjugate current $\mathsf{\bar{f}\_VVf}$ can also be defined as previously.

$\underline{\mathsf{f\_VV\bar{f}}^*(\bar{\mathsf{q}}_2; \mathsf{n}, \mathsf{f}_\mathsf{p}, \mathsf{f}_\mathsf{g})}$

This "restricted" current is the analogue of $\mathsf{f\_V\bar{f}}^*(\bar{\mathsf{q}}_2)$ with two electroweak bosons. The electroweak bosons can be both after the reference gluon ($f_g = f_p$), or both before ($f_g = f_p - 2$), or one before and one after ($f_g = f_p - 1$). The skeleton is the same as for $\mathsf{f\_VV\bar{f}}(\bar{\mathsf{q}}_2; \mathsf{n}_1, \mathsf{n}_2)$, with additional gluons added by

$$\begin{aligned}
\mathsf{f\_VV\bar{f}}^*(\bar{\mathsf{q}}_1; \mathsf{n}, \mathsf{f_p}, \mathsf{f_g}) = \delta_{\mathsf{f_p},\mathsf{f_g}} \Big(& \sum_{\mathsf{r}_1=1}^{\mathsf{f_g}-1} \mathsf{g\_}(\mathsf{r}_1) \otimes \mathsf{f\_VV\bar{f}}^*(\mathsf{n}-\mathsf{r}_1, \mathsf{f_p}-\mathsf{r}_1, \mathsf{f_g}-\mathsf{r}_1) \\
& + \sum_{\mathsf{r}_1=\mathsf{f_g}}^{\mathsf{n}} \mathsf{g\_}(\mathsf{r}_1) \otimes \mathsf{f\_VV\bar{f}}(\mathsf{n}-\mathsf{r}_1, 0) \Big) \\
& + \delta_{\mathsf{f_p}-1,\mathsf{f_g}} \Big(\mathsf{f\_V\bar{f}}(\mathsf{n}, 0) \otimes \mathsf{V} + \sum_{\mathsf{r}_1=1}^{\mathsf{f_g}-1} \mathsf{g\_}(\mathsf{r}_1) \otimes \mathsf{f\_VV\bar{f}}^*(\mathsf{n}-\mathsf{r}_1, \mathsf{f_p}-\mathsf{r}_1, \mathsf{f_g}-\mathsf{r}_1) \Big) \\
& + \delta_{\mathsf{f_p}-2,\mathsf{f_g}} \Big(\mathsf{f\_V\bar{f}}^*(\mathsf{n}, \mathsf{f_p}-1, \mathsf{f_g}) \otimes \mathsf{V} \\
& + \sum_{\mathsf{r}_1=1}^{\mathsf{f_g}-1} \mathsf{g\_}(\mathsf{r}_1) \otimes \mathsf{f\_VV\bar{f}}^*(\mathsf{n}-\mathsf{r}_1, \mathsf{f_p}-\mathsf{r}_1, \mathsf{f_g}-\mathsf{r}_1) \Big).
\end{aligned} \tag{4.3.42}$$

$\underline{\mathsf{g\_VVf\bar{f}}(\mathsf{q}_1, \bar{\mathsf{q}}_2, \mathsf{V}_1, \mathsf{V}_2; \mathsf{n}_1, \mathsf{n}_2, \mathsf{n}_3)}$
The skeleton for this current is

$$\begin{aligned}
\mathsf{g\_Vf\bar{f}}(\mathsf{q}_1, \bar{\mathsf{q}}_2) = & \mathsf{\bar{f}\_VVf}(\mathsf{q}_1, \mathsf{V}_2, \mathsf{V}_1) \otimes \mathsf{f\_\bar{f}}(\bar{\mathsf{q}}_2) + \mathsf{\bar{f}\_f}(\mathsf{q}_1) \otimes \mathsf{f\_VV\bar{f}}(\bar{\mathsf{q}}_2, \mathsf{V}_1, \mathsf{V}_2) \\
& + \mathsf{\bar{f}\_Vf}(\mathsf{q}_1, \mathsf{V}_1) \otimes \mathsf{f\_V\bar{f}}(\bar{\mathsf{q}}_2, \mathsf{V}_2).
\end{aligned} \tag{4.3.43}$$

The recursion relation is similar to those for $\mathsf{g\_f\bar{f}}$ and $\mathsf{g\_Vf\bar{f}}$:

$$\begin{aligned}
& \mathsf{g\_VVf\bar{f}}(\mathsf{q}_1, \bar{\mathsf{q}}_2, \mathsf{V}_1, \mathsf{V}_2; \mathsf{n}_1, \mathsf{n}_2, \mathsf{n}_3) = \\
& \sum_{\mathsf{r}_1=1}^{\mathsf{n}_1} \big(\mathsf{g\_}(\mathsf{r}_1) \otimes \mathsf{g\_VVf\bar{f}}(\mathsf{n}_1-\mathsf{r}_1, \mathsf{n}_2, \mathsf{n}_3) + \sum_{\mathsf{r}_3=0}^{\mathsf{n}_3-1} \mathsf{g\_VVf\bar{f}}(\mathsf{n}_1, \mathsf{n}_2, \mathsf{r}_3) \otimes \mathsf{g\_}(\mathsf{n}_3-\mathsf{r}_3) \big) \\
& + \sum_{\mathsf{r}_1=1}^{\mathsf{n}_1-1} \sum_{\mathsf{r}_2=\mathsf{r}_1+1}^{\mathsf{n}_1} \mathsf{g\_}(\mathsf{r}_1) \otimes \mathsf{g\_}(\mathsf{r}_2-\mathsf{r}_1) \otimes \mathsf{g\_VVf\bar{f}}(\mathsf{n}_1-\mathsf{r}_2, \mathsf{n}_2, \mathsf{n}_3) \\
& + \sum_{\mathsf{r}_1=1}^{\mathsf{n}_1} \sum_{\mathsf{r}_3=0}^{\mathsf{n}_3-1} \mathsf{g\_}(\mathsf{r}_1) \otimes \mathsf{g\_VVf\bar{f}}(\mathsf{n}_1-\mathsf{r}_1, \mathsf{n}_2, \mathsf{r}_3) \otimes \mathsf{g\_}(\mathsf{n}_3-\mathsf{r}_3) \\
& + \sum_{\mathsf{r}_3=0}^{\mathsf{n}_3-2} \sum_{\mathsf{r}_4=\mathsf{r}_3+1}^{\mathsf{n}_3-1} \mathsf{g\_VVf\bar{f}}(\mathsf{n}_1, \mathsf{n}_2, \mathsf{r}_3) \otimes \mathsf{g\_}(\mathsf{r}_4-\mathsf{r}_3) \otimes \mathsf{g\_}(\mathsf{n}_3-\mathsf{r}_4) \\
& + \sum_{\mathsf{r}_2=0}^{\mathsf{n}_2} \big(\mathsf{\bar{f}\_VVf}(\mathsf{q}_1, \mathsf{V}_2, \mathsf{V}_1; \mathsf{n}_1, \mathsf{r}_2) \otimes \mathsf{f\_\bar{f}}(\bar{\mathsf{q}}_2; \mathsf{n}_2-\mathsf{r}_2, \mathsf{n}_3) + \\
& + \mathsf{\bar{f}\_Vf}(\mathsf{q}_1, \mathsf{V}_1; \mathsf{n}_1, \mathsf{r}_2) \otimes \mathsf{f\_V\bar{f}}(\bar{\mathsf{q}}_2, \mathsf{V}_2; \mathsf{n}_2-\mathsf{r}_2, \mathsf{n}_3) \\
& + \mathsf{\bar{f}\_f}(\mathsf{q}_1; \mathsf{n}_1, \mathsf{r}_2) \otimes \mathsf{f\_VV\bar{f}}(\bar{\mathsf{q}}_2, \mathsf{V}_1, \mathsf{V}_2; \mathsf{n}_2-\mathsf{r}_2, \mathsf{n}_3) \Big).
\end{aligned} \tag{4.3.44}$$

$\underline{\mathsf{f\_VV\bar{f}f\bar{f}}(\bar{\mathsf{q}}_1, \mathsf{q}_2, \bar{\mathsf{q}}_3, \mathsf{V}_1, \mathsf{V}_2; \mathsf{s_w}; \mathsf{n}_1, \mathsf{n}_2, \mathsf{n}_3, \mathsf{n}_4)}$

The skeleton of this current consists of two quark-antiquark lines and two EW bosons. Only the s-channel contributes: the off-shell quark and $\bar{q}_1$ make up one quark-antiquark line, q_2 and $\bar{q}_3$ make up the other. The argument s_w again defines the location of the electroweak pair. The skeleton is

$$\begin{aligned}
&\mathsf{f\_VV\bar{f}f\bar{f}}(\bar{\mathsf{q}}_1, \mathsf{q}_2, \bar{\mathsf{q}}_3, \mathsf{V}_1, \mathsf{V}_2) = \\
&\qquad \left(\mathsf{f\_VV\bar{f}}(\bar{\mathsf{q}}_1, \mathsf{V}_1, \mathsf{V}_2) \otimes \mathsf{g\_f\bar{f}}(\mathsf{q}_2, \bar{\mathsf{q}}_3) + \mathsf{f\_V\bar{f}f\bar{f}}(\mathsf{V}_2; \mathsf{s_w} = 1) \otimes \mathsf{V}_1\right)\delta_{\mathsf{s_w}1} + \\
&\qquad \left(\mathsf{f\_V\bar{f}}(\bar{\mathsf{q}}_1, \mathsf{V}_2) \otimes \mathsf{g\_Vf\bar{f}}(\mathsf{q}_2, \bar{\mathsf{q}}_3, \mathsf{V}_1) + \mathsf{f\_V\bar{f}f\bar{f}}(\mathsf{V}_1; \mathsf{s_w} = 3) \otimes \mathsf{V}_2\right)\delta_{\mathsf{s_w}2} + \\
&\qquad \left(\mathsf{f\_\bar{f}}(\bar{\mathsf{q}}_1) \otimes \mathsf{g\_VVf\bar{f}}(\mathsf{q}_2, \bar{\mathsf{q}}_3, \mathsf{V}_1, \mathsf{V}_2)\right)\delta_{\mathsf{s_w}3}.
\end{aligned} \tag{4.3.45}$$

The skeleton is shown in figure 4.13. Again, the flavours are chosen such that the t-channel contributions of $\mathsf{f\_V\bar{f}f\bar{f}}$ vanish.

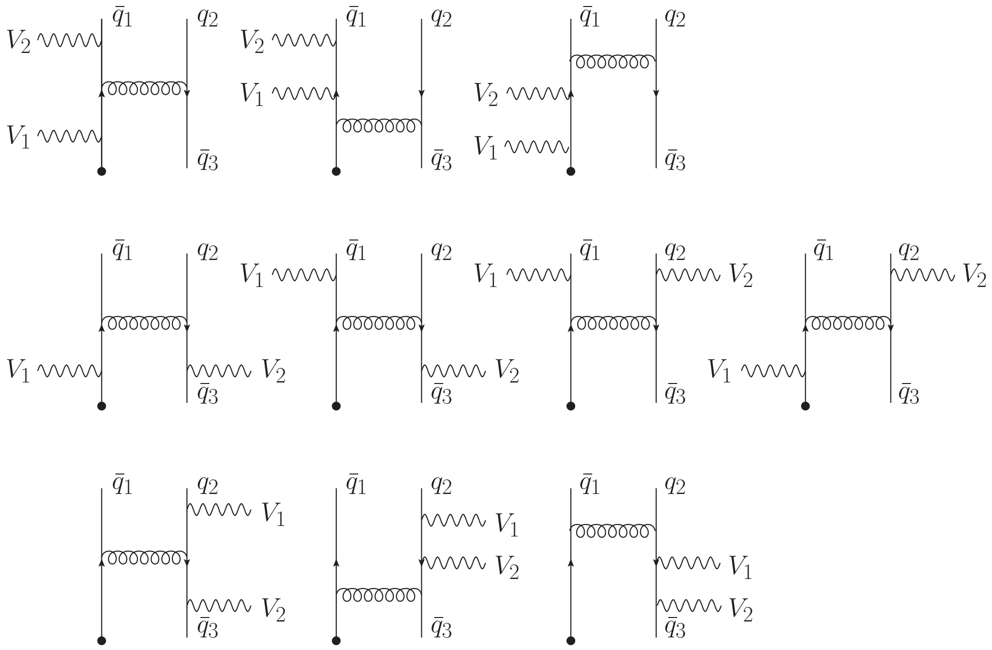

Figure 4.13: Current $\mathsf{f\_VV\bar{f}f\bar{f}}(\bar{\mathsf{q}}_1, \mathsf{q}_2, \bar{\mathsf{q}}_3, \mathsf{V}_1, \mathsf{V}_2; \mathsf{s_w}; \mathsf{n}_1, \mathsf{n}_2, \mathsf{n}_3, \mathsf{n}_4)$, with $s_w = 1$ shown on the top row, $s_w = 2$ on the middle row, and $s_w = 3$ on the bottom row.

On-shell gluons are added by the recursion relation

$$
\begin{aligned}
&\mathsf{f\_VV\bar{f}f\bar{f}}(\mathsf{\bar{q}_1, q_2, \bar{q}_3, V_1, V_2; n_1, n_2, n_3, n_4}) = \\
&\qquad \sum_{\mathsf{r_1=1}}^{\mathsf{n_1}} \mathsf{g\_(r_1)} \otimes \mathsf{f\_VV\bar{f}f\bar{f}(n_1 - r_1, n_2, n_3, n_4)} + \\
&\qquad + \sum_{\mathsf{r_4=0}}^{\mathsf{n_4-1}} \mathsf{f\_VV\bar{f}f\bar{f}(\bar{q}_1, q_2, \bar{q}_3; n_1, n_2, n_3, r_4)} \otimes \mathsf{g\_(n_4 - r_4)} \\
&\qquad + \Bigg(\sum_{\mathsf{r_2=0}}^{\mathsf{n_2}} \mathsf{f\_VV\bar{f}(\bar{q}_1, V_1, V_2; n_1, r_2)} \otimes \mathsf{g\_f\bar{f}(q_2, \bar{q}_3; n_2 - r_2, n_3, n_4)} \\
&\qquad + \mathsf{f\_V\bar{f}f\bar{f}(V_2; s_w = 1; n_1, n_2, n_3, n_4)} \otimes \mathsf{V_1} \Bigg) \delta_{\mathsf{s_w 1}} + \\
&\qquad + \Bigg(\sum_{\mathsf{r_2=0}}^{\mathsf{n_2}} \mathsf{f\_V\bar{f}(\bar{q}_1, V_2; n_1, r_2)} \otimes \mathsf{g\_Vf\bar{f}(q_2, \bar{q}_3, V_1; n_2 - r_2, n_3, n_4)} \\
&\qquad + \mathsf{f\_V\bar{f}f\bar{f}(V_1; s_w = 3; n_1, n_2, n_3, n_4)} \otimes \mathsf{V_2} \Bigg) \delta_{\mathsf{s_w 2}} + \\
&\qquad \Bigg(\sum_{\mathsf{r_2=0}}^{\mathsf{n_2}} \mathsf{f\_\bar{f}(\bar{q}_1; n_1, r_2)} \otimes \mathsf{g\_VVf\bar{f}(q_2, \bar{q}_3, V_1, V_2; n_2 - r_2, n_3, n_4)} \Bigg) \delta_{\mathsf{s_w 3}}.
\end{aligned}
\tag{4.3.46}
$$

Similarly, the conjugate current $\mathsf{\bar{f}\_VVf\bar{f}f}$ can be defined.

$\underline{\mathsf{f\_VV\bar{f}f\bar{f}\_1(\bar{q}_1, q_2, \bar{q}_3, V_1, V_2; s_w)}}$
This is similar to the previous current, but in the t-channel, and with the EW bosons fixed with respect to the gluon propagator between the quark-antiquark lines. The skeleton is

$$
\begin{aligned}
\mathsf{f\_VV\bar{f}f\bar{f}\_1(\bar{q}_1, q_2, \bar{q}_3, V_1, V_2; s_w)} = &\Big(\mathsf{f\_V\bar{f}f\bar{f}_t(V_2; s_w = 1)} \otimes \mathsf{V_1} \Big) \delta_{\mathsf{s_w 1}} + \\
&\Big(\mathsf{g\_VV\bar{f}f(\bar{q}_1, q_2, V_1, V_2)} \otimes \mathsf{f\_\bar{f}(\bar{q}_3)} \Big) \delta_{\mathsf{s_w 2}} + \\
&\Big(\mathsf{f\_V\bar{f}f\bar{f}_t(V_2; s_w = 3)} \otimes \mathsf{V_1} \Big) \delta_{\mathsf{s_w 3}} \\
&\Big(\mathsf{f\_V\bar{f}f\bar{f}(V_1; s_w = 2)} \otimes \mathsf{V_2} \Big) \delta_{\mathsf{s_w 4}}.
\end{aligned}
\tag{4.3.47}
$$

For this work, on-shell gluons are not necessary in this current. The skeleton is shown in figure 4.14.

$\underline{\mathsf{g\_VVf_1\bar{f}_1f_2\bar{f}_2(q_1, \bar{q}_2, q_3, \bar{q}_4, V_1, V_2; s_w)}}$
This current consists of an off-shell gluon with two quark-antiquark lines and two EW bosons making up the skeleton. The two quark-antiquark lines are made up from q_1

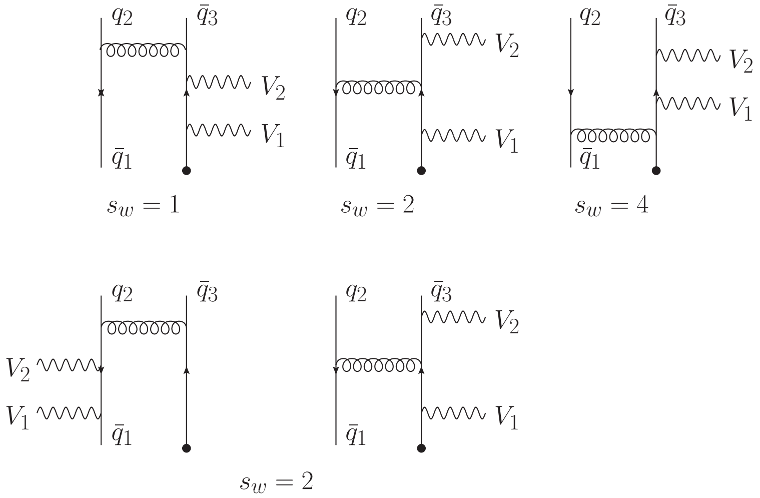

Figure 4.14: Current $\mathsf{f\_VV\bar{f}f\bar{f}\_1(\bar{q}_1, q_2, \bar{q}_3, V_1, V_2; s_w)}$ with $s_w = 1, s_w = 3$ and $s_w = 4$ shown on the top row, and $s_w = 2$ on the bottom row.

and $\bar{q}_2$, and q_3 and $\bar{q}_4$. Only the skeleton need be defined:

$$
\begin{aligned}
&\mathsf{g\_VVf_1\bar{f}_1f_2\bar{f}_2(q_1, \bar{q}_2, q_3, \bar{q}_4, V_1, V_2; s_w)} = \\
&\quad\Big(\mathsf{\bar{f}\_f(q_1)} \otimes \mathsf{f\_VV\bar{f}f\bar{f}(\bar{q}_2, q_3, \bar{q}_4; s_w = 1)} + \mathsf{\bar{f}\_Vf(q_1, V_1)} \otimes \mathsf{f\_V\bar{f}f\bar{f}(\bar{q}_2, q_3, \bar{q}_4, V_2; s_w = 1)} \\
&\quad+\mathsf{\bar{f}\_VVf(q_1)} \otimes \mathsf{f\_\bar{f}f\bar{f}_s(\bar{q}_2, q_3, \bar{q}_4)} + \mathsf{\bar{f}\_VVf\bar{f}f(q_1, \bar{q}_2, q_3, V_1, V_2; s_w = 2)} \otimes \mathsf{f\_\bar{f}(\bar{q}_4)} \\
&\quad+\mathsf{g\_VVf\bar{f}(q_1, \bar{q}_2)} \otimes \mathsf{g\_f\bar{f}(q_3, \bar{q}_4)}\Big)\delta_{\mathsf{s_w}2} \\
&\quad+\Big(\mathsf{\bar{f}\_f(q_1)} \otimes \mathsf{f\_VV\bar{f}f\bar{f}(\bar{q}_2, q_3, \bar{q}_4; s_w = 3)} + \mathsf{\bar{f}\_f\bar{f}f_s(q_1, \bar{q}_2, q_3)} \otimes \mathsf{f\_VV\bar{f}(\bar{q}_4)} \\
&\quad+\mathsf{\bar{f}\_Vf\bar{f}f(q_1, \bar{q}_2, q_3, V_1; s_w = 4)} \otimes \mathsf{f\_V\bar{f}(\bar{q}_4, V_2)}+ \\
&\quad+\mathsf{\bar{f}\_VVf\bar{f}f(q_1, \bar{q}_2, q_3; s_w = 4)} \otimes \mathsf{f\_\bar{f}(\bar{q}_4)} + \mathsf{g\_f\bar{f}(q_1, \bar{q}_2)} \otimes \mathsf{g\_VVf\bar{f}(q_3, \bar{q}_4)}\Big)\delta_{\mathsf{s_w}4}.
\end{aligned}
\tag{4.3.48}
$$

This can be visualised as the s-channel of the $\mathsf{g\_f_1\bar{f}_1f_2\bar{f}_2(q_1, \bar{q}_2, q_3, \bar{q}_4; n_1, n_2, n_3, n_4, n_5)}$ current (on the top line of figure 4.7) with all insertions for the two EW bosons on the $q_1\bar{q}_2$ line for $s_w = 2$, and on the $q_3\bar{q}_4$ line for $s_w = 4$.

Chapter 5

Hadroproduction of W^+W^+jj

5.1 Introduction

In this chapter, I will describe the application of the techniques discussed in the previous three chapters to the next-to-leading order QCD calculation of the production of a pair of W^+ bosons in association with two jets at the Large Hadron Collider (LHC). This chapter will largely follow ref. [77]. I consider leptonic decays of the W-bosons, so that the experimental signature is two charged leptons of the same sign, two jets, and missing energy from the neutrinos. As will be seen, the cross-section for this process is quite small, only a few femtobarns. Nevertheless, the distinctive signature should make it readily detectable once sufficient data have been been accumulated at the LHC, as there is very little background to this process.

The presence of two like-charged W-bosons places restrictions on the flavour structure of the amplitudes, as described in section 5.2. These restrictions allow the requirement of two observed jets to be lifted without the cross-section diverging. This unusual situation allows the production of a W^+-pair to be studied in association with zero, one, two, or more jets. Furthermore, it allows a relatively straightforward implementation in the next-to-leading order parton showering program `POWHEG` [148], the first $2 \to 4$ process to be implemented in such a program.

The production of $W^+W^+ + 2$ jets can proceed through electroweak (EW) or QCD mechanisms. At leading order in QCD, the former includes couplings α_{EW}^4, while the latter includes couplings $\alpha_s^2\alpha_{EW}^2$. In spite of this and the relative sizes of the strong and electroweak couplings, the cross-section of the QCD production is only about 50% larger than that of the electroweak production [149]. The NLO QCD corrections to the latter have been calculated [150]. The colour factor for the interference between the two mechanisms vanishes at leading order, but interference does occur at next-to-leading order. However, the interference term is subleading in colour, and furthermore vanishes unless all quarks involved in the interaction have the same flavour. The interference is therefore highly suppressed, and will be neglected entirely in this work, with only the QCD mechanism considered.

Finally, this process is also interesting as a background to the study of double parton scattering [149, 151–153], or to exotic Beyond the Standard Model (BSM) processes, such as R-parity violating supersymmetry [154], diquark prodution followed by decay to $t\bar{t}$ pairs [155], or doubly-charged Higgs production [156, 157]. Viewed as either a signal or a background, an accurate theoretical description of this process is desirable. As discussed in the Introduction, this necessitates a computation of the cross-sections and distributions to NLO in QCD.

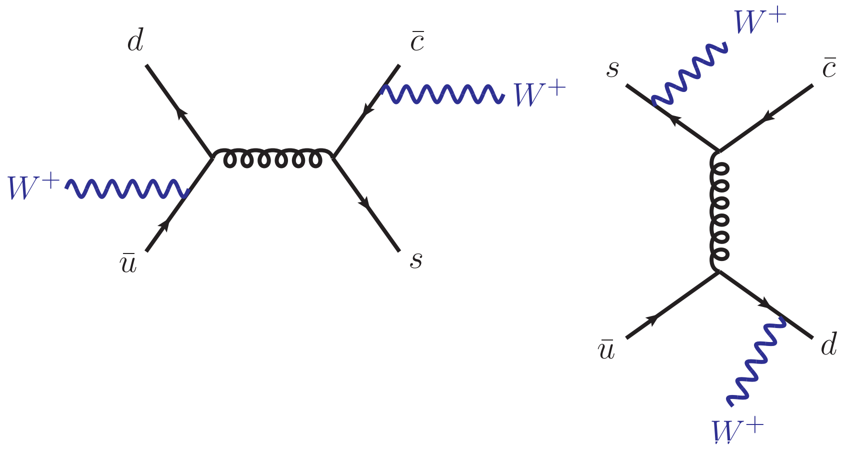

Figure 5.1: Sample Feynman diagrams for amplitudes $A_0(\bar{u}, d, \bar{c}, s)$, which occurs through the s-channel (left), and $A^0(\bar{u}, s, \bar{c}, d)$, which occurs through the t-channel (right).

5.2 Leading order amplitudes

I begin by describing the leading order calculation of the hadroproduction of $W^+W^+ +$ 2 jets. Any hadronic process with two final state jets involves two initial and two final state partons. Charge conservation with a W^+-pair means that these must consist of two quark-antiquark pairs, with a single W-boson radiated off each quark-antiquark line. The partonic amplitudes are thus $0 \to \bar{q}_1 q_2 \bar{q}_3 q_4 + W^+(\to \nu_e + e^+) + W^+(\to \nu_\mu + \mu^+)$, with all particles treated as outgoing. These amplitudes are only non-zero for one helicity configuration, which has both quarks left-handed and both antiquarks right-handed. Similarly, both charged leptons created in the decay of the W-bosons are right-handed. The tree-level matrix elements are

$$\mathcal{M}^0(\bar{q}_1, q_2, \bar{q}_3, q_4; \nu_e, e^+, \nu_\mu, \mu^+) = g_s^2 \Big(\frac{g_w}{\sqrt{2}}\Big)^4 \Big(\delta_{\bar{\imath}_1 i_4}\delta_{\bar{\imath}_3 i_2} - \frac{1}{N_c}\delta_{\bar{\imath}_1 i_2}\delta_{\bar{\imath}_3 i_4}\Big) A^0(\bar{q}_1, q_2, \bar{q}_3, q_4), \tag{5.2.1}$$

where g_s, g_w and $N_c = 3$ are the strong coupling, weak coupling, and number of colours, and A^0 is the tree-level partial amplitude with the lepton labels understood. The polarisations of the W-bosons are defined as in equation (4.2.24), which takes into account the decay into leptons as well as the propagating factor, including the finite width of the W-boson.

The partial amplitude A^0 is computed using the Berends-Giele current f_VVf̄ff̄ with $s_w = 2$ and no on-shell gluons, taking $\bar{q}_1$ to be the off-shell particle. This is combined with the spinor for $\bar{q}_1$ to give A_0. A unit Cabibbo-Kobayashi-Maskawa (CKM) matrix is used, restricting the number of allowed flavour combinations. Depending on the flavours of the quarks, it is possible to assign the quark and antiquarks to the fermion lines in two different ways: pairing $\bar{q}_1$ with q_2 and $\bar{q}_3$ with q_4, or pairing $\bar{q}_1$ with q_4 and $\bar{q}_3$ with q_2. With a slight abuse of notation, I will refer to these as the s- and t-channel respectively. Equation (5.2.1) gives the s-channel contribution – the t-channel can be obtained by swapping $2 \leftrightarrow 4$ in the labels of the quarks and the colour indices.

The colour-squared and averaged matrix element is

$$\begin{aligned}|\mathcal{M}^0|^2 =&S_{qq}g_s^4\Big(\frac{g_w}{\sqrt{2}}\Big)^8\Big\{2C_FN_c\Big(|A_s^0(\bar{q}_1,q_2,\bar{q}_3,q_4)|^2+|A_t^0(\bar{q}_1,q_4,\bar{q}_3,q_2)|^2\Big)\\ &-4C_F\mathrm{Real}\Big(A_s^0(\bar{q}_1,q_2,\bar{q}_3,q_4)A_t^{0*}(\bar{q}_1,q_4,\bar{q}_3,q_2)\Big)\Big\},\end{aligned} \tag{5.2.2}$$

where the colour factor is

$$C_F\equiv\frac{N_c^2-1}{2N_c}. \tag{5.2.3}$$

The s- and t-channel matrix elements may vanish depending on the flavours of the quarks, and the final term takes account of interference between the two channels if the flavour configuration is such that both are open. For example, if the flavours of $\bar{q}_1, q_2, \bar{q}_3, q_4$ are $\bar{u}, d, \bar{c}, s$ then only the s-channel is open; for $\bar{u}, s, \bar{c}, d$ only the t-channel is nonzero; and for $\bar{u}, d, \bar{u}, d$ both channels are open and mixing between the two is considered. There is no sum over helicities, since the amplitudes are only non-zero if both quarks are left-handed and both antiquarks are right-handed. The factor $S_{qq}=\frac{1}{4}\frac{1}{9}$ is the averaging over spins and colours of the initial state quarks. Any two of the quarks or antiquarks may be in the initial state, giving rise to $q\bar{q}$, $\bar{q}q$, qq and $\bar{q}\bar{q}$ initial state channels. Figure 5.1 shows typical s- and t-channel Feynman diagrams that contribute to A^0 in the $\bar{q}q$ channel. Equation (5.2.1) gives the $\bar{q}q$ channel, and again the other initial state channels are obtained from this by momentum exchange. As a check, the values of $|\mathcal{M}^0|^2$ are compared to those obtained from the public program `MadGraph` [158] for all allowed flavour combinations in all four initial state channels. This is done at a random phase space point:

$$\begin{aligned}p_1 =&(-500,0,0,-500)\\ p_2 =&(-500,0,0,500)\\ p_3 =&(54.2314070117999,-31.1330162081798,-7.92796656791140,43.6912823611163)\\ p_4 =&(214.488870161418,-27.0607980217775,-98.5198083786150,188.592247959949)\\ p_{\nu_e} =&(85.5312248384887,-8.22193223977868,36.1637837682033,-77.0725048002414)\\ p_{e^+} =&(181.428811610043,-57.8599829481937,-171.863734086635,-5.61185898481311)\\ p_{\nu_\mu} =&(82.8493010774356,-65.9095476235891,-49.8952157196287,5.51413360058664)\\ p_{\mu^+} =&(381.470385300815,190.185277041519,292.042940984587,-155.113300136598),\end{aligned} \tag{5.2.4}$$

with the convention (E, p_x, p_y, p_z) in GeV. The results are shown in table 5.1, with the momenta of the quarks assigned according to $f_1(-p_1)+f_2(-p_2)\rightarrow f_3(p_3)+f_4(p_4)$, where $f_i=\{u,d,c,s,\bar{u},\bar{d},\bar{c},\bar{s}\}$ for $i=1,2,3,4$ are the flavours of the quarks or antiquarks indicated in the table. The physical parameters of `MadGraph` are used: the W- and Z-bosons have masses $m_W=80.419$ GeV and $m_Z=91.188$ GeV and widths $\Gamma_W=2.04759951$ GeV and $\Gamma_Z=2.44140351$ GeV. The strong and weak coupling constants are $g_w=0.653232911$ and $g_s=1.482831732494382$, and the weak mixing angle is $\sin_w^\theta=0.22224653283333$. For the sake of uniformity, these values are used for all tables shown in sections 5.3, 5.4, 6.2, 6.3, and 6.4. Different values are used when presenting the results of the calculations, in sections 5.6 and 6.6.

Flavours	$\lvert\mathcal{M}^0\rvert^2$	$\lvert\mathcal{M}^0_{\mathrm{MG}}\rvert^2$
$u\bar{s} \to \bar{c}d$	4.358281874545754	4.358281874546167
$u\bar{d} \to \bar{u}d$	6.810057425524780	6.810057425525394
$u\bar{d} \to \bar{c}s$	2.643908832071381	2.643908832071595
$\bar{d}u \to \bar{u}d$	0.7666066104913936	0.7666066104914634
$\bar{d}u \to \bar{c}s$	0.3854538891754188	0.3854538891754537
$\bar{s}u \to \bar{c}d$	0.6034128234054804	0.6034128234055352
$uu \to dd$	0.8138896072944484	0.8138896072945169
$uc \to ds$	0.7695243824577899	0.7695243824578557
$\bar{d}\bar{d} \to \bar{u}\bar{u}$	15.01782935295681	15.01782935295810
$\bar{d}\bar{s} \to \bar{u}\bar{c}$	16.17512636645897	16.17512636646035

Table 5.1: Colour-squared and averaged matrix element for the leading order process $0 \to \bar{q}_1 q_2 \bar{q}_3 q_4 + W^+(\to \nu_e + e^+) + W^+(\to \nu_\mu + \mu^+)$ for the phase space point given in equation (5.2.4). Results are given for all possible quarks flavour configurations and all initial state channels, as shown in the first column. The physical parameters and momentum assignments are given in the text. The third column shows the result obtained from `MadGraph` for the given flavour combination. The units shown are 10^{-23} GeV^{-8}.

5.3 Real radiation amplitudes

In the previous section, the flavour structure of the Born amplitude was discussed in some detail. This is unchanged by NLO QCD corrections, so this discussion holds for both real emission as well as one-loop amplitudes. The matrix element for real emission in the s-channel is

$$
\begin{aligned}
&\mathcal{M}_s^0(\bar q_1, q_2, \bar q_3, q_4, g; \nu_e, e^+, \nu_\mu, \mu^+) = \\
&\quad g_s^3\Big(\frac{g_w}{\sqrt{2}}\Big)^4 \Big\{ (t^a)_{\bar i_1 i_4}\delta_{\bar i_3 i_2} A^0(\bar q_1, q_2, \bar q_3, q_4, g) + (t^a)_{\bar i_3 i_2}\delta_{\bar i_1 i_4} A^0(\bar q_1, q_2, g, \bar q_3, q_4) \\
&\quad + \frac{1}{N_c}(t^a)_{\bar i_1 i_2}\delta_{\bar i_3 i_4} A^0(\bar q_1, g, q_2, \bar q_3, q_4) + \frac{1}{N_c}(t^a)_{\bar i_3 i_4}\delta_{\bar i_1 i_2} A^0(\bar q_1, q_2, \bar q_3, g, q_4) \Big\},
\end{aligned} \tag{5.3.1}
$$

where the A^0 are primitive amplitudes with the position of the gluon relative to the four quarks indicated. They are calculated using the Berends-Giele current $\mathsf{f\_VV\bar{f}f\bar{f}}$ with $s_w = 2$ and one on-shell gluon, whose position is given by $n_4 = 1$ for the first term, $n_2 = 1$ for the second, $n_1 = 1$ for the third, and $n_3 = 1$ for the last term. As was the case for the leading-order matrix elements, either the s- or t-channel or both may be open depending on the flavours of the quarks, and the t-channel amplitude $\mathcal{M}_t^0$ is calculated from equation (5.3.1) with the same exchange $2 \leftrightarrow 4$ on the quarks and colour labels. There are eight initial state channels: $q\bar q$, $\bar q q$, qq, $\bar q\bar q$, $g\bar q$, $\bar q g$, gq and qg.

The colour-squared and averaged matrix element for real emission is

$$
\begin{aligned}
|\mathcal{M}^R|^2 =& S_i \sum_{h_g} g_s^6 \Big(\frac{g_w}{\sqrt{2}}\Big)^8 2C_F \Big\{ \Big(|\mathcal{M}_s^0(\bar q_1, q_2, \bar q_3, q_4, g)|^2 + |\mathcal{M}_t^0(\bar q_1, q_4, \bar q_3, q_2, g)|^2 \Big) \\
&\qquad + 2\ \mathrm{Real}\Big(\mathcal{M}_s^0(\bar q_1, q_2, \bar q_3, q_4, g)\mathcal{M}_t^{0*}(\bar q_1, q_4, \bar q_3, q_2, g) \Big) \Big\},
\end{aligned} \tag{5.3.2}
$$

where the matrix element squared in the s-channel is

$$
\begin{aligned}
|\mathcal{M}_s^0(\bar q_1, q_2, \bar q_3, q_4, g)|^2 =& N_c^2 \Big(|A^0(\bar q_1, q_2, g, \bar q_3, q_4)|^2 + |A^0(\bar q_1, q_2, \bar q_3, q_4, g)|^2 \Big) \\
&+ |A^0(\bar q_1, g, q_2, \bar q_3, q_4)|^2 + |A^0(\bar q_1, q_2, \bar q_3, g, q_4)|^2 \\
&+ 2\ \mathrm{Real}\Big(\big(A^0(\bar q_1, g, q_2, \bar q_3, q_4) + A^0(\bar q_1, q_2, \bar q_3, g, q_4) \big) \\
&\times \big(A^0(\bar q_1, q_2, g, \bar q_3, q_4) + A^0(\bar q_1, q_2, \bar q_3, q_4, g) \big)^* \Big),
\end{aligned} \tag{5.3.3}
$$

and similarly for the t-channel. The mixing between the channels is

$$
\begin{aligned}
&\mathcal{M}_s^0(\bar q_1, q_2, \bar q_3, q_4, g)\mathcal{M}_t^{0*}(\bar q_1, q_4, \bar q_3, q_2, g) = \\
&\quad N_c \Big(A^0(\bar q_1, q_2, \bar q_3, q_4, g) \big(A^0(\bar q_1, q_4, \bar q_3, q_2, g) + A^0(\bar q_1, q_4, g, \bar q_3, q_2) + A^0(\bar q_1, g, q_4, \bar q_3, q_2) \big)^* \\
&\quad + A^0(\bar q_1, q_2, g, \bar q_3, q_4) \big(A^0(\bar q_1, q_4, \bar q_3, q_2, g) + A^0(\bar q_1, q_4, g, \bar q_3, q_2) + A^0(\bar q_1, q_4, \bar q_3, g, q_2) \big)^* \\
&\quad + A^0(\bar q_1, g, q_2, \bar q_3, q_4) A^{0*}(\bar q_1, q_4, \bar q_3, q_2, g) + A^0(\bar q_1, q_2, \bar q_3, g, q_4) A^{0*}(\bar q_1, q_4, g, \bar q_3, q_2) \Big) \\
&\quad + \frac{1}{N_c} \Big(A^0(\bar q_1, g, q_2, \bar q_3, q_4) + A^0(\bar q_1, q_2, \bar q_3, g, q_4) \Big) \Big(A^0(\bar q_1, g, q_4, \bar q_3, q_2) + A^0(\bar q_1, q_4, \bar q_3, g, q_2) \Big)^* .
\end{aligned} \tag{5.3.4}
$$

The sum in equation (5.3.2) is over the helicities of the gluon. The factor S_i in equation (5.3.2) is the initial state averaging, with $S_i = \frac{1}{4}\frac{1}{9}$ if there are two quarks in the initial state, and $S_i = \frac{1}{4}\frac{1}{24}$ if there is a quark and a gluon in the initial state. The values of the matrix element squared equation (5.3.2) are shown in table 5.2, together with the results from `MadGraph`, for a given phase space point (in GeV):

$$\begin{aligned}
p_1 =&(-500, 0, 0, -500); \qquad p_2 = (-500, 0, 0, 500)\\
p_3 =&(51.09842528030303, -29.59882122336450, -1.91510389563769, 41.60878783842341)\\
p_4 =&(191.82026607198480, -33.82123290323604, -65.65381249647574, 177.03309178091453)\\
p_5 =&(130.00632077374939, 51.55381760464103, -95.44103752253108, -71.65790736643960)\\
p_{\nu_e} =&(72.87242470112021, -11.69341352221985, 39.78880352146413, -59.92082673285745)\\
p_{e^+} =&(143.84683964946802, -58.01940507009024, -131.47834077237431, 6.25362456467995)\\
p_{\nu_\mu} =&(71.03543116708296, -60.72621080797182, -35.38271257312147, 10.31617433775810)\\
p_{\mu^+} =&(339.32029235629170, 142.30526592224143, 290.08220373867613, -103.63294442247896).
\end{aligned} \tag{5.3.5}$$

Flavours	$\lvert\mathcal{M}^{\mathrm{R}}\rvert^2$	$\lvert\mathcal{M}^{\mathrm{R}}_{\mathrm{MG}}\rvert^2$
$u\bar{s} \to \bar{c}dg$	2.455080460493246	2.455080460493446
$u\bar{d} \to \bar{u}dg$	2.685962046637424	2.685962046637649
$u\bar{d} \to \bar{c}sg$	0.7582823136243569	0.7582823136244223
$\bar{d}u \to \bar{u}dg$	0.3213389727968009	0.3213389727968288
$\bar{d}u \to \bar{c}sg$	0.1838959696279038	0.1838959696279198
$\bar{s}u \to \bar{c}dg$	0.1831950876924623	0.1831950876924781
$uu \to ddg$	0.6226873230707548	0.6226873230708126
$uc \to dsg$	0.9592702314931371	0.9592702314932247
$\bar{d}\bar{d} \to \bar{u}\bar{u}g$	6.040526524615315	6.040526524615826
$\bar{d}\bar{s} \to \bar{u}\bar{c}g$	6.872376627196192	6.872376627196782
$ug \to \bar{u}dd$	0.06428883723798486	0.06428883723799013
$ug \to \bar{c}sd$	0.04938670511337863	0.04938670511338256
$gu \to \bar{u}dd$	0.8032403779867448	0.8032403779868180
$gu \to \bar{c}sd$	0.8425190119045392	0.8425190119046195
$\bar{d}g \to \bar{u}d\bar{u}$	0.09439056175463394	0.09439056175464198
$\bar{d}g \to \bar{c}s\bar{u}$	0.04481315884551068	0.04481315884551458
$g\bar{d} \to \bar{u}d\bar{u}$	3.290840945108729	3.290840945109010
$g\bar{d} \to \bar{c}s\bar{u}$	2.734148940071727	2.734148940071961

Table 5.2: Colour-squared and averaged matrix element for all channels and all flavour combinations of the real radiation process $0 \to \bar{q}_1 q_2 \bar{q}_3 q_4 g + W^+(\to \nu_e + e^+) + W^+(\to \nu_\mu + \mu^+)$ for the phase space point given in equation (5.3.5). The parameters are given in section 5.2. The first column shows the flavour configuration of the quarks, with the momentum assignment $f_1(-p_1) + f_2(-p_2) \to f_3(p_3) + f_4(p_4) + f_5(p_5)$, where $f_i = \{g, u, d, c, s, \bar{u}, \bar{d}, \bar{c}, \bar{s}\}$ for $i = 1, ..., 5$. The third column shows the results obtained from `MadGraph`. The units shown are 10^{-25} GeV^{-10}.

5.4 Virtual amplitudes

Again, the flavour structure is the same as discussed in section 5.2, so the focus is on the colour decomposition. The virtual amplitude can be written in terms of partial amplitudes A^1_A and A^1_B

$$\begin{aligned}\mathcal{M}^1(\bar{q}_1, q_2, \bar{q}_3, q_4; \nu_e, e^+, \nu_\mu, \mu^+) =& g_s^4 \Big(\frac{g_w}{\sqrt{2}}\Big)^4 \Big(\delta_{\bar{i}_1 i_4}\delta_{\bar{i}_3 i_2} A^1_A(\bar{q}_1, q_2, \bar{q}_3, q_4) \\ &+ \delta_{\bar{i}_1 i_2}\delta_{\bar{i}_3 i_4} A^1_B(\bar{q}_1, q_2, \bar{q}_3, q_4)\Big),\end{aligned} \tag{5.4.1}$$

where each partial amplitude consists of five primitive amplitudes in s-channel, and five in the t-channel. Written in terms of these primitives, the partial amplitudes are

$$\begin{aligned}A^1_A(\bar{q}_1, q_2, \bar{q}_3, q_4) =& \Big(N_c - \frac{2}{N_c}\Big) A^1_{1,s}(\bar{q}_1, q_2, \bar{q}_3, q_4) + \frac{2}{N_c} A^1_{2,s}(\bar{q}_1, q_2, \bar{q}_3, q_4) \\ &- \frac{1}{N_c} A^1_{3,s}(\bar{q}_1, q_2, \bar{q}_3, q_4) - \frac{1}{N_c} A^1_{4,s}(\bar{q}_1, q_2, \bar{q}_3, q_4) \\ &+ N_f A^1_{[1/2],s}(\bar{q}_1, q_2, \bar{q}_3, q_4) \\ &+ \frac{1}{N_c^2} A^1_{1,t}(\bar{q}_1, q_4, \bar{q}_3, q_2) - \Big(1 + \frac{1}{N_c^2}\Big) A^1_{2,t}(\bar{q}_1, q_4, \bar{q}_3, q_2) + \\ &+ \frac{1}{N_c^2} A^1_{3,t}(\bar{q}_1, q_4, \bar{q}_3, q_2) + \frac{1}{N_c^2} A^1_{4,t}(\bar{q}_1, q_4, \bar{q}_3, q_2) \\ &- \frac{N_f}{N_c^2} A^1_{[1/2],t}(\bar{q}_1, q_4, \bar{q}_3, q_2) \\ A^1_B(\bar{q}_1, q_2, \bar{q}_3, q_4) =& \frac{1}{N_c^2} A^1_{1,s}(\bar{q}_1, q_2, \bar{q}_3, q_4) - \Big(1 + \frac{1}{N_c^2}\Big) A^1_{2,s}(\bar{q}_1, q_2, \bar{q}_3, q_4) + \\ &+ \frac{1}{N_c^2} A^1_{3,s}(\bar{q}_1, q_2, \bar{q}_3, q_4) + \frac{1}{N_c^2} A^1_{4,s}(\bar{q}_1, q_2, \bar{q}_3, q_4) \\ &- \frac{N_f}{N_c^2} A^1_{[1/2],s}(\bar{q}_1, q_2, \bar{q}_3, q_4) \\ &+ \Big(N_c - \frac{2}{N_c}\Big) A^1_{1,t}(\bar{q}_1, q_4, \bar{q}_3, q_2) + \frac{2}{N_c} A^1_{2,t}(\bar{q}_1, q_4, \bar{q}_3, q_2) \\ &- \frac{1}{N_c} A^1_{3,t}(\bar{q}_1, q_4, \bar{q}_3, q_2) - \frac{1}{N_c} A^1_{4,t}(\bar{q}_1, q_4, \bar{q}_3, q_2) \\ &+ N_f A^1_{[1/2],t}(\bar{q}_1, q_4, \bar{q}_3, q_2).\end{aligned} \tag{5.4.2}$$

The s-channel primitives are shown in figure 5.2 with the electroweak bosons not shown; all insertions of these consistent with the flavours of the quarks must be used. The t-channel primitive amplitudes are identical with the usual exchange $q_2 \leftrightarrow q_4$. Primitives A^1_1 and A^1_2 are six-point amplitudes, the latter being a subleading colour (nonplanar) contribution with the intermediate gluons crossing. Using the $\mathcal{CP}$-relation, this can be related to A^1_1 by exchange of the helicities and momenta of two quarks

$$A^1_2(\bar{q}_1, q_2, \bar{q}_3, q_4) = -A^1_1(\bar{q}_1, q_2, q_4, \bar{q}_3). \tag{5.4.3}$$

The primitives A_3 and A_4 are five-point amplitudes formed by dressing either of the Born quark lines with a gluon loop. It is convenient to consider each primitive as

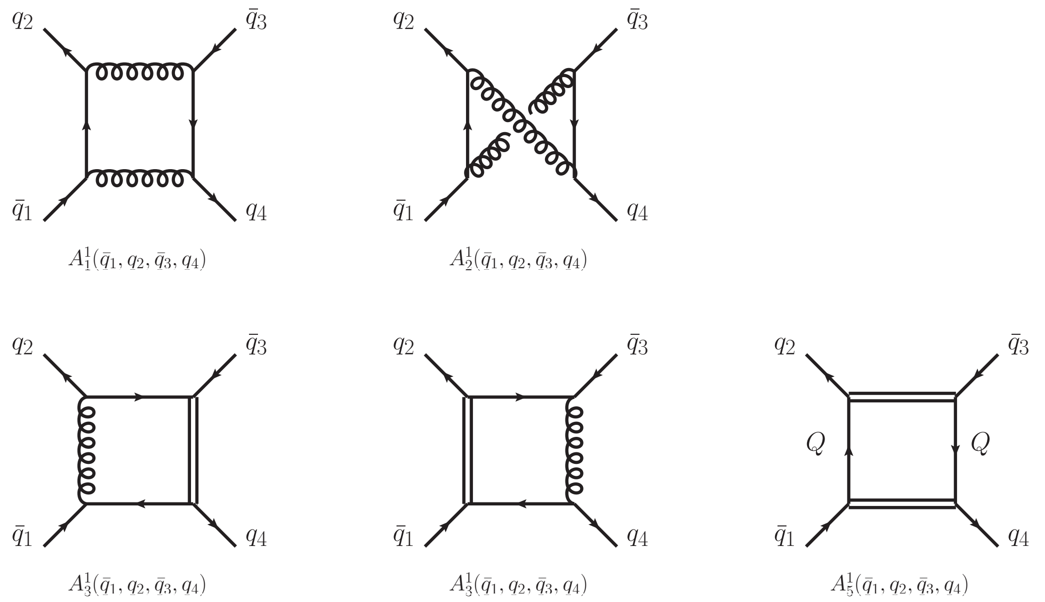

$A_1^1(\bar{q}_1, q_2, \bar{q}_3, q_4)$ $A_2^1(\bar{q}_1, q_2, \bar{q}_3, q_4)$

$A_3^1(\bar{q}_1, q_2, \bar{q}_3, q_4)$ $A_3^1(\bar{q}_1, q_2, \bar{q}_3, q_4)$ $A_5^1(\bar{q}_1, q_2, \bar{q}_3, q_4)$

Figure 5.2: Primitive amplitudes for the process $0 \to \bar{q}_1 q_2 \bar{q}_3 q_4 + W^+ W^+$ in the s-channel, with the W^+-bosons not shown. Double lines represent dummy lines which are not cut. The W^+-bosons do not couple to the internal quarks labeled Q.

having six propagators; this prompts the introduction of "dummy lines", shown as double lines in figure 5.2. Both gluons and electroweak bosons may couple to dummy lines, but dummy lines cannot be cut. It is obvious that these two primitives can be related by a swap of quark-antiquark lines

$$A_4(\bar{q}_1, q_2, \bar{q}_3, q_4) = A_3(\bar{q}_3, q_4, \bar{q}_1, q_2). \tag{5.4.4}$$

The primitive amplitudes may be computed through the use of *parent amplitudes.* These are calculational aids which give rise to one or more primitive amplitudes through exchange of the labels on external particles. Two parent amplitudes can be identified in this case: $\mathbb{A}_1$ and $\mathbb{A}_2$. The former corresponds exactly to primitive A_1, while the latter corresponds to the primitive A_3, with the W-boson on the $\bar{q}_1 q_2$ quark-antiquark line restricted to being below the gluon propagating between the quark-antiquark lines (i.e. closer to $\bar{q}_1$ than q_2). This is the motivation behind the construction of Berends-Giele currents with similar restrictions on the insertions of the electroweak bosons, e.g. $\mathsf{f\_V\bar{f}f\bar{f}_t}$, $\mathsf{g\_V\bar{f}f\bar{f}f\_1}$, and $\mathsf{f\_VV\bar{f}f\bar{f}\_1}$ (see section 4.3). The primitives A_1 and A_2 may then be calculated from $\mathbb{A}_1$:

$$\begin{aligned} A_1(\bar{q}_1, q_2, \bar{q}_3, q_4) =& \mathbb{A}_1(\bar{q}_1, q_2, \bar{q}_3, q_4) \\ A_2(\bar{q}_1, q_2, \bar{q}_3, q_4) =& - \mathbb{A}_1(\bar{q}_1, q_2, q_4, \bar{q}_3), \end{aligned} \tag{5.4.5}$$

where the second line is the quark exchange of equation (5.4.3). The primitives A_3 and A_4 are calculated from the other parent amplitude:

$$\begin{aligned} A_3(\bar{q}_1, q_2, \bar{q}_3, q_4) =& \mathbb{A}_2(\bar{q}_1, q_2, \bar{q}_3, q_4) + \mathbb{A}_2(q_2, \bar{q}_1, q_4, \bar{q}_3) \\ A_4(\bar{q}_1, q_2, \bar{q}_3, q_4) =& \mathbb{A}_2(\bar{q}_3, q_4, \bar{q}_1, q_2) + \mathbb{A}_2(q_4, \bar{q}_3, q_2, \bar{q}_1), \end{aligned} \tag{5.4.6}$$

where the first term in each expression corresponds to the W-boson being below the gluon propagator on the $\bar{q}_1 q_2$ line, and the second term has the W-boson above it. The exchange of quarks $(\bar{q}_1, q_2) \leftrightarrow (\bar{q}_3, q_4)$ shifts the gluon bubble from the one quark-antiquark line to the other. The use of these parent amplitudes does break electroweak gauge invariance, but this is recovered in the full primitive amplitude.

The final primitive amplitude, $A^1_{[1/2]}$, is due to a fermion loop in the intermediate gluon propagator. Charge conservation prevents the W-bosons from coupling to the quarks in this loop, which is reflected in the Q labels in figure 5.2. Thus this amplitude is simply a dressing of the tree-level amplitude. Indeed, it is not necessary to compute this with the full machinery of generalised unitarity, as will be done with the other primitive amplitudes. Instead, it can be computed directly from the Born amplitude, modifying a result from ref. [159]

$$\begin{aligned} A_{[1/2],s}(\bar{q}_1, q_2, \bar{q}_3, q_4) =& \Big(-\frac{2}{3\epsilon} - \frac{10}{9}\Big) A^0_s(\bar{q}_1, q_2, \bar{q}_3, q_4) \\ &+ \sum_{i=1}^{2} \Big(-\frac{2}{3} \log \frac{\mu^2}{s_{\bar{q}_1 q_2 W_i}}\Big) A^{0,i}_s(\bar{q}_1, W_i, q_2, \bar{q}_3, q_4), \end{aligned} \tag{5.4.7}$$

where the sum is over the two W-bosons and $A^{0,i}_s(\bar{q}_1, W_i, q_2, \bar{q}_3, q_4)$ is the part of the tree-level amplitude which has W_i on the $\bar{q}_1 q_2$ line. The momentum flowing through the gluon is $s_{\bar{q}_1 q_2 W_i} = (p_{\bar{q}_1} + p_{q_2} + p_{W_i})^2$.

The parent amplitudes are computed using the method of generalised unitarity elaborated in chapter 3, and through these the primitive and partial amplitudes are determined. The flavours are set as $(\bar{q}_1, q_2, \bar{q}_3, q_4) = (\bar{u}, d, \bar{c}, s)$, thus maintaining a clear distinction between the two quark-antiquark lines of the Berends-Giele currents, and allowing the s- and t-channel amplitudes to be computed independently.

The ratios of the single and double pole residues of the unrenormalised primitive amplitudes to the tree-level amplitudes are defined as

$$\begin{aligned} R^{(\epsilon^{-2})}_{i,s} =& \frac{1}{c_\Gamma} \frac{\mathrm{Res}_{\epsilon^{-2}} A^1_{i,s}(\bar{q}_1, q_2, \bar{q}_3, q_4)}{A^0(\bar{q}_1, q_2, \bar{q}_3, q_4)} \\ R^{(\epsilon^{-1})}_{i,s} =& \frac{1}{c_\Gamma} \frac{\mathrm{Res}_{\epsilon^{-1}} A^1_{i,s}(\bar{q}_1, q_2, \bar{q}_3, q_4)}{A^0(\bar{q}_1, q_2, \bar{q}_3, q_4)}, \end{aligned} \tag{5.4.8}$$

with

$$c_\Gamma = (4\pi)^{\epsilon-2} \frac{\Gamma(1+\epsilon)\Gamma^2(1-\epsilon)}{\Gamma(1-2\epsilon)}. \tag{5.4.9}$$

As mentioned in section 2.3, these can be calculated analytically [159], and are given by

$$\begin{array}{lclclcl} R^{(\epsilon^{-2})}_{1,s} & = & -2 & \quad R^{(\epsilon^{-1})}_{1,s} & = & -\log \frac{\mu^2}{-s_{14}} - \log \frac{\mu^2}{-s_{23}} + \frac{2}{3} \\ R^{(\epsilon^{-2})}_{2,s} & = & -2 & \quad R^{(\epsilon^{-1})}_{2,s} & = & -\log \frac{\mu^2}{-s_{13}} - \log \frac{\mu^2}{-s_{24}} + \frac{2}{3} \\ R^{(\epsilon^{-2})}_{3,s} & = & -1 & \quad R^{(\epsilon^{-1})}_{3,s} & = & -\log \frac{\mu^2}{-s_{12}} - \frac{3}{2} \\ R^{(\epsilon^{-2})}_{4,s} & = & -1 & \quad R^{(\epsilon^{-1})}_{4,s} & = & -\log \frac{\mu^2}{-s_{34}} - \frac{3}{2} \end{array} \tag{5.4.10}$$

where the momenta are denoted by $p_{\bar{q}_1} = p_1$; $p_{q_2} = p_2$; $p_{\bar{q}_3} = p_3$; $p_{q_4} = p_4$ and $s_{ij} = (p_i + p_j)^2$. The t-channel ratios $R_{i,t}$ are defined analogously, with the exchange $p_2 \leftrightarrow p_4$ in the analytic expressions. The logarithms are continued as written in equation (2.3.8). Agreement between the ratios as defined in equation (5.4.8) and their analytic forms of equation (5.4.10) is an important first check when the primitive amplitudes A_i^1 are computed. The former are shown in table 5.3 for the $q\bar{q}$ initial-state channel and the phase space point of equation (5.2.4), using the renormalisation scale $\mu = 150$ GeV. Also shown are the relative errors ϵ

$$\epsilon = \left| \frac{R - R_{\text{analytic}}}{R_{\text{analytic}}} \right| \tag{5.4.11}$$

between these values and those obtained from equation (5.4.10), denoted as R_{analytic}. As can be seen, there is excellent agreement, to the level of 10-13 figures.

Residue	Calculated value	Relative error ϵ
$R_{1,s}^{(\epsilon^{-2})}$	$-2.00000000000161 + i9.36 \times 10^{-12}$	4.7×10^{-12}
$R_{1,s}^{(\epsilon^{-1})}$	$2.27792687518148 - i2.41 \times 10^{-10}$	7.9×10^{-11}
$R_{2,s}^{(\epsilon^{-2})}$	$-1.99999999999881 + i2.85 \times 10^{-12}$	1.5×10^{-12}
$R_{2,s}^{(\epsilon^{-1})}$	$2.79396324524537 - i9.98 \times 10^{-11}$	3.6×10^{-11}
$R_{3,s}^{(\epsilon^{-2})}$	$-1.00000000000111 - i6.13 \times 10^{-13}$	1.3×10^{-12}
$R_{3,s}^{(\epsilon^{-1})}$	$2.29423996976934 - i3.14159265358449$	1.4×10^{-12}
$R_{4,s}^{(\epsilon^{-2})}$	$-0.999999999997615 - i5.52 \times 10^{-12}$	6.0×10^{-12}
$R_{4,s}^{(\epsilon^{-1})}$	$-3.35015155633674 - i3.14159265383248$	1.1×10^{-10}
$R_{1,t}^{(\epsilon^{-2})}$	$-1.99999999999498 + i1.98 \times 10^{-11}$	1.0×10^{-11}
$R_{1,t}^{(\epsilon^{-1})}$	$2.61075507916129 - i6.28318530763737$	9.4×10^{-11}
$R_{2,t}^{(\epsilon^{-2})}$	$-1.99999999999980 - i8.38 \times 10^{-13}$	4.3×10^{-13}
$R_{2,t}^{(\epsilon^{-1})}$	$2.79396324486542 + i1.31 \times 10^{-10}$	4.8×10^{-11}
$R_{3,t}^{(\epsilon^{-2})}$	$-1.00000000000899 - i9.08 \times 10^{-12}$	1.3×10^{-11}
$R_{3,t}^{(\epsilon^{-1})}$	$-1.3594027659435 - i1.59 \times 10^{-12}$	1.3×10^{-10}
$R_{4,t}^{(\epsilon^{-2})}$	$-0.999999999999341 + i1.90 \times 10^{-12}$	2.0×10^{-12}
$R_{4,t}^{(\epsilon^{-1})}$	$-0.0293370258756654 5 - i2.27 \times 10^{-11}$	4.9×10^{-11}

Table 5.3: Ratios of residues of double and single poles of the four primitive amplitudes to the tree-level amplitude. The s- and t-channel ratios for the $\bar{q}q$ initial state are shown. The third column shows the relative error between these values and the values obtained from the analytic expression of equation (5.4.10).

The interference between the virtual and tree-level amplitudes can be easily expressed in terms of the partial amplitudes

$$\begin{aligned} 2\text{Real}\Big(\mathcal{M}^0\mathcal{M}^{1*}\Big) =& 2S_{qq}g_s^6\Big(\frac{g_w}{\sqrt{2}}\Big)^8(N_c^2-1)\times \\ & \text{Real}\Big(A_s^0(\bar{q}_1,q_2,\bar{q}_3,q_4)A_A^{1*}(\bar{q}_1,q_2,\bar{q}_3,q_4) \\ & + A_t^0(\bar{q}_1,q_4,\bar{q}_3,q_2)A_B^{1*}(\bar{q}_1,q_2,\bar{q}_3,q_4)\Big). \end{aligned} \tag{5.4.12}$$

Note that mixing between s- and t-channels will occur if the flavours are such that both are open.

For the usual phase space point, table 5.4 shows the leading-order matrix element squared for the different initial state flavours, together with the ratio

$$R = \frac{4\pi}{\alpha_s} \frac{\mathrm{Real}\Big(\mathcal{M}^0 \mathcal{M}^{1*}\Big)}{|\mathcal{M}^0|^2} \tag{5.4.13}$$

for the residues of the double and single poles, as well as for the finite terms. The quark momentum assignment is the same as in section 5.2. There is a sum over all the allowed final state flavour configurations for both the LO and NLO results shown in table 5.4.

Flavours	$\|\mathcal{M}^0\|^2$	$R^{(\epsilon^{-2})}$	$R^{(\epsilon^{-1})}$	$R^{(\epsilon^{0})}$
$u\bar{s} \to \bar{c}d$	4.358282	-5.333333	5.083984	-9.593517
$u\bar{d} \to \bar{u}d + \bar{c}s$	9.453966	-5.333333	4.577633	-1.037184
$\bar{d}u \to \bar{u}d + \bar{c}s$	1.152060	-5.333333	5.066095	-7.270075
$\bar{s}u \to \bar{c}d$	0.6034128	-5.333333	4.567948	-9.319901
$uu \to dd$	0.8138896	-5.333333	4.737025	25.88984
$uc \to ds$	0.7695244	-5.333333	4.013234	-14.74962
$\bar{d}\bar{d} \to \bar{u}\bar{u}$	15.01783	-5.333333	4.641191	-11.66228
$\bar{d}\bar{s} \to \bar{u}\bar{c}$	16.17512	-5.333333	4.013234	-7.633957

Table 5.4: Leading order matrix element squared, and ratio R for double pole, single pole and finite part of the one-loop amplitude squared, for all initial state flavour configurations. The phase space point is given in equation (5.2.4), and the renormalisation scale is $\mu = 150$ GeV. The physical parameters are given in the text of section 5.2. The units of the $|\mathcal{M}^0|^2$ are 10^{-23} GeV^{-8}.

5.5 Checks, stability and running time

The colour-squared matrix elements for the Born, real radiation and virtual processes will be integrated over phase space using a Monte Carlo method (as implemented in `MCFM` [160]) to produce a cross-section. Before this is done, it is important to check that no errors have crept into the calculation. As has been seen in sections 5.2 and 5.3, the matrix elements can be checked against a public program such as `MadGraph` for the Born and real radiation processes. The dipole terms are checked to correctly subtract the divergent real radiation terms in soft and collinear regions of phase space. The poles of the virtual primitive amplitude can be checked against their simple analytic expression, as seen in section 5.4. At the level of the colour-squared interference between the leading order and virtual matrix elements, the poles should be removed by the integrated dipoles (see section 2.2). This is checked using a parameter α [161, 162] describing how soft or collinear a phase space point is. The cross-section is checked to be independent of α.

Finally, the virtual amplitudes are recomputed using the OPP method, but with the unitarity cuts applied to Feynman diagrams instead of primitive amplitudes, and the resulting tree-level helicity amplitudes computed using Feynman rules as opposed to using Berends-Giele recursion relations. The Feynman diagrams are generated using `Qgraf` [163] and the resulting expressions are evaluated using the symbolic manipulation program `FORM` [164], before being computed. Due to the large number of Feynman diagrams, this is several orders of magnitude slower than using primitive amplitudes and Berends-Giele currents, and is therefore not suitable for computing cross-sections. However, it does provide an independent cross-check on the virtual amplitudes, including the finite part[1].

The Monte Carlo integration over phase space and the computation of the matrix elements is performed in double precision as standard. At this level of accuracy, numerical instabilities sometimes appear. Two methods are used to identify such instabilities at the level of the primitive amplitudes. The first check is that the coefficients $\tilde{c}_i$ and $\tilde{b}_i$ correctly solve the OPP equations (3.4.26) and (3.4.30) for the unitarity coefficients. The remaining two OPP equations (3.4.22) and (3.4.31) almost never admit numerical instablities. This can be done by choosing a random value for the α_i used to construct the loop momentum l, and then re-evaluating the unitarity coefficients using first the explicit unitarity calculation with this value of l, and then using the coefficients $\tilde{c}_i$ and $\tilde{b}_i$. Requiring agreement between these two values to one significant figure is sufficient to identify instabilities. The second check is that the double and single pole residues reproduce the analytic values as given in equation (5.4.10) to four significant figures.

Around 4% of the primitive amplitudes fail one or both of these checks. In these cases, the primitive amplitude is recomputed using quadruple precision. This is costly in terms of the running time, but solves the numerical instabilities in all but the most

---

[1] Since the publication of ref. [77], a number of automated programs which compute virtual amplitudes for user-defined input particles have become available, such as `GoSam` [165, 166] and `HELAC-NLO` [167]. An independent check of both finite and singular parts of virtual amplitudes is now possible using these programs. Indeed, $pp \to W^+W^+jj$ was one of the processes used to test the `GoSam` package [165].

pathological of phase space points. For the negligible fraction of phase space points at which the primitives still fail these checks after being recomputed in quadruple precision, the primitive is set to zero.

The full virtual amplitude squared can be evaluated at the rate of 3-4 phase space points per second. A phase space grid is created, weighted by the leading order matrix element squared evaluated at each point. Using this grid, around 2×10^5 phase space points are needed to produce a virtual cross-section σ^{V} with a numerical error of 1-2%. Since a Monte Carlo integration is inherently parallelisable, σ^{V} can be calculated within a few hours. In fact, the time taken to compute the real radiation cross-section σ^{R} is a factor of 4-5 longer than this, despite the fact that the real radiation matrix element can be calculated much quicker. This is because the number of phase space points needed in the Monte Carlo integration is two orders of magnitude larger for the real radiation cross-section, due to the need to correctly sample the soft and collinear phase subspaces.

5.6 Results

The hadroproduction of W^+W^+jj will result in the distinctive signal of two same-sign leptons, two jets, and missing energy. Such a signal is interesting, regarded as either a background to New Physics, or as an exotic signal arising from the Standard Model. The Large Hadron Collider (LHC) has completed a groundbreaking run at centre-of-mass energy $\sqrt{s} = 7$ TeV, with more than 5 fb^{-1} of data recorded. A larger amount of data has already been recorded during the even more successful $\sqrt{s} = 8$ TeV run, and it is likely that $pp \to W^+W^+jj$ events have already been recorded. After the shutdown in 2013, the LHC will hopefully collect ~ 100 fb^{-1} of data at $\sqrt{s} = 13$–14 TeV, making a detailed study of these exotic signatures possible.

In this section, the results for $pp \to W^+W^+jj$ are shown at centre-of-mass energy $\sqrt{s} = 14$ TeV. The W-bosons are on-shell, and decay leptonically, $W^+W^+ \to \nu_e e^+ \nu_\mu \mu^+$. Spin correlations of the leptons are included, but final state lepton mixing is neglected, so that the production of a same-flavour lepton final state e^+e^+ has half the cross-section as that considered here. Therefore, the results presented here are to be multiplied by a factor of two when considering all leptonic flavours $\{e^+e^+, \mu^+\mu^+, e^+\mu^+\}$. As mentioned previously, only the strong production mechanism is considered.

The top quarks are approximated as infinitely massive, with the other five quarks being massless. This implies five flavours in the running of α_s and in the internal quark loops. This is justified since the momentum flowing through the loop is below the top production threshold. Furthermore, final state top quarks are neglected as they give rise to a different experimental signature. Initial and final state bottom quarks are also neglected since they originate from top quarks, through the splitting $t^* \to W^+b$. I remind the reader that a unit CKM matrix is assumed.

The W-boson has mass $m_W = 80.419$ GeV and width $\Gamma_W = 2.14$ GeV. The electromagnetic coupling is taken as $\alpha(m_Z) = 1/128.802$ and the weak coupling is obtained from this with weak mixing angle $\sin^2\theta_w = 0.2222$. MSTW08LO and MSTW08NLO parton distributions [98] are used for the LO and NLO calculations respectively. The strong coupling is set through these as $\alpha_s(m_Z) = 0.13939$ at LO and $\alpha_s(m_Z) = 0.12018$ at NLO. The factorisation and renormalisation scales are set equal to one another, $\mu_R = \mu_F = \mu$. Generic kinematic cuts are imposed. The leptons are required to have transverse momentum $p_{T,l} > 20$ GeV and pseudorapidity $|\eta_l| < 2.4$ [2] The missing transverse momentum must satisfy $p_{T,\text{miss}} > 30$ GeV. The anti-k_T algorithm [168] as implemented in FastJet [111, 169] is used to define jets, with jet separation

$$\Delta R_{j_1j_2} = \sqrt{\Delta\eta^2_{j_1j_2} + \Delta\phi^2_{j_1j_2}} = 0.4, \tag{5.6.1}$$

where $\Delta\eta_{j_1j_2}$ is the difference in jet pseudorapidity, and $\Delta\phi_{j_1j_2}$ is the azimuthal angle between the jets in the plane transverse to the beam direction. Jets are required to have transverse momentum $p_{T,j} > 30$ GeV.

It was mentioned in section 5.1 that the presence of a W-boson coupling to each

---

[2] The pseudorapidity is defined as $\eta \equiv \frac{1}{2}\ln\cot^2\frac{\theta}{2} = \frac{1}{2}\ln\frac{p+p_z}{p-p_z}$, where θ is the azimuthal angle between the momentum and the beam direction, and p is the magnitude of the momentum three-vector. This coincides with the rapidity $y \equiv \frac{1}{2}\ln\frac{E+p_z}{E-p_z}$ for massless particles.

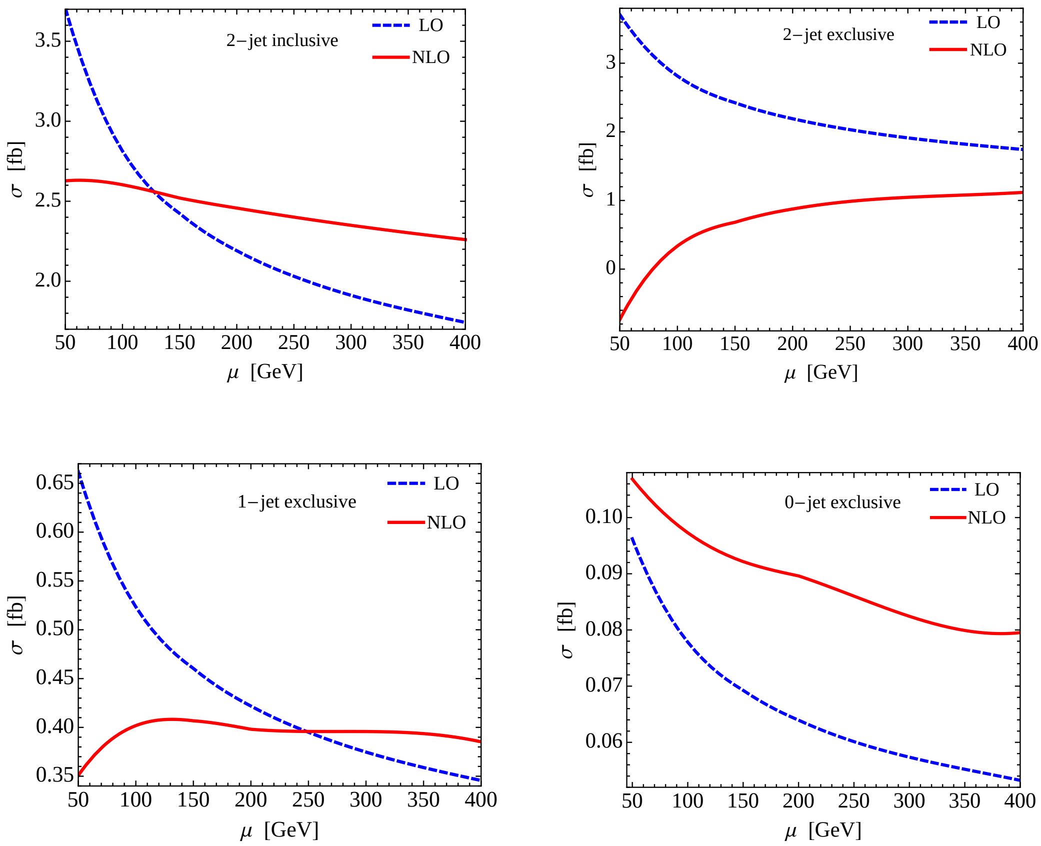

Figure 5.3: The dependence of the cross-sections for the process $pp \to W^+(\to \nu_e e^+)W^+(\to \nu_\mu \mu^+) + n$ jets ($n = 0, 1, 2, \geq 2$) at the $\sqrt{s} = 14$ TeV LHC on the factorisation and renormalisation scale μ. Leading-order (LO) cross-sections are in dashed blue; next-to-leading order (NLO) cross-sections are in solid red. The cuts used are described in the text.

quark-antiquark line guarantees a finite cross-section, even if a jet has vanishing transverse momentum. This is because the emission of a massive particle ensures that the gluon propagator $1/k^2 = 1/(p_q + p_{\bar{q}} + p_W)^2$ does not become singular even if the quarks are collinear or if one is soft. It is therefore possible to consider W^+W^+ production in association with zero, one, two, or greater than two jets. Experimental searches for new physics (for example, Higgs boson searches [170]) often bin signals according to the number of associated jets, in order to identify backgrounds. Looking at $W^+W^+ + n$ jet production therefore makes sense viewed as either a signal, or as a background to BSM signals. Figure 5.3 shows the dependence of the cross-sections for $n = 0, 1, 2, \geq 2$ jets on the factorisation and renormalisation scale μ. The leading order cross-sections σ_{LO} decrease as the scale increases, due to the decrease in the strong coupling. This leads to a scale uncertainty of 25-50%, increasing with the number of jets observed. The scale uncertainties in the next-to-leading order cross-sections σ_{NLO} are notably smaller, around 10% for the 0- and 1-jet exclusive and 2-jet inclusive cross-sections. It is interesting to note that the "optimal" scale, defined as the scale which minimises the NLO corrections, changes with the number of jets observed. The central values for the cross-sections shown in table 5.5 are for $\mu = 150$ GeV, and the scale variation shown is the difference between this and the cross-section at $\mu = 400$ GeV (superscript) and $\mu = 50$ GeV (subscript). The next-to-leading order corrections modify the central value of the cross-sections by 5-15%.

Final state	$\sigma_{\rm LO}$	$\sigma_{\rm NLO}$
2-jet incl	$2.42^{-0.68}_{+1.28}$	$2.52^{-0.26}_{+0.11}$
2-jet excl	$2.42^{-0.68}_{+1.28}$	$0.68^{+0.43}_{-1.42}$
1-jet excl	$0.46^{-0.11}_{+0.20}$	$0.41^{-0.02}_{-0.06}$
0-jet excl	$0.07^{-0.02}_{+0.03}$	$0.08^{-0.01}_{+0.01}$

Table 5.5: Leading and next-to-leading order cross-sections for the process $pp \to W^+(\to \nu_e e^+)W^+(\to \nu_\mu \mu^+) + nj$ at the $\sqrt{s} = 14$ TeV LHC. The central value is at a scale $\mu = 150$ GeV. The superscript (subscript) indicates the difference between this value and the cross-section at $\mu = 400$ (50) GeV. The cuts are described in the text.

In contrast to this, the NLO corrections have a significant effect on the exclusive 2-jet production cross-section, reversing the dependence on the scale. At $\mu = 150$ GeV, the NLO corrections reduce the LO result by approximately a factor 3. More alarmingly, the NLO cross-section becomes negative for $\mu \lesssim 70$ GeV (admittedly, this is a very low scale for a process involving two W-bosons and two jets). A possible explanation for this is that the $p_{T,j}$ cut is too small: relatively soft jets contribute to the inclusive cross-section rather than the exclusive, and this ruins the convergence of the pQCD expansion for the latter. However, this does not account for the small scale variation, presumably indicating good convergence, that is seen in the 2-jet inclusive cross-section, as well as in the 0- and 1-jet exclusive cross-sections. Furthermore, even with a very large jet cut, the 2-jet exclusive cross-section still shows a scale dependence comparable to that of the LO cross-section. It is evident though, looking at figure 5.4, that the scale variation of the 2-jet exclusive cross-section is reduced as $p_{T,j}$ is increased, with no comparable decrease for the 2-jet inclusive cross-section. It is not clear why this is the case, but it does suggest that by using a cut on the jet transverse momentum $p_{T,j} > 40$ GeV, the 2-jet exclusive cross-section can be kept positive for a reasonable scale range, and the scale variation can be reduced.

Figure 5.4 also shows that even for a relatively large cut on $p_{T,j}$, say $p_{T,j} > 60$ GeV, the inclusive cross-section is around a factor of 2 greater than the exclusive cross-section. This implies that a large percentage of events with at least two hard jets have a third jet. This may be understood as follows. In the t-channel production, the final state quarks which give rise to the jets are colour-correlated and emitted with a large pseudorapidity difference (see figure 5.5). This gives a large angle for the emission of a hard third jet. This feature might be useful in discriminating between this and other processes which give rise to the same experimental signature.

The full inclusive cross-section is the sum of the 0- and 1-jet exclusive and 2-jet inclusive cross-sections, and is approximately 3.0 fb. This is a small cross-section; however, due to the unusual experimental signature of two same-sign leptons, jets, and missing energy, it should be easily identifiable. The LHC is already delivering a large luminosity: given an integrated luminosity of 100 fb^{-1}, around 600 events (including all lepton flavour combinations) should be recorded, providing sufficient statistics to analyse kinematic distributions.

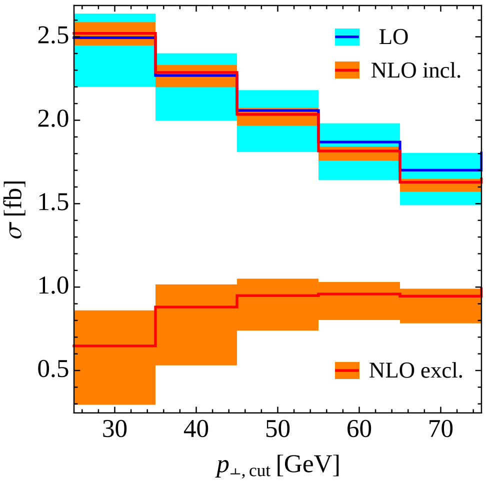

Figure 5.4: The dependence of the LO cross-section, and NLO inclusive and exclusive cross-sections, for the process $pp \to W^+(\to \nu_e e^+)W^+(\to \nu_\mu \mu^+)jj$ at the $\sqrt{s} = 14$ TeV LHC on the cut on the jet transverse momentum $p_{T,j}$. The LO cross-section is in blue, the NLO in red. The central values are at $\mu = 140$ GeV, and the bands show the effect of varying the scale between 100 and 200 GeV.

The 2-jet inclusive distributions for the jet kinematics are shown in figure 5.5. As with table 5.5, the central scale used is $\mu = 150$ GeV and the scale uncertainty for 50 GeV $\leq \mu \leq$ 400 GeV is shown. The transverse momentum and pseudorapidity of the hardest jet j_1 and the transverse momentum of the next-to-hardest jet j_2 are shown, together with the pseudorapidity difference between the jets $\Delta\eta_{j_1 j_2}$. The p_T distribution peaks at the relatively large values of about 100 GeV for the hardest jet and 40 GeV for the next-to-hardest jet. The reduced scale uncertainty at NLO can be clearly seen. The NLO corrections do not change the shape of the distributions considerably, other than to slightly reduce the differential cross-section for jets with very large transverse momentum. This is a common feature seen when LO distributions are computed at a fixed, as opposed to dynamic, scale. Indeed, at these values of transverse momentum, the scale of the process is larger than the largest choice of scale $\mu = 400$ GeV, and a dynamic scale would be preferable. This can be clearly seen in the $p_{T,j2}$ distribution, which becomes negative for $\mu \geq 400$ GeV. For such events, the scale of the process is around 1 TeV, so clearly the choice of μ is too small. Using a dynamic scale would give more reliable predictions for these high-end tails of the distributions.

Distributions for the transverse momentum and pseudorapidity of the positron, the missing transverse momentum, the invariant mass of the lepton system m_{ll}, the pseudorapidity difference between the leptons $\Delta\eta_{ll}$, and the transverse mass of the W-pair are shown in figure 5.6. This last quantity is defined as

$$m_{T,WW} = \sqrt{\left(E_{T,ll} + E_{T,\mathrm{miss}}\right)^2 - \left(\mathbf{p}_{T,ll} + \mathbf{p}_{T,\mathrm{miss}}\right)^2}, \tag{5.6.2}$$

with $E_{T,ll} = \sqrt{p_{T,ll}^2 + m_{ll}^2}$ and $E_{T,\mathrm{miss}} = \sqrt{\mathbf{p}_{T,\mathrm{miss}}^2 + m_{ll}^2}$. The depletion at large values is seen again in the distributions of the transverse momenta, invariant mass of the lepton system, and transverse mass of the W-pair. Otherwise, the shapes are unchanged, but the NLO results have a smaller scale uncertainty.

In figure 5.7, the angular distance between the leptons and the jets, defined as

$$R_{jl} = \sqrt{\left(\eta_l - \eta_j\right)^2 + \left(\phi_l - \phi_j\right)^2}, \tag{5.6.3}$$

is shown, together with the azimuthal angle between the leptons $\Delta\phi_{ll}$, and the total transverse momentum $H_{T,\mathrm{TOT}} = \sum_j p_{T,j} + p_{T,e^+} + p_{T,\mu^+} + p_{T,\mathrm{miss}}$. The angular distance R_{jl} is sharper for the hardest jet than for the next-to-hardest jet, although both peak at $R_{jl} \simeq 3$, with the NLO corrections increasing R_{jl}. The leptons in the transverse plane tend to be back-to-back, with a slight depletion from the NLO corrections. The $H_{T,\mathrm{TOT}}$ distribution displays the usual depletion at large values.

These distributions can play an important role in distinguishing between the $pp \to W^+W^+ + 2$ jet process and other processes with the same observed final state. For example, a W^+-pair produced in double parton scattering will have a relatively flat $\Delta\phi_{ll}$ distribution [152].

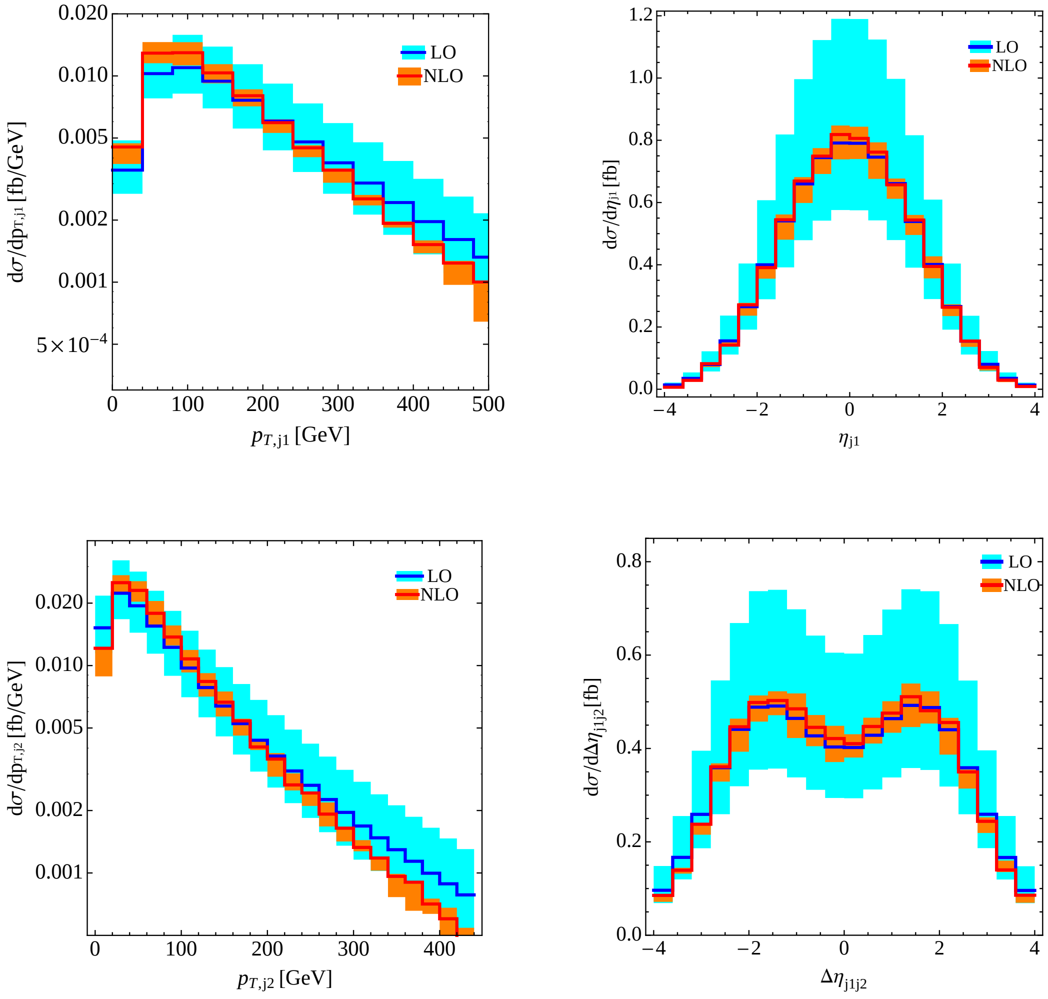

Figure 5.5: Jet distributions for the process $pp \to W^+(\to \nu_e e^+)W^+(\to \nu_\mu \mu^+)jj$ at the $\sqrt{s} = 14$ TeV LHC, at LO and NLO. The bands show the scale uncertainty 50 GeV $\leq \mu \leq$ 400 GeV, with a central scale $\mu = 150$ GeV. The cuts used are described in the text. Shown are the transverse momentum and pseudorapidity of the hardest jet, the transverse momentum of the next-to-hardest jet, and the pseudorapidity difference between the two jets.

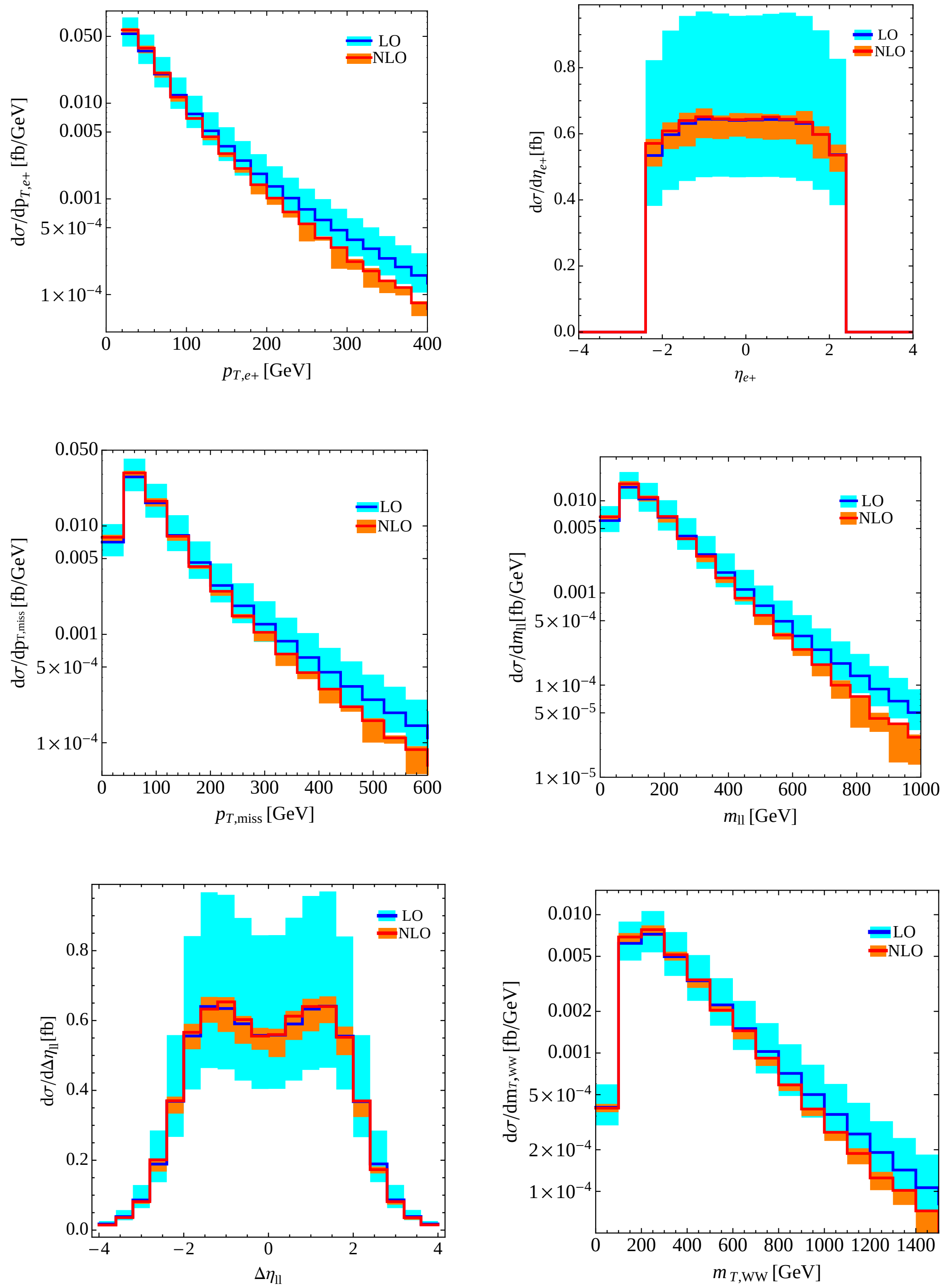

Figure 5.6: Lepton distributions for the process $pp \to W^+(\to \nu_e e^+)W^+(\to \nu_\mu \mu^+)jj$ at the $\sqrt{s} = 14$ TeV LHC, at LO and NLO. The bands show the scale uncertainty 50 GeV $\leq \mu \leq$ 400 GeV, with a central scale $\mu = 150$ GeV. The cuts used are described in the text. Shown are the transverse momentum and pseudorapidity of the positron, the missing transverse momentum, the invariant mass of the charged leptons, the pseudorapidity difference between the leptons, and the transverse mass of the W-pair.

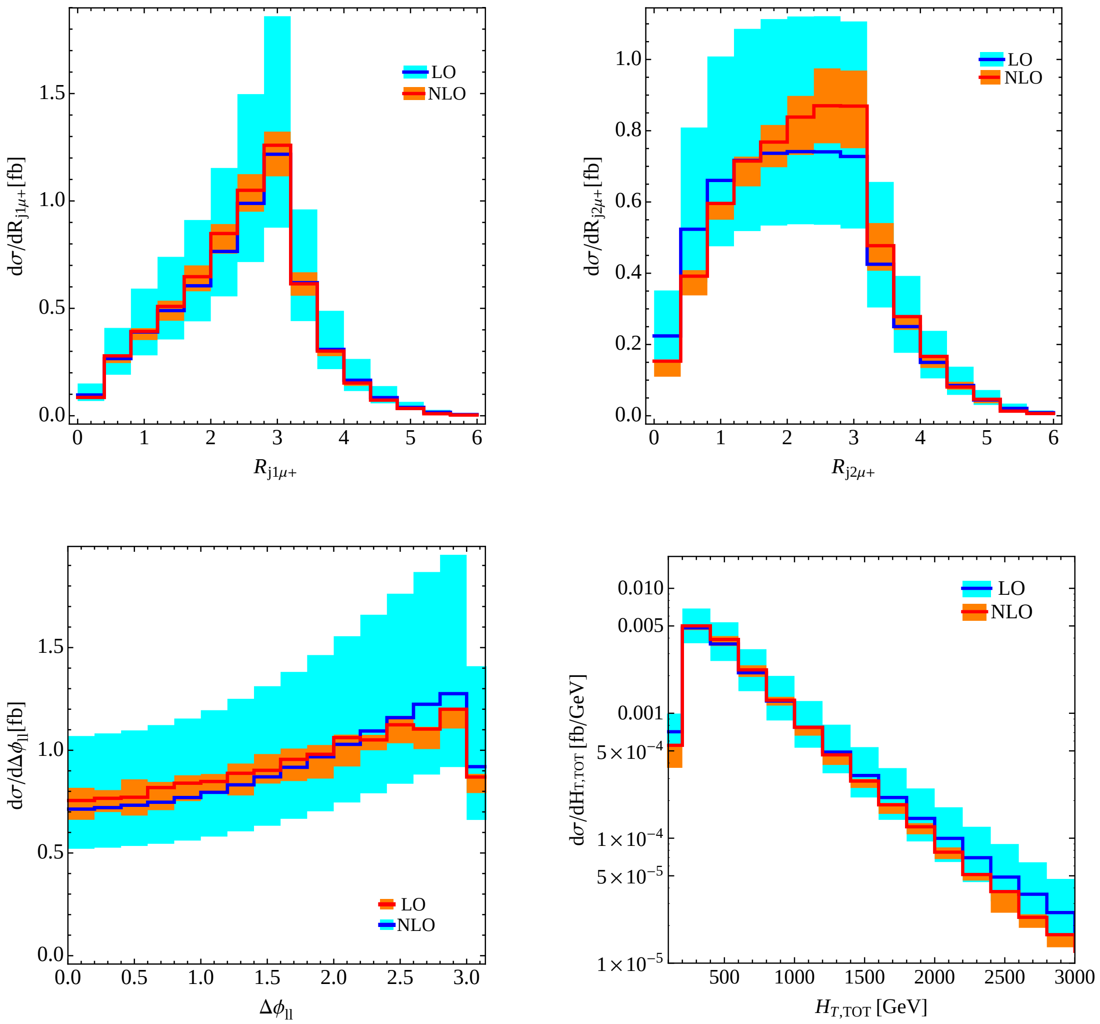

Figure 5.7: Kinematic distributions for the process $pp \to W^+(\to \nu_e e^+)W^+(\to \nu_\mu \mu^+)jj$ at the $\sqrt{s} = 14$ TeV LHC, at LO and NLO. The bands show the scale uncertainty 50 GeV $\leq \mu \leq$ 400 GeV, with a central scale $\mu = 150$ GeV. The cuts used are described in the text. Shown are the distance R_{jl} between each of the jets and the μ^+, the azimuthal angle between the charged leptons, and the sum of all transverse momenta $H_{T,TOT}$.

5.7 Conclusions

In this chapter, the next-to-leading order QCD computation of the cross-sections and distributions for the process $pp \to W^+W^+jj$ were shown. The one-loop amplitude was calculated using the methods of generalised unitarity and OPP subtraction, as detailed in chapters 3 and 4. The presence of two colour-neutral W-bosons did not cause undue problems, despite the use of colour-ordering. The presence of two same-sign W-boson put strong restrictions on the flavour structure, allowing the NLO cross-section to be defined in an infrared safe manner with 0,1,2, or more jets.

The leading-order cross-sections show a strong scale dependence, which is reduced by the next-to-leading order corrections for the 0- and 1-jet exclusive cross-sections, as well as for the 2-jet inclusive cross-section. The NLO corrections effect moderate changes to the central cross-section values. The cross-section across all jet channels, and allowing the W-bosons to decay into all lepton flavours, is around 6 fb: a sizeable cross-section given the distinctiveness of the experimental signature.

The 2-jet exclusive cross-section is not as well behaved. Here, the NLO corrections change the cross-sections dramatically. The scale dependence is reversed, however the magnitude of this dependence is only slightly reduced. The origin of these difficulties is unclear, but it could be in part due to too small a cut on the jet transverse momentum. Since the 2-jet exclusive cross-section is notably smaller than the 2-jet inclusive cross-section, more than half of the events with at least two hard jets also have a third. This characteristic may be useful in discriminating between this process and other processes with the same experimental signature. This may also be accomplished using kinematic distributions, which have a greatly reduced scale uncertainty when computed to NLO.

Chapter 6

Hadroproduction of W^+W^-jj

6.1 Introduction

This chapter, following largely from ref. [82], will focus on the hadroproduction of W^+W^- in association with two jets, at the Tevatron and the LHC. The W-bosons decay leptonically, so that the experimental signature is two opposite charged leptons, two jets, and missing energy. The production of two same-sign W-bosons, considered in the previous chapter, is a background to various exotic New Physics processes. In contrast, W^+W^- production is a background to arguably the most anticipated signal at the LHC: the Standard Model Higgs boson. The discovery of a new boson, consistent with the SM Higgs, has recently been announced [3, 4], with a mass in the region of 125–126 GeV. At these values, the dominant decay of the SM Higgs is to $b\bar{b}$. The subdominant decay is $H \to W^+W^-$, and given the experimental difficulties in the identification of final state b-quarks, this is a very important channel.

As mentioned in the Introduction, both the Tevatron and the LHC experiments bin putative Higgs production signals according to the number of jets produced, as these channels have different backgrounds. Of course, each additional jet costs a factor of α_s, but nevertheless Hjj production accounts for around 10% of the total Higgs production [22, 171]. Importantly, Hjj can be produced either through gluon fusion (the main Higgs production mechanism) or through weak boson fusion (WBF). The angular distribution of the two jets can provide information about the coupling of the Higgs to the top quark in gluon fusion [172], and about the coupling of the Higgs to the electroweak sector in WBF [173]. This may help in determining whether the newly discovered Higgs boson is SM-like or not. For either production mechanism, W^+W^-jj production is an irreducible background which needs to be fully understood if accurate identification of the Higgs is to be made. As discussed in the Introduction, this requires a NLO QCD calculation.

The process $pp(\bar{p}) \to W^+W^-jj$ involves two types of processes at a partonic level: the four partons (two initial state, two final state) involved may be either a quark-antiquark pair and two gluons, or two quark-antiquark pairs. The latter was described in the previous chapter; however, the difference in the charge of the W-pair drastically alters the flavour structure. I will discuss the leading order, real radiation and virtual amplitudes separately for the two partonic processes, which for convenience I will call “two quark, two gluon” and “four quark” processes respectively.

Hadroproduction of W^+W^-jj can occur through electroweak as well as strong mechanisms, and in fact the NLO QCD corrections to the electroweak production are known [174]. I will consider only strong production. As for W^+W^+jj production, interference between the two mechanisms is subleading in colour, and furthermore can only occur for the four quark partonic processes in strong production. Due to the large gluon flux at high-energy colliders and the colour enhancement of gluonic interactions, these partonic contributions turn out to account for only 15% of the total cross-section. Mixing is therefore ignored, and the calculation presented here is concerned only with the NLO QCD production of W^+W^-jj through the strong mechanism.

6.2 Leading order amplitudes

6.2.1 Two quark, two gluon amplitudes

I will begin by considering the leading order amplitude of the process $0 \to \bar{q}qggW^+(\to \nu_\mu + \mu^+) + W^-(\to e^- + \bar{\nu}_e)$, with all particles outgoing. There is a single quark-antiquark line to which the electroweak bosons are attached. The leptonic decay of the W-bosons is taken into account through the definition of the polarisation vectors from equation (4.2.24). I use a unit CKM matrix, so that the flavour of the two quarks is the same, and there is no mixing of quark generations. The tree-level amplitude is

$$\begin{aligned}\mathcal{M}^0_{gg}(\bar{q}_1, q_2, g_3, g_4; \nu_\mu, \mu^+, e^-, \bar{\nu}_e) =& g_s^2 \Big(\frac{g_w}{\sqrt{2}}\Big)^4 \Big[\big(t^{a_3} t^{a_4}\big)_{\bar{\imath}_1, i_2} A^0(\bar{q}_1, q_2, g_3, g_4) \\ &+ \big(t^{a_4} t^{a_3}\big)_{\bar{\imath}_1, i_2} A^0(\bar{q}_1, q_2, g_4, g_3)\Big],\end{aligned} \tag{6.2.1}$$

where g_s and g_w are again the strong and weak couplings, and two partial amplitudes are used, with the different ordering of the gluons indicated. The ordering of the W-bosons relative to each other is fixed by the flavour of the quark-antiquark pair, but all insertions of the W-pair relative to the gluons which respect this ordering must be considered. Furthermore, the W-pair may be coupled either directly to the quarks or via an intermediate Z-boson or photon. To make this explicit, the partial amplitude may be written

$$\begin{aligned}A^0(\bar{q}_1, q_2, g_3, g_4) =& A^{0,[WW]}([\bar{q}_1, W, W, q], g_3, g_4)\delta_{h_2,-1} \\ &+ C^{(q_2,h_2)} A^{0,[Z/\gamma]}([\bar{q}_1, Z/\gamma, q_2], g_3, g_4),\end{aligned} \tag{6.2.2}$$

where the couplings are

$$C^{(q,h)} = 2Q^{(q)} \sin^2\theta_w + P_Z(s_V)(T_3^{(h)} - 2Q^{(q)} \sin^2\theta_w). \tag{6.2.3}$$

In equation (6.2.3), $Q^{(q)}$ is the electromagnetic charge of the quark q, $h = \pm 1$ is its helicity, θ_w is the weak mixing angle, and $T_3^{(-1)} = 1$, $T_3^{(+1)} = 0$. The left-handed coupling of the W-bosons to the quarks is taken into account by the $\delta_{h_2,-1}$ factor in equation (6.2.2), which causes the first term to vanish if the quark is right-handed. The amplitudes $A^{0,[WW]}$ are calculated using the Berends-Giele current $\mathsf{f\_VV\overline{f}}$ with $n_1 = 0$ and $n_2 = 2$. The coupling of the off-shell boson to W^+W^- and subsequent leptonic decays is taken into account by considering the off-shell boson with momentum $p_V = p_{W^+} + p_{W^-} = p_{\nu_\mu} + p_{\mu^+} + p_{e^-} + p_{\bar{\nu}_e}$ and a polarisation vector following equation (4.2.25). These are used in the current $\mathsf{f\_V\overline{f}}$ with $n_1 = 0$ and $n_2 = 2$. Single resonant amplitudes are neglected. The Z-boson propagator is

$$P_Z(s_Z) = \frac{s_V}{s_V - m_Z^2 + i\Gamma_Z m_Z}, \tag{6.2.4}$$

with the momentum-squared $s_V = p_V^2$.

The matrix element squared is

$$\begin{aligned}|\mathcal{M}^0_{gg}(\bar{q}_1, q_2, &g_3, g_4, \nu_\mu, \mu^+, e^-, \bar{\nu}_e)|^2 = \\ & S \sum_{\text{hel}} g_s^4 \Big(\frac{g_w}{\sqrt{2}}\Big)^8 \Big\{4C_F^2 N_c\big(|A^0(\bar{q}_1, q_2, g_3, g_4)|^2 + A^0(\bar{q}_1, q_2, g_4, g_3)|^2\big) \\ & - 4C_F \mathrm{Real}\big(A^0(\bar{q}_1, q_2, g_3, g_4) A^{0*}(\bar{q}_1, q_2, g_4, g_3)\big)\Big\},\end{aligned} \tag{6.2.5}$$

where S accounts for the averaging over initial state colours and spins, as well as symmetric final states. There are seven initial state channels. The quark-antiquark channels require $S = S_{qq} = \frac{1}{4}\frac{1}{9}$, the gluon-gluon channel requires $S = S_{gg} = \frac{1}{4}\frac{1}{64}$, and the (anti)quark-gluon channels require $S = S_{qg} = \frac{1}{4}\frac{1}{24}$. The sum runs over the helicities of the gluons and the quark-antiquark pair. The results for the matrix elements squared for the different initial state configurations are shown in table 6.1, for the phase space point in equation (5.2.4). The gg initial state has four possible final state flavour combinations, and the sum is taken over these. The momentum assignment is again $f_1(-p_1) + f_2(-p_2) \to f_3(p_3) + f_4(p_4)$, where $f_{1,2,3,4} = \{g, u, d, c, s, \bar{u}, \bar{d}, \bar{c}, \bar{s}\}$. The `MadGraph` results are also shown for comparison.

Flavours	$\lvert\mathcal{M}^0_{gg}\rvert^2$	$\lvert\mathcal{M}^0_{\mathrm{MG}}\rvert^2$
$u\bar{u} \to gg$	7.406261963755649	7.406261963756443
$d\bar{d} \to gg$	8.901658442668893	8.901658442669804
$\bar{d}d \to gg$	1.830415190335487	1.830415190335636
$\bar{u}u \to gg$	4.491488196901598	4.491488196902073
$ug \to gu$	0.8199929405056734	0.8199929405057409
$dg \to gd$	0.4807022193576624	0.4807022193577046
$gu \to gu$	0.5289793305819081	0.5289793305819579
$gd \to gd$	0.2566280142351353	0.2566280142351584
$g\bar{u} \to g\bar{u}$	2.574748272111126	2.574748272111326
$g\bar{d} \to g\bar{d}$	4.334113722927112	4.334113722927462
$\bar{u}g \to g\bar{u}$	1.151410584692072	1.151410584692155
$\bar{d}g \to g\bar{d}$	1.525020087776809	1.525020087776924
$gg \to \bar{u}u + \bar{d}d + \bar{s}s + \bar{c}c$	0.03139299450851931	0.0313929945085216

Table 6.1: Colour-squared and averaged matrix element for all channels and all flavour combinations of the leading order process $0 \to \bar{q}qgg + W^+(\to \nu_\mu + \mu^+) + W^-(\to e^- + \bar{\nu}_e)$ for the phase space point given in equation (5.2.4). Production of W-bosons through an intermediate Z-boson or photon is considered; single resonant amplitudes are not. The third column shows the results obtained from `MadGraph`. The units shown are 10^{-19} GeV^{-8}, and the physical parameters used are described in section 5.2.

6.2.2 Four quark amplitudes

I will now consider the leading order amplitudes of the partonic process $0 \to \bar{q}_1 q_2 \bar{q}_1 q_2 + W^+(\to \nu_\mu + \mu^+) + W^-(\to e^- + \bar{\nu}_e)$. These amplitudes are similar to those used for W^+W^+ production in section 5.2, but with a more complicated flavour structure because the W^+W^- system carries no overall electromagnetic charge. As before, the tree-level amplitude can be envisioned as two quark-antiquark lines joined by an intermediate gluon, with both the s- and t-channel allowed. The s-channel matrix element is (cf. equation (5.2.1))

$$\mathcal{M}^0_{4q,s}(\bar{q}_1, q_2, \bar{q}_3, q_4; \nu_\mu, \mu^+, e^-, \bar{\nu}_e) = g_s^2 \Big(\frac{g_w}{\sqrt{2}}\Big)^4 \Big(\delta_{\bar{\imath}_1 i_4}\delta_{\bar{\imath}_3 i_2} - \frac{1}{N_c}\delta_{\bar{\imath}_1 i_2}\delta_{\bar{\imath}_3 i_4}\Big) B^0_s(\bar{q}_1, q_2, \bar{q}_3, q_4), \tag{6.2.6}$$

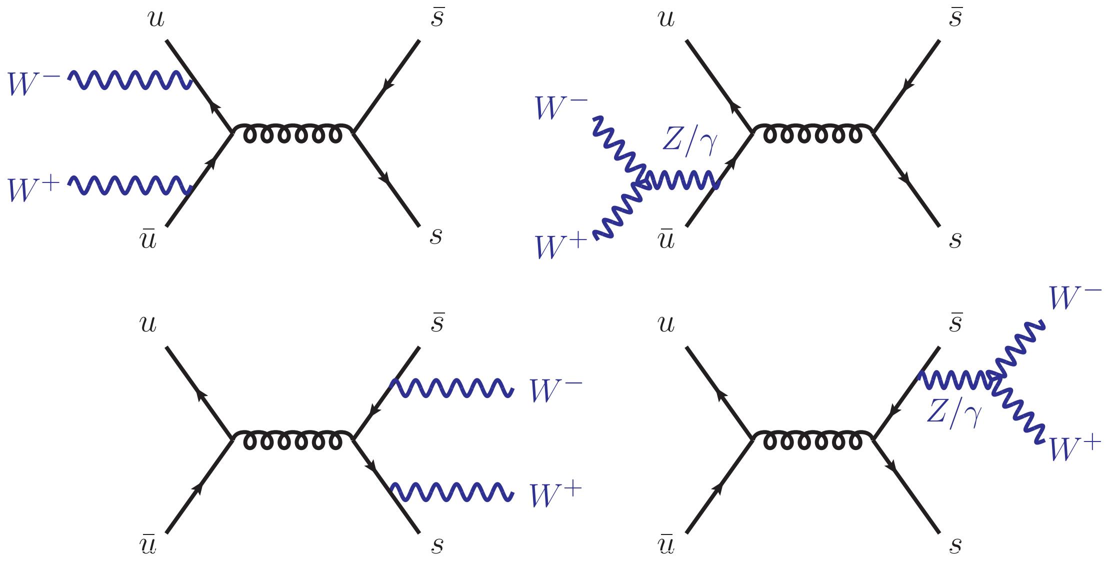

Figure 6.1: Typical Feynman diagrams for $B_s^0(\bar{u}, u, \bar{s}, s)$. Both W-bosons are attached to the same quark-antiquark line, and production through an intermediate Z-boson or photon is considered. The ordering of the W-bosons is determined by the flavours of the quarks.

with the t-channel obtained by swapping $2 \leftrightarrow 4$ in the labels of the quarks and the colour indices.

Considering the s-channel, if the flavours of $\bar{q}_1$ and q_2 are the same, then the flavours of $\bar{q}_3$ and q_4 must be the same, and both W-bosons are radiated from the same quark-antiquark line. (Recall that I use a unit CKM matrix). The flavours of the quarks determine the ordering of the W-pair. They may also be produced through an intermediate Z-boson or photon, which is handled using the polarisation vector of equation (4.2.25). By analogy with equation (6.2.2), the primitive amplitude can be written as

$$
\begin{aligned}
B_s^0(\bar{q}_1, q_2, \bar{q}_3, q_4) = & B_s^{0,[WW]}([\bar{q}_1, W, W, q_2], [\bar{q}_3, q_4])\delta_{h_2,-1} \\
& + B_s^{0,[WW]}([\bar{q}_1, q_2], [\bar{q}_3, W, W, q_4])\delta_{h_4,-1} \\
& + C^{(q_2,h_2)} B_s^{0,[Z/\gamma]}([\bar{q}_1, Z/\gamma, q_2], [\bar{q}_3, q_4]) \\
& + C^{(q_4,h_4)} B_s^{0,[Z/\gamma]}([\bar{q}_1, q_2], [\bar{q}_3, Z/\gamma, q_4]),
\end{aligned}
\tag{6.2.7}
$$

for amplitudes of this type, where the parentheses [ ] indicate the two quark-antiquark lines. The helicites of q_2 and q_4 are indicated by h_2 and h_4 respectively, and the δ factors in the first and second terms account for the left-handed coupling of the W-bosons to the quarks. The first and second terms are calculated using the current `f_VVf̄ff̄` with no external gluons and $s_w = 1$ and $s_w = 3$ respectively. The third and fourth terms are calculated using the current `f_Vf̄ff̄` with $s_w = 1$ and $s_w = 3$ respectively. The couplings $C^{(q,h)}$ are given in equation (6.2.3).

On the other hand, if there is a flavour change on the quark-antiquark lines, then one W-boson is radiated from each of the lines. In this case, the current `f_VVf̄ff̄` with $s_w = 2$ is used to calculate B_s^0. Which W-boson is radiated from which quark-antiquark line depends on the flavours of the quarks. Amplitudes of this second type occur only when both quarks are left-handed, as was the case for W^+W^+ production.

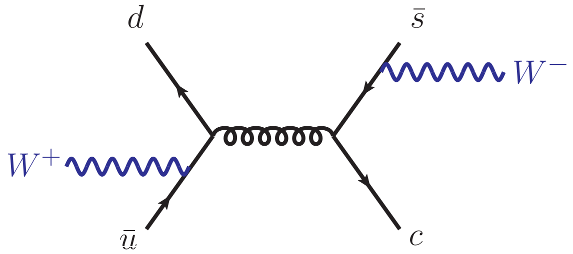

Figure 6.2: Typical Feynman diagram for $B_s^0(\bar{u}, d, \bar{s}, c)$. One W-boson is attached to each of the quark-antiquark lines; the flavours of the quarks determine which of the W-pair is attached to which line.

Typical Feynman diagrams for these two types of amplitude are shown in figures 6.1 and 6.2. The flavour structure of the t-channel is identical with the exchange $q_2 \leftrightarrow q_4$. A further complication is present if both s- and t-channel amplitudes are allowed by the flavour configuration, in which case amplitudes of both types need to be included. For example, if the flavours are $\bar{u}u\bar{d}d$, then the s-channel has quark-antiquark lines $\bar{u}u$ and $\bar{d}d$, and the amplitudes are of the first type. The t-channel has quark-antiquark lines $\bar{u}d$ and $\bar{d}u$ and has amplitudes of the second type.

The matrix element squared is identical to equation (5.2.2):

$$\begin{aligned}|\mathcal{M}_{4q}^0|^2 =& S_{qq} \sum_{\text{hel}} g_s^4 \Big(\frac{g_w}{\sqrt{2}}\Big)^8 \Big\{ 2C_F N_c \big(|B_s^0(\bar{q}_1, q_2, \bar{q}_3, q_4)|^2 + |B_t^0(\bar{q}_1, q_4, \bar{q}_3, q_2)|^2 \big) \\ & - 4C_F \text{Real}\big(B_s^0(\bar{q}_1, q_2, \bar{q}_3, q_4) B_t^{0*}(\bar{q}_1, q_4, \bar{q}_3, q_2) \big) \delta_{h_2 h_4} \Big\}.\end{aligned} \tag{6.2.8}$$

The sum is over the helicities of the quarks, and either the s- or t-channel may vanish depending on the flavours of the quarks. The $\delta_{h_2 h_4}$ factor in the last term ensures that the helicities of the quarks in the mixing terms match, meaning that mixing can only occur if the quark-antiquark lines are either both left-handed or both right-handed. A comparison with `MadGraph` is shown in table 6.2 for each initial flavour state, with a sum over all possible final state flavour configurations.

Flavours	$\lvert\mathcal{M}^0_{4q}\rvert^2$	$\lvert\mathcal{M}^0_{\mathrm{MG}}\rvert^2$
$u\bar{c} \to \bar{c}u + \bar{s}d$	0.5311485826186718	0.5311485826187159
$u\bar{s} \to \bar{s}u$	0.8417285426262163	0.8417285426262881
$u\bar{u} \to \bar{c}c + \bar{s}s + \bar{u}u + \bar{d}d$	12.65335452235076	12.65335452235214
$u\bar{d} \to \bar{d}u + \bar{s}c$	0.8775368878513676	0.8775368878514423
$d\bar{c} \to \bar{c}d$	0.4479436382010625	0.4479436382011002
$d\bar{s} \to \bar{s}d + \bar{c}u$	0.7243783567687887	0.7243783567688506
$d\bar{u} \to \bar{c}s + \bar{u}d$	0.4511754846394283	0.4511754846394664
$d\bar{d} \to \bar{c}c + \bar{s}s + \bar{u}u + \bar{d}d$	15.31656937269305	15.31656937269466
$\bar{u}c \to \bar{u}c + \bar{d}s$	0.13086235672735011	0.1308623567273641
$\bar{u}s \to \bar{u}s$	0.05827181215024162	0.05827181215024692
$\bar{u}u \to \bar{c}c + \bar{s}s + \bar{u}u + \bar{d}d$	8.384086053287545	8.384086053288434
$\bar{u}d \to \bar{u}d + \bar{c}s$	0.06137483858002959	0.06137483858003523
$\bar{d}c \to \bar{d}c$	0.1307811561658334	0.1307811561658477
$\bar{d}s \to \bar{d}s + \bar{u}c$	0.05633039749043258	0.05633039749043762
$\bar{d}u \to \bar{s}c + \bar{d}u$	0.1313850071465028	0.1313850071465171
$\bar{d}d \to \bar{c}c + \bar{s}s + \bar{u}u + \bar{d}d$	3.297455162121854	3.297455162122116
$uc \to uc$	0.1178743947541448	0.1178743947541531
$us \to us + dc$	0.04616745239462271	0.04616745239462550
$uu \to uu$	0.08071387406215721	0.08071387406216323
$ud \to ud$	0.04327618820700419	0.04327618820700679
$dc \to dc + us$	0.1292936613217951	0.12929366132180401
$ds \to ds$	0.05453298018958077	0.05453298018958417
$du \to du$	0.1318334929750386	0.1318334929750477
$dd \to dd$	0.07048471480409210	0.07048471480409762
$\bar{u}\bar{c} \to \bar{u}\bar{c}$	0.7886267560576286	0.7886267560576713
$\bar{u}\bar{s} \to \bar{u}\bar{s} + \bar{d}\bar{c}$	1.403120919032502	1.403120919032585
$\bar{u}\bar{u} \to \bar{d}\bar{u}$	0.5384004337712884	0.5384004337713221
$\bar{u}\bar{d} \to \bar{u}\bar{d}$	1.368204610278690	1.368204610278770
$\bar{d}\bar{c} \to \bar{d}\bar{c} + \bar{u}\bar{s}$	0.9838771971028136	0.9838771971028715
$\bar{d}\bar{s} \to \bar{d}\bar{s}$	1.619761763822084	1.619761763822183
$\bar{d}\bar{u} \to \bar{d}\bar{u}$	0.9878071990975874	0.9878071990976456
$\bar{d}\bar{d} \to \bar{d}\bar{d}$	1.616030017846718	1.616030017846834

Table 6.2: Colour-squared and averaged matrix elements for all initial state channels and flavour combinations of the leading order process $0 \to \bar{q}_1 q_2 \bar{q}_3 q_4 + W^+(\to \nu_\mu + \mu^+) + W^-(\to e^- + \bar{\nu}_e)$, for the phase space point given in equation (5.2.4). There is a sum over final state flavour configurations. Production of W-bosons through an intermediate Z-boson or photon is considered; single resonant amplitudes are not. The third column shows the results obtained from `MadGraph`. The units shown are 10^{-20} GeV^{-8}, and the physical parameters used are described in section 5.2.

6.3 Real radiation amplitudes

6.3.1 Two quark, two gluon amplitudes

In this section, I will consider real radiation through the emission of an extra gluon relative to the two quark, two gluon leading-order amplitudes. This is not the full story, since real radiation may also come about through the splitting of a gluon into a quark-antiquark pair. Such amplitudes will then involve two quark-antiquark pairs and a gluon, which will be the focus of the next section. There is no ambiguity in this division, as long as the subtraction terms and integrated dipoles are constructed with it in mind. I will therefore consider tree-level amplitudes with three gluons, $0 \to \bar{q}qggg + W^+(\to \nu_\mu + \mu^+) + W^-(\to e^- + \bar{\nu}_e)$. These may be written in terms of six partial amplitudes, with gluon orderings $(345, 354, 435, 453, 534, 543) = S_3$. The matrix element is

$$\begin{aligned}\mathcal{M}^{\rm R}_{gg} =& \mathcal{M}^0(\bar{q}_1, q_2, g, g, g; \nu_\mu, \mu^+, e^-, \bar{\nu}_e) = \\ & g_s^3 \Big(\frac{g_w}{\sqrt{2}}\Big)^4 \sum_{\sigma \in S_3} \Big(t^{a_{\sigma_3}} t^{a_{\sigma_4}} t^{a_{\sigma_5}}\Big)_{\bar{i}_1 i_2} A^0(\bar{q}_1, q_2, g_{\sigma_3}, g_{\sigma_4}, g_{\sigma_5}),\end{aligned} \tag{6.3.1}$$

with the primitive amplitudes calculated using the currents f_Vf̄ and f_VVf̄ with $n_1 = 0$ and $n_2 = 3$. The flavour structure is the same as in section 6.2.1.

The colour-squared matrix element can be written in matrix form as

$$|\mathcal{M}^R_{gg}|^2 = S_i \sum_{\rm hel} g_s^6 \Big(\frac{g_w}{\sqrt{2}}\Big)^8 \mathbf{A^0}^\dagger \mathbf{C} \mathbf{A^0}, \tag{6.3.2}$$

where, as in section 6.2.1, the averaging over initial state colours and spins, and symmetric final states, is taken into account by the factor S, with $S_{qq} = \frac{1}{4}\frac{1}{9}\frac{1}{6}$, $S_{qg} = \frac{1}{4}\frac{1}{24}\frac{1}{2}$, and $S_{gg} = \frac{1}{4}\frac{1}{64}$. The elements of $\mathbf{A^0}$ are the six partial amplitudes,

$$\mathbf{A^0} = (A^0_{345}, A^0_{354}, A^0_{435}, A^0_{453}, A^0_{534}, A^0_{543}) \tag{6.3.3}$$

with

$$A^0_{\sigma_3\sigma_4\sigma_5} \equiv A^0(\bar{q}_1, q_2, g_{\sigma_3}, g_{\sigma_4}, g_{\sigma_5}). \tag{6.3.4}$$

The colour matrix is

$$\mathbf{C} = \begin{pmatrix} C_1 & C_2 & C_2 & C_3 & C_3 & C_4 \\ C_2 & C_1 & C_3 & C_4 & C_2 & C_3 \\ C_2 & C_3 & C_1 & C_2 & C_4 & C_3 \\ C_3 & C_4 & C_2 & C_1 & C_3 & C_2 \\ C_3 & C_2 & C_4 & C_3 & C_1 & C_2 \\ C_4 & C_3 & C_3 & C_2 & C_2 & C_1 \end{pmatrix}, \tag{6.3.5}$$

with

$$\begin{array}{rclcr} C_1 &=& \mathrm{Tr}(t^{a_3}t^{a_4}t^{a_5}t^{a_5}t^{a_4}t^{a_3}) &=& 2C_F^4 N_c^2 \\ C_2 &=& \mathrm{Tr}(t^{a_3}t^{a_4}t^{a_5}t^{a_5}t^{a_3}t^{a_4}) &=& -C_F^3 N_c \\ C_3 &=& \mathrm{Tr}(t^{a_3}t^{a_4}t^{a_5}t^{a_4}t^{a_3}t^{a_5}) &=& 2C_F/N_c \\ C_4 &=& \mathrm{Tr}(t^{a_3}t^{a_4}t^{a_5}t^{a_3}t^{a_4}t^{a_5}) &=& 2C_F/N_c(N_c^2+1). \end{array} \tag{6.3.6}$$

The matrix elements squared are shown in table 6.3 for the phase space point in equation (5.3.5), together with the results from `MadGraph` for comparison. The quark momentum assignment is the same as in section 5.3: $f_1(-p_1) + f_2(-p_2) \to f_3(p_3) + f_4(p_4) + f_5(p_5)$, with $f_{1,2,3,4,5} = \{g, u, d, c, s, \bar{u}, \bar{d}, \bar{c}, \bar{s}\}$

Flavours	$\|\mathcal{M}^R_{gg}\|^2$	$\|\mathcal{M}^R_{\mathrm{MG}}\|^2$
$u\bar{u} \to ggg$	71.50797716783816	71.50797716784358
$d\bar{d} \to ggg$	94.63084358843460	94.63084358844203
$\bar{d}d \to ggg$	15.31402939008978	15.31402939009103
$\bar{u}u \to ggg$	27.08856538291897	27.08856538292079
$ug \to ugg$	3.811015437543343	3.811015437543649
$dg \to dgg$	1.671963111534979	1.671963111535112
$gu \to ugg$	2.052955149911785	2.052955149911935
$gd \to dgg$	2.097928037908580	2.097928037908755
$g\bar{u} \to \bar{u}gg$	10.13097654819845	10.13097654819917
$g\bar{d} \to \bar{d}gg$	18.32309679130728	18.32309679130855
$\bar{u}g \to \bar{u}gg$	5.350995512425657	5.350995512426039
$\bar{d}g \to \bar{d}gg$	8.074063326607667	8.074063326608200
$gg \to d\bar{d}g + u\bar{u}g + s\bar{s}g + c\bar{c}g$	2.618636801282472	2.61863680128271

Table 6.3: As for table 6.1, for the real radiation partonic process $0 \to \bar{q}qggg + W^+(\to \nu_\mu + \mu^+) + W^-(\to e^- + \bar{\nu}_e)$. The phase space point is given in equation (5.3.5). The units are 10^{-23} GeV^{-10}, and the physical parameters used are described in section 5.2.

6.3.2 Four quark amplitudes

I will now consider tree-level amplitudes $0 \to \bar{q}_1 q_2 \bar{q}_3 q_4 g + W^+(\to \nu_\mu + \mu^+) + W^-(\to e^- + \bar{\nu}_e)$. These may arise either from the two quark, two gluon leading-order amplitudes, through the splitting of a gluon into a quark-antiquark pair, or through the emission of a gluon from the four quark leading-order amplitudes. The colour decomposition is the same as in equation (5.3.1)

$$\begin{aligned}\mathcal{M}^{\mathrm{R}}_{4q} =& \mathcal{M}^0(\bar{q}_1, q_2, \bar{q}_3, q_4, g; \nu_\mu, \mu^+, e^-, \bar{\nu}_e) = \\ & g_s^3 \Big(\frac{g_w}{\sqrt{2}}\Big)^4 \Big\{ (t^a)_{\bar{i}_1 i_4} \delta_{\bar{i}_3 i_2} B^0(\bar{q}_1, q_2, \bar{q}_3, q_4, g) + (t^a)_{\bar{i}_3 i_2} \delta_{\bar{i}_1 i_4} B^0(\bar{q}_1, q_2, g, \bar{q}_3, q_4) \\ & + \frac{1}{N_c} (t^a)_{\bar{i}_1 i_2} \delta_{\bar{i}_3 i_4} B^0(\bar{q}_1, g, q_2, \bar{q}_3, q_4) + \frac{1}{N_c} (t^a)_{\bar{i}_3 i_4} \delta_{\bar{i}_1 i_2} B^0(\bar{q}_1, q_2, \bar{q}_3, g, q_4) \Big\}.\end{aligned}$$

The flavour structure of the partial amplitudes B^0 is identical to that described in section 6.2.2, with the Berends-Giele currents having arguments $n_4 = 1$, $n_2 = 1$, $n_1 = 1$ and $n_3 = 1$ for the four terms in equation (6.3.2). The colour-squaring involves a square of the s- and t-channels as well as mixing between the two, as given in equations (5.3.2),(5.3.3), and (5.3.4). The only modification needed is that the sum over helicities should include the helicities of the quarks as well as that of the gluon. A comparison of the matrix elements with `MadGraph` is shown in table 6.4, with the momentum assignment the same as for table 6.3.

Flavours	$\lvert\mathcal{M}^R_{4q}\rvert^2$	$\lvert\mathcal{M}^R_{\mathrm{MG}}\rvert^2$
$u\bar{c} \to u\bar{c}g + d\bar{s}g$	1.950373233665980	1.950373233666107
$u\bar{s} \to u\bar{s}g$	3.588072922906441	3.588072922906723
$u\bar{u} \to c\bar{c}g + s\bar{s}g + u\bar{u}g + d\bar{d}g$	42.11692878611027	42.11692878611423
$u\bar{d} \to u\bar{d}g + c\bar{s}g$	3.595861319569640	3.595861319569924
$d\bar{c} \to d\bar{c}g$	1.985275766734713	1.985275766734840
$d\bar{s} \to d\bar{s}g + u\bar{c}g$	3.609088610675031	3.609088610675315
$d\bar{u} \to s\bar{c}g + d\bar{u}g$	2.002330703251786	2.002330703251915
$d\bar{d} \to c\bar{c}g + s\bar{s}g + u\bar{u}g + d\bar{d}g$	57.22702901259529	57.22702901260091
$\bar{u}c \to \bar{u}cg + \bar{d}sg$	0.1749888140534349	0.1749888140534467
$\bar{u}s \to s\bar{u}g$	0.2937768447536484	0.2937768447536744
$\bar{u}u \to c\bar{c}g + s\bar{s}g + u\bar{u}g + d\bar{d}g$	16.96814635330832	16.96814635330974
$\bar{u}d \to d\bar{u}g + s\bar{c}g$	0.2945010991120792	0.2945010991121053
$\bar{d}c \to c\bar{d}g$	0.2727548242737637	0.2727548242737824
$\bar{d}s \to s\bar{d}g + c\bar{u}g$	0.4567923986529778	0.4567923986530172
$\bar{d}u \to c\bar{s}g + u\bar{d}g$	0.2806672074610187	0.2806672074610380
$\bar{d}d \to c\bar{c}g + s\bar{s}g + u\bar{u}g + d\bar{d}g$	10.06413846515941	10.06413846516029
$uc \to ucg$	0.1730824140605814	0.1730824140605909
$us \to usg + dcg$	0.08228130033029084	0.08228130033029642
$uu \to uug$	0.1656542501460754	0.1656542501460850
$ud \to udg$	0.07898437680305138	0.07898437680305678
$dc \to dcg + usg$	0.1993746943036023	0.1993746943036135
$ds \to dsg$	0.08942777892977130	0.08942777892977716
$du \to dug$	0.2068486091470884	0.2068486091471002
$dd \to ddg$	0.1937338698641218	0.1937338698641383
$\bar{u}\bar{c} \to \bar{u}\bar{c}g$	1.720700782572881	1.720700782572991
$\bar{u}\bar{s} \to \bar{u}\bar{s}g + \bar{d}\bar{c}g$	3.287172270595130	3.28717227059539170
$\bar{u}\bar{u} \to \bar{d}\bar{u}g$	1.580123048127067	1.580123048127181
$\bar{u}\bar{d} \to \bar{u}\bar{d}g$	3.269914732209236	3.269914732209495
$\bar{d}\bar{c} \to \bar{d}\bar{c}g + \bar{u}\bar{s}g$	2.131133518764605	2.13113351876474603
$\bar{d}\bar{s} \to \bar{d}\bar{s}g$	3.799417515547167	3.799417515547469
$\bar{d}\bar{u} \to \bar{d}\bar{u}g$	2.165184291798493	2.165184291798636
$\bar{d}\bar{d} \to \bar{d}\bar{d}g$	4.733774414881026	4.733774414881414
$ug \to c\bar{c}u + s\bar{s}u + u\bar{u}u + u\bar{d}d + c\bar{s}d$	1.498953049944160	1.498953049944295
$dg \to c\bar{c}d + s\bar{s}d + d\bar{d}d + d\bar{u}u + s\bar{c}u$	0.8252177180229951	0.8252557714340902
$gu \to c\bar{c}u, s\bar{s}u, u\bar{u}u, u\bar{d}d, c\bar{s}d$	0.5578083198294848	0.5578083198295341
$gd \to c\bar{c}d, s\bar{s}d, d\bar{d}d, d\bar{u}u, s\bar{c}u$	2.531110288019396	2.531110288019663
$\bar{u}g \to \bar{u}c\bar{c} + \bar{u}s\bar{s} + \bar{d}d\bar{u} + \bar{u}u\bar{u} + \bar{d}s\bar{c}$	2.621696704743119	2.621696704743369
$\bar{d}g \to \bar{d}c\bar{c} + \bar{d}s\bar{s} + \bar{u}u\bar{d} + \bar{d}d\bar{d} + \bar{u}c\bar{s}$	2.209028444843277	2.209028444843487
$g\bar{u} \to \bar{u}c\bar{c} + \bar{u}s\bar{s} + \bar{d}d\bar{u} + \bar{u}u\bar{u} + \bar{d}s\bar{c}$	5.663386035988881	5.663386035989460
$g\bar{d} \to \bar{d}c\bar{c} + \bar{d}s\bar{s} + \bar{u}u\bar{d} + \bar{d}d\bar{d} + \bar{u}c\bar{s}$	6.192671718884545	6.192671718885198

Table 6.4: As for table 6.2, but for the real emission partonic process $0 \to \bar{q}_1 q_2 \bar{q}_3 q_4 g + W^+(\to \nu_\mu + \mu^+) + W^-(\to e^- + \bar{\nu}_e)$ for the phase space point given in equation (5.3.5). There is a sum over all final state flavour configurations, shown in the first column. The units shown are 10^{-23} GeV^{-10}, and the physical parameters used are described in section 5.2.

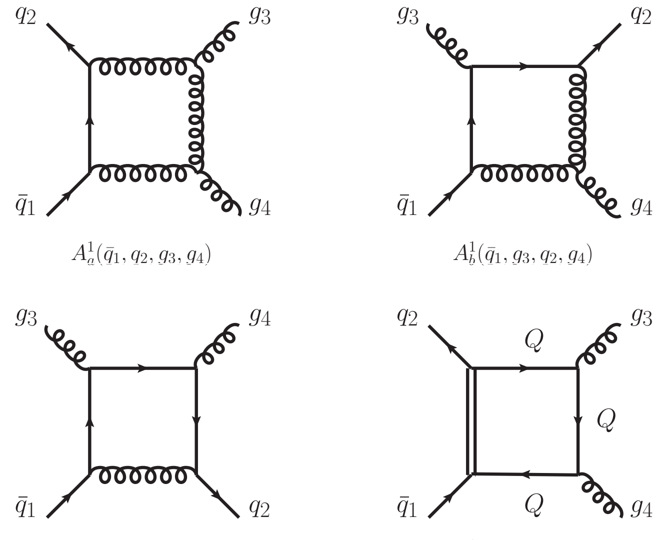

$A_a^1(\bar{q}_1, q_2, g_3, g_4)$ $A_b^1(\bar{q}_1, g_3, q_2, g_4)$

$A_c^1(\bar{q}_1, g_3, g_4, q_2)$ $A_{[1/2]}^1(\bar{q}_1, q_2, g_3, g_4)$

Figure 6.3: Primitive amplitudes for $0 \to \bar{q}_1 q_2 g_3 g_4 + W^+W^-$. Only those primitives with the ordering g_3, g_4 are shown. The W-bosons are not shown. A dummy line (shown as a double line) is used for primitive $A_{[1/2]}^1$, which consists of a fermion loop. W-bosons do not couple to the quarks labeled Q in this primitive.

6.4 Virtual amplitudes

6.4.1 Two quark, two gluon amplitudes

The decomposition of a two-quark n-gluon amplitude into partial and primitive amplitudes was considered by Bern, Dixon and Kosower in ref. [126]. The presence of electroweak particles does not change the decomposition. The virtual amplitude for $n = 2$ is

$$\begin{aligned}\mathcal{M}_{gg}^1(\bar{q}_1, q_2, g_3, g_4; \nu_\mu, \mu^+, e^-, \bar{\nu}_e) =& g_s^4 \left(\frac{g_w}{\sqrt{2}}\right)^4 \Big\{ N_c \big(t^{a_3} t^{a_4}\big)_{\bar{i}_1 i_2} A_{4;1}^1(\bar{q}_1, q_2, g_3, g_4) \\ &+ N_c \big(t^{a_4} t^{a_3}\big)_{\bar{i}_1 i_2} A_{4;1}^1(\bar{q}_1, q_2, g_4, g_3) \\ &+ \mathrm{Tr}\big(t^{a_3} t^{a_4}\big) \delta_{\bar{i}_1 i_2} A_{4;3}^1(\bar{q}_1, q_2, g_3, g_4)\end{aligned} \tag{6.4.1}$$

in terms of two partial amplitudes $A_{4;1}^1$ and $A_{4;3}^1$, with the colour-ordering of the gluons indicated. These can be decomposed into six gluonic left primitive amplitudes and two fermionic left primitive amplitudes

$$\begin{aligned}A_{4;1}^1(\bar{q}_1, q_2; g_3, g_4) =& A_a^1(\bar{q}_1, q_2, g_3, g_4) - \frac{1}{N_c^2} A_c^1(\bar{q}_1, g_4, g_3, q_2) + \frac{N_f}{N_c} A_{[1/2]}^1(\bar{q}_1, q_2, g_3, g_4) \\ A_{4;1}^1(\bar{q}_1, q_2; g_4, g_3) =& A_a^1(\bar{q}_1, q_2, g_4, g_3) - \frac{1}{N_c^2} A_c^1(\bar{q}_1, g_3, g_4, q_2) + \frac{N_f}{N_c} A_{[1/2]}^1(\bar{q}_1, q_2, g_4, g_3) \\ A_{4;3}^1(\bar{q}_1, q_2; g_3, g_4) =& A_a^1(\bar{q}_1, q_2, g_3, g_4) + A_a^1(\bar{q}_1, q_2, g_4, g_3) + A_b^1(\bar{q}_1, g_3, q_2, g_4) \\ &+ A_b^1(\bar{q}_1, g_4, q_2, g_3) + A_c^1(\bar{q}_1, g_3, g_4, q_2) + A_c^1(\bar{q}_1, g_4, g_3, q_2) \\ &- \frac{N_f}{N_c} A_{[1/2]}^1(\bar{q}_1, q_2, g_3, g_4) - \frac{N_f}{N_c} A_{[1/2]}^1(\bar{q}_1, q_2, g_4, g_3).\end{aligned} \tag{6.4.2}$$

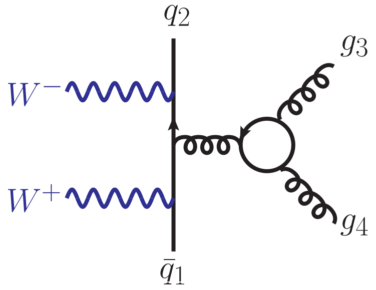

Figure 6.4: Alternative diagrammatic representation of the fermionic one-loop primitive amplitude $A^1_{[1/2]}(\bar{q}_1, q_2, g_3, g_4)$.

The primitive amplitudes A^1_a,A^1_b, A^1_c and $A^1_{[1/2]}$ are shown in figure 6.3 for the ordering $\bar{q}_1, q_2, g_3, g_4$. In this figure, $A^1_{[1/2]}$ is constructed with dummy propagators, as were used in section 5.4. These allow the amplitudes to have formally six propagators (including the W-bosons, which are not shown in figure 6.3). I remind the reader that dummy lines cannot be cut, but W-bosons can couple to them.

The primitive $A^1_{[1/2]}$ contains a virtual quark loop to which the gluons and the external quark lines are coupled, as shown in figure 6.4. Unlike the W^+W^+ process, the electroweak bosons can couple to the internal quark loop. Such amplitudes form a finite and electroweak gauge invariant subset of the one-loop amplitudes. However, these "light-by-light" contributions are neglected in this work[1], and the electroweak bosons only couple to the external quark-antiquark line in primitive $A^1_{[1/2]}$. This does not break electroweak gauge invariance. Aside from this omission, all insertions of the electroweak bosons consistent with the flavour structure discussed in section 6.2.1 need to be considered.

The one-loop amplitude could also be written as

$$\begin{aligned}\mathcal{M}^1_{gg}(\bar{q}_1, q_2, g_3, g_4; \nu_\mu, \mu^+, e^-, \bar{\nu}_e) =& g_s^4 \left(\frac{g_w}{\sqrt{2}}\right)^4 \sum_{\sigma \in S_2} \Big\{ \left(t^b t^{a_{\sigma_3}} t^{a_{\sigma_4}} t^b\right)_{\bar{i}_1 i_2} A^1_c(\bar{q}_1, g_{\sigma_4}, g_{\sigma_3}, q_2) \\ &+ \left(t^b t^{a_{\sigma_3}} t^c\right)_{\bar{i}_1 i_2} (f^{a_{\sigma_4}})_{cb}\ A^1_b(\bar{q}_1, g_{\sigma_3}, q_2, g_{\sigma_4}) \\ &+ \left(t^b t^c\right)_{\bar{i}_1 i_2} \left(f^{a_{\sigma_3}} f^{a_{\sigma_4}}\right)_{cb}\ A^1_a(\bar{q}_1, q_2, g_{\sigma_4}, g_{\sigma_3}) \\ &+ \frac{N_f}{N_c}\Big[N_c \left(t^{a_{\sigma_3}} t^{a_{\sigma_4}}\right)_{\bar{i}_1 i_2} - \mathrm{Tr}\left(t^{a_3} t^{a_4}\right) \delta_{\bar{i}_1 i_2}\Big] \\ &\quad \times A^1_{[1/2]}(\bar{q}_1, q_2, g_{\sigma_3}, g_{\sigma_4}) \Big\}\end{aligned} \tag{6.4.3}$$

as was done in ref. [82]. This makes the relationship of the primitive amplitudes in figure 6.3 to the full amplitude more explicit. Equation (6.4.3) can be reduced to equations (6.4.1) and (6.4.2).

The ratios $R^{(\epsilon^{-2})}$ and $R^{(\epsilon^{-1})}$ of the residues of the primitive amplitude double and

---

[1] After the publication of ref. [82], the hadroproduction of W^+W^- and two jets including these amplitudes was studied independently in ref. [175]. The effect of these amplitudes was found to be about 1%.

single poles to the leading-order amplitude are defined as

$$R^{(\epsilon^p)}_{a,b,c} = \frac{1}{c_\Gamma}\frac{\mathrm{Res}_{\epsilon^p} A^1_{a,b,c}}{A^0}; \qquad p = -2, -1, \tag{6.4.4}$$

where the colour ordering of A^0 and $A^1_{a,b,c}$ are the same. The analytic form of these ratios is known from ref. [159]:

$$\begin{array}{rclcl} R^{(\epsilon^{-2})}_a(\bar{q}_1, q_2, g_3, g_4) &=& R^{(\epsilon^{-2})}_a(\bar{q}_1, q_2, g_4, g_3) &=& -3 \\ R^{(\epsilon^{-2})}_b(\bar{q}_1, g_3, q_2, g_4) &=& R^{(\epsilon^{-2})}_b(\bar{q}_1, g_4, q_2, g_3) &=& -2 \\ R^{(\epsilon^{-2})}_c(\bar{q}_1, g_3, g_4, q_2) &=& R^{(\epsilon^{-2})}_c(\bar{q}_1, g_4, g_3, q_2) &=& -1 \end{array} \tag{6.4.5}$$

$$\begin{array}{rcl} R^{(\epsilon^{-1})}_a(\bar{q}_1, q_2, g_3, g_4) &=& -\log\frac{\mu^2}{-s_{23}} - \log\frac{\mu^2}{-s_{34}} - \log\frac{\mu^2}{-s_{41}} - \frac{3}{2} \\ R^{(\epsilon^{-1})}_a(\bar{q}_1, q_2, g_4, g_3) &=& -\log\frac{\mu^2}{-s_{24}} - \log\frac{\mu^2}{-s_{43}} - \log\frac{\mu^2}{-s_{31}} - \frac{3}{2} \\ R^{(\epsilon^{-1})}_b(\bar{q}_1, g_3, q_2, g_4) &=& -\log\frac{\mu^2}{-s_{24}} - \log\frac{\mu^2}{-s_{41}} - \frac{3}{2} \\ R^{(\epsilon^{-1})}_b(\bar{q}_1, g_4, q_2, g_3) &=& -\log\frac{\mu^2}{-s_{23}} - \log\frac{\mu^2}{-s_{31}} - \frac{3}{2} \\ R^{(\epsilon^{-1})}_c(\bar{q}_1, g_3, g_4, q_2) &=& -\log\frac{\mu^2}{-s_{12}} - \frac{3}{2} \\ R^{(\epsilon^{-1})}_c(\bar{q}_1, g_4, g_3, q_2) &=& -\log\frac{\mu^2}{-s_{12}} - \frac{3}{2}, \end{array} \tag{6.4.6}$$

where $s_{ij} = (p_i + p_j)^2$ and the momentum assignment is $p_{\bar{q}_1} = p_1;\ \ p_{q_2} = p_2;\ \ p_{g_3} = p_3;\ \ p_{g_4} = p_4$. The IR and UV singularities in the fermion loop primitive amplitudes $A^1_{[1/2]}$ cancel, so that this primitive is purely finite. Focusing on the $\bar{u}^+u^-g^-g^-$ channel, where the superscripts indicate helicities, the computed ratios are shown in table 6.5, together with the relative difference ϵ (as defined in equation (5.4.11)) between these values and those obtained from equations (6.4.5) and (6.4.6).

The interference between the leading order and virtual amplitudes is

$$\begin{aligned} 2\ \mathrm{Real}\Big(\mathcal{M}^0_{gg}\mathcal{M}^{1*}_{gg}\Big) &= 2S\sum_{\mathrm{hel}} g_s^6\big(\frac{g_w}{\sqrt{2}}\big)^8 2C_F N_c\times \\ &\mathrm{Real}\Big\{2C_F N_c\big(A_0(\bar{q}_1, q_2, g_3, g_4)A^*_{4;1}(\bar{q}_1, q_2, g_3, g_4) + A_0(\bar{q}_1, q_2, g_4, g_3)A^*_{4;1}(\bar{q}_1, q_2, g_4, g_3)\big) \\ &- A_0(\bar{q}_1, q_2, g_3, g_4)A^*_{4;1}(\bar{q}_1, q_2, g_4, g_3) - A_0(\bar{q}_1, q_2, g_4, g_3)A^*_{4;1}(\bar{q}_1, q_2, g_3, g_4) \\ &+ A_0(\bar{q}_1, q_2, g_3, g_4)A^*_{4;3}(\bar{q}_1, q_2, g_3, g_4) + A_0(\bar{q}_1, q_2, g_4, g_3)A^*_{4;3}(\bar{q}_1, q_2, g_3, g_4)\Big\}, \end{aligned} \tag{6.4.7}$$

where, as before, S denotes the colour- and spin-averaging factor for the various initial states. Table 6.6 shows the ratio R (defined in equation (5.4.13)) of the singular and finite terms of this quantity to the leading order matrix element squared, for the phase space point of equation (5.2.4) and scale $\mu = 150$ GeV. The leading-order matrix elements are the same as in table 6.1.

6.4.2 Four quark amplitudes

The decomposition into partial and primitive amplitudes of the one-loop corrections to four quark partonic amplitudes is the same as for the W^+W^+ process, equations

Residue	Calculated value	Relative error ϵ
$R_a^{(\epsilon^{-2})}(\bar{u}^+, u^-, g_3^-, g_4^-)$	$-3.00000000001131 + i2.53 \times 10^{-11}$	5.2×10^{-12}
$R_a^{(\epsilon^{-1})}(\bar{u}^+, u^-, g_3^-, g_4^-)$	$-1.73889134869819 - i3.14159265362008$	1.0×10^{-10}
$R_a^{(\epsilon^{-2})}(\bar{u}^+, u^-, g_4^-, g_3^-)$	$-3.00000000001588 - i1.60 \times 10^{-11}$	4.3×10^{-12}
$R_a^{(\epsilon^{-1})}(\bar{u}^+, u^-, g_4^-, g_3^-)$	$-1.22285497787148 - i3.14159265361691$	3.7×10^{-10}
$R_b^{(\epsilon^{-2})}(\bar{u}^+, g_3^-, u^-, g_4^-)$	$-2.00000000000743 + i4.36 \times 10^{-12}$	9.2×10^{-12}
$R_b^{(\epsilon^{-1})}(\bar{u}^+, g_3^-, u^-, g_4^-)$	$1.52621975164134 - i6.03 \times 10^{-12}$	6.9×10^{-11}
$R_b^{(\epsilon^{-2})}(\bar{u}^+, g_4^-, u^-, g_3^-)$	$-2.00000000001022 - i8.92 \times 10^{-12}$	1.6×10^{-11}
$R_b^{(\epsilon^{-1})}(\bar{u}^+, g_4^-, u^-, g_3^-)$	$-0.787662965630596 - i1.92 \times 10^{-10}$	3.6×10^{-11}
$R_c^{(\epsilon^{-2})}(\bar{u}^+, g_3^-, g_4^-, u^-)$	$-0.999999999996179 - i3.47 \times 10^{-12}$	6.8×10^{-12}
$R_c^{(\epsilon^{-1})}(\bar{u}^+, g_3^-, g_4^-, u^-)$	$2.29423997010836 - i3.14159265337122$	2.7×10^{-10}
$R_c^{(\epsilon^{-2})}(\bar{u}^+, g_4^-, g_3^-, u^-)$	$-1.00000000000324 + i1.55 \times 10^{-11}$	7.5×10^{-12}
$R_c^{(\epsilon^{-1})}(\bar{u}^+, g_4^-, g_3^-, u^-)$	$2.29423996970066 - i3.14159265346791$	1.2×10^{-10}

Table 6.5: Ratios of the singular parts of the primitive amplitudes to the leading-order amplitudes with the same colour-ordering, for the partonic process $0 \to \bar{u}^+ u^- g^- g^- + W^+ (\to \nu_\mu + \mu^+) + W^- (\to e^- + \bar{\nu}_e)$. The phase space point used is given in equation (5.2.4), and the renormalisation scale is $\mu = 150$ GeV. The middle column shows the ratios evaluated by taking the ratio of the computed virtual and leading-order amplitudes, the last column shows the relative error between these values and the values obtained from the analytic expression of equations (6.4.5) and (6.4.6).

(5.4.1) and (5.4.2):

$$\begin{aligned} \mathcal{M}^1_{4q}(\bar{q}_1, q_2, \bar{q}_3, q_4; \nu_\mu, \mu^+, e^-, \bar{\nu}_e) =& g_s^4 \Big(\frac{g_w}{\sqrt{2}}\Big)^4 \big(\delta_{\bar{i}_1 i_4} \delta_{\bar{i}_3 i_2} B^1_A(\bar{q}_1, q_2, \bar{q}_3, q_4) \\ & + \delta_{\bar{i}_1 i_2} \delta_{\bar{i}_3 i_4} B^1_B(\bar{q}_1, q_2, \bar{q}_3, q_4)\big) \end{aligned} \tag{6.4.8}$$

with

$$\begin{aligned} B^1_A(\bar{q}_1, q_2, \bar{q}_3, q_4) =& \Big(N_c - \frac{1}{N_c}\Big) B^1_{1,s}(\bar{q}_1, q_2, \bar{q}_3, q_4) + \frac{2}{N_c} B^1_{2,s}(\bar{q}_1, q_2, \bar{q}_3, q_4) \\ & - \frac{1}{N_c} B^1_{3,s}(\bar{q}_1, q_2, \bar{q}_3, q_4) - \frac{1}{N_c} B^1_{4,s}(\bar{q}_1, q_2, \bar{q}_3, q_4) \\ & + N_f B^1_{[1/2],s}(\bar{q}_1, q_2, \bar{q}_3, q_4) \\ & + \frac{1}{N_c^2} B^1_{1,t}(\bar{q}_1, q_4, \bar{q}_3, q_2) - \Big(1 + \frac{1}{N_c^2}\Big) B^1_{2,t}(\bar{q}_1, q_4, \bar{q}_3, q_2) + \\ & + \frac{1}{N_c^2} B^1_{3,t}(\bar{q}_1, q_4, \bar{q}_3, q_2) + \frac{1}{N_c^2} B^1_{4,t}(\bar{q}_1, q_4, \bar{q}_3, q_2) \\ & - \frac{N_f}{N_c^2} B^1_{[1/2],t}(\bar{q}_1, q_4, \bar{q}_3, q_2) \end{aligned} \tag{6.4.9}$$

Flavours	$R^{(\epsilon^{-2})}$	$R^{(\epsilon^{-1})}$	$R^{(\epsilon^{0})}$
$u\bar{u} \to gg$	-8.666667	-5.412754	0.7510186
$d\bar{d} \to gg$	-8.666667	-5.442197	5.554915
$\bar{d}d \to gg$	-8.666667	-5.448774	2.696111
$\bar{u}u \to gg$	-8.666667	-5.429640	10.38334
$ug \to gu$	-8.666667	10.44690	-1.882044
$dg \to gd$	-8.666667	10.90627	-10.26990
$gu \to gu$	-8.666667	2.085679	19.27530
$gd \to gd$	-8.666667	2.069165	-1.858877
$g\bar{u} \to g\bar{u}$	-8.666667	1.935494	-0.7683517
$g\bar{d} \to g\bar{d}$	-8.666667	1.856483	6.779307
$\bar{u}g \to g\bar{u}$	-8.666667	10.41266	-3.366571
$\bar{d}g \to g\bar{d}$	-8.666667	10.47201	-2.522289
$gg \to \bar{u}u + \bar{d}d + \bar{c}c + \bar{s}s$	-8.666667	14.11299	-11.90991

Table 6.6: The double pole, single pole and finite terms of the ratio R, for all flavour configurations. The phase space point is given in equation (5.2.4) and scale is $\mu = 150$ GeV. The quark momentum assignments are as in section 6.2.1, and the physical parameters are given in section 5.2.

and

$$\begin{aligned}
B^1_B(\bar{q}_1, q_2, \bar{q}_3, q_4) =& \frac{1}{N_c^2} B^1_{1,s}(\bar{q}_1, q_2, \bar{q}_3, q_4) - \big(1 + \frac{1}{N_c^2}\big) B^1_{2,s}(\bar{q}_1, q_2, \bar{q}_3, q_4) + \\
&+ \frac{1}{N_c^2} B^1_{3,s}(\bar{q}_1, q_2, \bar{q}_3, q_4) + \frac{1}{N_c^2} B^1_{4,s}(\bar{q}_1, q_2, \bar{q}_3, q_4) \\
&- \frac{N_f}{N_c^2} B^1_{5,s}(\bar{q}_1, q_2, \bar{q}_3, q_4) \\
&+ \big(N_c - \frac{1}{N_c}\big) B^1_{1,t}(\bar{q}_1, q_4, \bar{q}_3, q_2) + \frac{2}{N_c} B^1_{2,t}(\bar{q}_1, q_4, \bar{q}_3, q_2) \\
&- \frac{1}{N_c} B^1_{3,t}(\bar{q}_1, q_4, \bar{q}_3, q_2) - \frac{1}{N_c} B^1_{4,t}(\bar{q}_1, q_4, \bar{q}_3, q_2) \\
&+ N_f B^1_{[1/2],t}(\bar{q}_1, q_4, \bar{q}_3, q_2).
\end{aligned} \tag{6.4.10}$$

The primitives are shown in figure 5.2, with no electroweak bosons shown. The flavour structure is the same as discussed in section 6.2.2, and this is important for choosing the parent amplitudes. Looking at the s-channel, if both W-bosons are radiated off the same quark line, then four parent amplitudes are identified, all of which have the W-boson pair radiated off the first quark-antiquark line $\bar{q}_1 q_2$. The first parent amplitude, $\mathbb{B}_1$, has the same colour structure as primitive B_1, with two gluons between the quark-antiquark lines. Primitive B_2 can be obtained from it using the quark exchange

$$B_2(\bar{q}_1, q_2, \bar{q}_3, q_4) = B_1(\bar{q}_1, q_2, q_4, \bar{q}_3), \tag{6.4.11}$$

where the additional minus sign relative to equation (5.4.3) is due to an even number of Dirac matrices on each quark-antiquark line. Thus the first two primitives are

$$\begin{aligned}B_1(\bar{q}_1, q_2, \bar{q}_3, q_4) =&\mathbb{B}_1(\bar{q}_1, q_2, \bar{q}_3, q_4) + \mathbb{B}_1(\bar{q}_3, q_4, \bar{q}_1, q_2)\\ B_2(\bar{q}_1, q_2, \bar{q}_3, q_4) =&\mathbb{B}_1(\bar{q}_1, q_2, q_4, \bar{q}_3) + \mathbb{B}_1(\bar{q}_3, q_4, q_2, \bar{q}_1),\end{aligned} \tag{6.4.12}$$

where the second term in each expression allows for the W-pair to be radiated off the second quark-antiquark line.

The second and third parent amplitudes have the quark-antiquark line from which both W-bosons are radiated ($\bar{q}_1 q_2$) dressed with a gluon loop. In the second parent amplitude $\mathbb{B}_2$, the W-bosons are both restricted to being below the propagating gluon between the quark-antiquark lines (again, this motivates the use of restrictive Berends-Giele currents, such as $\mathsf{f\_VV\bar{f}f\bar{f}\_1}$). In the third parent amplitude, $\mathbb{B}_3$, one W-boson is below the propagating gluon and one is above it. The fourth parent amplitude, $\mathbb{B}_4$, has the second quark-antiquark line $\bar{q}_3 q_4$ dressed with a gluon loop. The primitive B_3 is

$$\begin{aligned}B_3(\bar{q}_1, q_2, \bar{q}_3, q_4) =&\mathbb{B}_2(\bar{q}_1, q_2, \bar{q}_3, q_4) + \mathbb{B}_2(q_2, \bar{q}_1, q_4, \bar{q}_3) + \mathbb{B}_3(\bar{q}_1, q_2, \bar{q}_3, q_4)\\ &+ \mathbb{B}_4(\bar{q}_3, q_4, \bar{q}_1, q_2).\end{aligned} \tag{6.4.13}$$

The first and second term allow for the W-bosons to be both below and both above the gluon propagator, while the fourth term takes into account the emission of the W-pair from the second quark-antiquark line. Similarly, the primitive B_4 is

$$\begin{aligned}B_4(\bar{q}_1, q_2, \bar{q}_3, q_4) =&\mathbb{B}_2(\bar{q}_3, q_4, \bar{q}_1, q_2) + \mathbb{B}_2(q_4, \bar{q}_3, q_2, \bar{q}_1) + \mathbb{B}_3(\bar{q}_3, q_4, \bar{q}_1, q_2)\\ &+ \mathbb{B}_4(\bar{q}_1, q_2, \bar{q}_3, q_4).\end{aligned} \tag{6.4.14}$$

The coupling of the W-bosons through an intermediate Z-boson or photon is contained in all the parent amplitudes except $\mathbb{B}_3$, where the W-bosons are always "split" by the intermediate gluon. Thus

$$\begin{aligned}\mathbb{B}_i(\bar{q}_1, q_2, \bar{q}_3, q_4) = &\mathbb{B}_i^{[WW]}([\bar{q}_1, W, W, q_2], [\bar{q}_3, q_4])\delta_{h_2,-1}\\ &+ C^{(q_2,h_2)}\mathbb{B}_i^{[Z/\gamma]}([\bar{q}_1, Z/\gamma, q_2], [\bar{q}_3, q_4])\end{aligned} \tag{6.4.15}$$

for $i = 1, 2, 4$, and with the couplings $C^{(q,h)}$ given in equation (6.2.3).

On the other hand, if one W-boson is emitted from each quark-antiquark line, then the parent amplitudes are the same as in section 5.4. These are denoted $\mathbb{B}_5$ and $\mathbb{B}_6$, with

$$\begin{aligned}B_1(\bar{q}_1, q_2, \bar{q}_3, q_4) =&\mathbb{B}_5(\bar{q}_1, q_2, \bar{q}_3, q_4)\\ B_2(\bar{q}_1, q_2, \bar{q}_3, q_4) =& -\mathbb{B}_5(\bar{q}_1, q_2, q_4, \bar{q}_3)\\ B_3(\bar{q}_1, q_2, \bar{q}_3, q_4) =&\mathbb{B}_6(\bar{q}_1, q_2, \bar{q}_3, q_4) + \mathbb{B}_6(q_2, \bar{q}_1, q_4, \bar{q}_3)\\ B_4(\bar{q}_1, q_2, \bar{q}_3, q_4) =&\mathbb{B}_6(\bar{q}_3, q_4, \bar{q}_1, q_2) + \mathbb{B}_6(q_4, \bar{q}_3, q_2, \bar{q}_1).\end{aligned} \tag{6.4.16}$$

To reiterate, which parent amplitudes are used, and hence whether equations (6.4.12), (6.4.13) and (6.4.14), or equation (6.4.16) are used to calculate the primitives, depends on the flavour configurations of the quarks. The t-channel is similar with the overall exchange $q_2 \leftrightarrow q_4$. As with the leading-order amplitudes, both s- and t-channels may be present for certain flavour configurations, in which case the primitive amplitude for one channel is calculated using equations (6.4.12),(6.4.13) and and (6.4.14), and the primitive amplitude for the other channel using equation (6.4.16).

The final primitive amplitude $B^1_{[1/2]}$ has an internal quark loop in the gluon propagator. As in section 6.4.1, contributions where the electroweak bosons couple directly to the internal quarks are neglected. Then the primitive $B^1_{[1/2]}$ can be calculated analytically, as in section 5.4:

$$B_{[1/2]}(\bar{q}_1, q_2, \bar{q}_3, q_4) = \Big(-\frac{2}{3\epsilon} - \frac{10}{9}\Big) B^0(\bar{q}_1, q_2, \bar{q}_3, q_4) - \frac{2}{3} L. \tag{6.4.17}$$

The term L involves the logarithm of the momentum squared flowing through the fermion loop. The expression for this in terms of the external momenta changes depending on where the W-bosons are attached. If both are attached to the same quark-antiquark lines, then the leading-order amplitudes are of the first kind, and L is

$$\begin{aligned} L = &\log \frac{\mu^2}{-s_{12WW}} \Big(B^{0,[WW]}([\bar{q}_1, W, W, q_2], [\bar{q}_3, q_4]) \delta_{h_2,-1} \\ &+ C^{(h_2,q_2)} B^{0,[Z/\gamma]}([\bar{q}_1, Z/\gamma, q_2], [\bar{q}_3, q_4]) \Big) \\ &+ \log \frac{\mu^2}{-s_{12}} \Big(B^{0,[WW]}([\bar{q}_1, q_2], [\bar{q}_3, W, W, q_4]) \delta_{h_4,-1} \\ &+ C^{(h_4,q_4)} B^{0,[Z/\gamma]}([\bar{q}_1, q_2], [\bar{q}_3, Z/\gamma, q_4]) \Big) \end{aligned} \tag{6.4.18}$$

where $s_{12WW} = (p_1 + p_2 + p_{W^+} + p_{W^-})^2$ and $s_{12} = (p_1 + p_2)^2$. If the W-bosons are each attached to a separate quark-antiquark line, then the leading-order amplitudes are of the second kind, and L is

$$L = \log \frac{\mu^2}{-s_{12W}} B^0(\bar{q}_1, q_2, \bar{q}_3, q_4) \tag{6.4.19}$$

where $s_{12W} = (p_1 + p_2 + p_{W^\pm})$, the sign of the W-boson being determined by the flavours of the quarks.

The ratios of the residues of the primitive amplitude double and single poles to the leading-order amplitudes are given by equation (5.4.8). To avoid confusion, in this section I will call these ratios $S_i^{(\epsilon^{-2})}$ and $S_i^{(\epsilon^{-1})}$. These ratios, and the relative difference ϵ between them and the values calculated using equation (5.4.10), are given in table 6.7 for the $\bar{u}\bar{u}uu$ flavour configuration, using the helicities $h_1 = h_3 = +1;\ h_2 = h_4 = -1$. The phase space point is given in equation (5.2.4), and the scale used is $\mu = 150$ GeV.

The interference with the leading order amplitude is the same as equation (5.4.12):

$$\begin{aligned} 2\ \text{Real}\Big(\mathcal{M}^0_{4q}\mathcal{M}^{1*}_{4q}\Big) = &2S_{qq} \sum_{\text{hel}} g_s^6 \Big(\frac{g_w}{\sqrt{2}}\Big)^8 (N_c^2 - 1) \times \\ &\text{Real}\Big(B^0_s(\bar{q}_1, q_2, \bar{q}_3, q_4) B^{1*}_A(\bar{q}_1, q_2, \bar{q}_3, q_4) \\ &+ B^0_t(\bar{q}_1, q_4, \bar{q}_3, q_2) B^{1*}_B(\bar{q}_1, q_2, \bar{q}_3, q_4) \Big). \end{aligned} \tag{6.4.20}$$

Residue	Calculated value	Relative error ϵ
$S_{1,s}^{(\epsilon^{-2})}$	$-2.00000000000361 + i1.95 \times 10^{-12}$	2.1×10^{-12}
$S_{1,s}^{(\epsilon^{-1})}$	$2.27792687492828 - i6.55 \times 10^{-11}$	3.1×10^{-11}
$S_{2,s}^{(\epsilon^{-2})}$	$-2.00000000001044 + i1.16 \times 10^{-11}$	7.8×10^{-12}
$S_{2,s}^{(\epsilon^{-1})}$	$2.61075507985411 - i6.28318530743432$	4.1×10^{-11}
$S_{3,s}^{(\epsilon^{-2})}$	$-0.999999999998909 + i1.10 \times 10^{-12}$	1.5×10^{-12}
$S_{3,s}^{(\epsilon^{-1})}$	$-2.25832593972456 + i2.68 \times 10^{-12}$	1.5×10^{-12}
$S_{4,s}^{(\epsilon^{-2})}$	$-0.999999999999035 + i3.25 \times 10^{-13}$	1.0×10^{-12}
$S_{4,s}^{(\epsilon^{-1})}$	$1.38562251813323 - i1.18 \times 10^{-10}$	8.5×10^{-11}
$S_{1,t}^{(\epsilon^{-2})}$	$-2.00000000001069 - i6.46 \times 10^{-12}$	5.3×10^{-12}
$S_{1,t}^{(\epsilon^{-1})}$	$2.79396324510457 - i8.05 \times 10^{-13}$	8.0×10^{-12}
$S_{2,t}^{(\epsilon^{-2})}$	$-1.99999999998831 + i8.03 \times 10^{-12}$	7.1×10^{-12}
$S_{2,t}^{(\epsilon^{-1})}$	$2.61075508150681 - i6.28318530716388$	2.6×10^{-10}
$S_{3,t}^{(\epsilon^{-2})}$	$-0.999999999999177 + i4.11 \times 10^{-13}$	9.2×10^{-13}
$S_{3,t}^{(\epsilon^{-1})}$	$-1.35940276594094 + i2.30 \times 10^{-12}$	1.8×10^{-12}
$S_{4,t}^{(\epsilon^{-2})}$	$-1.00000000000075 - i1.33 \times 10^{-12}$	1.5×10^{-12}
$S_{4,t}^{(\epsilon^{-1})}$	$-0.0293370258094962 - i8.47 \times 10^{-11}i$	2.9×10^{-9}

Table 6.7: Ratios of the double and single poles of the four primitive amplitudes to the leading-order amplitudes, for the process $0 \to \bar{u}u\bar{u}u + W^+(\to \nu_\mu + \mu^+) + W^-(\to e^- + \bar{\nu}_e)$ with left-handed quarks. The scale is $\mu = 150$ GeV, and the phase space point is given in equation (5.2.4). Both s- and t-channel amplitudes are shown. The middle column shows the ratios evaluated by taking the ratio of the computed primitive and tree-level amplitudes, the last column shows the relative error between these values and the values obtained from the analytic expression of equation (5.4.10).

As before, the interference between leading-order and virtual contributions can only occur if the helicities of the quarks are the same; in particular, mixing between s- and t-channels is only allowed if both quarks are either left- or right-handed.

The ratios

$$S = \frac{4\pi}{\alpha_s} \frac{\mathrm{Real}\Big(\mathcal{M}_{4q}^{0}\mathcal{M}_{4q}^{1*}\Big)}{|\mathcal{M}_{4q}^{0}|^2} \tag{6.4.21}$$

are shown in table 6.8 at the usual phase space point given in equation (5.2.4) and scale $\mu = 150$ GeV. The double and single pole residues as well as the finite part are shown. The quark momenta assignments are the same as in section 6.2.2.

Flavours	$S^{(\epsilon^{-2})}$	$S^{(\epsilon^{-1})}$	$S^{(\epsilon^{0})}$
$u\bar{c} \to \bar{c}u + \bar{s}d$	-5.333333	5.750651	0.4524014
$u\bar{s} \to \bar{s}u$	-5.333333	5.750651	3.750180
$u\bar{u} \to \bar{c}c + \bar{s}s + \bar{u}u + \bar{d}d$	-5.333333	4.934021	5.095183
$u\bar{d} \to \bar{d}u + \bar{s}c$	-5.333333	5.748697	3.540692
$d\bar{c} \to \bar{c}d$	-5.333333	5.750651	3.142645
$d\bar{s} \to \bar{s}d + \bar{c}u$	-5.333333	5.750651	6.138216
$d\bar{u} \to \bar{c}s + \bar{u}d$	-5.333333	5.713771	3.114761
$d\bar{d} \to \bar{c}c + \bar{s}s + \bar{u}u + \bar{d}d$	-5.333333	4.927865	10.47116
$\bar{u}c \to \bar{u}c + \bar{d}s$	-5.333333	5.234614	27.41621
$\bar{u}s \to \bar{u}s$	-5.333333	5.234614	11.46348
$\bar{u}u \to \bar{c}c + \bar{s}s + \bar{u}u + \bar{d}d$	-5.333333	5.696549	16.77058
$\bar{u}d \to \bar{u}d + \bar{c}s$	-5.333333	5.219374	11.32847
$\bar{d}c \to \bar{d}c$	-5.333333	5.234614	26.92679
$\bar{d}s \to \bar{d}s + \bar{u}c$	-5.333333	5.234614	10.98327
$\bar{d}u \to \bar{s}c + \bar{d}u$	-5.333333	5.231760	26.28934
$\bar{d}d \to \bar{c}c + \bar{s}s + \bar{u}u + \bar{d}d$	-5.333333	5.719133	10.38244
$uc \to uc$	-5.333333	4.679901	33.77764
$us \to us + dc$	-5.333333	4.679901	14.08678
$uu \to uu$	-5.333333	5.073850	27.11092
$ud \to ud$	-5.333333	4.647071	14.64257
$dc \to dc + us$	-5.333333	4.679901	32.56174
$ds \to ds$	-5.333333	4.679901	14.50912
$du \to du$	-5.333333	4.698136	32.13524
$dd \to dd$	-5.333333	5.526318	9.415604
$\bar{u}\bar{c} \to \bar{u}\bar{c}$	-5.333333	4.679901	4.258128
$\bar{u}\bar{s} \to \bar{u}\bar{s} + \bar{d}\bar{c}$	-5.333333	4.679901	14.80830
$\bar{u}\bar{u} \to \bar{d}\bar{u}$	-5.333333	5.069817	8.736124
$\bar{u}\bar{d} \to \bar{u}\bar{d}$	-5.333333	4.682434	13.74283
$\bar{d}\bar{c} \to \bar{d}\bar{c} + \bar{u}\bar{s}$	-5.333333	4.679901	4.555774
$\bar{d}\bar{s} \to \bar{d}\bar{s}$	-5.333333	4.679901	14.75539
$\bar{d}\bar{u} \to \bar{d}\bar{u}$	-5.333333	4.700852	5.104717
$\bar{d}\bar{d} \to \bar{d}\bar{d}$	-5.333333	5.288125	10.10712

Table 6.8: The double pole, single pole and finite terms of the ratio S, for all initial state flavour configurations at the phase space point given in equation (5.2.4). There is a sum over all final state flavours. The scale is $\mu = 150$ GeV. The quark momentum assignments are as in section 6.2.2, and the physical parameters are given in section 5.2.

6.5 Checks, stability and running time

As with the $W^+W^+ + 2$ jets process, the calculations of the leading-order, real radiation and virtual matrix elements are embedded in the program `MCFM`, and the Monte Carlo integration over phase space is done in this framework. The leading-order and real radiation matrix elements squared for the various flavour configurations are checked against `MadGraph`, as seen in sections 6.2 and 6.3. The dipoles are checked to cancel the singularities of the real radiation in the soft and collinear regions. The integrated dipoles are checked by confirming the independence of the cross-section on the parameter α [161, 162]. The double and single poles of the virtual amplitude are checked against their analytic values at the level of primitive amplitudes and at the level of virtual matrix element squared, as shown in section 6.4. The virtual amplitudes are also computed using the Feynman diagram-based OPP program mentioned in 5.5, which provides a semi-independent check on its finite part.

As mentioned in section 5.5, the computation is performed in double precision as standard, and two checks are used to test the accuracy of each primitive amplitude: the poles are checked against their analytically known value, and the OPP equations (3.4.26) and (3.4.30) are recalculated to ensure that the coefficients in the expansion of the unitarity coefficients satisfy these equations. If either test fails then the primitive is recomputed using quadruple precision. A degree of tuning is involved in determining the required accuracy for each test, weighing the increased accuracy against a large increase in running time. For two quark, two gluon amplitudes, requiring the poles to be reproduced to within three significant figures, and the OPP equations to be solved to within two significant figures, establishes a good balance between accuracy and speed. For the four quark amplitudes, the required accuracy of the poles is four significant figures, and the accuracy of the OPP solutions is one figure. Overall, approximately 0.4% of the points are recomputed using quadruple precision.

The more complicated flavour structure, and the greater number of helicities for which the matrix elements are nonzero, lead to longer run times than was the case for the $W^+W^+ + 2$ jets process. It takes about 2.5 seconds to evaluate the virtual matrix element squared in a given initial state channel for a single phase space point for the two quark, two gluon contributions, and about 2 seconds for the four quark contributions. For the former, we require about 2×10^5 phase space points for a stable cross-section, and about 4×10^5 phase space points for the latter, using a phase space grid weighted by the leading-order matrix elements squared. Since these computations can easily be parallelised, a cross-section can be obtained with 15-20 hours of running time. Again, the time required to compute the real radiation cross-section σ^{R} is longer than this (by a factor of about two), because the number of phase space points required for an accurate result is $\sim 10^7$.

6.6 Results

In this section, I will present the cross-sections and kinematic distributions for the hadroproduction of W^+W^- in association with two jets, to next-to-leading order (NLO) in QCD, at both the Tevatron and the LHC at centre-of-mass energy $\sqrt{s} = 7$ TeV. Production at the Tevatron will be considered as a background to Higgs production in association with two jets, and apposite experimental cuts will be used. On the other hand, production at the LHC will be considered as a signal process, with some comments about the future discrimination between this process and Higgs production.

As before, the W-bosons decay leptonically, $W^+W^- \to \nu_\mu \mu^+ e^- \bar{\nu}_e$, including spin correlations. Results for all possible final lepton states $\mu^+e^-, e^+\mu^-, e^+e^-, \mu^+\mu^-$ can be obtained by multiplying these results by a factor four. Since the leptons have opposite charge, there is no chance of mixing. Single resonant amplitudes are neglected, although including these via the polarisation of the Z-boson and photon given in equation (4.2.26) would not be particularly difficult. As discussed in the section 6.1, electroweak production is ignored. The W-bosons are produced with a Breit-Wigner distribution around a mass $m_W = 80.419$ GeV with a width $\Gamma_W = 2.141$ GeV. The mass and width of the Z-boson are $m_Z = 91.188$ GeV and $\Gamma_Z = 2.49$ GeV respectively. The electroweak couplings are defined through $\alpha(m_Z) = 1/128.802$ and the weak mixing angle $\sin^2\theta_w = 0.2222$. The parton distributions used are MSTW08LO at leading-order and MSTW08NLO at next-to-leading order [98], corresponding to strong couplings $\alpha_s(m_Z) = 0.13939$ and $\alpha_s(m_Z) = 0.12018$ respectively.

Top quarks are taken to be infinitely massive, and hence never appear as virtual particles. All other quarks are massless. Final state tops have a distinct experimental signature and will not be considered – tops in fact do not appear anywhere in these calculations. It is then difficult to see how bottom quarks could be included (using a unit CKM matrix) without breaking electroweak gauge invariance. On the other hand, the bottom quark flux of protons and antiprotons is small, and final state bottoms can be separately identified through the b-tagging of jets. It is therefore a good approximation to ignore the third quark generation entirely[2]. It is possible, however, to include third generation quarks with realistic masses in the unitarity framework, and indeed top phenomenology has been studied using this approach [71, 74, 78, 88–92].

6.6.1 Results at the Tevatron

Although the Tevatron shut down in October 2011, the analysis of more than 10 fb^{-1} of data is ongoing. Hints of a Higgs boson with a mass in the region of 120 GeV have been observed [1], and it is hoped that further analysis will provide independent corroboration of the LHC Higgs discovery. As mentioned previously, putative Higgs signals are binned according to the number of jets produced, with the 0-jet bin contributing around 60% of the total signal, the 1-jet bin around 30%, and the $\geq$ 2-jet bin around 10% [25]. As W^+W^-jj production is an irreducible background to the

---

[2] The effect of the third quark generation on the cross-section is found to be approximately 3% in ref. [175].

latter, it is important to investigate its cross-sections and kinematic distributions in the Higgs search setup.

The results for $p\bar{p} \to W^+W^-jj$ at centre-of-mass energy $\sqrt{s} = 1.96$ TeV are shown. The cuts of ref. [25], which are themselves derived from the Higgs boson search at CDF [176], are used. The hardest lepton is required to have transverse momentum $p_{T,l_1} > 20$ GeV and pseudorapidity $|\eta_{l_1}| < 0.8$, and the other lepton must have transverse momentum $p_{T,l_2} > 10$ GeV and pseudorapidity $|\eta_{l_2}| < 1.1$. The leptons must have an invariant mass $m_{ll} > 16$ GeV to prevent production by soft photons. A lepton isolation requirement is also imposed: a jet within a distance $\Delta R < 0.4$ of a lepton must be soft, $p_{T,j} < 0.1 p_{T,l}$. Here, the quantity ΔR is defined in the usual way: $\Delta R = \sqrt{(\Delta\eta)^2 + (\Delta\phi)^2}$, where $\Delta\eta$ and $\Delta\phi$ are the differences in pseudorapidity and azimuthal angle of the two particles, respectively. The cut on the missing energy is performed through the missing relative transverse energy, defined as

$$E_{T,\text{miss}}^{\text{rel}} = |\mathbf{p}_{T,\text{miss}}| \sin \Delta\phi_{\text{min}}, \tag{6.6.1}$$

where $\mathbf{p}_{T,\text{miss}}$ is the missing tranverse momentum and $\Delta\phi_{\text{min}} = \min\big(\Delta\phi, \pi/2\big)$, with $\Delta\phi$ the angle between $\mathbf{p}_{T,\text{miss}}$ and the nearest lepton or jet. The cut is $E_{T,\text{miss}}^{\text{rel}} > 25$ GeV. Jets are defined through the k_t algorithm with separation $\Delta R_{j_1 j_2} = 0.4$, and are cut on transverse momentum $p_{T,j} > 15$ GeV and pseudorapidity $|\eta_j| < 2.5$.

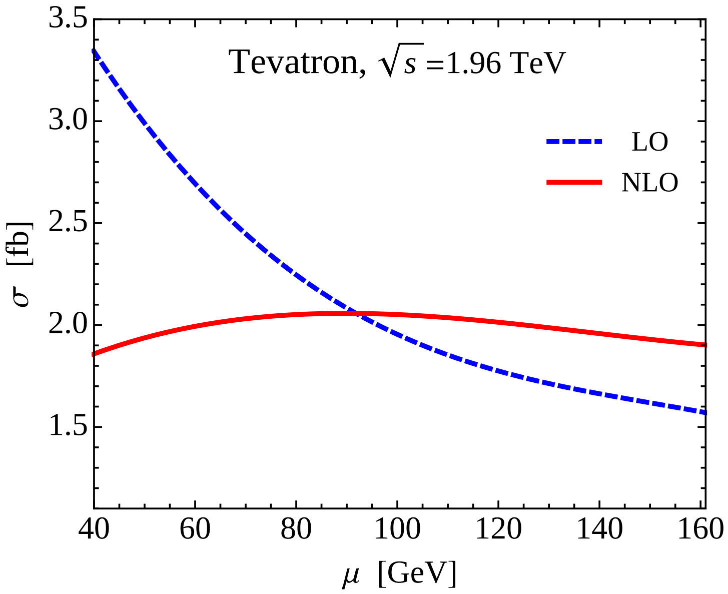

Figure 6.5: Dependence of the cross-section of $p\bar{p} \to W^+(\to \nu_\mu\mu^+)W^-(\to e^-\bar{\nu}_e)jj$ at $\sqrt{s} = 1.96$ TeV on the factorisation and renormalisation scale μ, at leading-order (blue) and next-to-leading order (red) in QCD. The cuts used are described in the text.

The factorisation and renormalisation scales are set equal to one another, $\mu_F = \mu_R = \mu$, and varied between $\mu = m_W/2$ and $\mu = 2m_W$. The dependence of the cross-section at LO and NLO on the scale is shown in figure 6.5. The decrease in the LO cross-section as the scale increases is driven by the decreasing strong coupling. The LO cross-section is $\sigma_{\text{LO}} = 2.2^{-0.7}_{+1.1}$ fb, where the central value is taken at $\mu =$

m_W and superscript (subscript) is the difference between the central value and the value at $\mu = 2m_W$ ($\mu = 1/2m_W$). At NLO, this becomes $\sigma_{\text{NLO}} = 2.0^{-0.1}_{-0.2}$ fb. The approximately 40% scale uncertainty at LO falls to less than 10% once the NLO corrections are taken into account, and the central value itself also drops by 20%. The Hjj cross-section in this setup, with decay $H \to W^+W^- \to \nu_\mu\mu^+e^-\bar{\nu}_e$ and $m_H = 125$ GeV, is approximately 0.05 fb with a large scale uncertainty. This is more than an order of magnitude smaller than the *scale uncertainty* on the LO cross-section for the W^+W^-jj background. Clearly, a detailed study of the properties of the Higgs boson is not possible in such a situation. While using the NLO cross-section does reduce the scale uncertainty by almost an order of magnitude, it is still comparable to the signal Higgs cross-section.

Kinematic distributions are of great help in discriminating between signal and background processes. In the decay $H \to W^+W^- \to l^+l^-\nu\nu$, the W-bosons have anti-correlated spins due to the scalar nature of the Higgs, and will tend to be back-to-back. The left-handed coupling of the W-bosons to fermions means that one W-boson will decay into a lepton travelling in the same direction, while the other will give rise to a lepton travelling in the opposite direction. The azimuthal angle between the leptons $\Delta\phi_{ll}$ coming from a Higgs is thus expected to be small. This is in contrast to the angular distribution for leptons arising from W^+W^- production, which peaks at π. This is shown in figure 6.6. The NLO corrections make the leptons slightly less back-to-back, and greatly reduce the scale uncertainty. Related to this is the distribution of the invariant mass of the lepton system m_{ll}, also shown in figure 6.6. The NLO corrections do little to change the shape, except to soften it slightly, but the scale uncertainty is of course reduced. Also shown in figure 6.6 is the transverse mass of the W-pair $m_{T,WW}$, defined in equation (5.6.2). The NLO effects deplete the differential cross-sections slightly at large values of $m_{T,WW}$, as well as reducing the scale uncertainty. This distribution shows a more dramatic peak and drop-off when the W-bosons are created through Higgs decay [172].

Another distribution of great interest is the difference in jet pseudorapidity $\Delta\eta_{j_1j_2} = \eta_{j_1} - \eta_{j_2}$. This is because it has a different shape in Higgs production depending on the method of production: small values of $|\Delta\eta_{j_1j_2}|$ are favoured if the production is through gluon fusion, while larger values of $|\Delta\eta_{j_1j_2}|$ are favoured if the production is through weak boson fusion (see e.g. ref. [25]). Differentiating between these is important since the former probes the Yukawa couplings of the Higgs to the quarks, while the latter probes the interactions between the Higgs and the electroweak bosons. The $\Delta\eta_{j_1j_2}$ distribution for the background is shown in figure 6.7. The shape is similar to that of a Higgs created through gluon fusion: strongly peaked at small values of $|\Delta\eta_{j_1j_2}|$ with a small number of events found at large $|\Delta\eta_{j_1j_2}|$.

The pseudorapidities of the two leptons and the transverse momentum of the electron are also shown in figure 6.6. The reduction of scale uncertainties is most strikingly seen in the lepton pseudorapidity plots. These are slightly antisymmetric due to the antisymmetric $p\bar{p}$ initial state. The p_{T,e^-} distribution shows a depletion at large transverse momenta due to the NLO corrections. This was also observed in section 5.6, where it was mentioned that this is due (at least in part) to a fixed scale being used at LO. Using a dynamic scale at LO can often lead to modifications of distributions similar to those caused by NLO corrections.

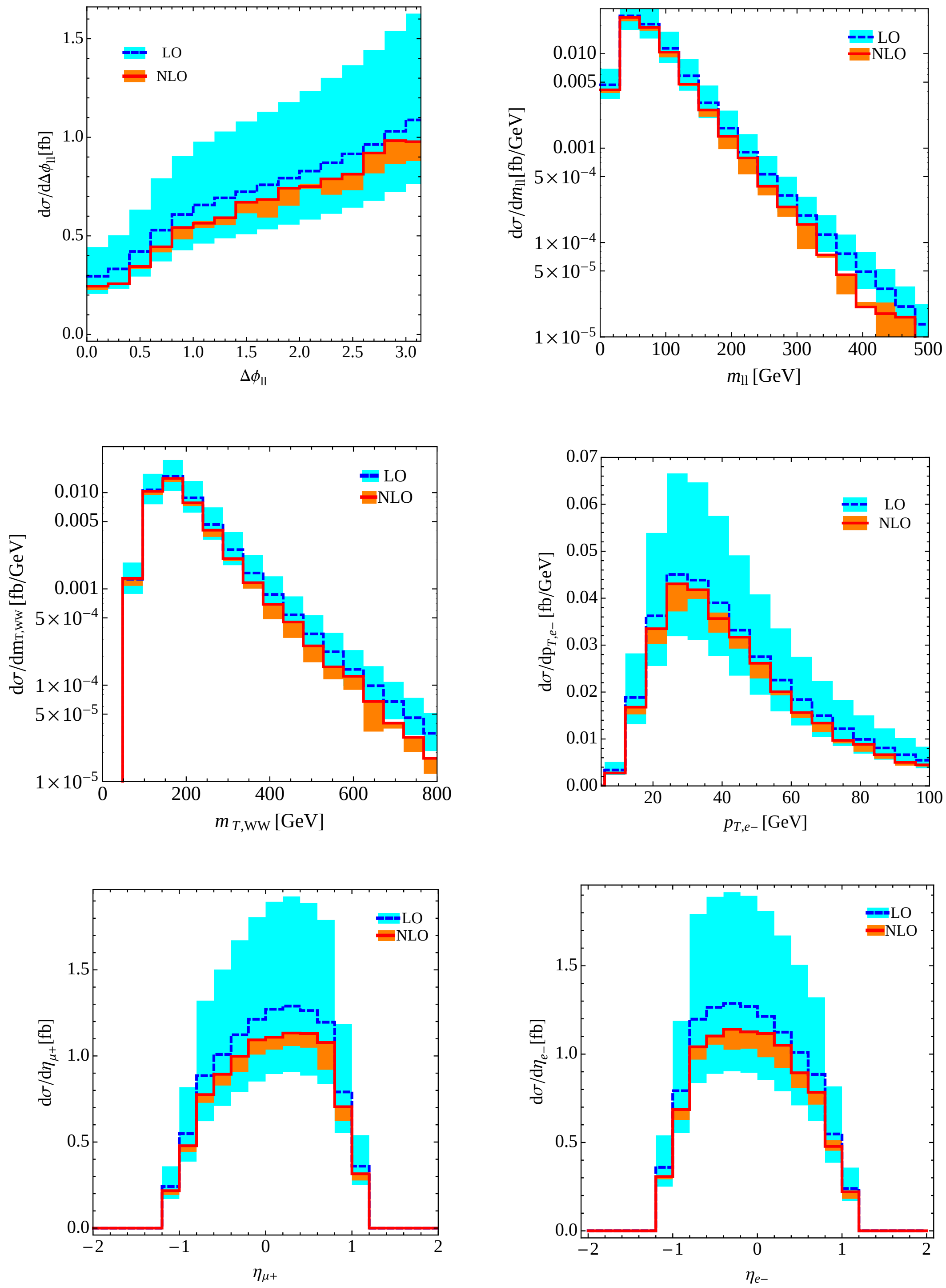

Figure 6.6: Leptonic kinematic distributions for $p\bar{p} \to W^+(\to \nu_\mu \mu^+)W^-(\to e^-\bar{\nu}_e)jj$ at $\sqrt{s} = 1.96$ TeV, at LO and NLO. The cuts used are described in the text. The bands show the scale uncertainty for $m_W/2 \leq \mu \leq 2m_W$, with the central value at $\mu = m_W$. Shown are the azimuthal angle between the leptons $\Delta\phi_{ll}$, the invariant mass of the leptons m_{ll}, the transverse mass of the W-pair $m_{T,WW}$, the transverse momentum of the electron p_{T,e^-} and the pseudorapidities of the leptons η_{e^-} and η_{μ^+}.

.

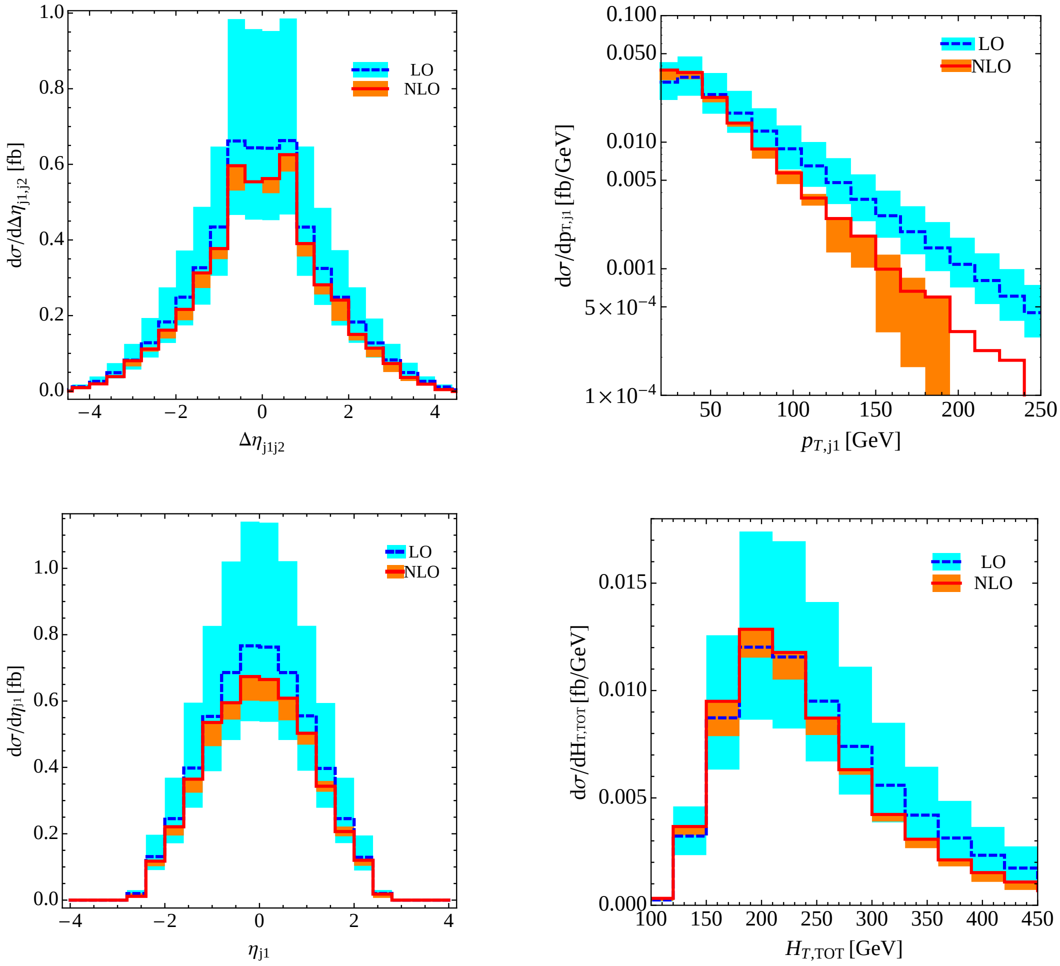

Figure 6.7: Jet distributions for $p\bar{p} \to W^+(\to \nu_\mu \mu^+)W^-(\to e^- \bar{\nu}_e)jj$ at $\sqrt{s} = 1.96$ TeV, at LO and NLO. The cuts used are described in the text. The bands show the scale uncertainty for $m_W/2 \leq \mu \leq 2m_W$, with the central value at $\mu = m_W$. Shown are the difference in jet pseudorapidities $\Delta\eta_{j_1 j_2}$, the transverse momentum and pseudorapidity of the hardest jet $p_{T,j}$ and η_j, and the sum of all transverse momenta $H_{T,TOT}$.

Figure 6.7 also shows the distributions of the transverse momentum and pseudorapidity of the hardest jet, as well as the quantity $H_{T,TOT}$, the sum of the tranverse momenta of the jets, leptons, and missing particles. The reduction in scale uncertainty at NLO can be seen, as can the softening of $p_{T,j}$ and $H_{T,TOT}$ at NLO.

6.6.2 Results at the LHC

The LHC recently announced the discovery of the Higgs boson by both the ATLAS [3] and CMS [4] experiments. CMS reports a preferred mass of $m_H \simeq 125.3$ GeV, while ATLAS favours a slightly higher mass of $m_H \simeq 126.5$ GeV. While the properties of this particle are consistent with the Standard Model Higgs boson, this needs to be confirmed. Data collected during the remainder of the current $\sqrt{s} = 8$ TeV run, as well as the longer $\sqrt{s} = 13$–14 TeV run, will hopefully give further insight into the exact nature of the Higgs. To do so, observation of the Higgs produced in association

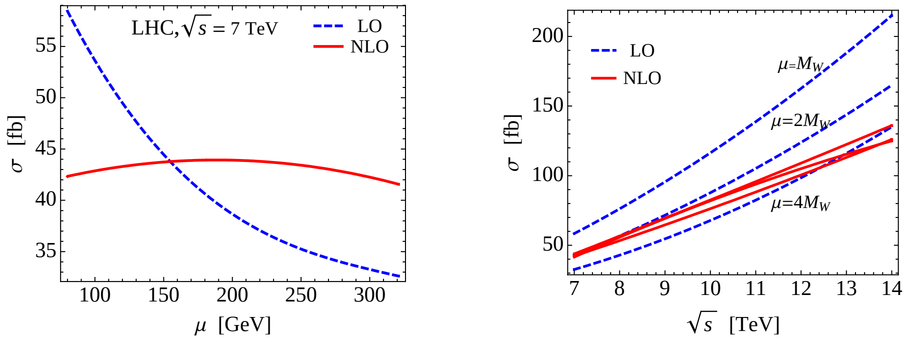

Figure 6.8: Dependence of the cross-section of $pp \to W^+(\to \nu_\mu \mu^+)W^-(\to e^-\bar{\nu}_e)jj$ at $\sqrt{s} = 7$ TeV on the factorisation and renormalisation scale μ (left pane), and on centre-of-mass energy $\sqrt{s}$ (right pane). Cross-sections at leading-order are shown in blue, and at next-to-leading order in red. The cuts used are described in the text.

with two jets is important, and the understanding of W^+W^-jj production as an irreducible background is equally so.

In this section, I will show the results for $pp \to W^+W^-jj$ at the $\sqrt{s} = 7$ TeV LHC run. This may seem a bit dated, but it can easily be scaled to the appropriate energy, since I will also show that the dependence of the cross-section on the centre-of-mass energy is close to linear. The process is regarded as a signal rather than a background, and the cuts used are inspired by $t\bar{t}$ studies at the LHC [177, 178]. Both charged leptons are required to have transverse momenta $p_{T,l} > 20$ GeV and pseudorapidities $|\eta_l| < 2.4$. The missing transverse momentum must satisfy $p_{T,\text{miss}} > 30$ GeV. The jets are reconstructed using the FastJet implementation of the anti-k_t algorithm [111, 168, 169] with $\Delta R_{j_1 j_2} = 0.4$, and are required to have transverse momentum $p_{T,j} > 30$ GeV and pseudorapidity $|\eta_j| < 3.2$. These rather generic cuts allow the a sizeable cross-section W^+W^-jj production cross-section.

The factorisation and renormalisation scales are set equal to each other, $\mu_F = \mu_R = \mu$, and the scale is varied between $m_W \leq \mu \leq 4m_W$ with the central value at $\mu = 2m_W$. The dependence of the LO and NLO cross-sections on the scale is shown on the left of figure 6.8. The fall of the LO cross-section as the scale increases is familiar and caused by the decreasing strong coupling. The cross-sections are $\sigma_{\text{LO}} = 46^{-11}_{+15}$ fb and $\sigma_{\text{NLO}} = 44^{+2.3}_{-1.7}$ fb at LO and NLO respectively. Again, the scale uncertainty decreases by an almost order of magnitude from the LO to the NLO result. The central value is also reduced by the NLO corrections, although not as severely as seen in the production at the Tevatron.

Given that the LHC has already gathered large data sets at two centre-of-mass energies, with at least one more run at a higher energy in the future, it is useful to know how the cross-section varies with energy. This is shown in the right-hand panel of figure 6.8, where it can be seen that this dependence is close to linear. Furthermore, it can be seen that the scale at which the NLO corrections are the smallest changes from $\mu \simeq 2m_W$ at $\sqrt{s} = 7$ TeV to $\mu \simeq 4m_W$ at $\sqrt{s} = 14$ TeV. This is useful, since experimental collaborations often use LO calculations only, in which case the scale can be chosen to minimise the effect of the neglected higher order corrections.

In figure 6.9, I show the distributions $\Delta\phi_{ll}$, m_{ll}, $m_{T,WW}$ and $\Delta\eta_{j_1 j_2}$, which are important in Higgs searches, as discussed in the previous section. The shapes are

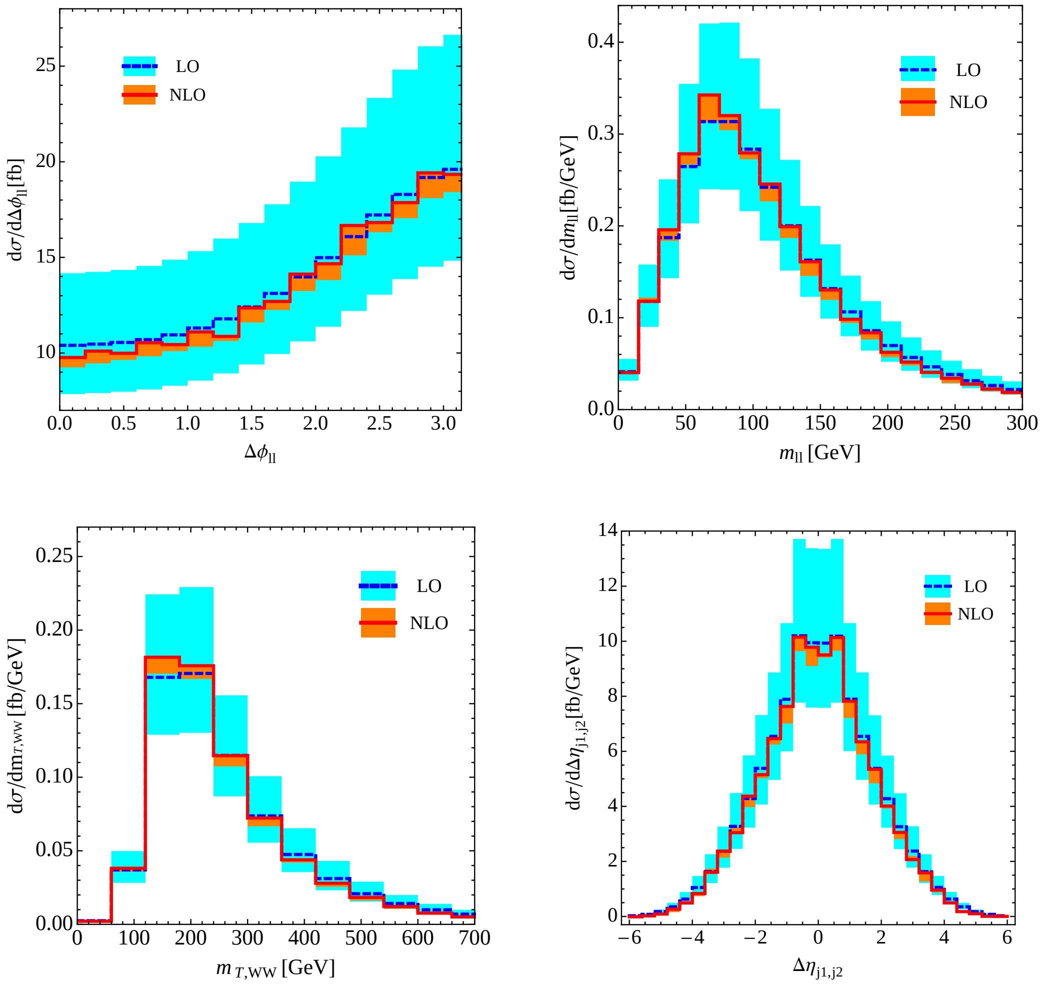

Figure 6.9: Kinematic distributions for $pp \to W^+(\to \nu_\mu \mu^+)W^-(\to e^-\bar{\nu}_e)jj$ at $\sqrt{s} = 7$ TeV, at LO and NLO. The cuts used are described in the text. The bands show the scale uncertainty for $m_W \le \mu \le 4m_W$, with the central value at $\mu = 2m_W$. Shown are the azimuthal angle between the leptons $\Delta\phi_{ll}$, the invariant mass of the leptons m_{ll}, the transverse mass of the W-pair $m_{T,WW}$, and the difference in jet pseudorapidities $\Delta\eta_{j1j2}$.

.

similar to those seen in figures 6.6 and 6.7: the leptons are preferentially produced back-to-back, and the jet pseudorapidity difference distribution peaks at small values of $|\Delta\eta_{j_1 j_2}|$. The NLO corrections have very little effect on the shape of the distributions, but reduce the scale uncertainty drastically.

Figures 6.10 and 6.11 show other distributions: the transverse momenta and pseudorapidities of the hardest and next-to-hardest jets, p_{T,j_1}, η_{j_2}, p_{T,j_2}, and η_{j_2}; the transverse momentum p_{T,μ^+} and the pseudorapidity η_{e^-}, the missing transverse momentum $p_{T,\text{miss}}$, and the sum of all transverse momenta $H_{T,TOT}$. The transverse momentum distributions all show characteristic softening by NLO effects. The lepton pseudorapidities are symmetric as the initial state pp is symmetric. All distributions display a large decrease in scale uncertainties once NLO QCD corrections are taken into account.

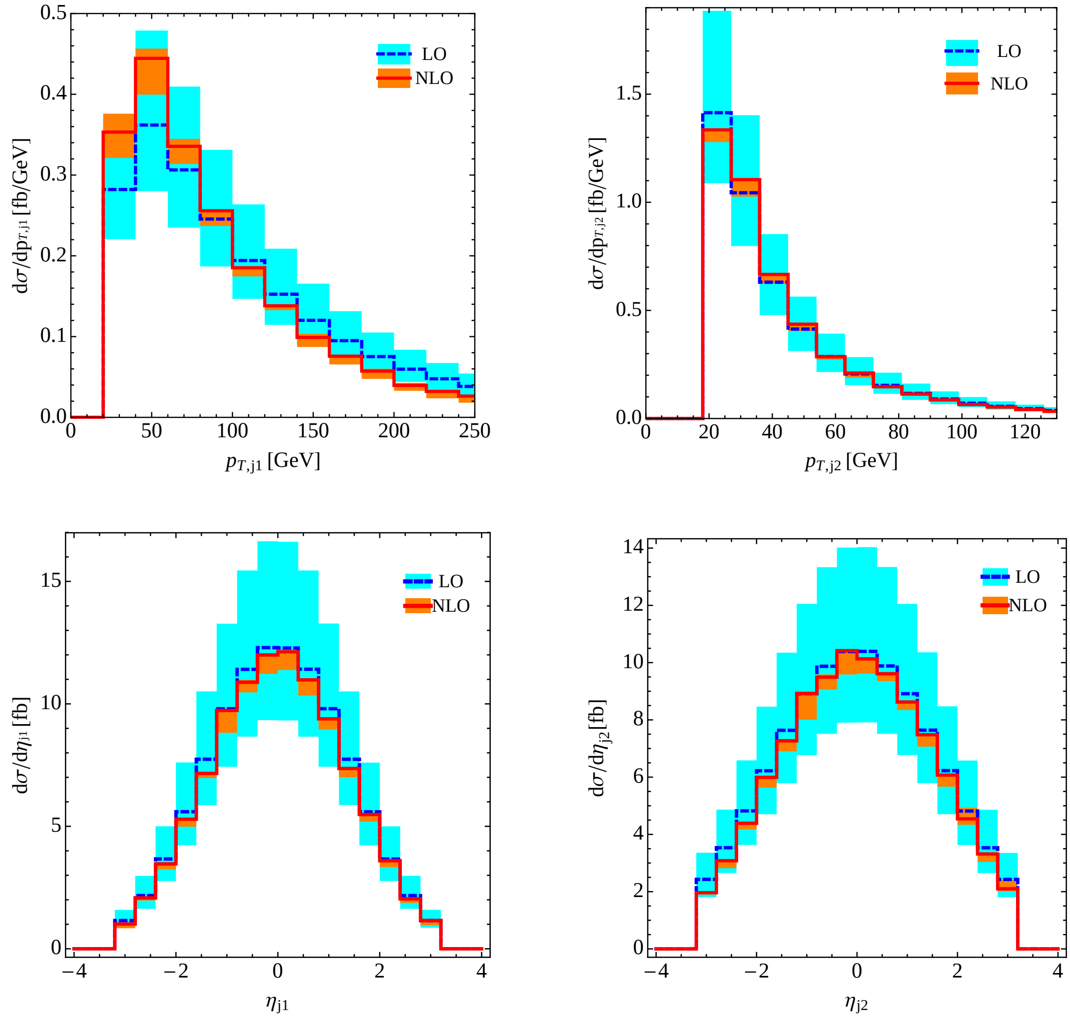

Figure 6.10: Jet distributions for $pp \to W^+(\to \nu_\mu \mu^+)W^-(\to e^-\bar{\nu}_e)jj$ at $\sqrt{s} = 7$ TeV, at LO and NLO. The cuts used are described in the text. The bands show the scale uncertainty for $m_W \leq \mu \leq 4m_W$, with the central value at $\mu = 2m_W$. Shown are the transverse momenta and pseudorapidities for hardest and next-to-hardest jets.

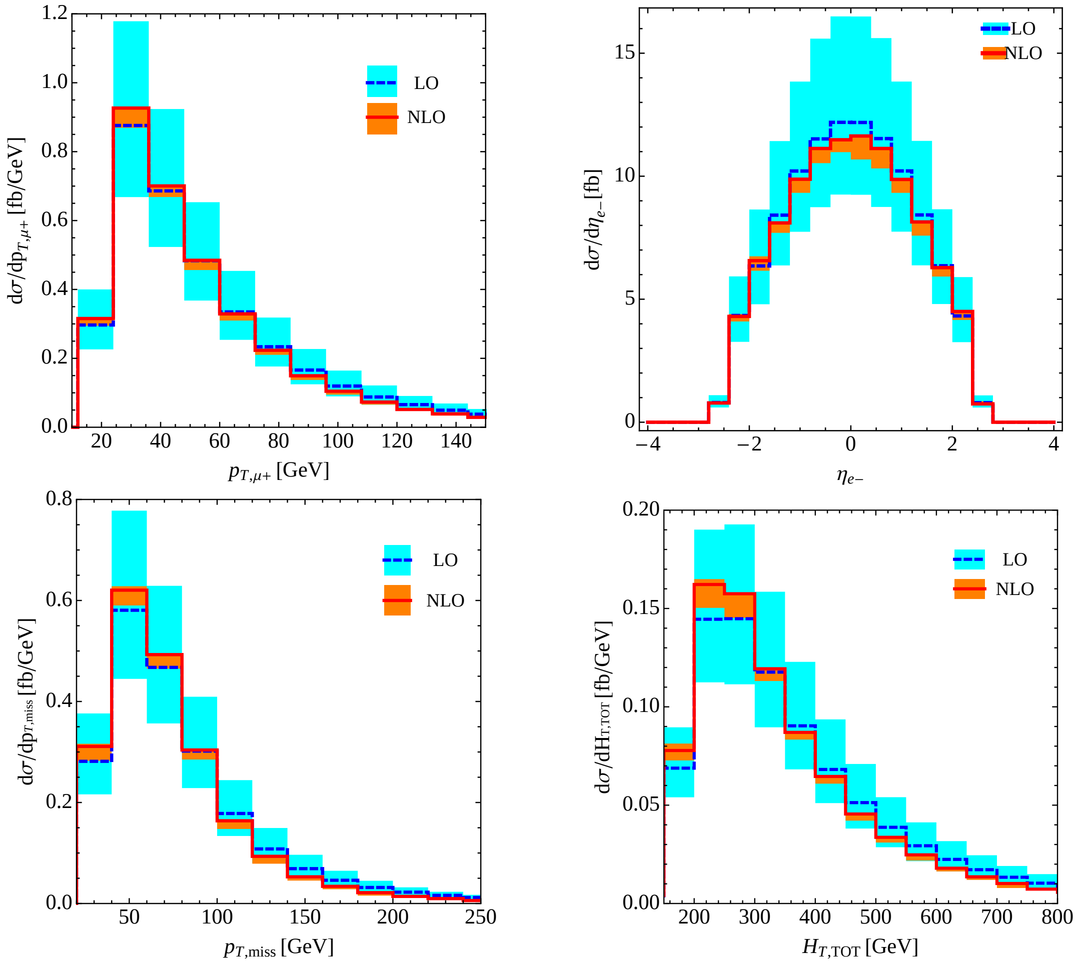

Figure 6.11: Leptonic distributions for $pp \to W^+(\to \nu_\mu \mu^+)W^-(\to e^-\bar{\nu}_e)jj$ at $\sqrt{s} = 7$ TeV, at LO and NLO. The cuts used are described in the text. The bands show the scale uncertainty for $m_W \le \mu \le 4m_W$, with the central value at $\mu = 2m_W$. Shown are the momentum of the positron, the pseudorapidity of the μ^+, the missing transverse momentum and the sum of all transverse momenta $H_{T,TOT}$.

6.7 Conclusion

In this chapter, the generalised unitarity method was put to work in calculating the hadroproduction of W^+W^-jj. Production in two partonic modes, namely $\bar{q}qgg$ and $\bar{q}q\bar{q}q$, was considered, with the former being dominant. The flavour structure was much more complicated than that considered in chapter 5, due to the electromagnetic neutrality of the W-pair. This made the computation more intricate, and the running time longer, but did not cause any particular difficulties. Likewise, the presence of two colour-neutral particles is easily handled.

Phenomenology at both the Tevatron and LHC was studied. In both cases, the NLO corrections reduce the scale uncertainties present in both total cross-sections and distributions by an order of magnitude, to the level of around 5-10%. Indeed, this was one of the main motivations for performing calculations to NLO in QCD discussed in the Introduction. The NLO corrections are also found to reduce the central cross-section value by around 20% at the Tevatron and 10% at the $\sqrt{s} = 7$ TeV LHC. The LHC cross-section shows a close to linear dependence on the centre-of-mass energy. This suggests a quick manner in which the results presented here may be scaled to future energies, in order to get a first estimate of the effect of NLO corrections. Furthermore, it is suggested that the scale choice minimising the effect of the NLO corrections also increases with centre-of-mass energy, from $\mu \simeq 2m_W$ at $\sqrt{s} = 7$ TeV to $\mu \simeq 4m_W$ at $\sqrt{s} = 14$ TeV.

The role of certain kinematic distributions in discriminating between a Higgs signal and W^+W^- production was briefly discussed. The NLO corrections have little effect on the shape of the distributions, other than softening the transverse momentum and mass distributions at large values. However, it is advantageous to use distributions calculated to NLO, since the much smaller scale uncertainty translates into a more reliable discrimination.

Chapter 7

Hadroproduction of W^+W^-j through a Fermion Loop

7.1 Introduction

In this chapter, I will discuss the production of W^+W^-j through gluon-gluon fusion[1]. The partonic process $0 \to ng + W^+W^-$ $(n \geq 2)$ does not occur at tree-level: the lowest-order amplitude $\mathcal{M}_f^{\mathrm{V}}$ involves a quark loop to which the W-bosons couple (see figure 7.1). This has two important consequences. First, the virtual amplitude is finite, in contrast to the virtual amplitudes encountered in the previous two chapters which had both ultraviolet and infrared poles. The virtual amplitude is also electroweak gauge invariant. Second, at leading order (LO) and next-to-leading order (NLO), the initial states are either quark-quark or quark-gluon. The gluon fusion amplitude therefore does not contribute to the NLO cross-section, since there is no tree-level amplitude with which it can be colour-multiplied (see equation (2.1.2)). The gluon fusion amplitude enters the cross-section at next-to-next-to-leading order (NNLO) through its square

$$\delta\sigma_{\mathrm{NNLO}} = \int d\Phi_N \sum_{\mathrm{hel}} |\mathcal{M}_f^{\mathrm{V}}|^2. \tag{7.1.1}$$

Of course, this cross-section is suppressed by an additional power of α_s relative to the NLO cross-section, and one might think that therefore the NNLO corrections are negligible. In fact, this is not necessarily the case, since the LHC has a large gluon flux at small momentum transfers $x \sim \frac{2m_W}{\sqrt{s}}$. It is unclear *a priori* whether this enhancement compensates sufficiently for the additional α_s factor to make $\delta\sigma_{\mathrm{NNLO}}$ sizeable compared to the NLO cross-section for a given process.

This question was first studied by Binoth, Ciccolini, Kauer, and Kramer [42,43] for the process $gg \to W^+W^-$. They found that the relative size of the $\delta\sigma_{\mathrm{NNLO}}$ contribution is highly cut dependent. For inclusive cuts, it increases the NLO cross-section by around 5%, but this increases to 30% when cuts designed for Higgs searches

---

[1] These processes are similar to the "light-by-light" virtual amplitudes neglected in the previous chapter.

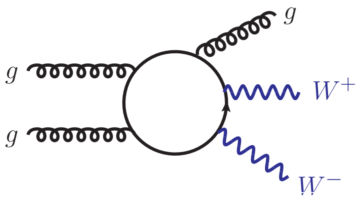

Figure 7.1: Diagrammatic representation of the production of W^+W^-j by gluon fusion, through a virtual quark loop.

in gluon fusion are applied. In fact, for these cuts the $\delta\sigma_{\mathrm{NNLO}}$ correction is a factor of about seven larger than the NLO corrections.

Given that Higgs searches are binned according to the number of jets produced, it is interesting to see whether this level of significance is also present when the W-pair is created in association with a jet, and whether the effect of the gluon-fusion contribution is so strongly cut dependent.

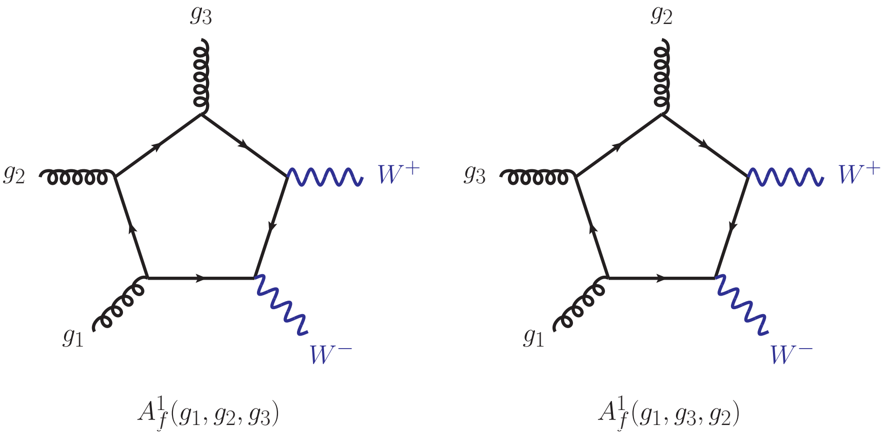

Figure 7.2: Primitive amplitudes $A^1_f(g_1,g_2,g_3)$ (left) and $A^1_f(g_1,g_3,g_2)$ (right), for the process $0 \to gggW^+W^-$. One ordering of the W-bosons is shown; all insertions relative to the gluons are included in these primitives.

7.2 Virtual amplitudes

The production of W^+W^-j through gluon fusion involves the partonic process $0 \to gggW^+(\to \nu_e e^+)W^-(\to \mu^-\bar{\nu}_\mu)$. As before, the W-bosons decay leptonically, using equation (4.2.24) to define the polarisation states. However, single resonant production is now included, using equation (4.2.26) to define the polarisation vectors of intermediate Z-bosons or photons. The virtual amplitude is

$$\begin{aligned}\mathcal{M}^{\mathrm{V}}_f(g_1,g_2,g_3;\nu_e,e^+,\mu^-,\bar{\nu}_\mu) =& g_s^3\left(\frac{g_w}{\sqrt{2}}\right)^4\Big\{\mathrm{Tr}\Big(t^{a_1}t^{a_2}t^{a_3}\Big)A^1_f(g_1,g_2,g_3)\\ &+\mathrm{Tr}\Big(t^{a_1}t^{a_3}t^{a_2}\Big)A^1_f(g_1,g_3,g_2)\Big\},\end{aligned} \tag{7.2.1}$$

where g_w and g_s are the weak and strong couplings respectively, and the partial amplitudes A^1_f serve also as the primitive amplitudes, shown in figure 7.2.

Unlike in the previous chapters, all flavours of quarks are considered circulating in the loop, with the top and bottom quarks being massive and the other two generations being massless. The primitive amplitudes can then be written in terms of massless and massive primitives

$$A^1_f = 2A^1_{f,0} + A^1_{f,m}, \tag{7.2.2}$$

where the unit CKM matrix ensures that no massless quarks appear in the massive primitive amplitude, or vice versa. The massless and massive primitives may be split into their contributions from the W-bosons coupling directly to the virtual quarks, and their coupling through a virtual Z-boson (axial and vector) and through a photon

$$\begin{aligned}A^1_{f,0} =& A^{[WW]}_{f,ud} + \sum_{q=\{u,d\}}\Big(C^{(q)}_{Z_V}A^{[Z_V]} + C^{(q)}_{Z_A}A^{[Z_A]} + C^{(q)}_{\gamma}A^{[\gamma]}\Big),\\ A^1_{f,m} =& A^{[WW]}_{f,tb} + \sum_{q=\{t,b\}}\Big(C^{(q)}_{Z_V}A^{[Z_V]} + C^{(q)}_{Z_A}A^{[Z_A]} + C^{(q)}_{\gamma}A^{[\gamma]}\Big).\end{aligned} \tag{7.2.3}$$

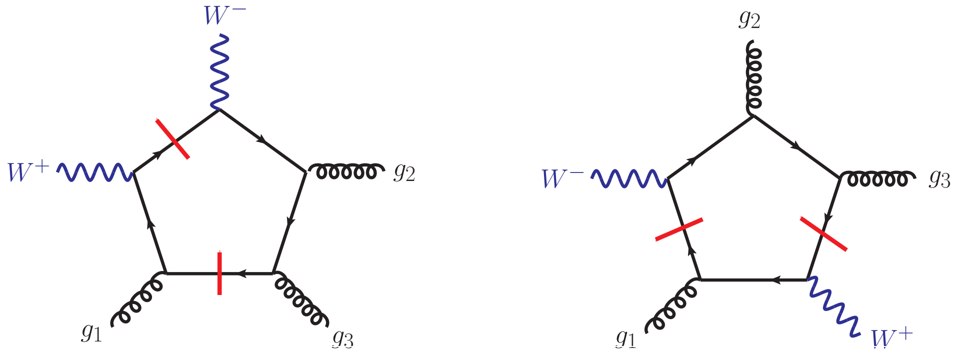

Figure 7.3: Two different unitarity double cuts (shown in red) on the primitive $A_f^1(g_1, g_2, g_3)$ with different orderings of the W-bosons with respect to the gluons. This can lead to double-counting of unitarity cuts, as described in the text.

The presence of single resonant amplitudes makes this expression more complicated than equation (6.2.2), since the single resonant current equation (4.2.26) is different for an intermediate Z-boson than for a intermediate photon. The couplings are

$$C_{Z_V}^{(q)} = T_3^{(q)} - 2Q^{(q)} \sin^2\theta_w; \quad C_{Z_A}^{(q)} = -T_3^{(q)}; \quad C_\gamma^{(q)} = 2Q^{(q)} \sin\theta_w, \tag{7.2.4}$$

with $T_3^{(u,c,t)} = 1/2$ and $T_3^{(d,s,b)} = -1/2$, and $Q^{(q)}$ is the electric charge of the quark. In all terms in equation (7.2.3), all orderings of the electroweak bosons relative to the gluons are considered: this leads to 12 insertions for the W-pair (taking into account the orderings W^+W^- and W^-W^+) and 3 insertions for the Z-boson or photon.

Unlike previous primitive amplitudes, A_f^1 is completely cyclic. This leads to an issue when using the usual Berends-Giele currents $\mathsf{f\_V\bar{f}}$ and $\mathsf{f\_VV\bar{f}}$. Consider two orderings of the W-pair relative to the gluons in the primitive $A_f^1(g_1, g_2, g_3)$, each with a different unitarity double cut, as shown in figure 7.3. If the tree-level amplitude containing g_1 and W^+ is computed using current $\mathsf{f\_V\bar{f}}$, both orderings g_1W^+ and W^+g_1 will contribute. The tree-level amplitudes resulting from these two cuts are thus identical, so the cuts are equivalent, and including both would be double counting. This problem is not restricted to double cuts; nor is it a result of the two orderings of the W-pair, since it is present when amplitudes with the Z-boson or photon are evaluated too. Since the unitarity indices – the label of the propagating quarks which are cut – are not the same, it is difficult to automatically identify such double counting during the evaluation of primitives.

This problem is the motivation behind the Berends-Giele currents $\mathsf{f\_V\bar{f}g}^*$, and $\mathsf{f\_VV\bar{f}g}^*$. As discussed in section 4.3, these currents have a “reference” gluon, and the W-bosons are restricted to being attached to the quark-antiquark line either before or after this gluon. For this reason, they are referred to as “restricted” currents. The reference gluon is always chosen to be g_1. If a current includes this gluon, then restricted currents are used. The tree-level amplitude arising from the left diagram in figure 7.3 will be computed using $\mathsf{f\_V\bar{f}g}^*$ with arguments $f_p = f_g = 1$. The W-boson will be attached to the quark-antiquark line *after* the gluon (reading clockwise). The tree-level amplitude arising from the right diagram will be computed using $\mathsf{f\_V\bar{f}g}^*$ with arguments $f_p = 2$ and $f_g = 1$. The W-boson is attached *before* the gluon.

Double counting is thus avoided. The unmodified currents `f_Vf̄` and `f_VVf̄` can be used for tree-level amplitudes that do not contain g_1.

Numerical values for $A^1_{f,0}$ and $A^1_{f,m}$, and their sum A^1_f, are shown in table 7.1 for the eight combinations of the gluon helicities . The parameters used are quoted in the next section. The phase space point used is (in GeV)

$$
\begin{aligned}
p_{g_1} &= (-500, 0, 0, -500)\\
p_{g_2} &= (-500, 0, 0, 500)\\
p_{g_3} &= (86.3540681437814, -15.2133893202618, 37.6335512949163, -76.2187226821854)\\
p_{\nu_e} &= (280.118181809376, -83.1261116505822, -263.203856758651, 47.7490851160266)\\
p_{e^+} &= (127.522529569661, -90.4490412959935, -83.1783077030789, 34.0930433392580)\\
p_{\mu^-} &= (414.130068374543, 232.145564945939, 332.7544367808, -82.9857518524426)\\
p_{\bar\nu_\mu} &= (91.8751521026384, -43.3570226791011, -24.0058236140057, 77.3623460793435).
\end{aligned}
\tag{7.2.5}
$$

Ordering and helicities	$\lvert A^1_{f,0}\rvert$	$\lvert A^1_{f,m}\rvert$	$\lvert A^1_f\rvert$
g_1^-, g_2^-, g_3^-	23.21330	26.65234	71.74573
g_1^-, g_2^-, g_3^+	32.40065	37.56669	101.3440
g_1^-, g_2^+, g_3^-	6.205020	6.628405	18.87935
g_1^-, g_2^+, g_3^+	4.773174	5.031766	14.41761
g_1^+, g_2^-, g_3^-	3.522647	6.204687	4.826768
g_1^+, g_2^-, g_3^+	5.936161	8.474948	5.884032
g_1^+, g_2^+, g_3^-	5.699256	1.606166	9.799904
g_1^+, g_2^+, g_3^+	3.844351	0.9542655	6.734822
g_1^-, g_3^-, g_2^-	24.00377	26.87233	73.79497
g_1^-, g_3^-, g_2^+	31.42718	38.80862	100.7887
g_1^-, g_3^+, g_2^-	6.930642	6.370970	19.94051
g_1^-, g_3^+, g_2^+	4.540278	5.275261	14.06054
g_1^+, g_3^-, g_2^-	5.124427	5.388578	6.081942
g_1^+, g_3^-, g_2^+	4.211189	8.456738	4.243700
g_1^+, g_3^+, g_2^-	6.729332	0.6778853	12.91303
g_1^+, g_3^+, g_2^+	3.882990	1.094038	6.673465

Table 7.1: Matrix elements for the massless and massive primitives, $A^1_{f,0}$ and $A^1_{f,m}$, as well as the total primitives A^1_f, for both orderings of the gluons, and all eight gluon helicities, at the phase space point of equation (7.2.5). Units are 10^{-6} GeV^{-3}.

The matrix element squared is

$$
\begin{aligned}
|\mathcal{M}^{\rm V}_f|^2 =& S_{gg} g_s^6 \Big(\frac{g_w}{\sqrt{2}}\Big)^8 \sum_{\rm hel} 2C_F \Big\{ \big(2C_F N_c - 1\big)\big(|A^1_f(g_1, g_2, g_3)|^2 + |A^1_f(g_1, g_3, g_2)|^2\big)\\
&- 4 \;\mathrm{Real}\big(A^1_f(g_1, g_2, g_3) A^{1,*}_f(g_1, g_3, g_2)\big)\Big\}.
\end{aligned}
\tag{7.2.6}
$$

For the above phase space point, the numerical value of the virtual matrix element squared is 7.830968×10^{-7} GeV^{-6}. If only one massless generation is used in the loop, this results becomes 8.348897×10^{-8} GeV^{-6}. If one massive generation is used, then this result is 1.128414×10^{-7} GeV^{-6}.

7.3 Checks, stability and running time

The computation of the virtual matrix elements as described in the previous section was implemented in the private program `TOPAZ`, written by M. Schulze and K. Melnikov. This program has previously been used in top phenomenology studies [88–92]. This program performs the Monte Carlo integration over the phase space too. The virtual amplitude should be finite, and indeed the residues of the poles of the virtual amplitude were found to be 9-15 orders of magnitude smaller than the finite parts. This level of agreement is comparable with that shown in tables 5.3, 6.5 and 6.7. The finite parts were checked against the Feynman diagram-based OPP computation, as in sections 5.5 and 6.5, and agreement was found. As a further check, the amplitude $A^{[WW]}_{f,ud}$ was checked against the public program `GoSam` [165, 166], an automated implementation of the OPP procedure based again on the evaluation of conventional Feynman diagrams. Agreement was found to the level of 4 significant figures.

The computation of the primitive amplitudes was performed in double precision as standard, with the usual two checks on the accuracy of the result performed: the poles were checked to be smaller than 10^{-4}, and the OPP equations were checked to have been solved to an accuracy 10^{-2}. The computation proved surprisingly unstable: around 25% of all primitive amplitudes evaluated failed one or both of these checks. In these cases, the OPP equations were solved in quadruple precision, using the tree-level helicity amplitudes calculated in double precision. Typically, about half the primitive amplitudes recalculated in this manner still failed one or both of the checks. For these primitive amplitudes, the full calculation was repeated in quadruple precision: tree-level amplitudes were recomputed and the OPP equations again solved. After this, only about 0.05% of the primitives fail one or both of the checks, and these are set to zero. It is unclear why such a high percentage of primitive amplitudes fail the checks after the initial computation, although it is predominantly the amplitudes $A^{[WW]}_{f,tb}$ which fail.

As a result of the large number of recomputations in quadruple precision that are required, the computational time is larger than would be expected for a $2 \to 3$ process: it takes over five seconds for the virtual matrix element to be evaluated at a single phase space point. The phase space grid was created using tree-level $pp \to W^+W^-j$ production with gluonic fluxes for the initial state partons. With this grid, around 10^5 phase space points are required to give a cross-section with an error of a few percent. However, by parallelising the computation, it can be accomplished within a few days.

7.4 Results

In this section, I will present results for $pp \to W^+W^-j$ at the LHC with centre-of-mass energies $\sqrt{s} = 8$ TeV and $\sqrt{s} = 14$ TeV [84]. The gluon fusion contribution to the NNLO correction is included, as described in the previous chapter. The cross-section to NLO is calculated using an implementation similar to that discussed in chapter 6, and in fact using the leading-order matrix elements described in section 6.2 to compute the real radiation contributions. As a byproduct, the NLO computation was made publicly available, as an add-on to `MCFM v6.1`[2]. This calculation will not be discussed further in this work.

Since an important motivation for this work were the studies of the importance of gluon fusion in the production of W^+W^- [42, 43], these calculations are repeated here. The cross-sections to NLO were computed using `MCFM` [24], and the gluon fusion contributions were computed in the same manner as $0 \to gggW^+W^-$, described in section 7.2.

As before, the W-bosons decay leptonically, $W^+W^- \to \nu_e e^+ \mu^- \bar{\nu}_\mu$, with the results summed over all lepton flavours being a factor of four larger than the results shown in this section. As mentioned in section 7.2, single resonant W-production is included at all levels. The masses of the W- and Z-bosons are taken to be $m_W = 80.399$ GeV and $m_Z = 91.1876$ GeV respectively, and their widths are $\Gamma_W = 2.085$ GeV and $\Gamma_Z = 2.4952$ GeV. The weak couplings are defined through the Fermi constant $G_F = 1.166364 \times 10^{-5}$ GeV^{-2} and $g_w^2 = 8/\sqrt{2} G_F m_W^2$. The electromagnetic coupling is obtained from this using the weak angle $\sin^2\theta_w = 1 - m_W^2/m_Z^2$. All quarks are taken to be massless except the top and bottom quarks, which have masses $m_t = 172.9$ GeV and $m_b = 4.19$ GeV respectively. Jets are defined using the anti-k_t algorithm [168] implemented in FastJet [111, 169], with $\Delta R_{j_1 j_2} = 0.4$. The parton distributions are from the MSTW08 set [98]. The gluon fusion contribution is considered as an approximation to the full NNLO cross-section, and is therefore calculated using the NNLO distribution. One could equally well argue that since the fermion loop amplitudes are the leading-order amplitudes in gluon fusion, LO PDFs should be used. Since the gluon flux is less at NNLO than at LO, this would increase the gluon fusion contribution by around 30%. The LO and NLO cross-sections are computed using LO and NLO PDFs. The LO, NLO, and NNLO PDFs use strong couplings $\alpha_s(m_Z) = 0.13939$, $\alpha_s(m_Z) = 0.12018$, and $\alpha_s(m_Z) = 0.11707$, respectively.

Two sets of kinematic cuts are used. The first, referred to as "standard cuts", are generic cuts for an experimental signature involving charged leptons, jets, and missing energy. These cuts require the leptons to have transverse momentum $p_{T,l} > 20$ GeV and pseudorapidity $|\eta_{l_1}| < 2.5$, the jets to have transverse momentum $p_{T,j} > 20$ GeV and pseudorapidity $|\eta_j| < 3.2$, and the missing transverse momentum to satisfy $p_{T,\text{miss}} > 30$ GeV.

---

[2] This code is available from http://www-thphys.physics.ox.ac.uk/people/TomMelia/tommelia.html or from http://mcfm.fnal.gov/. Note that the public code does not include the fermion loop contributions to the NLO cross-section, the effect of which is negligible.

Standard Cuts

		σ_{LO} (fb)	$\sigma^{\text{incl}}_{\text{NLO}}$ (fb)	$\sigma^{\text{excl}}_{\text{NLO}}$ (fb)	$\delta\sigma_{\text{NNLO}}$ (fb)	$\delta\sigma_{\text{NNLO}}/\sigma^{\text{incl}}_{\text{NLO}}$
8 TeV	WW	$141.0(1)^{+2.8}_{-4.0}$	$232.0(4)^{-5.8}_{+7.5}$	$143.8(2)^{+4.2}_{-4.1}$	$8.1(1)^{-1.7}_{+2.2}$	3.5%
	WWj	$87.8(1)^{-10.9}_{+13.5}$	$111.3(2)^{-5.5}_{+4.9}$	$66.6(2)^{+4.4}_{-9.0}$	$3.4(1)^{-1.0}_{+1.6}$	3.1%
14 TeV	WW	$259.6(2)^{+14.2}_{-17.2}$	$448.3(5)^{-7.4}_{+11.6}$	$242.0(3)^{+9.2}_{-8.6}$	$23.6(1)^{-4.1}_{+5.2}$	5.3%
	WWj	$203.4(1)^{-19.9}_{+22.9}$	$254.5(4)^{-10.2}_{+9.0}$	$127.6(4)^{+14.8}_{-24.1}$	$11.8(4)^{-3.2}_{+4.7}$	4.6%

Table 7.2: Cross-sections for $pp \to W^+(\to \nu_e e^+)W^-(\to \mu^- \bar{\nu}_\mu) + n$ jets, $n = 0, 1$ at the $\sqrt{s} = 8$ TeV and $\sqrt{s} = 14$ TeV LHC. The standard cuts are used. The central values are computed at scale $\mu = 2m_W$, with the statistical errors shown in parentheses. The upper and lower values for cross-sections are obtained with the scale $\mu = m_W$ (subscript) and $\mu = 4m_W$ (superscript). The last column shows the relative size of the NNLO contribution to the inclusive NLO cross-section for the central scale choice.

The second set of cuts ("Higgs cuts") are similar to the cuts used by ATLAS collaboration[3] in their recent Higgs searches in the WW decay channel [170]. The hardest and next-to-hardest leptons are required to have transverse momentum $p_{T,l_{\max}} > 25$ GeV and $p_{T,l_{\min}} > 15$ GeV; both must have pseudorapidity $|\eta_l| < 2.5$. The two leptons must be separated by $\Delta R_{ll} > 0.3$. The missing relative transverse energy must satisfy $E^{\text{rel}}_{T,\text{miss}} > 25$ GeV. The definition used for this quantity is similar to equation (6.6.1):

$$E^{\text{rel}}_{T,\text{miss}} = |\mathbf{p}_{T,\text{miss}}| \sin \Delta\phi_{\min}, \tag{7.4.1}$$

with $\mathbf{p}_{T,\text{miss}}$ the missing tranverse momentum and $\Delta\phi_{\min} = \min\bigl(\Delta\phi, \pi/2\bigr)$, with $\Delta\phi$ the angle between $\mathbf{p}_{T,\text{miss}}$ and the nearest lepton or jet. Additionally, the nearest lepton or jet is now constrained to have $p_T > 25$ GeV. In section 6.6, I mentioned that W-bosons originating from Higgs decay will themselves decay to leptons with a small opening angle, and consequently the invariant mass of the charged lepton system m_{ll} will also be small. This motivates the cuts on the azimuthal angle between the leptons $\Delta\phi_{ll} < 1.8$ and on the invariant mass of the leptons 10 GeV $< m_{ll} < 50$ GeV (the lower bound on m_{ll} reduces photon background). The WW process with no jets has an additional cut: the transverse momentum of the charged lepton systems must be $p_{T,ll} > 30$ GeV. There are no further cuts to suppress the 2-jet production cross-section.

The results for W^+W^- and W^+W^-j production using the standard cuts are shown in table 7.2, at centre-of-mass energies $\sqrt{s} = 8$ TeV and $\sqrt{14}$ TeV. The cross-sections are shown at LO and NLO (inclusive and exclusive), together with the gluon fusion NNLO contribution. The statistical errors in the final digit are shown in parentheses. The factorisation and renormalisation scales are set equal to one another, $\mu_R = \mu_F = \mu$. The central value is computed using $\mu = 2m_W$, and the variations between this value and those obtained at scales $\mu = m_W$ and $\mu = 4m_W$ are shown

---

[3] Details related to the detector are ignored, so that the cuts used here are slightly simpler than those used by ATLAS.

Higgs search cuts

		σ_{LO} (fb)	$\sigma^{\mathrm{incl}}_{\mathrm{NLO}}$ (fb)	$\sigma^{\mathrm{excl}}_{\mathrm{NLO}}$ (fb)	$\delta\sigma_{\mathrm{NNLO}}$ (fb)	$\delta\sigma_{\mathrm{NNLO}}/\sigma^{\mathrm{excl}}_{\mathrm{NLO}}$
8 TeV	WW	$35.6(1)^{+0.9}_{-1.3}$	$51.1(1)^{-0.4}_{+0.9}$	$38.8(1)^{+1.0}_{-0.8}$	$2.7(1)^{-0.5}_{+0.7}$	7.0%
	WWj	$12.6(1)^{-1.5}_{+1.8}$	$10.8(1)^{+0.3}_{-0.7}$	$10.6(1)^{+0.3}_{-0.9}$	$0.6(1)^{-0.2}_{+0.2}$	5.7%
14 TeV	WW	$63.4(1)^{+3.9}_{-4.7}$	$91.9(2)^{-0.1}_{+0.4}$	$63.4(2)^{+2.1}_{-2.0}$	$7.5(1)^{-1.2}_{+1.5}$	11.8%
	WWj	$28.7(1)^{-2.6}_{+2.9}$	$21.6(1)^{+1.2}_{-2.1}$	$20.5(1)^{+1.7}_{-2.2}$	$1.8(2)^{-0.5}_{+0.7}$	8.8%

Table 7.3: As for table 7.2, but using the Higgs cuts described in the text.

as subscript and superscript respectively. The effect of the NLO corrections is large for W^+W^- production, enhancing the LO cross-section by 65% at $\sqrt{s} = 8$ TeV and 75% at $\sqrt{s} = 14$ TeV. The effect of these corrections is smaller for the production in association with a jet: the cross-section is enhanced by around 25%, still a significant effect. By contrast, the NNLO contribution enhances the NLO cross-section by 3-5% for either process. While this effect is not large, it is not negligible either; indeed, the NNLO contribution is comparable to the scale uncertainty of the NLO cross-section. The enhancement is larger for the higher centre-of-mass energy – a reflection of the larger gluon flux – and is slightly smaller for the W^+W^-j process than for the W^+W^- process. The physical parameters, kinematic cuts and PDFs used here are different to those of refs. [42, 43]; nevertheless, the effect of the gluon fusion contribution to the process W^+W^- shown in table 7.2 is similar to that reported in these references.

Table 7.3 shows the cross-sections using the Higgs cuts, with the same setup as table 7.2. The inclusive NLO cross-sections for W^+W^- are enhanced by around 50% with respect to the LO results, but the exclusive NLO cross-sections for this process are similar to the LO cross-sections. This indicates that 25-40% of W^+W^- events include final state jets, with the percentage increasing with $\sqrt{s}$, as might be expected. The gluon fusion contributions become more important using these cuts: for this process they amount to 7% of the exclusive NLO cross-section at $\sqrt{s} = 8$ TeV and almost 12% at $\sqrt{s} = 14$ TeV. Furthermore, these contributions are significantly larger than the scale uncertainty in the NLO cross-section. They are, however, much smaller than the $\sim 30\%$ effect of refs. [42, 43]. The reason for this is that the Higgs cuts used here are more inclusive than those used in refs. [42, 43]. In particular, these references use cuts on the lepton transverse momentum $p_{T,l_{\max}} > 35$ GeV and $p_{T,l_{\min}} > 25$ GeV, on the azimuthal angle between the leptons $\Delta\phi_{ll} < 0.78$, and on the invariant mass of the lepton system $m_{ll} < 35$ GeV. Therefore, it would appear that for cuts used at present in Higgs searches at the LHC, 10-15% is a better estimate of the effect of gluon fusion contributions to W^+W^- production than 30%.

Table 7.3 shows that the effect of the NLO corrections on the W^+W^-j cross-sections is negative, and the inclusive and exclusive cross-sections are similar. This is not indicative of a very small probability of a second jet being emitted, since the LO cross-section for W^+W^-jj production at $\sqrt{s} = 8$ TeV using these cuts is approximately 4.5 fb. Rather, the small difference between the inclusive and exclusive W^+W^-j cross-sections could be due to the action of the dipoles. In W^+W^-jj production, the two jets are usually emitted in the same hemisphere, where the effect of the dipoles is most pronounced. The effect of gluon fusion is around 6% at $\sqrt{s} = 8$

TeV and around 9% at $\sqrt{s} = 14$ TeV. Again, gluon fusion has less of an effect in this process than in W^+W^- production. However, these effects are still comparable to the scale uncertainty in the NLO cross-section, and thus should not be neglected.

The importance of the gluon fusion contributions is further emphasised when the *signal* $H \to W^+W^- \to \nu_e e^+ \mu^- \bar{\nu}_\mu$ is considered. With no jet produced, the cross-section for this process to NLO in QCD is approximately 5 fb at $\sqrt{s} = 8$ TeV and 12 fb at $\sqrt{s} = 14$ TeV. With a jet present, the cross-sections are 2 fb at $\sqrt{s} = 8$ TeV and 5 fb at $\sqrt{s} = 14$ TeV. (These results were obtained using `MCFM`). Therefore the gluon fusion contributions – an NNLO effect – to the background amount to about half of the signal production cross-section.

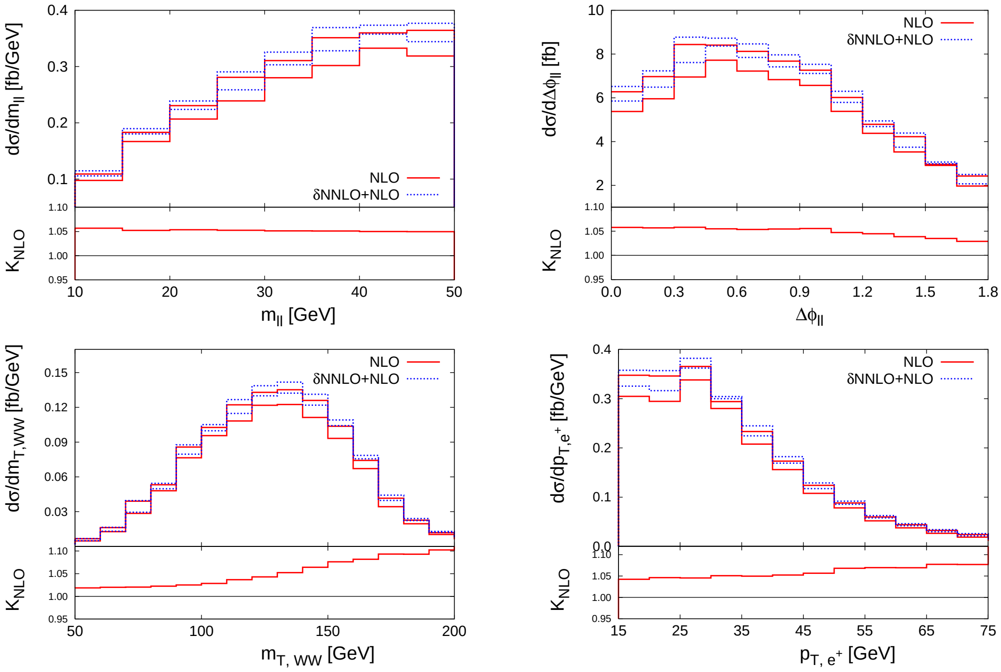

Figure 7.4: Distributions of the invariant mass of the charged lepton system m_{ll}, azimuthal angle between the leptons $\Delta\phi_{ll}$, transverse mass of the W-pair $m_{T,WW}$, and transverse momentum of the positron p_{T,e^+}, for the process $pp \to W^+(\to \nu_e e^+)W^-(\to \mu^-\bar{\nu}_\mu)j$ at the $\sqrt{s} = 8$ TeV LHC. The Higgs cuts described in the text are used. The NLO differential cross-section is shown in red; this cross-section plus the NNLO contribution arising from gluon fusion is shown in blue. The upper and lower bands show the scale variation between $\mu = m_W$ and $\mu = 4m_W$. The factor K_{NLO} as defined in equation (7.4.2) is shown in the lower panes.

Four distributions of interest in Higgs searches at $\sqrt{s} = 8$ TeV – the invariant mass of the lepton system m_{ll}, the azimuthal angle between the leptons $\Delta\phi_{ll}$, the transverse mass of the W-pair $m_{T,WW}$ (defined in equation (5.6.2)), and the transverse momentum of the positron p_{T,e^+} – are shown in figure 7.4. The NLO distributions have been studied in ref. [46]; of interest here is the effect of the gluon fusion contribution $\delta\sigma_{\text{NNLO}}$. The differential *NLO K*-factor is defined as

$$K_{\text{NLO}} = \frac{\sigma_{\text{NLO}} + \delta\sigma_{\text{NNLO}}}{\sigma_{\text{NLO}}} \qquad (7.4.2)$$

evaluated at the central scale $\mu = 2m_W$. This is shown together with the NLO differential cross-sections, with and without δNNLO, for the Higgs cuts. The K-factor is relatively flat in all the distributions except $m_{T,WW}$, where it increases drastically between $m_{T,WW} = 50$ GeV and $m_{T,WW} = 200$ GeV. This distribution is used to test for a Higgs signal [170], since it displays a much sharper drop-off for the signal than for the WW-background [172]. A cut around the Higgs mass $m_H \sim 125$ GeV in this distribution could therefore further increase the signal-to-background ratio, and it is possible that such a cut will be used in future. This would decrease the effect of the NNLO contribution. This further emphasises the highly cut-dependent nature of this contribution: if the experimental setup changes markedly, a re-evaluation of the importance of the background originating from gluon fusion is necessary.

7.5 Conclusion

The gluon fusion contributions to the production of W^+W^- and W^+W^-j at the LHC were studied in this chapter. At lowest order, these amplitudes proceed via a fermion loop, which was computed using generalised unitarity. Consequently, the one-loop amplitude is finite, and first enters the diboson production cross-section as an NNLO correction. This contribution is enhanced by the large gluon flux at the LHC, and thus may be important.

Regarded as a self-contained contribution to the NNLO cross-section, gluon fusion enhances the NLO cross-section of W^+W^- and W^+W^-j by a moderate amount of 3-5%, if generic cuts are used. However, if cuts designed to separate the Higgs from the WW-background are used, then the contribution from gluon fusion becomes more important. The NLO cross-section to W^+W^- is increased by 7-12%, and the NLO cross-section to W^+W^-j is increased by 6-9%. These effects are comparable to the NLO scale uncertainty, as well as to the Higgs signal cross-section. It is noteworthy that the contribution is highly cut dependent. While refs. [42,43] found an enhancement by around 30% due to gluon fusion, this was obtained using much more stringent cuts than those presently employed at the LHC. The current experimental setup justifies a conservative estimate for the gluon fusion effect of 10-15% of the NLO cross-section. The results in this chapter would need to be reviewed should the experimental cuts change drastically.

Chapter 8

Summary and Outlook

8.1 Summary

In this thesis, I have discussed the computation of hadroproduction observables to next-to-leading order (NLO) in perturbative QCD. At this level, both ultraviolet and infrared singularities are present. The UV divergences are dealt with using the process of renormalisation, while IR divergences cancel between the real and virtual (one-loop) cross-sections. On a numerical level, this cancellation is realised within a subtraction scheme using Catani-Seymour dipoles, as described in chapter 2.

In chapter 3, I presented a detailed discussion of the generalised unitarity approach to performing the Ossola-Papadoupoulos-Pittau (OPP) subtraction. This enables one-loop amplitudes to be expressed in terms of known scalar integrals and unitarity coefficients. The functional form of the unitarity coefficients is known, allowing these to be found by solving linear algebraic equations. To do so, virtual particles are put on-shell and tree-level amplitudes are computed. An extension of this procedure to higher dimensions for the internal momenta and polarisations allows the rational part of the amplitude to be found in various regularisation schemes.

I presented techniques used to compute tree-level amplitudes, including the assignment of polarisation vectors in higher dimensions and Berends-Giele currents, in chapter 4. These off-shell currents allow gluons to be added recursively to currents with up to three quark-antiquark pairs and up to two electroweak bosons. They are an efficient yet flexible way to compute colour-ordered primitive amplitudes.

I presented the application of these techniques to the NLO computation of two processes of interest in hadron collider phenomenology: the hadroproduction of W^+W^+jj (chapter 5) and of W^+W^-jj (chapter 6). The hadroproduction of W^+W^+jj is unusual in that the restriction of two observed jets may be lifted without the cross-section diverging. This allows the study of W^+W^+ production in association with zero, one, two, or more jets. The cross-sections for exclusive production in association with zero and one jets and inclusive production in association with two jets show a moderate change from the NLO corrections. However, the factorisation and renormalisation scale dependence is greatly reduced. The same is true of the kinematic distributions. The exclusive production in association with two jets is less satisfactory: the NLO corrections do not reduce the scale uncertainty, and in fact allow the cross-section to become negative for small scales. It is suggested that increasing the jet cut will ameliorate this situation. These results imply that the jets produced in this event are typically quite hard, and that a sizeable number of events with at least two associated jets will have three.

The hadroproduction of W^+W^-jj is of particular interest as a background to Higgs production in association with two jets, with the Higgs decaying via the second-most important channel, $H \to WW$. Production at the Tevatron using a Higgs-search setup, and at the LHC using a more generic setup, were studied. In both cases, the NLO corrections serve to decrease the cross-section by 10-20%, and again greatly reduce the scale uncertainty of both cross-sections and distributions. The dependence of the LHC cross-section on the centre-of-mass energy is found to be close to linear, suggesting a way to scale these results to future energies. Kinematic distributions relevant to Higgs searches, mostly involving the angular distribution of leptons and jets, were also discussed.

Finally, the hadroproduction of W^+W^-j through gluon-fusion was studied in chapter 7. This process first appears at one loop, and thus contributes to the next-to-next-to-leading order (NNLO) corrections. However, in view of the fact that these contributions are both finite and gauge invariant, they can be investigated in isolation from the other NNLO corrections. The large gluon flux at high-energy hadron colliders compensates in part for the additional strong coupling factor. It is found that the effect of these contributions is around 3-5% for generic cuts, but increases to 6-9% for cuts designed to suppress the background relative to Higgs production. This enhancement is much smaller than previously calculated for gluon-induced W^+W^- production, due to the Higgs search cuts being less aggressive. Nevertheless, these NNLO contributions should be taken into account for accurate background calculations.

8.2 Outlook

It is remarkable to think that, as little as twenty years ago, calculations of even simple processes to NLO in pQCD were challenging. Even more remarkable is the fact that, in the 6 years since the first $2 \to 4$ process was computed to this accuracy, almost all of the phenomenologically interesting processes appearing on the Les Houches Experimentalists' Wishlist [64–66] have been computed to NLO. However, I believe there is still progress to be made on (at least) three important fronts.

First, there is the issue of accessibility of NLO computations. Most computations are performed using private codes and the results made public for a choice of experimental setup (centre-of-mass energy, cuts, etc.). If the experimental setup changes, then the results may no longer be valid. Ideally, computations should be publicly available, so that experimentalists can obtain new results if there is a major change in experimental conditions. Availability can be made along two models. The first model is along the lines of `MCFM`: a central program with a large list of available processes, from which the user selects a process and a few simple options reflecting the experimental setup. The second model is more along the lines of `MadEvent`: the user enters arbitrary initial and final state particles, and the experimental setup. The first is simpler to create and faster to run, the second is more flexible. Progress is being made along both fronts: the W^+W^-j process is now available in `MCFM`, while the `GoSam` and `HELAC-NLO` programs perform NLO calculations for processes with user-defined particles. Related to this point are several unanswered questions related to the optimisation of unitarity – for example, are on-shell recursion relations more efficient than off-shell ones [179]?

Second, it is a known fact that NLO calculations are only reliable for inclusive observables. Exclusive observables may be affected significantly by parton showering. Two methods of relating NLO partonic level calculations to parton showering have emerged: `POWHEG` and `MC@NLO`. Implementing more processes, especially processes with jets, in these frameworks is also important. Analytic resummations of large logarithms originating from these low transverse momentum emissions is also an important avenue of progress (see e.g. refs. [180] and [181]).

The third front is NNLO computations. These are challenging even for $2 \to 2$ processes. Yet the gluon-induced W^+W^- NNLO corrections can amount to more than 10% of the total cross-section. It is true that other NNLO corrections may reduce this, but it is not possible to say *a priori* what the effect of a full NNLO calculation would be. Again, progress in this direction is being made (e.g. an NNLO subtraction scheme was suggested in ref. [182], and top pair production is being studied at this order [183, 184]).

With the discovery of the Higgs boson, the study of the electroweak symmetry breaking mechanism has truly begun. Fully understanding the Higgs properties, as well as searching for Beyond the Standard Model Physics, will be a process lasting the rest of the lifetime of the LHC, if not longer. As the experimental programme at the Large Hadron Collider intensifies, the demand for accurate theoretical predictions for both signals and backgrounds will become even greater.

Bibliography

[1] **Tevatron New Physics Higgs Working Group, CDF Collaboration, D0 Collaboration** , *Updated Combination of CDF and D0 Searches for Standard Model Higgs Boson Production with up to 10.0 fb^{-1} of Data*, `arXiv:1207.0449`.

[2] **LEP Working Group for Higgs boson searches, ALEPH Collaboration, DELPHI Collaboration, L3 Collaboration, OPAL Collaboration** , R. Barate et al., *Search for the standard model Higgs boson at LEP*, *Phys.Lett.* **B565** (2003) 61–75, [`hep-ex/0306033`].

[3] **ATLAS Collaboration** , G. Aad et al., *Observation of a new particle in the search for the Standard Model Higgs boson with the ATLAS detector at the LHC*, *Phys.Lett.* **B716** (2012) 1–29, [`arXiv:1207.7214`].

[4] **CMS Collaboration** , S. Chatrchyan et al., *Observation of a new boson at a mass of 125 GeV with the CMS experiment at the LHC*, *Phys.Lett.* **B716** (2012) 30–61, [`arXiv:1207.7235`].

[5] G. Venanzoni, *Latest on g-2 from experiment*, *Frascati Phys.Ser.* **54** (2012) 52–67, [`arXiv:1203.1501`].

[6] **CDF Collaboration** , T. Aaltonen et al., *Evidence for a Mass Dependent Forward-Backward Asymmetry in Top Quark Pair Production*, *Phys.Rev.* **D83** (2011) 112003, [`arXiv:1101.0034`].

[7] S. Dittmaier, S. Dittmaier, C. Mariotti, G. Passarino, R. Tanaka, et al., *Handbook of LHC Higgs Cross Sections: 2. Differential Distributions*, `arXiv:1201.3084`.

[8] J. M. Butterworth, A. R. Davison, M. Rubin, and G. P. Salam, *Jet substructure as a new Higgs search channel at the LHC*, *Phys.Rev.Lett.* **100** (2008) 242001, [`arXiv:0802.2470`].

[9] J. M. Campbell, J. Huston, and W. Stirling, *Hard Interactions of Quarks and Gluons: A Primer for LHC Physics*, *Rept.Prog.Phys.* **70** (2007) 89, [`hep-ph/0611148`].

[10] **LHC Higgs Cross Section Working Group** , S. Dittmaier et al., *Handbook of LHC Higgs Cross Sections: 1. Inclusive Observables*, `arXiv:1101.0593`.

[11] A. Djouadi, M. Spira, and P. Zerwas, *Production of Higgs bosons in proton colliders: QCD corrections*, *Phys.Lett.* **B264** (1991) 440–446.

[12] D. Graudenz, M. Spira, and P. Zerwas, *QCD corrections to Higgs boson production at proton proton colliders*, *Phys.Rev.Lett.* **70** (1993) 1372–1375.

[13] M. Spira, A. Djouadi, D. Graudenz, and P. Zerwas, *Higgs boson production at the LHC*, *Nucl.Phys.* **B453** (1995) 17–82, [`hep-ph/9504378`].

[14] R. V. Harlander and W. B. Kilgore, *Next-to-next-to-leading order Higgs production at hadron colliders*, *Phys.Rev.Lett.* **88** (2002) 201801, [`hep-ph/0201206`].

[15] C. Anastasiou and K. Melnikov, *Higgs boson production at hadron colliders in NNLO QCD*, *Nucl.Phys.* **B646** (2002) 220–256, [`hep-ph/0207004`].

[16] V. Ravindran, J. Smith, and W. L. van Neerven, *NNLO corrections to the total cross-section for Higgs boson production in hadron hadron collisions*, *Nucl.Phys.* **B665** (2003) 325–366, [`hep-ph/0302135`].

[17] D. de Florian, M. Grazzini, and Z. Kunszt, *Higgs production with large transverse momentum in hadronic collisions at next-to-leading order*, *Phys.Rev.Lett.* **82** (1999) 5209–5212, [`hep-ph/9902483`].

[18] V. Ravindran, J. Smith, and W. Van Neerven, *Next-to-leading order QCD corrections to differential distributions of Higgs boson production in hadron hadron collisions*, *Nucl.Phys.* **B634** (2002) 247–290, [`hep-ph/0201114`].

[19] C. J. Glosser and C. R. Schmidt, *Next-to-leading corrections to the Higgs boson transverse momentum spectrum in gluon fusion*, *JHEP* **0212** (2002) 016, [`hep-ph/0209248`].

[20] T. Figy, C. Oleari, and D. Zeppenfeld, *Next-to-leading order jet distributions for Higgs boson production via weak boson fusion*, *Phys.Rev.* **D68** (2003) 073005, [`hep-ph/0306109`].

[21] E. L. Berger and J. M. Campbell, *Higgs boson production in weak boson fusion at next-to-leading order*, *Phys.Rev.* **D70** (2004) 073011, [`hep-ph/0403194`].

[22] J. M. Campbell, R. K. Ellis, and G. Zanderighi, *Next-to-Leading order Higgs + 2 jet production via gluon fusion*, *JHEP* **0610** (2006) 028, [`hep-ph/0608194`].

[23] J. M. Campbell, R. K. Ellis, F. Maltoni, and S. Willenbrock, *Higgs-Boson production in association with a single bottom quark*, *Phys.Rev.* **D67** (2003) 095002, [`hep-ph/0204093`].

[24] J. M. Campbell, R. K. Ellis, and C. Williams, *Gluon-Gluon Contributions to W^+W^- Production and Higgs Interference Effects*, *JHEP* **1110** (2011) 005, [`arXiv:1107.5569`].

[25] J. M. Campbell, R. K. Ellis, and C. Williams, *Hadronic production of a Higgs boson and two jets at next-to-leading order*, *Phys.Rev.* **D81** (2010) 074023, [`arXiv:1001.4495`].

[26] M. Ciccolini, A. Denner, and S. Dittmaier, *Strong and electroweak corrections to the production of Higgs + 2 jets via weak interactions at the LHC*, *Phys.Rev.Lett.* **99** (2007) 161803, [`arXiv:0707.0381`].

[27] M. Ciccolini, A. Denner, and S. Dittmaier, *Electroweak and QCD corrections to Higgs production via vector-boson fusion at the LHC*, *Phys.Rev.* **D77** (2008) 013002, [`arXiv:0710.4749`].

[28] K. Arnold, M. Bahr, G. Bozzi, F. Campanario, C. Englert, et al., *VBFNLO: A Parton level Monte Carlo for processes with electroweak bosons*, *Comput.Phys.Commun.* **180** (2009) 1661–1670, [`arXiv:0811.4559`].

[29] T. Sjostrand, S. Mrenna, and P. Z. Skands, *A Brief Introduction to PYTHIA 8.1*, *Comput.Phys.Commun.* **178** (2008) 852–867, [`arXiv:0710.3820`].

[30] M. Bahr, S. Gieseke, M. Gigg, D. Grellscheid, K. Hamilton, et al., *Herwig++ Physics and Manual*, *Eur.Phys.J.* **C58** (2008) 639–707, [`arXiv:0803.0883`].

[31] S. Alioli, P. Nason, C. Oleari, and E. Re, *NLO Higgs boson production via gluon fusion matched with shower in POWHEG*, *JHEP* **0904** (2009) 002, [`arXiv:0812.0578`].

[32] P. Nason and C. Oleari, *NLO Higgs boson production via vector-boson fusion matched with shower in POWHEG*, *JHEP* **1002** (2010) 037, [`arXiv:0911.5299`].

[33] J. M. Campbell, R. K. Ellis, R. Frederix, P. Nason, C. Oleari, et al., *NLO Higgs Boson Production Plus One and Two Jets Using the POWHEG BOX, MadGraph4 and MCFM*, *JHEP* **1207** (2012) 092, [`arXiv:1202.5475`].

[34] S. Hoeche, F. Krauss, M. Schonherr, and F. Siegert, *A critical appraisal of NLO+PS matching methods*, *JHEP* **1209** (2012) 049, [`arXiv:1111.1220`].

[35] J. Ohnemus, *An Order $\alpha^{-}s$ calculation of hadronic $W^{\pm}Z$ production*, *Phys.Rev.* **D44** (1991) 3477–3489.

[36] S. Frixione, *A Next-to-leading order calculation of the cross-section for the production of $W^{+}W^{-}$ pairs in hadronic collisions*, *Nucl.Phys.* **B410** (1993) 280–324.

[37] L. J. Dixon, Z. Kunszt, and A. Signer, *Helicity amplitudes for O(alpha-s) production of $W^{+}W^{-}$, $W^{\pm}Z$, ZZ, $W^{\pm}\gamma$, or $Z\gamma$ pairs at hadron colliders*, *Nucl.Phys.* **B531** (1998) 3–23, [`hep-ph/9803250`].

[38] L. J. Dixon, Z. Kunszt, and A. Signer, *Vector boson pair production in hadronic collisions at order α_s : Lepton correlations and anomalous couplings*, *Phys.Rev.* **D60** (1999) 114037, [`hep-ph/9907305`].

[39] J. M. Campbell and R. K. Ellis, *An Update on vector boson pair production at hadron colliders*, *Phys.Rev.* **D60** (1999) 113006, [`hep-ph/9905386`].

[40] T. Melia, P. Nason, R. Röntsch, and G. Zanderighi, *$W^{+}W^{-}$, WZ and ZZ production in the POWHEG BOX*, *JHEP* **1111** (2011) 078, [`arXiv:1107.5051`].

[41] S. Frixione and B. R. Webber, *Matching NLO QCD computations and parton shower simulations*, *JHEP* **0206** (2002) 029, [`hep-ph/0204244`].

[42] T. Binoth, M. Ciccolini, N. Kauer, and M. Kramer, *Gluon-induced WW background to Higgs boson searches at the LHC*, *JHEP* **0503** (2005) 065, [`hep-ph/0503094`].

[43] T. Binoth, M. Ciccolini, N. Kauer, and M. Kramer, *Gluon-induced W-boson pair production at the LHC*, *JHEP* **0612** (2006) 046, [`hep-ph/0611170`].

[44] J. M. Campbell, R. K. Ellis, and G. Zanderighi, *Next-to-leading order predictions for $WW+1$ jet distributions at the LHC*, *JHEP* **0712** (2007) 056, [`arXiv:0710.1832`].

[45] S. Dittmaier, S. Kallweit, and P. Uwer, *NLO QCD corrections to WW+jet production at hadron colliders*, *Phys.Rev.Lett.* **100** (2008) 062003, [`arXiv:0710.1577`].

[46] S. Dittmaier, S. Kallweit, and P. Uwer, *NLO QCD corrections to pp/ppbar → WW +jet+X including leptonic W-boson decays*, *Nucl.Phys.* **B826** (2010) 18–70, [`arXiv:0908.4124`].

[47] A. Denner and S. Dittmaier, *Reduction of one loop tensor five point integrals*, *Nucl.Phys.* **B658** (2003) 175–202, [`hep-ph/0212259`].

[48] A. Denner and S. Dittmaier, *Reduction schemes for one-loop tensor integrals*, *Nucl.Phys.* **B734** (2006) 62–115, [`hep-ph/0509141`].

[49] T. Binoth, J. P. Guillet, G. Heinrich, E. Pilon, and C. Schubert, *An Algebraic/numerical formalism for one-loop multi-leg amplitudes*, *JHEP* **0510** (2005) 015, [`hep-ph/0504267`].

[50] G. Passarino and M. Veltman, *One Loop Corrections for e+ e- Annihilation Into mu+ mu- in the Weinberg Model*, *Nucl.Phys.* **B160** (1979) 151.

[51] A. Bredenstein, A. Denner, S. Dittmaier, and S. Pozzorini, *NLO QCD corrections to pp →t anti-t b anti-b + X at the LHC*, *Phys.Rev.Lett.* **103** (2009) 012002, [`arXiv:0905.0110`].

[52] A. Denner, S. Dittmaier, S. Kallweit, and S. Pozzorini, *NLO QCD corrections to WWbb production at hadron colliders*, *Phys.Rev.Lett.* **106** (2011) 052001, [`arXiv:1012.3975`].

[53] A. Bredenstein, A. Denner, S. Dittmaier, and S. Pozzorini, *NLO QCD Corrections to Top Anti-Top Bottom Anti-Bottom Production at the LHC: 2. full hadronic results*, *JHEP* **1003** (2010) 021, [`arXiv:1001.4006`].

[54] F. Campanario, C. Englert, M. Rauch, and D. Zeppenfeld, *Precise predictions for $W\gamma\gamma$ +jet production at hadron colliders*, *Phys.Lett.* **B704** (2011) 515–519, [`arXiv:1106.4009`].

[55] R. Britto, F. Cachazo, and B. Feng, *Coplanarity in twistor space of N=4 next-to-MHV one-loop amplitude coefficients*, *Phys.Lett.* **B611** (2005) 167–172, [`hep-th/0411107`].

[56] R. Britto, F. Cachazo, and B. Feng, *Generalized unitarity and one-loop amplitudes in N=4 super-Yang-Mills*, *Nucl.Phys.* **B725** (2005) 275–305, [`hep-th/0412103`].

[57] G. Ossola, C. G. Papadopoulos, and R. Pittau, *Reducing full one-loop amplitudes to scalar integrals at the integrand level*, *Nucl.Phys.* **B763** (2007) 147–169, [`hep-ph/0609007`].

[58] D. Forde, *Direct extraction of one-loop integral coefficients*, *Phys.Rev.* **D75** (2007) 125019, [`arXiv:0704.1835`].

[59] S. Badger, *Direct Extraction Of One Loop Rational Terms*, *JHEP* **0901** (2009) 049, [`arXiv:0806.4600`].

[60] P. Mastrolia, *Double-Cut of Scattering Amplitudes and Stokes' Theorem*, *Phys.Lett.* **B678** (2009) 246–249, [`arXiv:0905.2909`].

[61] R. K. Ellis, W. Giele, and Z. Kunszt, *A Numerical Unitarity Formalism for Evaluating One-Loop Amplitudes*, *JHEP* **0803** (2008) 003, [`arXiv:0708.2398`].

[62] W. T. Giele, Z. Kunszt, and K. Melnikov, *Full one-loop amplitudes from tree amplitudes*, *JHEP* **0804** (2008) 049, [`arXiv:0801.2237`].

[63] R. K. Ellis, W. T. Giele, Z. Kunszt, and K. Melnikov, *Masses, fermions and generalized D-dimensional unitarity*, *Nucl.Phys.* **B822** (2009) 270–282, [`arXiv:0806.3467`].

[64] C. Buttar, S. Dittmaier, V. Drollinger, S. Frixione, A. Nikitenko, et al., *Les houches physics at TeV colliders 2005, standard model and Higgs working group: Summary report*, `hep-ph/0604120`.

[65] **NLO Multileg Working Group** , Z. Bern et al., *The NLO multileg working group: Summary report*, `arXiv:0803.0494`.

[66] **SM and NLO Multileg Working Group** , J. Andersen et al., *The SM and NLO Multileg Working Group: Summary report*, `arXiv:1003.1241`.

[67] T. Binoth, N. Greiner, A. Guffanti, J. Reuter, J.-P. Guillet, et al., *Next-to-leading order QCD corrections to pp $\to$ b anti-b b anti-b + X at the LHC: the quark induced case*, *Phys.Lett.* **B685** (2010) 293–296, [`arXiv:0910.4379`].

[68] C. Berger, Z. Bern, L. J. Dixon, F. Febres Cordero, D. Forde, et al., *Next-to-Leading Order QCD Predictions for W+3-Jet Distributions at Hadron Colliders*, *Phys.Rev.* **D80** (2009) 074036, [`arXiv:0907.1984`].

[69] R. K. Ellis, K. Melnikov, and G. Zanderighi, *Generalized unitarity at work: first NLO QCD results for hadronic W+ 3 jet production*, *JHEP* **0904** (2009) 077, [`arXiv:0901.4101`].

[70] R. K. Ellis, K. Melnikov, and G. Zanderighi, *W+3 jet production at the Tevatron*, *Phys.Rev.* **D80** (2009) 094002, [`arXiv:0906.1445`].

[71] G. Bevilacqua, M. Czakon, C. Papadopoulos, R. Pittau, and M. Worek, *Assault on the NLO Wishlist: pp $\to$ t anti-t b anti-b*, *JHEP* **0909** (2009) 109, [`arXiv:0907.4723`].

[72] G. Bevilacqua, M. Czakon, M. Garzelli, A. van Hameren, Y. Malamos, et al., *NLO QCD calculations with HELAC-NLO*, *Nucl.Phys.Proc.Suppl.* **205-206** (2010) 211–217, [`arXiv:1007.4918`].

[73] G. Bevilacqua, M. Czakon, A. van Hameren, C. G. Papadopoulos, and M. Worek, *Complete off-shell effects in top quark pair hadroproduction with leptonic decay at next-to-leading order*, *JHEP* **1102** (2011) 083, [`arXiv:1012.4230`].

[74] G. Bevilacqua, M. Czakon, C. Papadopoulos, and M. Worek, *Dominant QCD Backgrounds in Higgs Boson Analyses at the LHC: A Study of pp $\to$ t anti-t + 2 jets at Next-To-Leading Order*, *Phys.Rev.Lett.* **104** (2010) 162002, [`arXiv:1002.4009`].

[75] C. Berger, Z. Bern, L. J. Dixon, F. Febres Cordero, D. Forde, et al., *Precise Predictions for W + 4 Jet Production at the Large Hadron Collider*, *Phys.Rev.Lett.* **106** (2011) 092001, [`arXiv:1009.2338`].

[76] C. Berger, Z. Bern, L. J. Dixon, F. Febres Cordero, D. Forde, et al., *Next-to-Leading Order QCD Predictions for Z, γ^* +3-Jet Distributions at the Tevatron*, *Phys.Rev.* **D82** (2010) 074002, [`arXiv:1004.1659`].

[77] T. Melia, K. Melnikov, R. Röntsch, and G. Zanderighi, *Next-to-leading order QCD predictions for W^+W^+jj production at the LHC*, *JHEP* **1012** (2010) 053, [`arXiv:1007.5313`].

[78] G. Bevilacqua, M. Czakon, C. Papadopoulos, and M. Worek, *Hadronic top-quark pair production in association with two jets at Next-to-Leading Order QCD*, *Phys.Rev.* **D84** (2011) 114017, [`arXiv:1108.2851`].

[79] N. Greiner, A. Guffanti, T. Reiter, and J. Reuter, *NLO QCD corrections to the production of two bottom-antibottom pairs at the LHC*, *Phys.Rev.Lett.* **107** (2011) 102002, [`arXiv:1105.3624`].

[80] H. Ita, Z. Bern, L. Dixon, F. Febres Cordero, D. Kosower, et al., *Precise Predictions for Z + 4 Jets at Hadron Colliders*, *Phys.Rev.* **D85** (2012) 031501, [`arXiv:1108.2229`].

[81] Z. Bern, G. Diana, L. Dixon, F. Febres Cordero, S. Hoeche, et al., *Four-Jet Production at the Large Hadron Collider at Next-to-Leading Order in QCD*, *Phys.Rev.Lett.* **109** (2012) 042001, [`arXiv:1112.3940`].

[82] T. Melia, K. Melnikov, R. Röntsch, and G. Zanderighi, *NLO QCD corrections for W^+W^- pair production in association with two jets at hadron colliders*, *Phys.Rev.* **D83** (2011) 114043, [`arXiv:1104.2327`].

[83] **SM AND NLO MULTILEG and SM MC Working Groups** , J. Alcaraz Maestre et al., *The SM and NLO Multileg and SM MC Working Groups: Summary Report*, `arXiv:1203.6803`.

[84] T. Melia, K. Melnikov, R. Röntsch, M. Schulze, and G. Zanderighi, *Gluon fusion contribution to W^+W^- + jet production*, *JHEP* **1208** (2012) 115, [`arXiv:1205.6987`].

[85] R. K. Ellis, Z. Kunszt, K. Melnikov, and G. Zanderighi, *One-loop calculations in quantum field theory: from Feynman diagrams to unitarity cuts*, *Phys.Rept.* **518** (2012) 141–250, [`arXiv:1105.4319`].

[86] R. K. Ellis, W. Giele, Z. Kunszt, K. Melnikov, and G. Zanderighi, *One-loop amplitudes for W^+ 3 jet production in hadron collisions*, *JHEP* **0901** (2009) 012, [`arXiv:0810.2762`].

[87] K. Melnikov and G. Zanderighi, *W+3 jet production at the LHC as a signal or background*, *Phys.Rev.* **D81** (2010) 074025, [`arXiv:0910.3671`].

[88] S. Biswas, K. Melnikov, and M. Schulze, *Next-to-leading order QCD effects and the top quark mass measurements at the LHC*, *JHEP* **1008** (2010) 048, [`arXiv:1006.0910`].

[89] K. Melnikov and M. Schulze, *NLO QCD corrections to top quark pair production in association with one hard jet at hadron colliders*, *Nucl.Phys.* **B840** (2010) 129–159, [`arXiv:1004.3284`].

[90] K. Melnikov and M. Schulze, *Top quark spin correlations at the Tevatron and the LHC*, *Phys.Lett.* **B700** (2011) 17–20, [`arXiv:1103.2122`].

[91] K. Melnikov, A. Scharf, and M. Schulze, *Top quark pair production in association with a jet: QCD corrections and jet radiation in top quark decays*, *Phys.Rev.* **D85** (2012) 054002, [`arXiv:1111.4991`].

[92] K. Melnikov, M. Schulze, and A. Scharf, *QCD corrections to top quark pair production in association with a photon at hadron colliders*, *Phys.Rev.* **D83** (2011) 074013, [`arXiv:1102.1967`].

[93] M. Peskin and D. Schroeder, *An Introduction to Quantum Field Theory.* Westview Press, 1995.

[94] R. K. Ellis, W. Stirling, and B. Webber, *QCD and Collider Physics.* Cambridge University Press, 1996.

[95] Y. L. Dokshitzer, *Calculation of the Structure Functions for Deep Inelastic Scattering and e+ e- Annihilation by Perturbation Theory in Quantum Chromodynamics.*, *Sov.Phys.JETP* **46** (1977) 641–653.

[96] V. Gribov and L. Lipatov, *Deep inelastic e p scattering in perturbation theory*, *Sov.J.Nucl.Phys.* **15** (1972) 438–450.

[97] G. Altarelli and G. Parisi, *Asymptotic Freedom in Parton Language*, *Nucl.Phys.* **B126** (1977) 298.

[98] A. Martin, W. Stirling, R. Thorne, and G. Watt, *Parton distributions for the LHC*, *Eur.Phys.J.* **C63** (2009) 189–285, [`arXiv:0901.0002`].

[99] R. D. Ball, L. Del Debbio, S. Forte, A. Guffanti, J. I. Latorre, et al., *A first unbiased global NLO determination of parton distributions and their uncertainties*, *Nucl.Phys.* **B838** (2010) 136–206, [`arXiv:1002.4407`].

[100] H.-L. Lai, M. Guzzi, J. Huston, Z. Li, P. M. Nadolsky, et al., *New parton distributions for collider physics*, *Phys.Rev.* **D82** (2010) 074024, [`arXiv:1007.2241`].

[101] S. Glashow, *Partial Symmetries of Weak Interactions*, *Nucl.Phys.* **22** (1961) 579–588.

[102] S. Weinberg, *A Model of Leptons*, *Phys.Rev.Lett.* **19** (1967) 1264–1266.

[103] A. Salam, *Weak and Electromagnetic Interactions*, *Conf.Proc.* **C680519** (1968) 367–377.

[104] P. W. Higgs, *Broken symmetries, massless particles and gauge fields*, *Phys.Lett.* **12** (1964) 132–133.

[105] P. W. Higgs, *Broken Symmetries and the Masses of Gauge Bosons*, *Phys.Rev.Lett.* **13** (1964) 508–509.

[106] P. W. Higgs, *Spontaneous Symmetry Breakdown without Massless Bosons*, *Phys.Rev.* **145** (1966) 1156–1163.

[107] F. Englert and R. Brout, *Broken Symmetry and the Mass of Gauge Vector Mesons*, *Phys.Rev.Lett.* **13** (1964) 321–323.

[108] A. Denner, *Techniques for calculation of electroweak radiative corrections at the one loop level and results for W physics at LEP-200*, *Fortsch.Phys.* **41** (1993) 307–420, [`arXiv:0709.1075`].

[109] S. D. Ellis and D. E. Soper, *Successive combination jet algorithm for hadron collisions*, *Phys.Rev.* **D48** (1993) 3160–3166, [`hep-ph/9305266`].

[110] S. Catani, Y. L. Dokshitzer, M. Seymour, and B. Webber, *Longitudinally invariant K_t clustering algorithms for hadron hadron collisions*, *Nucl.Phys.* **B406** (1993) 187–224.

[111] M. Cacciari, G. P. Salam, and G. Soyez, *The Anti-k(t) jet clustering algorithm*, *JHEP* **0804** (2008) 063, [`arXiv:0802.1189`].

[112] G. 't Hooft and M. Veltman, *Regularization and Renormalization of Gauge Fields*, *Nucl.Phys.* **B44** (1972) 189–213.

[113] R. Gastmans and R. Meuldermans, *Dimensional regularization of the infrared problem*, *Nucl.Phys.* **B63** (1973) 277–284.

[114] Z. Kunszt, A. Signer, and Z. Trocsanyi, *Singular terms of helicity amplitudes at one loop in QCD and the soft limit of the cross-sections of multiparton processes*, *Nucl.Phys.* **B420** (1994) 550–564, [`hep-ph/9401294`].

[115] R. K. Ellis, D. Ross, and A. Terrano, *The Perturbative Calculation of Jet Structure in e+ e- Annihilation*, *Nucl.Phys.* **B178** (1981) 421.

[116] S. Catani and M. Seymour, *A General algorithm for calculating jet cross-sections in NLO QCD*, *Nucl.Phys.* **B485** (1997) 291–419, [`hep-ph/9605323`].

[117] S. Catani and M. Seymour, *The Dipole formalism for the calculation of QCD jet cross-sections at next-to-leading order*, *Phys.Lett.* **B378** (1996) 287–301, [`hep-ph/9602277`].

[118] S. Catani, S. Dittmaier, M. H. Seymour, and Z. Trocsanyi, *The Dipole formalism for next-to-leading order QCD calculations with massive partons*, *Nucl.Phys.* **B627** (2002) 189–265, [`hep-ph/0201036`].

[119] S. Frixione, Z. Kunszt, and A. Signer, *Three jet cross-sections to next-to-leading order*, *Nucl.Phys.* **B467** (1996) 399–442, [`hep-ph/9512328`].

[120] S. Frixione, *A General approach to jet cross-sections in QCD*, *Nucl.Phys.* **B507** (1997) 295–314, [`hep-ph/9706545`].

[121] D. A. Kosower, *Antenna factorization of gauge theory amplitudes*, *Phys.Rev.* **D57** (1998) 5410–5416, [`hep-ph/9710213`].

[122] A. Gehrmann-De Ridder, T. Gehrmann, and E. N. Glover, *Antenna subtraction at NNLO*, *JHEP* **0509** (2005) 056, [`hep-ph/0505111`].

[123] Z. Nagy and D. E. Soper, *Parton showers with quantum interference*, *JHEP* **0709** (2007) 114, [`arXiv:0706.0017`].

[124] C. Chung, M. Kramer, and T. Robens, *An alternative subtraction scheme for next-to-leading order QCD calculations*, *JHEP* **1106** (2011) 144, [`arXiv:1012.4948`].

[125] Z. Bern and D. A. Kosower, *Color decomposition of one loop amplitudes in gauge theories*, *Nucl.Phys.* **B362** (1991) 389–448.

[126] Z. Bern, L. J. Dixon, and D. A. Kosower, *One loop corrections to two quark three gluon amplitudes*, *Nucl.Phys.* **B437** (1995) 259–304, [`hep-ph/9409393`].

[127] D. Melrose, *Reduction of Feynman diagrams*, *Nuovo Cim.* **40** (1965) 181–213.

[128] W. van Neerven and J. Vermaseren, *Large Loop Integrals*, *Phys.Lett.* **B137** (1984) 241.

[129] Z. Bern, L. J. Dixon, and D. A. Kosower, *Dimensionally regulated one loop integrals*, *Phys.Lett.* **B302** (1993) 299–308, [`hep-ph/9212308`].

[130] G. 't Hooft and M. Veltman, *Scalar One Loop Integrals*, *Nucl.Phys.* **B153** (1979) 365–401.

[131] A. Denner, U. Nierste, and R. Scharf, *A Compact expression for the scalar one loop four point function*, *Nucl.Phys.* **B367** (1991) 637–656.

[132] R. K. Ellis and G. Zanderighi, *Scalar one-loop integrals for QCD*, *JHEP* **0802** (2008) 002, [`arXiv:0712.1851`].

[133] R. Cutkosky, *Singularities and discontinuities of Feynman amplitudes*, *J.Math.Phys.* **1** (1960) 429–433.

[134] Z. Bern, L. J. Dixon, D. C. Dunbar, and D. A. Kosower, *Fusing gauge theory tree amplitudes into loop amplitudes*, *Nucl.Phys.* **B435** (1995) 59–101, [`hep-ph/9409265`].

[135] Z. Bern, L. J. Dixon, and D. A. Kosower, *One loop amplitudes for e+ e- to four partons*, *Nucl.Phys.* **B513** (1998) 3–86, [`hep-ph/9708239`].

[136] Z. Bern, L. J. Dixon, and D. A. Kosower, *On-Shell Methods in Perturbative QCD*, *Annals Phys.* **322** (2007) 1587–1634, [`arXiv:0704.2798`].

[137] M. L. Mangano and S. J. Parke, *Multiparton amplitudes in gauge theories*, *Phys.Rept.* **200** (1991) 301–367, [`hep-th/0509223`].

[138] T. Binoth, J. P. Guillet, and G. Heinrich, *Algebraic evaluation of rational polynomials in one-loop amplitudes*, *JHEP* **0702** (2007) 013, [`hep-ph/0609054`].

[139] Z. Xiao, G. Yang, and C.-J. Zhu, *The Rational Part of QCD Amplitude. III. The Six-Gluon*, *Nucl.Phys.* **B758** (2006) 53–89, [`hep-ph/0607017`].

[140] G. Ossola, C. G. Papadopoulos, and R. Pittau, *Numerical evaluation of six-photon amplitudes*, *JHEP* **0707** (2007) 085, [`arXiv:0704.1271`].

[141] Z. Bern, L. J. Dixon, and D. A. Kosower, *Bootstrapping multi-parton loop amplitudes in QCD*, *Phys.Rev.* **D73** (2006) 065013, [`hep-ph/0507005`].

[142] C. F. Berger, Z. Bern, L. J. Dixon, D. Forde, and D. A. Kosower, *Bootstrapping One-Loop QCD Amplitudes with General Helicities*, *Phys.Rev.* **D74** (2006) 036009, [`hep-ph/0604195`].

[143] C. F. Berger, Z. Bern, L. J. Dixon, D. Forde, and D. A. Kosower, *All One-loop Maximally Helicity Violating Gluonic Amplitudes in QCD*, *Phys.Rev.* **D75** (2007) 016006, [`hep-ph/0607014`].

[144] Z. Bern, A. De Freitas, L. J. Dixon, and H. Wong, *Supersymmetric regularization, two loop QCD amplitudes and coupling shifts*, *Phys.Rev.* **D66** (2002) 085002, [`hep-ph/0202271`].

[145] F. A. Berends and W. Giele, *Recursive Calculations for Processes with n Gluons*, *Nucl.Phys.* **B306** (1988) 759.

[146] J. Collins, *An Introduction to Renormalization, the Renormalization Group and the Operator-Product Expansion.* Cambridge University Press, 1984.

[147] W. Giele and G. Zanderighi, *On the Numerical Evaluation of One-Loop Amplitudes: The Gluonic Case*, *JHEP* **0806** (2008) 038, [`arXiv:0805.2152`].

[148] T. Melia, P. Nason, R. Röntsch, and G. Zanderighi, *W^+W^+ plus dijet production in the POWHEGBOX*, *Eur.Phys.J.* **C71** (2011) 1670, [`arXiv:1102.4846`].

[149] A. Kulesza and W. J. Stirling, *Like sign W boson production at the LHC as a probe of double parton scattering*, *Phys.Lett.* **B475** (2000) 168–175, [`hep-ph/9912232`].

[150] B. Jager, C. Oleari, and D. Zeppenfeld, *Next-to-leading order QCD corrections to W^+W^+ jj and W^-W^- jj production via weak-boson fusion*, *Phys.Rev.* **D80** (2009) 034022, [`arXiv:0907.0580`].

[151] E. Maina, *Multiple Parton Interactions in Z+4j, $W^{+-}W^{+-}$ + 0/2j and W^+W^- + 2j production at the LHC*, *JHEP* **0909** (2009) 081, [`arXiv:0909.1586`].

[152] J. R. Gaunt, C.-H. Kom, A. Kulesza, and W. J. Stirling, *Same-sign W pair production as a probe of double parton scattering at the LHC*, *Eur.Phys.J.* **C69** (2010) 53–65, [`arXiv:1003.3953`].

[153] P. Bartalini, E. Berger, B. Blok, G. Calucci, R. Corke, et al., *Multi-Parton Interactions at the LHC*, `arXiv:1111.0469`.

[154] H. Dreiner, S. Grab, M. Kramer, and M. Trenkel, *Supersymmetric NLO QCD corrections to resonant slepton production and signals at the Tevatron and the CERN LHC*, *Phys.Rev.* **D75** (2007) 035003, [`hep-ph/0611195`].

[155] T. Han, I. Lewis, and T. McElmurry, *QCD Corrections to Scalar Diquark Production at Hadron Colliders*, *JHEP* **1001** (2010) 123, [`arXiv:0909.2666`].

[156] J. Maalampi and N. Romanenko, *Single production of doubly charged Higgs bosons at hadron colliders*, *Phys.Lett.* **B532** (2002) 202–208, [`hep-ph/0201196`].

[157] A. Akeroyd and S. Moretti, *Production of doubly charged scalars from the decay of a heavy SM-like Higgs boson in the Higgs Triplet Model*, *Phys.Rev.* **D84** (2011) 035028, [`arXiv:1106.3427`].

[158] J. Alwall, P. Demin, S. de Visscher, R. Frederix, M. Herquet, et al., *MadGraph/MadEvent v4: The New Web Generation*, *JHEP* **0709** (2007) 028, [`arXiv:0706.2334`].

[159] Z. Kunszt, A. Signer, and Z. Trocsanyi, *One loop helicity amplitudes for all $2 \to 2$ processes in QCD and $N = 1$ supersymmetric Yang-Mills theory*, *Nucl.Phys.* **B411** (1994) 397–442, [`hep-ph/9305239`].

[160] `mcfm.fnal.gov/`.

[161] Z. Nagy, *Next-to-leading order calculation of three jet observables in hadron hadron collision*, *Phys.Rev.* **D68** (2003) 094002, [`hep-ph/0307268`].

[162] Z. Nagy and Z. Trocsanyi, *Next-to-leading order calculation of four jet observables in electron positron annihilation*, *Phys.Rev.* **D59** (1999) 014020, [`hep-ph/9806317`].

[163] P. Nogueira, *Automatic Feynman graph generation*, *J.Comput.Phys.* **105** (1993) 279–289.

[164] J. Vermaseren, *New features of FORM*, `math-ph/0010025`.

[165] G. Cullen, N. Greiner, G. Heinrich, G. Luisoni, P. Mastrolia, et al., *GoSam: A Program for Automated One-Loop Calculations*, *J.Phys.Conf.Ser.* **368** (2012) 012056, [`arXiv:1111.6534`].

[166] G. Cullen, N. Greiner, G. Heinrich, G. Luisoni, P. Mastrolia, et al., *Automated One-Loop Calculations with GoSam*, `arXiv:1201.2782`.

[167] G. Bevilacqua, M. Czakon, M. Garzelli, A. van Hameren, A. Kardos, et al., *HELAC-NLO*, `arXiv:1110.1499`.

[168] M. Cacciari and G. P. Salam, *Dispelling the N^3 myth for the k_t jet-finder*, *Phys.Lett.* **B641** (2006) 57–61, [`hep-ph/0512210`].

[169] M. Cacciari, G. P. Salam, and G. Soyez, *FastJet User Manual*, *Eur.Phys.J.* **C72** (2012) 1896, [`arXiv:1111.6097`].

[170] **ATLAS Collaboration** , *Search for the Standard Model Higgs boson in the $H \to WW^{(*)} \to l\nu l\nu$ decay mode with 4.7 fb^{-1} of ATLAS data at $\sqrt{s} = 7$ TeV*, *ATLAS-CONF-2012-12* (2012).

[171] C. Anastasiou, G. Dissertori, M. Grazzini, F. Stockli, and B. R. Webber, *Perturbative QCD effects and the search for a $H \to WW \to l\nu l\nu$ signal at the Tevatron*, *JHEP* **0908** (2009) 099, [`arXiv:0905.3529`].

[172] G. Klämke and D. Zeppenfeld, *Higgs plus two jet production via gluon fusion as a signal at the CERN LHC*, *JHEP* **0704** (2007) 052, [`hep-ph/0703202`].

[173] V. Hankele, G. Klämke, D. Zeppenfeld, and T. Figy, *Anomalous Higgs boson couplings in vector boson fusion at the CERN LHC*, *Phys.Rev.* **D74** (2006) 095001, [`hep-ph/0609075`].

[174] B. Jager, C. Oleari, and D. Zeppenfeld, *Next-to-leading order QCD corrections to W^+W^- production via vector-boson fusion*, *JHEP* **0607** (2006) 015, [`hep-ph/0603177`].

[175] N. Greiner, G. Heinrich, P. Mastrolia, G. Ossola, T. Reiter, et al., *NLO QCD corrections to the production of W^+W^- plus two jets at the LHC*, *Phys.Lett.* **B713** (2012) 277–283, [`arXiv:1202.6004`].

[176] **CDF Collaboration** , *Search for $H \to WW^*$ production at CDF using 4.8 fb^{-1} of data*, *CDF Note 9887.*

[177] **ATLAS Collaboration** , G. Aad et al., *Measurement of the top quark-pair production cross section with ATLAS in pp collisions at $\sqrt{s} = 7$ TeV*, *Eur.Phys.J.* **C71** (2011) 1577, [`arXiv:1012.1792`].

[178] **CMS Collaboration** , V. Khachatryan et al., *First Measurement of the Cross Section for Top-Quark Pair Production in Proton-Proton Collisions at $\sqrt{s} = 7$ TeV*, *Phys.Lett.* **B695** (2011) 424–443, [`arXiv:1010.5994`].

[179] S. Badger, B. Biedermann, L. Hackl, J. Plefka, T. Schuster, et al., *Comparing efficient computation methods for massless QCD tree amplitudes: Closed Analytic Formulae versus Berends-Giele Recursion*, `arXiv:1206.2381`.

[180] D. de Florian, G. Ferrera, M. Grazzini, and D. Tommasini, *Transverse-momentum resummation: Higgs boson production at the Tevatron and the LHC*, *JHEP* **1111** (2011) 064, [`arXiv:1109.2109`].

[181] S. Dawson, T. Han, W. Lai, A. Leibovich, and I. Lewis, *Resummation Effects in Vector-Boson and Higgs Associated Production*, *Phys.Rev.* **D86** (2012) 074007, [`arXiv:1207.4207`].

[182] R. Boughezal, K. Melnikov, and F. Petriello, *A subtraction scheme for NNLO computations*, *Phys.Rev.* **D85** (2012) 034025, [`arXiv:1111.7041`].

[183] P. Baernreuther, M. Czakon, and A. Mitov, *Percent Level Precision Physics at the Tevatron: First Genuine NNLO QCD Corrections to $q\bar{q} \to t\bar{t} + X$*, *Phys.Rev.Lett.* **109** (2012) 132001, [`arXiv:1204.5201`].

[184] M. Czakon, A. Mitov, and A. Mitov, *NNLO corrections to top-pair production at hadron colliders: the all-fermionic scattering channels*, `arXiv:1207.0236`.